RECENT ADVANCES IN RECOGNITION OF BIOACTIVE PHYTONUTRIENTS FOR SPECIFIC TARGETS IN PLANT FOODS

EDITED BY: Zhiqiang Wang, Mingquan Guo and Soon Sung Lim
PUBLISHED IN: Frontiers in Nutrition

frontiers Research Topics

ISSN 1664-8714
ISBN 978-2-83250-532-8
DOI 10.3389/978-2-83250-532-8

About Frontiers

Frontiers is more than just an open-access publisher of scholarly articles: it is a pioneering approach to the world of academia, radically improving the way scholarly research is managed. The grand vision of Frontiers is a world where all people have an equal opportunity to seek, share and generate knowledge. Frontiers provides immediate and permanent online open access to all its publications, but this alone is not enough to realize our grand goals.

Frontiers Journal Series

The Frontiers Journal Series is a multi-tier and interdisciplinary set of open-access, online journals, promising a paradigm shift from the current review, selection and dissemination processes in academic publishing. All Frontiers journals are driven by researchers for researchers; therefore, they constitute a service to the scholarly community. At the same time, the Frontiers Journal Series operates on a revolutionary invention, the tiered publishing system, initially addressing specific communities of scholars, and gradually climbing up to broader public understanding, thus serving the interests of the lay society, too.

Dedication to Quality

Each Frontiers article is a landmark of the highest quality, thanks to genuinely collaborative interactions between authors and review editors, who include some of the world's best academicians. Research must be certified by peers before entering a stream of knowledge that may eventually reach the public - and shape society; therefore, Frontiers only applies the most rigorous and unbiased reviews.
Frontiers revolutionizes research publishing by freely delivering the most outstanding research, evaluated with no bias from both the academic and social point of view. By applying the most advanced information technologies, Frontiers is catapulting scholarly publishing into a new generation.

What are Frontiers Research Topics?

Frontiers Research Topics are very popular trademarks of the Frontiers Journals Series: they are collections of at least ten articles, all centered on a particular subject. With their unique mix of varied contributions from Original Research to Review Articles, Frontiers Research Topics unify the most influential researchers, the latest key findings and historical advances in a hot research area! Find out more on how to host your own Frontiers Research Topic or contribute to one as an author by contacting the Frontiers Editorial Office: frontiersin.org/about/contact

RECENT ADVANCES IN RECOGNITION OF BIOACTIVE PHYTONUTRIENTS FOR SPECIFIC TARGETS IN PLANT FOODS

Topic Editors:
Zhiqiang Wang, Hebei University, China
Mingquan Guo, Wuhan Botanical Garden, Chinese Academy of Sciences (CAS), China
Soon Sung Lim, Hallym University, South Korea

Citation: Wang, Z., Guo, M., Lim, S. S., eds. (2022). Recent Advances in Recognition of Bioactive Phytonutrients for Specific Targets in Plant Foods. Lausanne: Frontiers Media SA. doi: 10.3389/978-2-83250-532-8

Table of Contents

frontiers | Frontiers in Nutrition

TYPE Editorial
PUBLISHED 03 October 2022
DOI 10.3389/fnut.2022.1018946

OPEN ACCESS

EDITED AND REVIEWED BY
Siau Hui Mah,
Taylor's University, Malaysia

*CORRESPONDENCE
Zhiqiang Wang
wangzq2017@hbu.edu.cn

SPECIALTY SECTION
This article was submitted to
Food Chemistry,
a section of the journal
Frontiers in Nutrition

RECEIVED 14 August 2022
ACCEPTED 22 September 2022
PUBLISHED 03 October 2022

CITATION
Wang Z, Guo M and Lim SS (2022) Editorial: Recent advances in recognition of bioactive phytonutrients for specific targets in plant foods. *Front. Nutr.* 9:1018946. doi: 10.3389/fnut.2022.1018946

Editorial: Recent advances in recognition of bioactive phytonutrients for specific targets in plant foods

Zhiqiang Wang[1]*, Mingquan Guo[2] and Soon Sung Lim[3]

[1]Key Laboratory of Public Health Safety of Hebei Province, School of Public Health, Hebei University, Baoding, China, [2]Key Laboratory of Plant Germplasm Enhancement and Specialty Agriculture, Wuhan Botanical Garden, Chinese Academy of Sciences, Wuhan, China, [3]Department of Food Science and Nutrition, Hallym University, Chuncheon, South Korea

KEYWORDS

phytonutrients, new analytical methods, target-based recognition, metabolomics, biological activity

Editorial on the Research Topic
Recent advances in recognition of bioactive phytonutrients for specific targets in plant foods

Changes in lifestyle have resulted in an increased susceptibility to aging and various life-threatening diseases, such as cancers, coronary heart disease, obesity, and diabetes mellitus. Plant-based foods have received much attention in recent decades, as they provide major nutrients and are indispensable sources of bioactive phytonutrients, which have long been shown to be beneficial in preventing aging and the aforementioned diseases (1). Many phytonutrients interact with the biologically active sites of target proteins that are involved in the pathologies of aging and associated diseases. Therefore, there is an increase in research interest in the exploration of non-nutritive bioactive components in plant foods, especially the identification of phytonutrients with specific targets that facilitate the characterization of their chemical diversity and pharmacological activities (2). This Research Topic highlights recent advances in the identification of bioactive phytonutrients, which have long been known to exist in plant-based foods, but their specific protein targets have remained elusive.

Diabetes mellitus is a metabolic disorder of the endocrine system characterized by hyperglycemia. It has become one of the most intractable global public health challenges (3). Plant-based foods, as source of a diverse range of phytonutrients, are considered potential therapeutics for diabetes. They exhibit multiple therapeutic effects on the pathologies of abnormal glucose and lipid metabolism, and possess beneficial antioxidant activity. Consequently, Xie et al. reported the *in vitro*/*in vivo* hypoglycemic and antioxidant activities of the *Amomum taso-ko* fruit; Huang et al. reported the effects of red ginseng on lipid metabolism in an animal model of type 2 diabetes mellitus, and Wang, Tong et al. reported the hypoglycemic activity and associated mechanisms of ginseng berry using ultra high performance liquid chromatography (LC)-mass spectrometry (MS)-based metabolomics. Moreover, the identification of bioactive phytonutrients from *Amomum taso-ko* fruit, red ginseng, and ginseng berry, which may contribute to the hypoglycemic activity, was performed using high-resolution LC-MS/MS. Based on their results, LC-MS/MS, as an important untargeted metabolite profiling tool, is a powerful technique for the identification of bioactive phytonutrients in plant-based foods.

The isolation of bioactive phytonutrients is a well-established and non-substitutable approach that relies on subjecting mixtures of phytonutrients to iterative steps of fractionation and biological testing. The underlying strategy is aimed at reducing the complexity of plant-based food composition until a group of phytonutrients or a single phytonutrient with specific biological activity is obtained, and the structures and biological activity of the purified phytonutrients can be fully characterized. In this context, the selection of reliable targets or model assays for the assessment of biological activity is of great concern. For example, pancreatic lipase inhibitor therapy is an effective method of preventing and treating obesity. In the past few decades, porcine pancreatic lipase has been widely used for screening pancreatic lipase inhibitors. In contrast, efficacious inhibitors of human pancreatic lipase have rarely been reported. Although the amino acid sequence identity between porcine and human pancreatic lipases is relatively high (∼86%), remarkable intra-species differences in inhibitor responses have been reported (4). Herein, the establishment of a fluorescence-based high-throughput assay is reported by Qin et al.. In this assay, human pancreatic lipase was used as the specific target and a near-infrared fluorogenic substrate was used as the probe. Phytonutrients with activity against human pancreatic lipase were identified after their isolation from *Ampelopsis grossedentata*.

However, the isolation process has also been criticized for real and perceived weaknesses, such as being time-consuming and labor-intensive, and the ease by which trace phytonutrients are lost. Therefore, with progress in the development of new technologies and materials in the field of analytical chemistry, new strategies for the *in situ* identification of bioactive phytonutrients for specific targets in plant-based foods, without the requirement for tedious purification processes, are being developed. In particular, magnetic-ligand fishing is a feasible strategy. To reduce the false-positive rate in ligand fishing due to the non-specific binding of immobilized enzymes, Chi et al. prepared and applied GO@Fe3O4@SiO2-COX-2 nanoparticles to fishing ligands of cyclooxygenase-2 in *Choerospondias axillaris*, since graphene oxide maintains the ligand structure and physiological activity when combined with protein targets. Microfluidic platforms are versatile tools for screening bioactive molecules from plant-based foods. A rapid microfluidic chip-based ligand fishing platform for discovering matrix metalloproteinase-2 inhibitors from *Rosa roxburghii* was developed by Tao et al.. They used a layer-by-layer assembly approach to fabricate core-shell CdSSe@ZnS-quantum-dot-encoded superparamagnetic iron oxide microspheres to serve as a carrier for matrix metalloproteinase-2. Affinity-based ultrafiltration combined with LC-MS/MS is another feasible strategy for the *in situ* identification of bioactive compounds in plant-based foods. Herein, the investigation of potential anti-aging components of *Moringa oleifera* leaves is reported by Xu et al., who used affinity-based ultrafiltration with multiple drug targets. Meanwhile, a combination of high-speed counter-current chromatography, affinity-based ultrafiltration, and LC-MS/MS was reported by Wang, Wang et al. for the *in situ* identification of minor tyrosinase inhibitors from *Dryopteris crassirhizoma* rhizomes. Based on these results, affinity-based techniques, combined with modern analytical methods, provide a solution for the rapid identification of bioactive phytonutrients with specific targets in plant-based foods, without the need for further time-consuming and labor-intensive isolation and purification steps.

However, the specific targets of the identified phytonutrients should be explored and validated using molecular mechanisms. For example, (-)-epigallocatechin-3-gallate (EGCG) has been shown to be involved in the proliferation and apoptosis of human nasopharyngeal carcinoma (NPC) cells; however, little is known about the potential targets of EGCG in NPC cells. Jiang et al. reported that EGCG inhibits cell proliferation and induces apoptosis by downregulating SIRT1 expression levels. In another case, the adjuvant potential of lycopene against the metastasis of lung cancer cells was reported by Chan et al.. The results of their study suggested that lycopene and sorafenib additively inhibit the mitogen-activated protein kinase pathway by reducing the phosphorylation of ERK1/2, JNK1/2, and p38.

In conclusion, the present Research Topic provides several examples of advanced techniques used for the screening, identification, and subsequent investigations of the mechanisms of action of bioactive phytonutrients with specific protein targets, in plant-based foods. Moreover, this collection will promote further research and development activities on the plant-based foods described in this issue, and provide new ideas and techniques for the further development and utilization of other plant-based foods.

Author contributions

ZW drafted the manuscript. MG and SL provided critical review and insight and revised the final version of the editorial. All authors contributed to the article and approved the submitted version.

Funding

The financial support for this work was provided by National Natural Science Foundation of China (81803401) and Natural Science Foundation of Hebei Province (H2022201021).

Acknowledgments

The editors of this topic would like to thank all authors and reviewers for their contributions to the present collection. We also would like to acknowledge the financial support provided by National Natural Science Foundation of China and Natural Science Foundation of Hebei Province.

Conflict of interest

The authors declare that the research was conducted in the absence of any commercial or financial relationships that could be construed as a potential conflict of interest.

Publisher's note

References

1. Monjotin N, Amiot MJ, Fleurentin J, Morel JM, Raynal S. Clinical evidence of the benefits of phytonutrients in human healthcare. *Nutrients.* (2022) 14:1712. doi: 10.3390/nu14091712

2. Wang M, Xu X, Wang H, Wang H, Liu M, Hu W, et al. A multi-dimensional liquid chromatography/high-resolution mass spectrometry approach combined with computational data processing for the comprehensive characterization of the multicomponents from *Cuscuta chinensis*. *J Chromatogr A.* (2022) 1675:463162. doi: 10.1016/j.chroma.2022.463162

3. Wang Z, Zhang Y, Yan H. *In situ* net fishing of α-glucosidase inhibitors from evening primrose (*Oenothera biennis*) defatted seeds by combination of LC-MS/MS, molecular networking, affinity-based ultrafiltration, and molecular docking. *Food Funct.* (2022) 13:2545. doi: 10.1039/D1FO03975J

4. Point V, Pavan Kumar KV, Marc S, Delorme V, Parsiegla G, Amara S, et al. Analysis of the discriminative inhibition of mammalian digestive lipases by 3-phenyl substituted 1,3,4-oxadiazol-2(3H)-ones. *Eur J Med Chem.* (2012) 58:452–63. doi: 10.1016/j.ejmech.2012.10.040

frontiers in Nutrition

ORIGINAL RESEARCH
published: 31 January 2022
doi: 10.3389/fnut.2021.794193

Magnetic Ligand Fishing Using Immobilized Cyclooxygenase-2 for Identification and Screening of Anticoronary Heart Disease Ligands From *Choerospondias axillaris*

Miaomiao Chi[1], Hongsen Wang[2], Zhankuan Yan[2], Lei Cao[1], Xun Gao[1,3,4] and Kunming Qin[1]**

[1] Jiangsu Key Laboratory of Marine Pharmaceutical Compound Screening, Jiangsu Ocean University, Lianyungang, China, [2] Jiangsu Original Drug Research and Development Co., Ltd., Lianyungang, China, [3] Jiangsu Institute of Marine Resources Development, Jiangsu Ocean University, Lianyungang, China, [4] Co-Innovation Center of Jiangsu Marine Bio-industry Technology, Jiangsu Ocean University, Lianyungang, China

Inhibition of cyclooxygenase-2 (COX-2) activity is an effective way for treatment of coronary heart disease. And as an important source of COX-2 inhibitors, bioactive compounds of *Choerospondias axillaris* and pharmacological mechanisms remained lacking in prospective researches. Therefore, for the purpose of accelerating the discovery of natural products targeting designed inhibitors, the COX-2 microreactor composed of functionalized microspheres and magnetic ligand fishing was developed and applied in *Choerospondias axillaris*, and the physicochemical properties of the COX-2 functionalized microspheres were characterized using Fourier transform infrared spectroscopy (FT-IR), vibrating sample magnetometer (VSM), scanning electron microscopy (SEM), and transmission electron microscopy (TEM). Furthermore, the bioactive compounds singled out from ethanol decoction without prepurification were dissociated and identified by ultraperformance liquid chromatography plus Q-Exactive Orbitrap tandem mass spectrometry (UPLC-Q-Exactive Orbitrap-MS/MS). Consequently, 21 bioactive compounds consisting of 6 organic acids, 8 flavonoids, and 7 others were separated and characterized from *Choerospondias axillaris*, which were reported to participate in the COX-2 inhibitory pathway to varying degrees. Therefore, this method could provide a prospective solution for the extraction and identification of active pharmaceutical ingredients and the rapid screening of some enzyme inhibitors in the complex mixtures.

Keywords: cyclooxygenase-2, magnetic ligand fishing, *Choerospondias axillaris*, UPLC-Q-Exactive Orbitrap-MS/MS, traditional Chinese medicine

Edited by:
Zhiqiang Wang,
Hebei University, China

Reviewed by:
Enade Perdana Istyastono,
Sanata Dharma University, Indonesia
Xian-Hua Wang,
Tianjin Medical University, China

****Correspondence:***
Xun Gao
gaoxun_2017@163.com
Kunming Qin
qinkm123@126.com

Specialty section:
This article was submitted to
Food Chemistry,
a section of the journal
Frontiers in Nutrition

Received: *13 October 2021*
Accepted: *29 December 2021*
Published: *31 January 2022*

Citation:
Chi M, Wang H, Yan Z, Cao L, Gao X and Qin K (2022) Magnetic Ligand Fishing Using Immobilized Cyclooxygenase-2 for Identification and Screening of Anticoronary Heart Disease Ligands From Choerospondias axillaris. Front. Nutr. 8:794193. doi: 10.3389/fnut.2021.794193

INTRODUCTION

In most countries, the prevalence of the cardiovascular disease is still on the rise. *Choerospondias axillaris* has been used in China to treat the coronary heart disease as early as the eighth century (1). Modern pharmacological researches also showed that *Choerospondias axillaris* was used to treat cardiovascular diseases because of its antiarrhythmia and antimyocardial ischemia effects (2, 3).

However, due to its complex chemical composition, there are few studies on the specific functional components representing the specific pharmacological activities of *Choerospondias axillaris* and their corresponding targets (4).

The results of network pharmacology and pharmacokinetic studies suggest that the flavonoids and organic acids may be the material basis for the prevention and treatment of coronary heart disease in *Choerospondias axillaris* (5). Flavonoids may mediate the cGMP-PKG signaling pathway, and organic acids such as gallic acid, protocatechuic acid, and chlorogenic acid may mediate the Wnt signaling pathway to jointly play the role of preventing and treating coronary heart disease. Moreover, the prevention and treatment of coronary heart disease may be related to related biological processes such as stress response, immune-inflammatory response, signal transduction, and atherosclerotic plaque instability by *Choerospondias axillaris*. COX-2 was reported to be a key enzyme that participated in platelet aggregation, and regulate the resistance of peripheral blood vessels and the distribution of renal blood flow (6–8). Therefore, it is of great importance that started with COX-2 to study the active pharmaceutical compounds and their mechanism of action from *Choerospondias axillaris*.

Screening methods for active compounds of COX-2 inhibitors in Chinese medicine mainly include classic separation and activity testing methods (9), chip technology (10), high-throughput screening methods (11), and virtual ligand screening methods using structural information (12); however, the above methods have disadvantages such as large workload, long cycle, and easy loss of active compounds. Since drugs in the body exert their pharmacological effects by interacting with a variety of related biological target molecules, such as enzymes, receptors, DNA, and RNA, during the development of the disease, the ligand capture technology has become an efficient screening method guided by biological activity and based on affinity screening, which can not only quickly and target the active ingredients of traditional Chinese medicines, but also help to explain the mechanism of action of traditional Chinese medicines at the molecular level, thereby providing new methods and ideas for the treatment of diseases.

Magnetic ligand fishing is a combination of specific ligand affinity and magnetic separation, which has been proven to be a convenient and effective tool for extracting biologically active ingredients in extracts of plant. Though modern analytical techniques such as HPLC, LC-MS, and SPE-HPLC-NMR can achieve rapid identification and full structural characterization of constituents in complex matrixes, it was difficult that provide related information about biologically active ingredients. Magnetic ligand fishing detects active ingredients by binding affinity directly from the crude extract without the process of prepurification (13). However, when some ingredients produced false-positive results in ligand fishing due to the non-specific binding of immobilized enzymes, the risk can be effectively reduced by docking the protein structure of COX-2. When combined with proteins, graphene oxide (GO) can maintain the ligand structure and physiological activity because of the hydrophobic and hydrogen bonding with proteins, which indicated that GO can be used in magnetic ligand fishing. Magnetic ligand fishing has been applied to isolate the ligands of human serum albumin (14), α-amylase (15), α-glucosides (16), cyclooxygenase-1 (COX-1) (17), and acetylcholine ester (18).

With the continued need for fast and sensitive methods for the identification of COX-2 inhibitory compounds of natural origin, we established the first application of *Choerospondias axillaris* by a combination of GO-based magnetic ligand fishing and UPLC-Q-Exactive Orbitrap-MS/MS. Because of the binding affinity of the COX-2 ligand, the use of the newly magnetic nanomaterials in ligand fishing is not limited to the crude extracts of *Choerospondias axillaris*, and the materials showed excellent specificity, good precision, and high reusability in the experiment.

MATERIALS AND METHODS

Chemicals and Reagents

Graphene oxide was purchased from the Nanjing Jicang Nano Technology Co., Ltd (Nanjing, China). Human recombinant COX-2 and methanol (HPLC grade) were supplied by Sigma (St. Louis, MO, USA). 3-aminopropyltriethoxysilane (APTES), tetraethyl orthosilicate (TEOS), glutaraldehyde (25% (w/v) aqueous solution), acetic acid (HPLC grade), ethanol, acetonitrile, $FeCl_3 \cdot 6H_2O$ (99%), $FeCl_2 \cdot 4H_2O$ (99%) were obtained from Aladdin (Shanghai, China). Water used throughout the work was produced by a Milli-Q ultrapure water system (Millipore, Bedford, Massachusetts, USA).

Instrumental

The magnetite nanoparticles were characterized by transmission electron microscopy (TEM), Fourier-transform infrared (FT-IR) spectroscopy, scanning electron microscope (SEM), and vibration sample magnetometer (VSM). TEM micrographs were obtained by the JEM2100F system (JEOL, Japan). SEM microstructure of nanoparticles was recorded by the S4800 system (Hitachi, Japan). The FT-IR spectra were recorded using KBr pellets on Nicolet iS50 spectrophotometer (Thermo Fisher Scientific, Waltham, Massachusetts, USA). The magnetic properties of nanoparticles were investigated by a VSM7407 (Lakeshore, Louisiana, USA).

High-Performance Liquid Chromatography Analysis

Chromatographic separation was performed on an analytical symmetry C18 column (250 × 4.6 mm i.d., 5 μm, Waters, Milford, Massachusetts, USA). The isocratic mobile phase consisted of water-methanol (15:85, v/v) with a flow rate of 1.0 ml/min was prepared for celecoxib analysis at 25°C and the chromatograms were acquired at 254 nm.

UPLC-Q-Exactive Orbitrap-MS/MS

The UPLC-MS/MS analysis of the eluent was performed on an analytical Shim-pack XR-ODS II (75 × 3.0 mm i.d., 1.7 μm, Shimadzu, Kyoto). The UPLC system mainly consisted of an Ultimate 3000 series ultra-high-performance liquid chromatography (Thermo Fisher Scientific, San Jose, USA) equipped with an online degasser, a quaternary pump, an

TABLE 1 | The elution gradient of UPLC-Q-Exactive Orbitrap-MS/MS.

Time (min)	Flow rate (ml/min)	A (%)	B (%)
0–2	0.3	95–85	5–15
2–3	0.3	85–75	15–25
3–7	0.3	75–55	25–45
7–9	0.3	55–40	45–60
9–10	0.3	40–25	60–75
10.01–12	0.3	95	5

autosampler, and a column temperature compartment; it was connected to a Q-Exactive Orbitrap tandem mass spectrometer (Thermo Fisher Scientific, San Jose, USA) *via* an electrospray ionization interface (ESI). The mobile phase consisted of C (0.4% acetic acid in water) and D (acetonitrile) at 30°C, and the elution gradient as shown in **Table 1**. All the mobile phases were prepared daily.

Mass spectra were acquired in both the positive and negative ion mode through full MS and higher-energy collisional dissociation data-dependent MS/MS analysis. Full-scan high-resolution accurate-mass data acquisition captures all the sample data, enabling identification of untargeted compounds and retrospective data analysis without rerunning the samples.

Ion source parameters were shown as follows: spray voltage −3.0 kV (negative polarity) and 3.3 kV (positive polarity), sheath gas 35 arbitrary units, auxiliary gas 10 arbitrary units, capillary temperature 350°C, S-lens RF level 55, auxiliary gas heater temperature 350°C. Automatic gain control was set at 1e6, and the maximum injection time at 50 ms, and the isolation window at 2.0 *m/z*. The collision energy was varied in the range of 20–40 eV and scan range *m/z* 60–900 to obtain representative product ion spectra. The mass tolerance window was set to 5 ppm for the two analysis modes (2002/657/EC). Data analysis and processing have been performed using the Xcalibur 4.1 software (Thermo Scientific, USA).

Preparation of GO@Fe_3O_4@SiO_2-COX-2 Nanoparticles

Based on the previous report, some modifications were made to coat COX-2 on the GO layer (19).

The magnetic GO@Fe_3O_4 (MGO) nanoparticles were prepared by the chemical coprecipitation of Fe^{3+} and Fe^{2+}. At first, 0.50 g of GO was dispersed in 100 ml of distilled water and heated to 70°C. A total of 2.16 g of $FeCl_3 \cdot 6H_2O$ and 0.80 g of $FeCl_2 \cdot 4H_2O$ were dissolved in 40.0 ml of distilled water, and then added to the aforementioned dispersion suspension. After adjusting the pH to 10 with ammonia water (25%, w/v), the dispersion solution continued to be 70°C for 6 h. The whole process of the reaction was carried out under a stream of pure nitrogen. When the reaction finished, the suspension was filtered and washed three times with distilled water and ethanol, respectively.

Second, 6.3 ml of distilled water and 2.1 ml of TEOS were stirred for 3 min and sonicated for 1 min to obtain a milky solution. The milky solution was added to 49.5 ml of absolute ethanol including 0.50 g of magnetic GO@Fe_3O_4 nanoparticles. After stirring at 0°C for 10 min, 2.0 ml of glutaraldehyde was added dropwise to the dispersion solution. Then, the reaction lasted for 10 h. At last, separated by a magnet, GO@Fe_3O_4@SiO_2 (SMGO) nanoparticles were sequentially washed with 2% HNO_3, distilled water, and absolute ethanol in turn.

Finally, 0.10 g of SMGO nanoparticles were suspended in 50 ml ethanol-water solution (1:1, v/v), and adjusted the pH to 3–4 with 0.1 mol L^{-1} HCl. Followed by 1.0 ml APTES dropwise, the mixture was continued to be stirred for 5 h at 50°C. SMGO-NH_2 nanoparticles were separated by a permanent magnet and washed 4 times with ethanol. After being suspended in 5.0 ml of 5% glutaraldehyde solution for 1 h, the SMGO-NH_2 nanoparticles were retrieved by magnetic separation and washed with Tris-HCl buffer (100 mM, pH 8.0) three times to remove excess glutaraldehyde. Then shaken SMGO-NH_2 nanoparticles with 2.0 ml of tris-HCl buffer containing 50 units of COX-2 at 37°C for 2 h, the COX-2 functionalized magnetic microspheres (SMGO-COX-2) were synthesized.

Magnetic Ligand Fishing in *Choerospondias axillaris*

A total of 5.0 g of *Choerospondias axillaris* powder was extracted with 500 ml of 75% (v/v) ethanol three times in parallel at 85°C for 1.5 h. After filtering on three layers of gauze of the diameter of 4.5 mm, the extraction solutions were combined, freeze-dried, and dissolved to 2 mg ml^{-1}. A total of 5 mg of COX-2 functional magnetic microspheres were suspended in 2 ml of extraction solution and incubated at 37°C for 30 min. Then, it was washed 3 times with 2 ml Tris-HCl buffer (pH 8.0) to remove non-specific binding ligands, and incubated with 1 ml of methanol for 1 h to dissociate the extracted ligand. After the nanoparticles were separated by a magnet, the elution solution had been filtered through a 0.22 μm membrane and then introduced into UPLC-Q-Exactive Orbitrap-MS/MS for analysis. Meanwhile, celecoxib was incubated with MGO, SMGO, and SMGO-inactive COX-2.

RESULTS AND DISCUSSION

Characterization of the Nanoparticles

Fourier-transform infrared spectroscopy analysis was used to record the surface functional groups and chemical bonds of synthetic materials. The infrared spectra of GO, MGO, SMGO, SMGO-NH_2 were shown in **Figure 1A**. The peak at 541 cm^{-1} was due to the tensile vibration of Fe-O-Fe. The strong absorption band at 1,066 cm^{-1} was attributable to the symmetric and asymmetric vibrations of Si-O-Si, indicating that GO was covered by Fe_3O_4 and SiO_2. The absorption at 1,300 cm^{-1} was attributed to the stretching vibration of C-N, indicating that SMGO was modified with the amino groups. Therefore, the results of FTIR analysis confirmed the formation of SMGO-NH_2 nanoparticles. The magnetic properties of the material were studied by VSM at room temperature. According to the curve in **Figure 1B**, the saturation magnetization of SMGO and SMGO-COX-2 was 98.42 and 69.60 emu·g^{-1}, respectively, which were enough to separate nanomaterials from the sample solution under an external magnetic field. Compared with SMGO, the

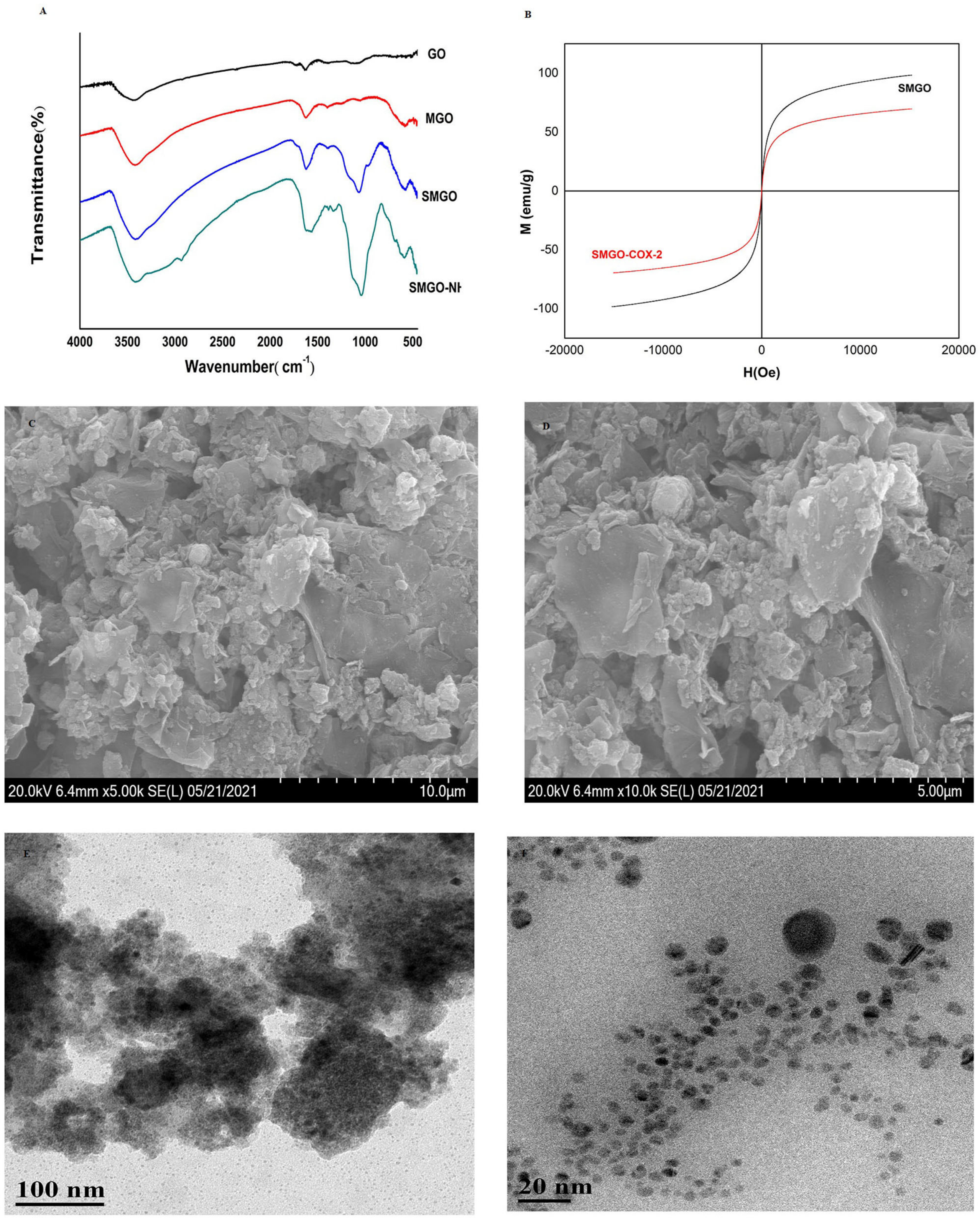

FIGURE 1 | (A) Fourier-transform infrared (FT-IR) spectra of GO, MGO, SMGO, and SMGO-NH2. **(B)** Magnetization curves of SMGO, SMGO@COX-2. **(C,D)** SEM images of SMGO@COX-2; **(E,F)** TEM images of SMGO@COX-2.

magnetization of SMGO-COX-2 was reduced by 28.82 emu·g^{-1}, which was attributed to the enzyme grafted on the surface of SiO_2. The morphology study of SMGO@COX-2 nanocomposite was shown in **Figures 1C,D**. Previous studies showed that GO was a single flake layer (19). After combining Fe_3O_4 particles, the surface becomes rough with spherical or elliptical substances. After coating SiO_2, the agglomeration phenomenon was reduced. After being connected to COX-2, the flake layer of GO was almost invisible, and the gaps created by the prevention of agglomeration of SiO_2 were also filled, and the entire surface became rougher and fuller. The structural morphology of SMGO@COX-2 nanocomposite was shown in **Figures 1E,F**. The black dots (SMGO@COX-2) on the cross-section were evenly anchored on the surface of the nanomaterial, and the shell-like layered structure could be seen inside the material.

Assay Verification

It is well known that compared with COX-1, celecoxib exhibits an extremely high-selective inhibitory effect on COX-2. The HPLC analysis were shown in **Figure 2**. When the COX-2 was bound to the surface of SMGO, the peak area of celecoxib in the elution solution increased significantly. Meanwhile, as shown in **Supplementary Figure S1**, when the inactive COX-2 was bound to the surface of SMGO, the peak area of celecoxib in the elution solution could be ignored. And extracted with MGO and SMGO, the celecoxib in the elution solution was rarely detected. Therefore, the results demonstrated the specificity of this magnetic ligand fishing for the screening of COX-2 ligands.

The stable activity of the immobilized enzyme COX-2 was a key prerequisite for capturing the same number of ligands during a series of binding-dissociation cycles. Therefore, the repeatability of SMGO@COX-2 was evaluated by specifically capturing celecoxib. To avoid the loss of SMGO@COX-2 nanoparticles during the cycles, it was necessary to expose them to a magnetic field for 1 min. After 5 consecutive association-dissociation cycles, as shown in **Supplementary Figure S2**, the binding efficiency was still as high as 90% of the first cycle by calculating the peak area of celecoxib in the elution solution. The results showed a stable combination of SMGO and COX-2 and a high COX-2 ligand-binding capacity. After 5 days of storage at 4°C, as shown in **Supplementary Figure S3**, there was no significant loss on the celecoxib binding efficiency ($RSD < 8\%$, $n = 5$), and three batches of SMGO@COX-2 showed similar binding efficiency ($RSD < 10\%$).

Identification of COX-2 Inhibitors by UPLC-Q-Exactive Orbitrap-MS/MS

According to the retention time of each component, mass spectrum information, and related references, 21 COX-2 ligands were preliminarily determined in the eluted solution using magnetic ligand fishing technique as listed in **Table 2** and **Figures 3**, **4**. Both negative and positive ions were applied in the UPLC-Q-Exactive Orbitrap-MS/MS system to analyze the ligands of COX-2 separated from *Choerospondias axillaris*. The results in **Figure 3** showed that the eluted solution had better resolution of the references and more observable fragment ions in negative ion mode, which mainly attributed to the large amounts of phenolic acids and flavonoids.

Identification of Flavonoids

A total of 8 flavonoids have been identified in the elution solution of *Choerospondias axillaris*, accounting for more than 38%. In the negative mode ESI-MS spectra, the $[M\text{-}H]^-$ ion was observed for all the compounds. In the negative mode ESI-MS^2 spectra,

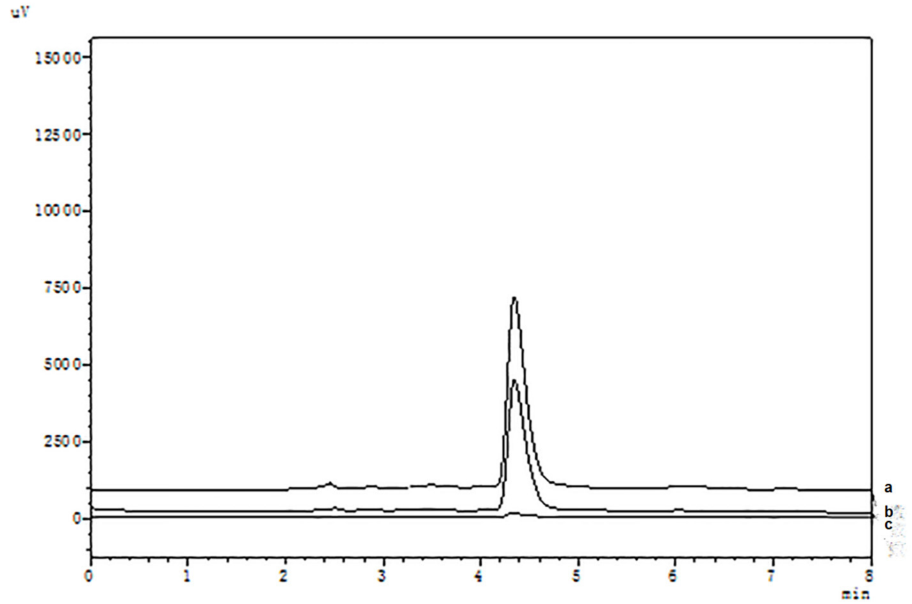

FIGURE 2 | High-performance liquid chromatography (HPLC) chromatograms of celecoxib (a) and ligand fishing assay eluent by SMGO-COX-2 (b), and SMGO (c).

TABLE 2 | Identification of elution solution by UPLC-Q-Exactive Orbitrap-MS/MS.

No.	Compounds	Chemical formula	R$_t$ (min)	Ion mode	Observe mass (Da)	Error (ppm)	MS/MS	Confidential levels
1	Hydroquinone	$C_6H_6O_2$	5.03	−	109.02915	−3.325	81.03429[M-CO-H]$^-$	2
2	Succinic acid	$C_4H_6O_4$	0.43	−	117.01905	−2.409	73.02924[M-CO$_2$-H]$^-$	2
3	Protocatechualdehyde	$C_7H_6O_3$	4.69	−	137.02397	−3.265	93.03431[M-CO$_2$-H]$^-$	2
4	Protocatechuic acid	$C_7H_6O_4$	3.99	−	153.01891	−2.758	109.02916[M-CO$_2$-H]$^-$ 81.03448[M-CO$_2$-CO-H]$^-$	2
5	Isovanillin	$C_8H_8O_3$	0.18	+	153.05443	−1.246	/	2
			3.80	−	151.03976	−2.035	136.01616[M-CH$_3$-H]$^-$ 108.02154[M-CH$_3$-CO-H]$^-$	
6	Vanillic acid	$C_8H_8O_4$	5.02	−	167.03418	−4.801	152.01100[M-CH$_3$-H]$^-$ 108.02141[M-CH$_3$-CO$_2$-H]$^-$	1
7	Gallic acid	$C_7H_6O_5$	1.2	−	169.01341	−4.95	125.02403[M-CO$_2$-H]$^-$	2
8	Caffeic acid	$C_9H_8O_4$	7.77	−	179.03459	−2.19	135.04480[M-CO$_2$-H]$^-$	1
9	Syringaldehyde	$C_9H_{10}O_4$	4.63	−	181.05003	−3.325	166.02614[M-CH$_3$-H]$^-$ 151.00313[M-2CH$_3$-H]$^-$	2
10	Quinic acid	$C_7H_{12}O_6$	1.05	−	191.05539	−3.776	173.04510[M-H$_2$O-H]$^-$	2
11	Citric acid	$C_6H_8O_7$	6.03	−	191.01825	−7.726	111.00851[M-2H$_2$O-CO$_2$-H]$^-$ 87.00853[M-2CO$_2$-OH]$^-$	1
12	Pantothenic acid	$C_9H_{17}NO_5$	3.39	+	220.11786	−0.405	202.10732[M-H$_2$O+H]$^+$ 124.07572[M-C$_2$H$_8$O$_4$+H]$^+$	2
13	Palmitic acid	$C_{16}H_{32}O_2$	11.04	−	255.23247	−1.874	/	3
14	Pinocembrin	$C_{15}H_{12}O_4$	10.72	−	255.06573	−2.615	213.05482[M-C$_2$H$_2$O-H]$^-$ 151.00323[M-C$_8$H$_8$-H]$^-$	2
15	Naringenin	$C_{15}H_{12}O_5$	8.56	−	271.06122	0.086	177.01860[M-C$_6$H$_7$O-H]$^-$ 151.00316[M-C$_6$H$_7$O-2CH$_3$-H]$^-$	2
16	Kaempferol	$C_{15}H_{10}O_6$	7.57	−	285.04062	0.557	257.04523[M-CO-H]$^-$	2
17	Catechin	$C_{15}H_{14}O_6$	4.56	−	289.07175	0.039	245.08098[M-CO$_2$-H]$^-$ 203.07045[M-C$_4$H$_6$O$_2$-H]$^-$	1
18	Ellagic acid	$C_{14}H_6O_8$	5.45	−	300.99771	−4.254	283.99567[M-H$_2$O-H]$^-$ 273.04050[M-CO-H]$^-$ 229.04938[M-CO-CO$_2$-H]$^-$	1
19	Quercetin	$C_{15}H_{10}O_7$	7.65	−	301.03439	−3.275	151.00316[M-C$_7$H$_6$O$_2$-CO-H]$^-$ 178.99800[M-C$_7$H$_6$O$_2$-H]$^-$ 107.01353[M-C$_8$H$_6$O$_3$-CO$_2$-H]$^-$ 121.02917[M-C$_8$H$_4$O$_5$-H]$^-$	1
20	Taxifolin	$C_{15}H_{12}O_7$	6.05	−	303.04874	−7.543	285.04025[M-H$_2$O-H]$^-$ 125.02387[M-C$_9$H$_6$O$_4$-H]$^-$	1
21	Rutin	$C_{27}H_{30}O_{16}$	4.96	−	609.14532	−1.293	300.02667[M-C$_{12}$H$_{20}$O$_9$-H]$^-$ 301.03378[M-C$_{12}$H$_{21}$O$_9$-H]$^-$ 271.02411[M-C$_{12}$H$_{20}$O$_9$-H$_2$O-H]$^-$ 255.02911[M-C$_{12}$H$_{22}$O$_{11}$-H]$^-$	1

Confidential level 1: Compounds that matched to reference standard.
Confidential level 2: Compounds that matched to robust spectral or literatures.
Confidential level 3: Compounds that classified.

the [M-A-H]$^-$ ion was observed for 6 compounds, such as compounds 14, 15, 16, 19, 20, and 21 (A represents various groups with more than 6 carbon atoms). The [M-CH$_3$-H]$^-$ ion was observed for 2 compounds, such as compounds 9 and 15. The [M-H$_2$O-H]$^-$ ion was observed for 2 compounds, such as compounds 20 and 21. The [M-CO-H]$^-$ ion was observed for 2 compounds, such as compounds 16 and 19. The [M-CO$_2$-H]$^-$ ion was observed for 2 compounds, compounds 17 and 19. From this result, it can be seen that [M-H]$^-$ is the most fragmented ions, followed by [M-A-H]$^-$.

Identification of Phenolic Acids

A total of 6 phenolic acids have been identified in the elution solution of *Choerospondias axillaris*, accounting for more than 28%. In the negative mode ESI-MS spectra, the [M-H]$^-$ ion was observed for all the compounds. In the negative mode

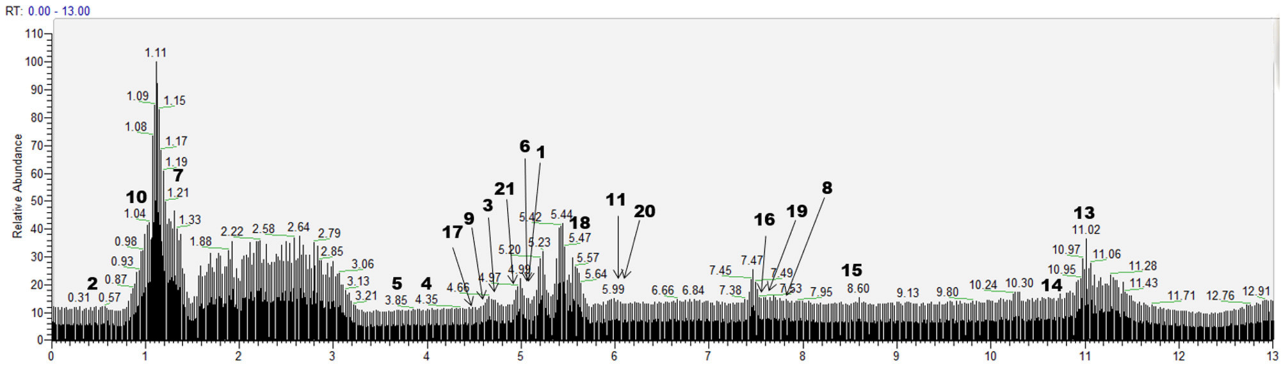

FIGURE 3 | Base peak chromatogram of the elution solution of *Choerospondias axillaris* by UPLC-Q-Exactive Orbitrap-MS/MS in the negative mode.

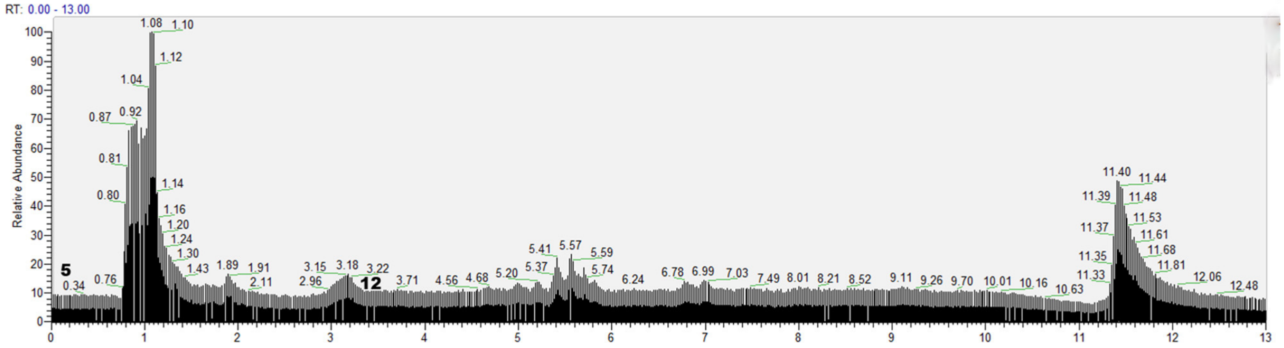

FIGURE 4 | Base peak chromatogram of the elution solution of *Choerospondias axillaris* by UPLC-Q-Exactive Orbitrap-MS/MS in the positive mode.

ESI-MS^2 spectra, the $[M\text{-}CO_2\text{-}H]^-$ ion was observed for all the compounds. The $[M\text{-}CH_3\text{-}H]^-$ ion was observed for 1 compound, compounds 6. The $[M\text{-} H_2O\text{-}H]^-$ ion was observed for 1 compound, compounds 11. The $[M\text{-}CO\text{-}H]^-$ ion was observed for 1 compound, compounds 4. From this result, it can be seen that $[M\text{-}H]^-$ and $[M\text{-}CO_2\text{-}H]^-$ are the most fragmented ions in phenolic acids.

Identification of Other Compounds

A total of 6 other compounds including 2 aromatic aldehydes, 2 organic acids, and 2 phenols, have been identified in the elution solution of *Choerospondias axillaris*, accounting for more than 28%. In the negative mode ESI-MS spectra, the $[M\text{-}H]^-$ ion was observed for all the compounds. In the negative mode ESI-MS^2 spectra, the $[M\text{-}CO\text{-}H]^-$ ion was observed for 2 phenols and 1 aromatic aldehyde, compounds 1, 5, and 18. The $[M\text{-}CO_2\text{-}H]^-$ ion was observed for 1 phenol and 1 aromatic aldehyde, compounds 3 and 18. The $[M\text{-} H_2O\text{-}H]^-$ ion was observed for 1 organic acid and 1 aromatic aldehyde, compounds 10 and 18. And in the positive mode ESI-MS spectra, the $[M+H]^-$ ion was observed for all the compounds. In the positive mode ESI-MS spectra, the $[M\text{-} H_2O +H]^-$ ion was observed for 1 compound, compounds 12. From this result, it can be seen that $[M\text{-}H]^-$ and $[M\text{-}CO\text{-}H]^-$ are the most fragmented ions in other compounds.

Evaluate of COX-2 Inhibitors in *Choerospondias axillaris*

Consistent with our results, 21 bioactive compounds were reported to participate in the COX-2 inhibitory pathway in different forms. It is well known that LPS-induced reactive oxygen species production leads to COX-2 induction, and compounds 1, 3, 9, 15, 16, 19, and 20 were found to effectively inhibit the production of LPS-induced COX-2 metabolites (20–23). It has been reported that compound 8 suppressed UVB-induced COX-2 expression by blocking Fyn kinase activity (24). Meanwhile, compounds 4, 6, 13, and 14 suppressed the NF-κB signaling pathways to limit the expression of COX-2 (25–28). Differently, compounds 7, 10, 17, 18, and 21 were proven to reduce COX-2 levels by reducing nitric oxide overproduction from inducible nitric oxide synthase (29–31). Considering the aforementioned facts, we can still conclude that, the compounds analyzed by UPLC-Q-Exactive Orbitrap MS/MS were consistent.

CONCLUSION

Choerospondias axillaris has complex components and diverse structures, which has the effect on multiple targets. Network pharmacology showed that their anticoronary heart disease action pathway was mainly through anti-inflammation, which provided theoretical support to choose the target of COX-2. And this study aimed to establish a fast and simple method to target and screen out the active compounds that interacted with COX-2 from *Choerospondias axillaris*, and it was the first time that synthesized COX-2 magnetic microspheres were applied to extract COX-2 inhibitors. Meanwhile, the COX-2 functionalized magnetic microspheres in this method had excellent specificity, good precision, low cost, and high-throughput screening efficiency. Therefore, the method could be used to immobilize macromolecular targets and provide convenient conditions for screening many specific biologically active compounds from complex natural products.

DATA AVAILABILITY STATEMENT

The original contributions presented in the study are included in the article/**Supplementary Material**, further inquiries can be directed to the corresponding author/s.

AUTHOR CONTRIBUTIONS

MC helped in writing the original draft, data curation, and formal analysis. HW was involved in methodology, project administration, and validation. ZY helped with the investigation and resources. LC worked with software and visualization. XG was involved in the reviewing and editing and funding acquisition. KQ helped with supervision and conceptualization. All authors contributed to the article and approved the submitted version.

FUNDING

This work was supported by the National Natural Science Foundation of China (No. 82104349) and Project Funded by the Priority Academic Program Development of Jiangsu Higher Education Institutions (PAPD).

SUPPLEMENTARY MATERIAL

The Supplementary Material for this article can be found online at: https://www.frontiersin.org/articles/10.3389/fnut.2021.794193/full#supplementary-material

Supplementary Figure S1 | The HPLC chromatograms of celecoxib (a) and ligand fishing assay eluent by SMGO-COX-2 (b), MGO (c), SMGO-inactive COX-2 (d), and SMGO (e).

Supplementary Figure S2 | The HPLC chromatograms of celecoxib in five consecutive association-dissociation cycles of ligand fishing assay eluent by SMGO-COX-2.

Supplementary Figure S3 | The HPLC chromatograms of celecoxib in ligand fishing assay eluent by SMGO-COX-2 during five days of storage at 4°C.

REFERENCES

1. Zhou J, Mei SG. Research progress of Mongolian Medicine Guangzhao. *Strait Pharm J.* (2017) 29:1–5. doi: 10.3969/j.issn.1006-3765.2017.06.001
2. Li L, Li J, Yi J, Liu H, Lei H. Dose–effect of irbesartan on cyclooxygenase-2 and matrix metalloproteinase-9 expression in rabbit atherosclerosis. *J Cardiovasc Pharmacol.* (2018) 71:82. doi: 10.1097/FJC.0000000000000544
3. Dang Z, Su S, Jin G, Nan X, Ma L, Li Z, et al. Tsantan Sumtang attenuated chronic hypoxia-induced right ventricular structure remodeling and fibrosis by equilibrating local ACE-AngII-AT1R/ACE2-Ang1-7-Mas axis in rat. *J Ethnopharmacol.* (2019) 250:112470. doi: 10.1016/j.jep.2019.112470
4. Morrison A, Li J. PPAR-γ and AMPK-Advantageous targets for myocardial ischemia/reperfusion therapy. *Biochem Pharmacol.* (2011) 82:195–200. doi: 10.1016/j.bcp.2011.04.004
5. Gao X, Mu J, Guan S, Li Q, Du Y, Zhang H, et al. Simultaneous determination of phenolic acids and diterpenoids and their comparative pharmacokinetic study in normal and acute blood stasis rats by UFLC–MS/MS after oral administration of Guan-Xin-Shu-Tong capsules. *J Chromatogr B.* (2018) 1072:221–8. doi: 10.1016/j.jchromb.2017.11.017
6. Smith JP, Haddad EV, Downey JD, Breyer RM, Boutaud O. PGE2 decreases reactivity of human platelets by activating EP2 and EP4. *Thromb Res.* (2010) 126:23–9. doi: 10.1016/j.thromres.2010.04.003
7. Sanak M, Plutecka H, Szczeklik W, Piwowarska W, Rostoff P, Szczeklik A. Functional promoter polymorphism of cyclooxygenase-2 modulates the inflammatory response in stable coronary heart disease. *Polskie Arch Med Wewntrznej.* (2010) 120:82–8 doi: 10.1371/journal.pmed.1000222
8. Liu J, Wang S, Tan W, Lv B, Dai Y, Wang Y. Dual-screening of anti-inflammatory and antioxidant active ingredients of shenxiang suhe pill and its potential multi-target therapy for coronary heart disease. *Biomed Pharmacother.* (2020) 129:110283. doi: 10.1016/j.biopha.2020.110283
9. Bagdas D, Muldoon PP, AlSharari S, Carroll FI, Negus SS, Damaj MI. Expression and pharmacological modulation of visceral pain-induced conditioned place aversion in mice. *Neuropharmacology.* (2016) 102:236–43. doi: 10.1016/j.neuropharm.2015.11.024
10. Mosaddeque F, Mizukami S, Teklemichael AA, Mizuta S, Tanaka Y, Taniguchi M, et al. Prediction Model for Antimalarial Activities of Hemozoin Inhibitors by Using Physicochemical Properties. Antimicrob Agents Chemother.(2018) 62:e02424-17. doi: 10.1128/AAC.02424-17
11. Geromichalos GD, Alifieris CE, Geromichalou EG, Trafalis DT. Overview on the current status on virtual high-throughput screening and combinatorial chemistry approaches in multi-target anticancer drug discovery; Part II. *J Balkan Union Oncol.* (2016) 21:1337–58
12. Cerqueira NM, Gesto D, Oliveira EF, Santos-Martins D, Brás NF, Sousa SF, et al. Receptor-based virtual screening protocol for drug discovery. *Arch Biochem Biophys.* (2015) 582:56–67. doi: 10.1016/j.abb.2015.05.011
13. Zaouak A, Noomen A, Jelassi H. Gamma radiation induced degradation of the phenoxy acid herbicide diclofop-methyl in aqueous solutions. *Appl Rad Isotopes.* (2020) 156:108939. doi: 10.1016/j.apradiso.2019.108939
14. Zhang Y, Nie M, Shi S, You Q, Guo J, Liu L. Integration of magnetic solid phase fishing and off-line two-dimensional high-performance liquid chromatography-diode array detector-mass spectrometry for screening and identification of human serum albumin binders from Radix Astragali. *Food Chem.* (2014) 146:56–64. doi: 10.1016/j.foodchem.2013.09.030
15. Li Y, Chen Y, Xiao C, Chen D, Xiao Y, Mei Z. Rapid screening and identification of alpha-amylase inhibitors from Garcinia xanthochymus using enzyme-immobilized magnetic nanoparticles coupled with HPLC and MS. *J Chromatogr B Anal Technol Biomed Life Sci.* (2014) 960:166–73. doi: 10.1016/j.jchromb.2014.04.041
16. Tao Y, Zhang Y, Cheng Y, Wang Y. Rapid screening and identification of α-glucosidase inhibitors from mulberry leaves using enzyme-immobilized magnetic beads coupled with HPLC/MS and NMR. *Biomed Chromatogr.* (2013) 27:148–55. doi: 10.1002/bmc.2761
17. Zhang Y, Shi S, Chen X, Peng M. Functionalized magnetic nanoparticles coupled with mass spectrometry for screening and identification of cyclooxygenase-1 inhibitors from natural products. *J Chromatogr B Anal Technol Biomed Life Sci.* (2014) 960:126–32. doi: 10.1016/j.jchromb.2014.04.032

18. Vanzolini KL, Ainsworth S, Bruyneel B, Herzig V, Seraus MG, Somsen GW, et al. Rapid ligand fishing for identification of acetylcholinesterase-binding peptides in snake venom reveals new properties of dendrotoxins. *Toxicon.* (2018) 152:1–8. doi: 10.1016/j.toxicon.2018.06.080
19. Suo L, Zhao J, Dong X, Gao X, Li X, Xu J, Zhao L. Functionalization of a SiO2-coated magnetic graphene oxide composite with polyaniline–polypyrrole for magnetic solid phase extraction of ultra-trace Cr(iii) and Pb(ii) in water and food samples using a Box–Behnken design. *New J Chem.* (2019) 43:12126–36. doi: 10.1039/c9nj02038a
20. Stanikunaite R, Khan SI, Trappe JM, Ross SA. Cyclooxygenase-2 inhibitory and antioxidant compounds from the truffle *Elaphomyces granulatus*. *Phytother Res.* (2009) 23:575–8. doi: 10.1002/ptr.2698
21. Hämäläinen M, Nieminen R, Asmawi MZ, Vuorela P, Vapaatalo H, Moilanen E. Effects of flavonoids on prostaglandin E2 production and on COX-2 and mPGES-1 expressions in activated macrophages. *Planta Med.* (2011) 77:1504–11. doi: 10.1055/s-0030-1270762
22. Chang ZQ, Gebru E, Lee SP, Rhee MH, Kim JC, Cheng H, et al. In vitro antioxidant and anti-inflammatory activities of protocatechualdehyde isolated from *Phellinus gilvus*. *J Nutr Sci Vitaminol.* (2011) 57:118–22. doi: 10.3177/jnsv.57.118
23. Ajayi AM, Badaki VB, Ariyo OO, Ben-Azu B, Asejeje FO, Adedapo AD. Chrysophyllum albidum fruit peel attenuates nociceptive pain and inflammatory response in rodents by inhibition of pro-inflammatory cytokines and COX-2 expression through suppression of NF-κB activation. *Nutr Res.* (2020) 77:73–84. doi: 10.1016/j.nutres.2020.03.004
24. Kang NJ, Lee KW, Shin BJ, Jung SK, Hwang MK, Bode AM, Dong Z. Caffeic acid, a phenolic phytochemical in coffee, directly inhibits Fyn kinase activity and UVB-induced COX-2 expression. *Carcinogenesis.* (2008) 30: 321–330. doi: 10.1093/carcin/bgn282
25. Giri SS, Sen SS, Sukumaran V, Park SC. Pinocembrin attenuates lipopolysaccharide-induced inflammatory responses in Labeo rohita macrophages *via* the suppression of the NF-κB signalling pathway. *Fish Shellfish Immunol.* (2016) 56:459–66. doi: 10.1016/j.fsi.2016.07.038
26. de Souza CO, Valenzuela CA, Baker EJ, Miles EA, Rosa Neto JC, Calder PC. Palmitoleic acid has stronger anti-inflammatory potential in human endothelial cells compared to oleic and palmitic acids. *Mol Nutr Food Res.* (2018) 62:e1800322. doi: 10.1002/mnfr.201800322
27. Huang X, Xi Y, Mao Z, Chu X, Zhang R, Ma X, et al. Vanillic acid attenuates cartilage degeneration by regulating the MAPK and PI3K/AKT/NF-κB pathways. *Eur J Pharmacol.* (2019) 859:172481. doi: 10.1016/j.ejphar.2019.172481
28. Adeyanju AA, Asejeje FO, Molehin OR, Owoeye O, Olatoye EO, Ekpo EN. Protective role of protocatechuic acid in carbon tetrachloride-induced oxidative stress *via* modulation of proinflammatory cytokines levels in brain and liver of Wistar rats. *J Basic Clin Physiol Pharmacol.* (2021) 3:20200202. doi: 10.1515/jbcpp-2020-0202
29. BenSaad LA, Kim KH, Quah CC, Kim WR, Shahimi M. Anti-inflammatory potential of ellagic acid, gallic acid and punicalagin A and B isolated from *Punica granatum*. *BMC Complement Altern Med.* (2017) 17:47. doi: 10.1186/s12906-017-1555-0
30. Lee KP, Choi NH, Kim HS, Ahn S, Park IS, Lee DW. Anti-neuroinflammatory effects of ethanolic extract of black chokeberry (*Aronia melanocapa* L.) in lipopolysaccharide-stimulated BV2 cells and ICR mice. *Nutr Res Pract.* (2018) 12:13–19. doi: 10.4162/nrp.2018.12.1.13
31. Amparo TR, Seibert JB, Mathias FA, Vieira JF, Soares RD, Freitas KM, et al. Anti-inflammatory activity of *Protium spruceanum* (Benth.) Engler is associated to immunomodulation and enzymes inhibition. *J Ethnopharmacol.* (2019) 241:112024. doi: 10.1016/j.jep.2019.112024

Conflict of Interest: Authors HW and ZY were employed by Jiangsu Original Drug Research and Development Co., Ltd.

The remaining authors declare that the research was conducted in the absence of any commercial or financial relationships that could be construed as a potential conflict of interest.

frontiers in Nutrition

ORIGINAL RESEARCH
published: 25 February 2022
doi: 10.3389/fnut.2022.844195

Discovery and Characterization of the Naturally Occurring Inhibitors Against Human Pancreatic Lipase in *Ampelopsis grossedentata*

Xiao-Ya Qin[1,2†], Xu-Dong Hou[2,3†], Guang-Hao Zhu[2†], Yuan Xiong[2], Yun-Qing Song[2], Liang Zhu[4], Dong-Fang Zhao[2], Shou-Ning Jia[4], Jie Hou[3*], Hui Tang[1*] and Guang-Bo Ge[2*]

[1] Key Laboratory of Xinjiang Phytomedicine Resource and Utilization, Ministry of Education, Pharmacy School of Shihezi University, Xinjiang, China, [2] Shanghai Frontiers Science Center of TCM Chemical Biology, Institute of Interdisciplinary Integrative Medicine Research, Shanghai University of Traditional Chinese Medicine, Shanghai, China, [3] College of Basic Medical Sciences, Dalian Medical University, Dalian, China, [4] Qinghai Hospital of Traditional Chinese Medicine, Xining, China

Pancreatic lipase (PL) inhibitor therapy has been validated as an efficacious way for preventing and treating obesity and overweight. In the past few decades, porcine PL (pPL) is widely used as the enzyme source for screening the PL inhibitors, which generates a wide range of pPL inhibitors. By contrast, the efficacious inhibitors against human PL (hPL) are rarely reported. This study aims to discover the naturally occurring hPL inhibitors from edible herbal medicines (HMs) and to characterize the inhibitory mechanisms of the newly identified hPL inhibitors. Following the screening of the inhibition potentials of more than 100 HMs against hPL, *Ampelopsis grossedentata* extract (AGE) displayed the most potent hPL inhibition activity. After that, the major constituents in AGE were identified and purified, while their anti-hPL effects were assayed *in vitro*. The results clearly showed that two abundant constituents in AGE (dihydromyricetin and iso-dihydromyricetin) were moderate hPL inhibitors, while myricetin and quercetin were strong hPL inhibitors [half-maximal inhibitory concentration (IC_{50}) values were around 1.5 μM]. Inhibition kinetic analyses demonstrated that myricetin and quercetin potently inhibited hPL-catalyzed near-infrared fluorogenic substrate of human pancreatic lipase (DDAO-ol) hydrolysis in a non-competitive inhibition manner, with K_i values of 2.04 and 2.33 μM, respectively. Molecular dynamics simulations indicated that myricetin and quercetin could stably bind on an allosteric site of hPL. Collectively, this study reveals the key anti-obesity constituents in AGE and elucidates their inhibitory mechanisms against hPL, which offers convincing evidence to support the anti-obesity and lipid-lowering effects of this edible herb.

Keywords: human pancreatic lipase (hPL), obesity, *Ampelopsis grossedentata*, myricetin, inhibition mechanism

OPEN ACCESS

Edited by:
Zhiqiang Wang,
Hebei University, China

Reviewed by:
Ihab Almasri,
Al-Azhar University–Gaza, Palestine
Nidal Jaradat,
An-Najah National University, Palestine

****Correspondence:***
Guang-Bo Ge
geguangbo@dicp.ac.cn
Hui Tang
th_pha@shzu.edu.cn
Jie Hou
houjie@dmu.edu.cn

[†] These authors have contributed equally to this work

Specialty section:
This article was submitted to Food Chemistry, a section of the journal Frontiers in Nutrition

Received: *27 December 2021*
Accepted: *25 January 2022*
Published: *25 February 2022*

Citation:
Qin X-Y, Hou X-D, Zhu G-H, Xiong Y, Song Y-Q, Zhu L, Zhao D-F, Jia S-N, Hou J, Tang H and Ge G-B (2022) Discovery and Characterization of the Naturally Occurring Inhibitors Against Human Pancreatic Lipase in Ampelopsis grossedentata. Front. Nutr. 9:844195. doi: 10.3389/fnut.2022.844195

INTRODUCTION

Obesity and obesity-associated metabolic disorders are serious and global public health problems (1, 2). Although many factors (including genetic, physiological, medicinal, and behavioral factors) participate in the etiology of obesity (3), the most common reason leading to this metabolic disorder is a long-term imbalance between food intake and energy expenditure (4, 5). Over the past 50 years, accompanied by the increase in high-fat and high-sugar diets, as well as insufficient physical activity (6, 7), ∼1.9 billion adults in the world were overweight and at least 650 million of them were obese (8, 9). More startlingly, the prevalence of overweight and obesity among children and adolescents has risen dramatically from just 4% in 1975 to over 18% in 2016 (10). The prevalence of obesity is strongly associated with a variety of metabolic disorders, such as hypertension, cardiovascular diseases, non-alcoholic liver disease, type II diabetes, stroke, and various types of cancer (11–13). Consequently, reducing the morbidity related to obesity has become a public health priority. Over the past few decades, several feasible strategies have been proposed for preventing and treating obesity, such as blocking lipid absorption, accelerating lipid metabolism, regulating lipid accumulation, and lipid signal transduction, as well as gastrectomy (14). Among all reported strategies for preventing and treating obesity, blocking lipid absorption by using food or herbal products to lose weight is very popular for obese patients (15, 16).

Pancreatic lipase (PL), a key digestive enzyme responsible for the hydrolysis of dietary triglycerides in the gastrointestinal tract, has gained considerable attention as an important anti-obesity target (17). In the past few decades, a variety of edible herbal medicines (HMs) and their constituents have been reported with anti-PL effects (18–20). However, in most studies, porcine PL (pPL) is frequently used as the enzyme source for screening and characterizing PL inhibitors, which generates a wide range of pPL inhibitors (21–24). By contrast, the efficacious inhibitors against human PL (hPL) are rarely reported. Although the amino acid sequence identity between the pPL and hPL was relatively high (∼86%), the large species differences in inhibitor response have been reported (25–27). Thus, it is urgent and necessary to find more efficacious hPL inhibitors as anti-obesity agents by using hPL as the enzyme source. Ideal orally administrated hPL inhibitors for preventing and treating obesity or obesity-associated complications should meet the following three requirements, good safety profile (28), high efficacy (29), high local exposure to the gastrointestinal tract, and very low exposure into the circulatory system which could minimize the influence on the endogenous metabolism in the liver or other deep organs (30, 31). To the best of our knowledge, the ideal orally administrated anti-obesity products *via* inhibiting hPL that meet the above-mentioned requirements are rarely reported. Therefore, it is urgent and necessary to discover more efficacious anti-PL agents or products with good safety profiles for preventing and treating obesity-associated complications.

Recently, a fluorescence-based high-throughput assay for screening hPL inhibitors was established by us in which hPL was used as the enzyme source and a near-infrared fluorogenic substrate (DDAO-ol) was used as probe substrate (32). With the help of this newly developed hPL inhibition assay, more than one hundred HMs extracts were collected and their anti-hPL activities were assayed. The preliminary screening results clearly showed that an edible herbal product, *A. grossedentata* extract (AGE), displayed the most potent anti-hPL effect. *A. grossedentata* has traditionally been used as a health tea and folk HM by ethnic minorities in China and displayed a wide variety of beneficial properties, such as clearing away heat, detoxification, activating blood circulation, and dissipating blood stasis (33). In this case, the bioactive substances in AGE and their anti-hPL mechanisms were carefully investigated by using a panel of techniques, such as liquid chromatography-time of flight tandem mass spectrometer (LC–TOF–MS/MS)-based chemical profiling, reversed-phase liquid chromatographic separation, hPL inhibition assay, and molecular dynamics simulations. This study aims to reveal the key anti-obesity constituents in AGE and elucidate their inhibitory mechanisms against hPL, which will offer direct evidence to support the anti-obesity and lipid-lowering effects of AGE.

MATERIALS AND METHODS

Chemicals and Materials

A. grossedentata extract was provided by Eastsign Foods Co., Ltd. (Quzhou, China), other HMs were provided by Tianjiang Pharmaceutical Co., Ltd (Jiangsu, China). Dihydromyricetin, iso-dihydromyricetin, myricitrin, and myricetin were isolated by reverse-phase liquid chromatography. Taxifolin was purchased from Sichuan Weikeqi Biotechnology. Quercetin was purchased from the Shanghai Standard Technology Co., Ltd (Shanghai, China). Reynoutrin was obtained from the BioBioPha Co., Ltd. The positive inhibitors (sanggenone C and orlistat) were purchased from the Dalian Meilun Biotech Co., Ltd (Dalian, China). The purity of all compounds was higher than 98%. The stock solutions of each inhibitor and positive inhibitors were solubilized in grade dimethyl sulfoxide (DMSO, Tedia, USA). The specific substrate (DDAO-ol) and its hydrolytic product (DDAO) were obtained from the previous study (32). Expression and purification of hPL were performed according to the previous study (32). Porcine bile salt was obtained from the Dalian Meilun Biotech Co., Ltd (Dalian, China). Tris was purchased from Roche Diagnostics GmbH (Mannheim, Germany). Tris-HCl buffer (pH 7.4, 25 mM, 150 mM NaCl, 1 mM $CaCl_2$) was prepared by using Milli-Q Water (Millipore, USA). LC grade formic acid, acetonitrile, and methanol were purchased from Tedia Company (Fairfield, USA). All the other chemicals, such as NaCl and $CaCl_2$, were of analytical grade and obtained from the Sinopharm Chemical Reagent Co., Ltd (Shanghai, China).

PL Inhibition Assay

The inhibitory activity of each inhibitor against hPL was measured by using DDAO-ol as substrate, while orlistat and sanggenone C were used as positive inhibitors against hPL. Briefly, the incubation mixtures (100 µl, total volume) contained 66 µl Tris-HCl buffer, 10 µl hPL solution (0.5 µg/ml, final concentration), 20 µl porcine bile salt (0.1 mg/ml, final concentration), and 2 µl each inhibitor. After pre-incubating at 37°C for 3 min, the substrate of DDAO-ol (20 µM, final concentration) was added to the initial reaction. Subsequently, the fluorescent signals of the hydrolytic product of DDAO-ol (DDAO) were quantified by using the microplate reader (Spectra Max M4, Austria), with the wavelength of 600 and 660 nm for excitation and emission, respectively. The standard curve was plotted using DDAO as product standard (**Supplementary Figure S6**). The control incubations without inhibitors were also performed.

Chemical Profiling of AGE by Liquid Chromatography–Time of Flight Tandem Mass Spectrometer

To identify and characterize the naturally occurring hPL inhibitors in AGE, a UFLC system (Kyoto, Japan) coupling with a Triple TOF 5600 Mass Spectrometer system (Foster City, CA, USA) was performed to analyze predominant constituents. The chromatographic separation was employed by the Shimadzu VP-ODS C_{18} column (2.0 mm × 250 mm, 4.6 μm) with a flow rate of 0.4 ml/min. The mobile phase was made up of water (0.1% formic acid) (A) and acetonitrile (B). The mobile phase program was shown in **Supplementary Table S1**. The column temperature was set at 40°C. The AGE sample (10 mg/ml) injection volume was 3 μl. The constituents were further analyzed *via* LC–TOF–MS/MS equipped with an electrospray ionization (ESI) source in negative ion mode. The MS parameters settings were shown in **Supplementary Table S2**.

Inhibition Kinetic Analyses

To investigate the inhibition kinetic types and to determine the inhibition constants (K_i) of two flavonoids (such as myricetin and quercetin) against hPL, the inhibition kinetics were carefully investigated *via* performing a series of kinetic analyses (34–36). Briefly, increasing concentrations of each inhibitor were mixed with hPL in the above-mentioned incubation system, while the reactions were started by adding DDAO-ol (at various concentrations) following 3 min pre-incubation at 37°C. The inhibition constants (K_i) were calculated as depicted in previous studies (37, 38).

Molecular Dynamic Simulations

To explore the allosteric mechanism of the newly identified inhibitors against hPL, docking simulations and molecular dynamic (MD) simulations were conducted. Prior to MD simulations, each ligand was emplaced into the allosteric pocket of hPL that was predicted by Cavityplus (39). The lipase–colipase complex structure of hPL (PDB code: 1LPA) was acquired from Protein Date Bank (https://www.rcsb.org/) (40, 41). First, the coordinate files of macromolecule (hPL) and each ligand (myricetin and quercetin) were ameliorated by AutoDockTools 1.5.6, such as only retaining hydrogen atoms of polarity, calculating atomic electric charges, and defining AD4 atom types (42). Second, the allosteric pocket of hPL was defined as the ligand-binding sites for each ligand. Then, top docking poses computed by Autodock Vina were collected for the following MD simulations.

The MD simulations of hPL-allosteric agent complexes were operated by GROMACS (43). Systems of receptor–ligand topology were constructed for simulations. In the previous step of MD simulations, a 50,000-step steepest descent energy minimization was operated. ApohPL and hPL-ligand atom coordinates were solvated with the rigid water model that has a Lennard-Jones site on the Oxygen and bare charge sites on the Hydrogens (TIP3P) water model, and the system was neutralized by sodium or chlorine ions. Next, the system was balanced by 100-ps constant volume and temperature (NVT) heating to 310 K and 100-ps performing the simulation with constant pressure and temperature (NPT). The initial energy-minimized balanced topology of systems was subjected to 100 ns MD at 310 K (V-rescale thermostat) and 1 bar (Parrinello–Rahman barostat). To go a step further on the allosteric binding modes between hPL and inhibitors, equilibrium conformations were clustered, and the largest center structure was kept for ligand–receptor interaction analysis *via* Discovery Studio Visualizer (BIOVIA Discovery Studio 2019, Dassault Systèmes, San Diego, USA).

Statistical Analysis

All inhibition assays were performed in triplicate, while the data were expressed as mean ± SD. IC_{50} values and K_i values were determined by GraphPad Prism 8.0 (GraphPad Software, Inc., La Jolla, USA).

RESULTS

Discovery of the HMs With Strong hPL Inhibition Activity

First, the hPL inhibitory activities of more than 100 HMs were assayed under identical conditions by using a high dosage (100 μg/ml, final concentration) (44, 45). As shown in **Figure 1**, although most of the tested HMs displayed weak anti-hPL effects, AGE showed the most potent anti-hPL effect. Next, to quantitatively characterize the inhibitory effects of AGE against hPL, the dose-inhibition curve of AGE against hPL-catalyzed DDAO-ol hydrolysis was plotted using increasing concentrations of AGE. As shown in **Supplementary Figure S1**, AGE dose-dependently inhibited hPL-catalyzed DDAO-ol hydrolysis in recombinant hPL, with a calculated IC_{50} value of 6.15 ± 0.71 μg/ml. Meanwhile, the time-dependent inhibition assay showed that the hPL inhibition potential of AGE was not changed following long pre-incubation time (**Supplementary Figure S2**), suggesting that the constituents in AGE were not time-dependent inhibitors of hPL. These results demonstrate that AGE inhibits hPL-catalyzed DDAO-ol hydrolysis *via* a dose-dependent and reversible manner, implying that this HM contains naturally occurring hPL inhibitor(s).

Chemical Profiling and Isolation of the Major Constituents in AGE

Next, the chemical constituents in AGE were characterized by a reliable LC–TOF–MS/MS method under the negative ion mode. As shown in **Supplementary Figure S3**, a total of nine major constituents in AGE, including 3-dihydroxyquercetin, dihydromyricetin, iso-dihydromyricetin, myricitrin, taxifolin, reynoutrin, quercetin-3-*O*-α-L-rhamnopyranoside, myricetin, and quercetin, were tentatively identified and their fragment ions were carefully characterized (33). The detailed fragment ions of nine identified constituents were listed in **Table 1** and **Supplementary Figures S7–S15**. Four abundant constituents in AGE, including dihydromyricetin, iso-dihydromyricetin, myricitrin, and myricetin, were purified by reverse-phase liquid chromatography and fully characterized by ^{1}H

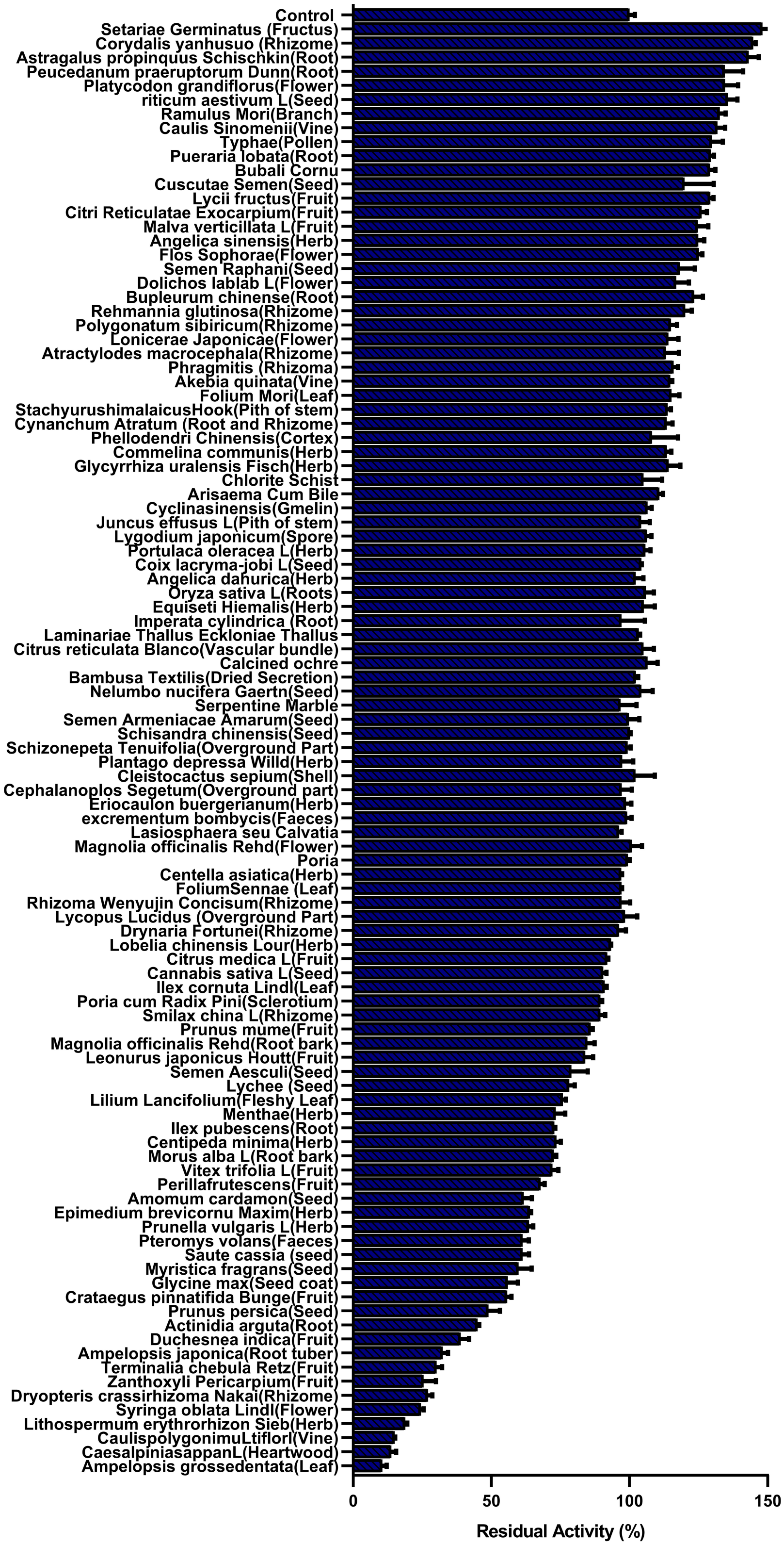

FIGURE 1 | The residual activity of human pancreatic lipase (hPL) in the presence of all tested herbal medicines (100 μg/ml, final concentration) was measured by catalyzed DDAO-ol hydrolysis. Data were shown as mean ± SD.

TABLE 1 | Identification of the main constituents in *Ampelopsis grossedentata* extract (AGE) by using LC–TOF–MS/MS.

No.	RT (min)	Pseudo-molecular ion	m/z observed	Formula	Identification	MS/MS spectra
1.	6.959	$[M-H]^-$	319.0461	$C_{15}H_{12}O_8$	3-dihydroxyquercetin	319.0503,301.0357,257.0469,233.0463, 215.0355,193.0147
2.	10.611	$[M-H]^-$	319.0462	$C_{15}H_{12}O_8$	Dihydromyricetin	319.0476,301.0366,257.0465, 215.0357,193.0152,175.0044
3.	11.413	$[M-H]^-$	319.0462	$C_{15}H_{12}O_8$	Iso-dihydromyricetin	319.0473,301.0370,257.0464, 233.0470,215.0358,193.0149
4.	12.894	$[M-H]^-$	463.0884	$C_{21}H_{20}O_{12}$	Myricitrin	463.0884,316.0229,287.0204,271.0254
5.	13.464	$[M-H]^-$	303.0515	$C_{15}H_{12}O_7$	Taxifolin	303.0527,285.0417,275.0579,259.0631, 217.0520,199.0410,175.0414,151.0040
6.	14.004	$[M-H]^-$	433.0774	$C_{20}H_{18}O_{11}$	Reynoutirn	433.0772,300.0290,271.0259,255.0304
7.	14.571	$[M-H]^-$	447.0938	$C_{21}H_{20}O_{11}$	Quercetin-3-*O*-α-L-rhamnopyranoside	447.0949,300.0293,271.0265,255.0316, 243.0314
8.	15.521	$[M-H]^-$	317.031	$C_{15}H_{10}O_8$	Myricetin	317.0337,299.0221,289.0381227.0363, 179.0014,151.0053,137.0260,109.0304
9.	18.091	$[M-H]^-$	301.0359	$C_{15}H_{10}O_7$	Quercetin	301.0392,273.0429,179.0008, 151.0056,121.0307,107.0147

NMR and ^{13}C nuclear magnetic resonance (NMR) spectra (**Supplementary Figures S16–S19**). Meanwhile, taxifolin, reynoutrin, and quercetin were confirmed by comparing their retention times on reverse-phase liquid chromatography, UV spectra, and MS/MS spectra with that of authentic standards. The chemical structures of the identified flavonoids in AGE were shown in **Figure 2**.

The Anti-hPL Effects of the Major Constituents in AGE

Subsequently, the anti-hPL effects of seven major constituents in AGE were tested at three inhibitor concentrations (1, 10, and 100 µM). The results showed that myricetin and quercetin displayed potent anti-hPL effects (**Figure 3**), with the residual activities of <15% at 10 µM. By contrast, dihydromyricetin, iso-dihydromyricetin, taxifolin displayed moderate hPL inhibition activities **(Figure 3)**, while myricitrin and reynoutrin did not inhibit hPL even at high dose (100 µM). Further investigations showed that myricetin and quercetin (46) dose-dependently inhibited hPL-catalyzed DDAO-ol hydrolysis, with the IC_{50} values of 1.34 ± 0.18 µM, 1.53 ± 0.10 µM, respectively (**Figure 4**, **Table 2**). Notably, the anti-hPL effects of these two flavonoids isolated from AGE are more potent than that of Sanggenone C (IC_{50} = 3.46 µM), a previously reported naturally occurring reversible hPL inhibitor. Meanwhile, the IC_{50} values of dihydromyricetin, iso-dihydromyricetin, and taxifolin (47) were also determined as 34.28 ± 4.63 µM, 14.37 ± 1.21 µM, and 27.83 ± 2.92 µM, respectively (**Figure 4**, **Table 2**). These results clearly demonstrate that five flavonoids from AGE are naturally occurring hPL inhibitors, while two flavonoids (myricetin and quercetin) display strong hPL inhibition activity, which encourages us to further investigate the inhibition kinetics and inhibitory mechanisms of these two flavonoids.

Determination of the Contents of Major Constituents in AGE With hPL Inhibition Activity

Subsequently, the contents of four major constituents (including dihydromyricetin, iso-dihydromyricetin, taxifolin, and myricetin) in AGE with hPL inhibition activity were determined by LC–UV. Prior to quantitative determination, the standard curves of these four ingredients in AGE were plotted and depicted in **Supplementary Figure S20**. After that, the contents of dihydromyricetin, iso-dihydromyricetin, taxifolin, and myricetin in AGE were determined as 88.15 µg/mg, 45.65 µg/mg, 4.81 µg/mg, and 8.22 µg/mg, respectively (as listed in **Table 2**). These findings suggest that the contents of dihydromyricetin and iso-dihydromyricetin in AGE are extremely high, while the contents of taxifolin and myricetin are at a moderate level (ranging from 4.81 to 8.22 µg/mg).

The Inhibitory Behaviors of Two Potent hPL Inhibitors in AGE

Next, the inhibition kinetics and the inhibition constants (K_i) of two flavonoids (myricetin and quercetin) with strong hPL inhibition activity were investigated. Prior to inhibition kinetic analyses, the time-dependent inhibition assays of myricetin and quercetin were performed. As shown in **Supplementary Figure S2**, the anti-hPL effects of myricetin and quercetin were not time-dependent, suggesting that these two flavonoids isolated from AGE were reversible hPL inhibitors rather than time-dependent inactivators. After that, the inhibition kinetics of myricetin and quercetin against hPL-catalyzed DDAO-ol hydrolysis were carefully characterized. The Lineweaver–Burk plots demonstrated that myricetin and quercetin potently inhibited the hPL in a non-competitive manner (**Figure 5**), with the apparent K_i values of 2.04 ± 0.75 µM and 2.33 ± 0.71 µM, respectively (**Table 2**). These

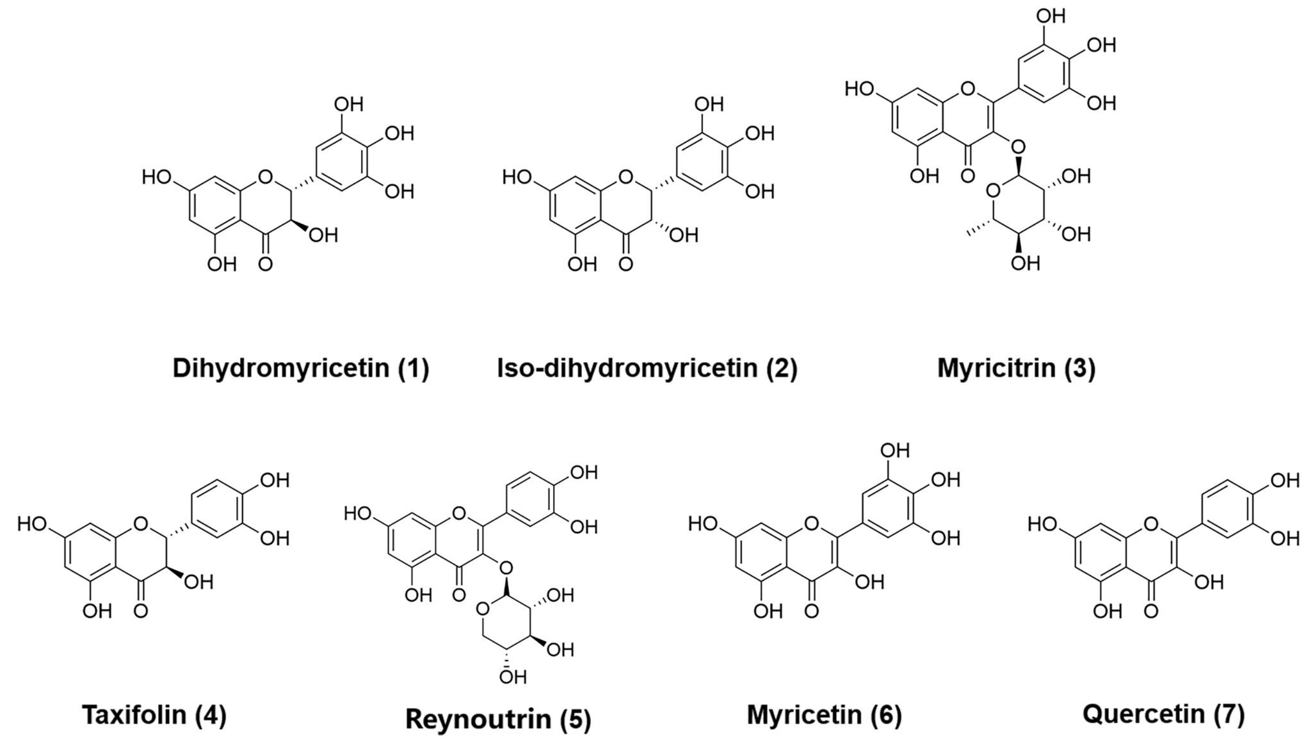

FIGURE 2 | The chemical structures of dihydromyricetin 1, iso-dihydromyricetin 2, myricitrin 3, taxifolin 4, reynoutrin 5, myricetin 6, and quercetin 7.

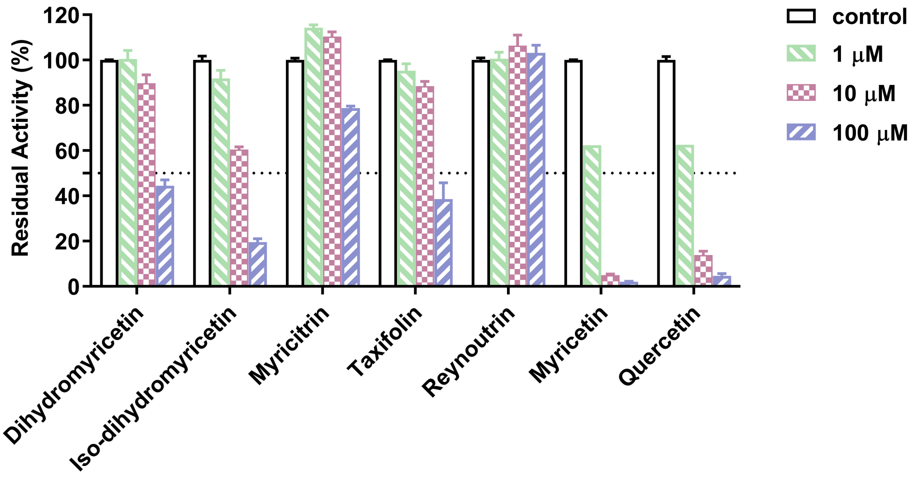

FIGURE 3 | Inhibitory effects of seven major constituents in the *Ampelopsis grossedentata* extract (AGE) against hPL-catalyzed DDAO-ol hydrolysis. Data were shown as mean ± SD.

observations clearly demonstrate that myricetin and quercetin strongly inhibit hPL in a non-competitive inhibition mode, with the K_i values of less than 2.5 μM.

Molecular Dynamic Simulations

Finally, MD simulations were carefully conducted to explore the binding poses of myricetin and quercetin on hPL. Each ligand was firstly docked into a predicted allosteric site of hPL (**Supplementary Figure S21**), and then MD simulations of hPL-ligand systems were operated as described in Section **Molecular Dynamic Simulations**. As shown in **Figure 6**, following docked with myricetin or quercetin, the gyro-radius of hPL could be remarkably stabilized. Notably, these ligands could form a strong hydrogen bonding interaction with Asp272, a key residue right below the catalytic pocket of hPL (**Figure 7**). Meanwhile, the binding of quercetin caused a shift on the

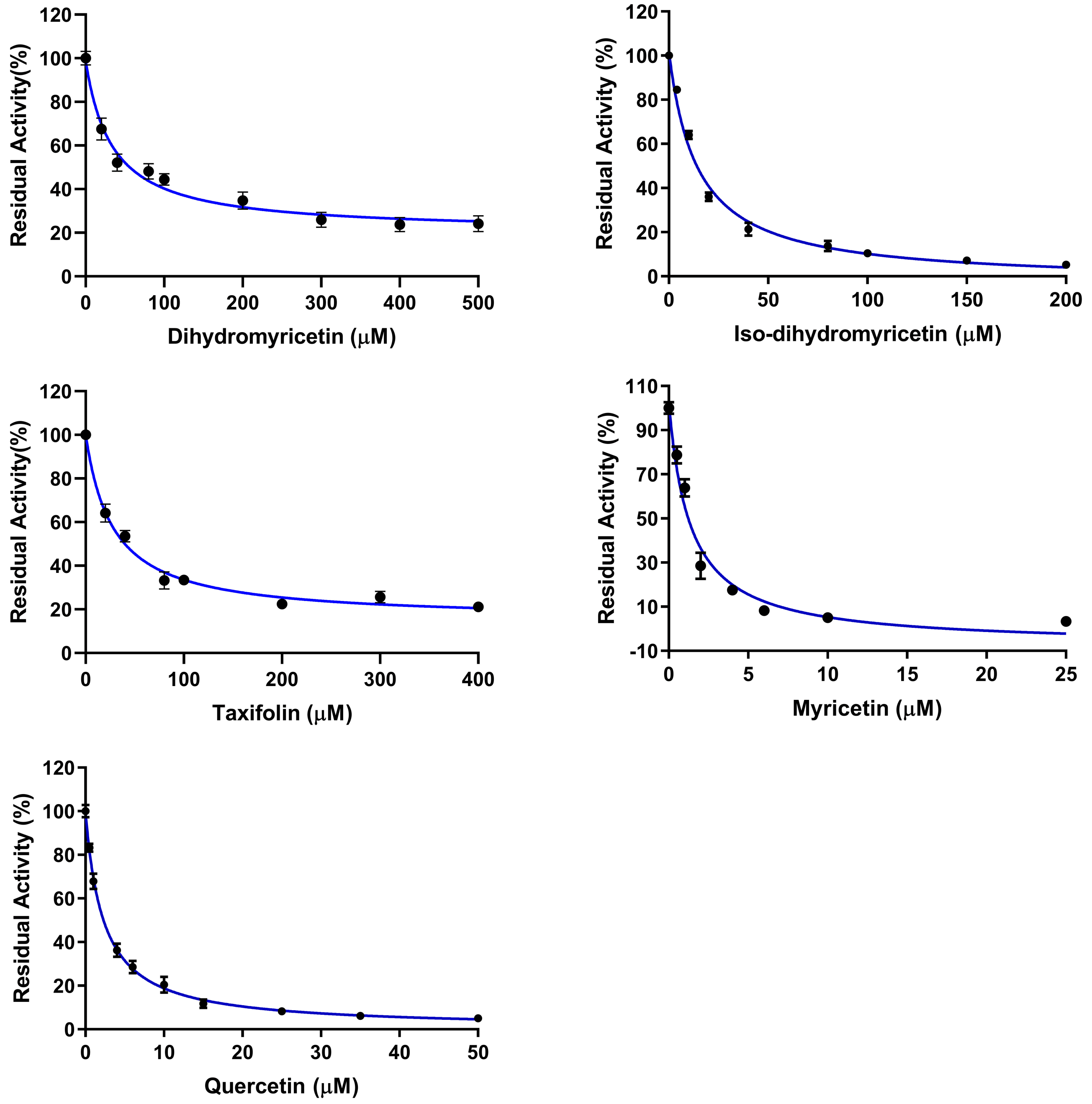

FIGURE 4 | Dose-inhibition curves of dihydromyricetin, iso-dihydromyricetin, taxifolin, myricetin, and quercetin against hPL-catalyzed DDAO-ol hydrolysis. Data were shown as mean ± SD.

"flap" of hPL, as depicted in **Supplementary Figure S22**. It has been reported that the flap played a significant role in catalytic activity, whose designated motion makes the catalytic residues accessible to the substrate (48). Such irregular conformational change could be mortal to the hydrolytic activity of hPL. Apart from the H-bonding interactions between Asp272 and these two inhibitors, myricetin formed Pi-alkyl interaction with Val 275, while quercetin formed complex hydrophobic interactions (Pi-alkyl and Pi-sigma) with a panel of residues in hPL (such as Thr271, Lys95, and Lys91), as depicted in **Figure 7** and **Supplementary Figures S23, S24**. These hydrophobic interactions were mainly directing the conjugated structure of each flavonoid, which was of importance for the binding of these inhibitors. These observations suggest that myricetin and quercetin can bind on hPL firmly in an allosteric way, which is consistent with the inhibition kinetics

TABLE 2 | The contents, IC_{50} values, K_i values, and the inhibition modes of the bioactive constituents in AGE against human pancreatic lipase (hPL).

Compound	MW	Content (µg/mg)	IC_{50} (µM)	K_i (µM)	Inhibition mode	Goodness of fit (R^2)
Myricetin	318.24	8.22	1.34 ± 0.18	2.04 ± 0.75	Non-competitive	0.99
Quercetin	302.24	–	1.53 ± 0.10	2.33 ± 0.71	Non-competitive	0.99
Iso-dihydromyricetin	320.25	45.65	14.37 ± 1.21	–	–	–
Dihydromyricetin	320.25	88.15	34.28 ± 4.63	–	–	–
Taxifolin	304.25	4.81	27.83 ± 2.92	–	–	–
Myricitrin	464.38	–	>100	–	–	–
Reynoutirn	434.35	–	>100	–	–	–
SanggenoneC[a]	708.71	–	3.46 ± 0.07	–	–	–
Orlistat[a]	495.73	–	6.16 ± 0.22 nM	–	–	–

[a] *Sanggenone C and orlistat were used as positive inhibitors of hPL.*

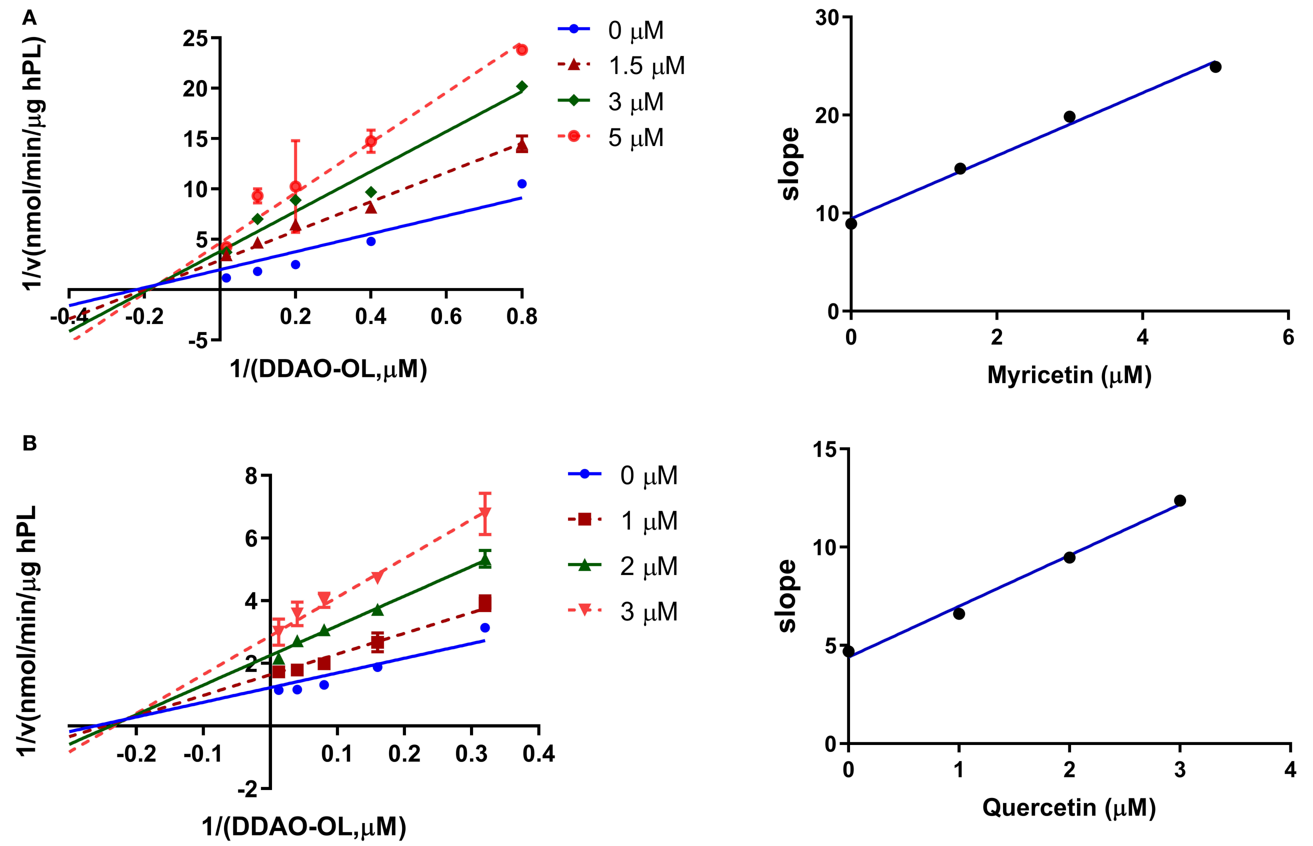

FIGURE 5 | Inhibition kinetics of myricetin **(A)**, and quercetin **(B)** toward the activity of hPL. Left, Lineweaver–Burk plots for each compound against hPL-catalyzed DDAO-ol hydrolysis. Right, the second plot of slopes from the Lineweaver–Burk plots.

results that myricetin and quercetin potently inhibit hPL in an allosteric manner.

DISCUSSION

It is well-known that hPL is one of the most important enzymes responsible for the digestion of dietary lipid (such as triacylglycerols) in the intestinal tract (14, 49), while hPL inhibitor therapy has been validated as an efficacious and cost-effective way for preventing and treating obesity and overweight. Orlistat, a potent and irreversible inhibitor of mammalian PL, has been approved for obesity treatment for over 20 years. However, this anti-PL agent has been found with a variety of adverse effects (gastrointestinal toxicity, pancreatic damage, metabolic system abnormalities, and high cancer risk) following long-term use (50–52). Thus, there is an urgent need for discovering more

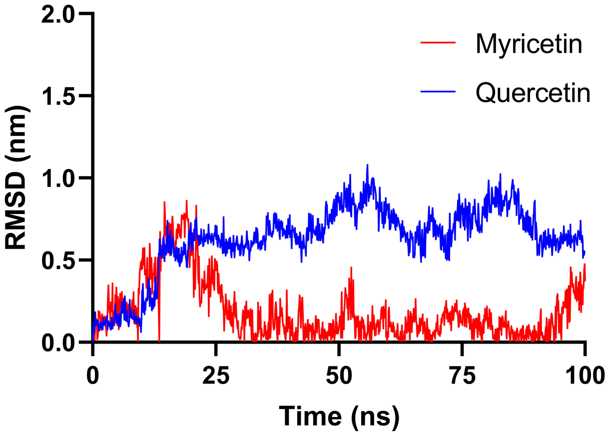

FIGURE 6 | The Root Mean Square Deviation (RMSD) fluctuation of hPL and complex bound with myricetin and quercetin.

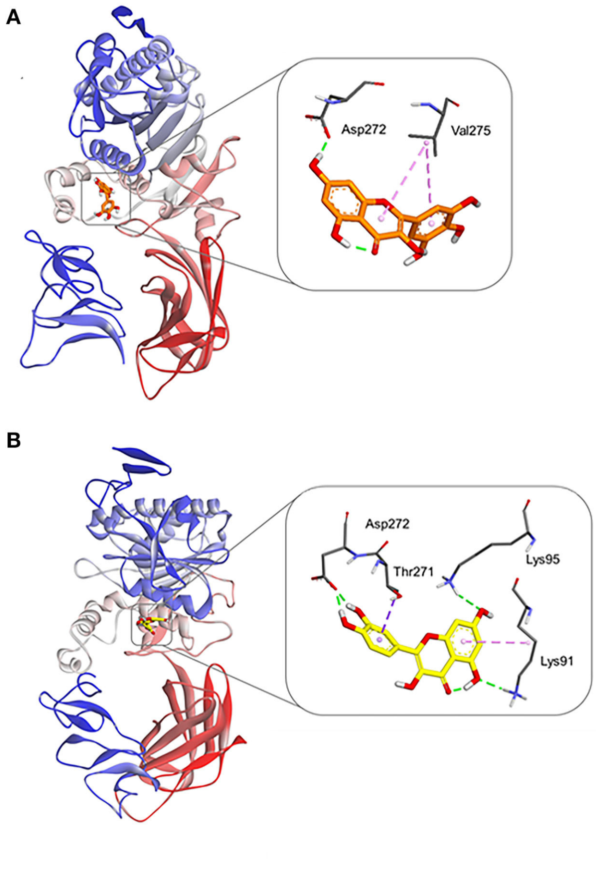

FIGURE 7 | Molecular docking results of myricetin and quercetin into the crystal structure of hPL (PDB ID: 1LPA) by Autodock Vina. Equilibrium conformations of myricetin **(A)**, and quercetin **(B)** in stereo overview and detailed view.

efficacious hPL inhibitors or for developing more practical anti-obesity products with good safety profiles for combating obesity. In the past few decades, many studies have reported that a range of HMs (such as the extract of *Ginkgo biloba* and *Cortex Mori Radicis*) are beneficial for the treatment of obesity and obesity-related metabolic diseases (53–56). Meanwhile, these HMs have several inherent advantages for weight loss and treating obesity-associated metabolic disorders, including a good safety profile, high anti-PL efficacy, as well as high gastrointestinal exposure but extremely low exposure in the circulation system. However, most previous studies use pPL to replace hPL as the enzyme source for screening and characterizing PL inhibitors, the inhibition potentials of known edible HMs against hPL and related key anti-hPL constituents are poorly investigated.

This study aims to investigate the inhibition potentials of edible HMs against hPL and to discover and characterize the naturally occurring hPL inhibitors from the most potent anti-hPL HM. Among all tested edible HMs, AGE was found with the most potent anti-hPL effect, with the estimated IC_{50} value of 6.15 μg/ml. *A. grossedentata* is known as the "king of flavonoids", while the content of total flavonoids in AGE is up to 45% (57). Herein, a total of nine flavonoids in AGE were identified and characterized by LC–MS/MS-based chemical profiling. Among them, five flavonoids (including dihydromyricetin, iso-dihydromyricetin, taxifolin, myricetin, and quercetin) were identified as the key constituents responsible for hPL inhibition. Although dihydromyricetin and iso-dihydromyricetin (the most abundant constituents) show moderate hPL inhibition activity, the contents of these two flavonoids are very high (88.15 μg/mg for dihydromyricetin and 45.65 μg/mg for iso-dihydromyricetin). It is estimated that the local exposure of these two agents in the gastrointestinal tract may be over 100 μM (206.08 μM for dihydromyricetin and 106.90 μM for iso-dihydromyricetin, *via* calculating the daily dose of each agent divided by the volume of the human gastrointestinal system), following oral administration with AGE at the daily dosage of this herbal product recommended by Chinese Materia Medica (58). In addition, the local exposure of the other flavonoids (such as taxifolin and myricetin) in AGE in the gastrointestinal tract can reach 11.85 and 19.37 μM, respectively, which are all much higher than their IC_{50} values (around 1.5 μM). Moreover, although myricitrin and reynoutrin in AGE display weak inhibitory effects against hPL, these two glycosides can be readily hydrolyzed by gut microbial to form myricetin and quercetin in the gastrointestinal tract, which can potently inhibit hPL (59). Thus, it is easily conceivable from these data that drinking *A. grossedentata* could efficiently inhibit hPL and display satisfactory anti-hPL effects *in vivo*, which in turn, reduce lipid absorption and lose body weight. It is also reported that the local exposure of dihydromyricetin (the most abundant constituent in *A. grossedentata*) in the stomach and small intestine is much higher than that in other deep organs (such as heart, liver, spleen, lung, kidney, and brain) following oral administration, suggesting that dihydromyricetin has very poor oral bioavailability and this agent hardly affects the endogenous metabolism in the liver (60, 61).

Since the flavonoids of AGE play an important role in hPL inhibition, the total flavonoids or AGE can be developed as HMs or other commercial products (such as drinking foods) in the future. It is noteworthy that there are significant differences in the flavonoid content from different batches of *A. grossedentata* (62), the possible reasons for the differences in flavonoid content of *A. grossedentata* are presumably due to seasonal and geographic factors, as well as processing schemes. Therefore, to obtain high-quality raw materials of *A. grossedentata* with satisfactory anti-hPL effect, it is necessary to critically analyze the influence of regions, seasons, and processing techniques on the contents of several anti-hPL flavonoids in *A. grossedentata*. Furthermore, a previous study has reported that dihydromyricetin can be converted into iso-dihydromyricetin (63), while the anti-hPL effect of iso-dihydromyricetin is much stronger than that of dihydromyricetin. In the future, the processing scheme of *A. grossedentata* can be intentionally optimized to convert more dihydromyricetin into iso-dihydromyricetin, which will strongly enhance the anti-hPL effect of AGE products.

CONCLUSION

In summary, this work reported the discovery of the bioactive anti-hPL substances from AGE, edible folk medicine in South China, and characterized the inhibitory mechanisms of the newly identified anti-hPL substances from this edible herb. Our results clearly demonstrated that almost all identified flavonoids in AGE were naturally occurring hPL inhibitors in which two abundant flavonoids in AGE (dihydromyricetin and iso-dihydromyricetin) were moderate hPL inhibitors, while myricetin and quercetin were identified as potent hPL inhibitors, with the IC_{50} values were around 1.5 μM. A panel of inhibition kinetic assays demonstrated that myricetin and quercetin potently inhibited hPL in a non-competitive manner, with the K_i values of $<2.5\,\mu$M. MD simulations suggested that myricetin and quercetin could tightly bind on hPL at an allosteric site. Collectively, our findings reveal the key anti-obesity constituents in AGE and elucidate their inhibitory mechanisms against hPL, all these data offer solid evidence to support the anti-obesity and the lipid-lowering effects of AGE and suggest that this edible herb can be developed as dietary supplements for preventing and treating obesity or obesity-associated complications.

DATA AVAILABILITY STATEMENT

The original contributions presented in the study are included in the article/**Supplementary Material**, further inquiries can be directed to the corresponding authors.

AUTHOR CONTRIBUTIONS

X-YQ: methodology, validation, data curation, and writing–original draft. X-DH: validation, data curation, and writing–original draft. G-HZ and YX: methodology and data curation. Y-QS: investigation. LZ: methodology. D-FZ: formal analysis. S-NJ: resources and funding acquisition. JH: writing–review and editing and project administration. HT: conceptualization, supervision, and project administration. G-BG: conceptualization, supervision, writing–review and editing, and project administration. All authors contributed to the article and approved the submitted version.

FUNDING

This work was supported by the National Natural Science Foundation of China (82160739, 81922070, 81973286, and 81973393), Innovation Team and Talents Cultivation Program of National Administration of Traditional Chinese Medicine (No. ZYYCXTD-D-202004), Shuguang Program (No. 18SG40) supported by Shanghai Education Development Foundation and Shanghai Municipal Education Commission, the Program for Innovative Leading Talents of Qinghai Province (2018 and 2019), the Key R&D and Transformation Science and Technology Cooperation Project of Qinghai Province (2019-HZ-819).

SUPPLEMENTARY MATERIAL

The Supplementary Material for this article can be found online at: https://www.frontiersin.org/articles/10.3389/fnut.2022.844195/full#supplementary-material

REFERENCES

1. Obesity: causes, consequences, treatments, and challenges. *J Mol Cell Biol.* (2021) 13:463–5. doi: 10.1093/jmcb/mjab056
2. Müller TD, Blüher M, Tschöp MH, DiMarchi RD. Anti-obesity drug discovery: advances and challenges. *Nat Rev Drug Discov.* (2021) 1–23. doi: 10.1038/s41573-021-00337-8
3. Qasim A, Turcotte M, de Souza RJ, Samaan MC, Champredon D, Dushoff J, et al. On the origin of obesity: identifying the biological, environmental and cultural drivers of genetic risk among human populations. *Obes Rev.* (2018) 19:121–49. doi: 10.1111/obr.12625
4. Nola IA, Doko Jelinić J, Bergovec M, Ruzić A, Persić V. [Dietary habits and cardiovascular diseases]. *Acta medica Croatica: casopis Hravatske akademije medicinskih znanosti.* (2010) 64:89–95.
5. Blüher M. Obesity: global epidemiology and pathogenesis. *Nat Rev Endocrinol.* (2019) 15:288–98. doi: 10.1038/s41574-019-0176-8
6. González-Muniesa P, Mártinez-González M-A, Hu FB, Després J-P, Matsuzawa Y, Loos RJF, et al. Obesity. *Nat Rev Dis Primers.* (2017) 3:17034. doi: 10.1038/nrdp.2017.34
7. Popkin BM, Adair LS, Ng SW. Global nutrition transition and the pandemic of obesity in developing countries. *Nutr Rev.* (2012) 70:3–21. doi: 10.1111/j.1753-4887.2011.00456.x
8. Afshin A, Forouzanfar MH, Reitsma MB, Sur P, Estep K, Lee A, et al. Health effects of overweight and obesity in 195 countries over 25 Years. *N Engl J Med.* (2017) 377:13–27. doi: 10.1056/NEJMoa1614362
9. Jane M, Hagger M, Foster J, Ho S, Pal S. Social media for health promotion and weight management: a critical debate. *BMC Public Health.* (2018) 18:932. doi: 10.1186/s12889-018-5837-3

10. Stavridou A, Kapsali E, Panagouli E, Thirios A, Polychronis K, Bacopoulou F, et al. Obesity in children and adolescents during COVID-19 pandemic. *Children*. (2021) 8:135. doi: 10.3390/children8020135
11. Piché ME, Tchernof A, Després JP. Obesity phenotypes, diabetes, and cardiovascular diseases. *Circ Res*. (2020) 126:1477–500. doi: 10.1161/CIRCRESAHA.120.316101
12. Martin KA, Mani MV, Mani A. New targets to treat obesity and the metabolic syndrome. *Eur J Pharmacol*. (2015) 763:64–74. doi: 10.1016/j.ejphar.2015.03.093
13. Peña-Romero AC, Navas-Carrillo D, Marín F, Orenes-Piñero E. The future of nutrition: nutrigenomics and nutrigenetics in obesity and cardiovascular diseases. *Crit Rev Food Sci Nutr*. (2018) 58:3030–41. doi: 10.1080/10408398.2017.1349731
14. Ko CW, Qu J, Black DD, Tso P. Regulation of intestinal lipid metabolism: current concepts and relevance to disease. *Nat Rev Gastroenterol Hepatol.* (2020) 17:169–83. doi: 10.1038/s41575-019-0250-7
15. Birari RB, Bhutani KK. Pancreatic lipase inhibitors from natural sources: unexplored potential. *Drug Discov Today*. (2007) 12:879–89. doi: 10.1016/j.drudis.2007.07.024
16. Bello M, Basilio-Antonio L, Fragoso-Vázquez J, Avalos-Soriano A, Correa-Basurto J. Molecular recognition between pancreatic lipase and natural and synthetic inhibitors. *Int J Biol Macromol.* (2017) 98:855–68. doi: 10.1016/j.ijbiomac.2017.01.150
17. Kumar A, Chauhan S. Pancreatic lipase inhibitors: the road voyaged and successes. *Life Sci.* (2021) 271:119115. doi: 10.1016/j.lfs.2021.119115
18. Doi K, Kojima T, Makino M, Kimura Y, Fujimoto Y. Studies on the constituents of the leaves of Morus alba L. *Chem Pharm Bull.* (2001) 49:151–3. doi: 10.1248/cpb.49.151
19. Jiao P, Tseng-Crank J, Corneliusen B, Yimam M, Hodges M, Hong M, et al. Lipase inhibition and antiobesity effect of Atractylodes lancea. *Planta Med.* (2014) 80:577–82. doi: 10.1055/s-0034-1368354
20. Chen T, Li Y, Zhang L. Nine different chemical species and action mechanisms of pancreatic lipase ligands screened out from forsythia suspensa leaves all at one time. *Molecules*. (2017) 22:795. doi: 10.3390/molecules22050795
21. Eom SH, Lee MS, Lee EW, Kim YM, Kim TH. Pancreatic lipase inhibitory activity of phlorotannins isolated from Eisenia bicyclis. *Phytother Res.* (2013) 27:148–51. doi: 10.1002/ptr.4694
22. Bustos AS, Håkansson A, Linares-Pastén JA, Peñarrieta JM, Nilsson L. Interaction of quercetin and epigallocatechin gallate (EGCG) aggregates with pancreatic lipase under simplified intestinal conditions. *PLoS ONE.* (2020) 15:e0224853. doi: 10.1371/journal.pone.0224853
23. Park JY, Kim CS, Park KM, Chang PS. Inhibitory characteristics of flavonol-3-O-glycosides from *Polygonum aviculare* L. (common knotgrass) against porcine pancreatic lipase. *Sci Rep*. (2019) 9:18080. doi: 10.1038/s41598-019-54546-8
24. Chen X, Xue S, Lin Y, Luo J, Kong L. Immobilization of porcine pancreatic lipase onto a metal-organic framework, PPL@MOF: a new platform for efficient ligand discovery from natural herbs. *Anal Chim Acta.* (2020) 1099:94–102. doi: 10.1016/j.aca.2019.11.042
25. Aboualham A, Verger R. Egg yolk lipoproteins as substrates for lipases. *Biochim Biophys Acta.* (2000) 1485:56–62. doi: 10.1016/S1388-1981(00)00033-0
26. Gargouri Y, Bensalah A, Douchet I, Verger R. Kinetic behaviour of pancreatic lipase in five species using emulsions and monomolecular films of synthetic glycerides. *Biochim Biophys Acta.* (1995) 1257:223–9. doi: 10.1016/0005-2760(95)00071-J
27. Point V, Pavan Kumar KV, Marc S, Delorme V, Parsiegla G, Amara S, et al. Analysis of the discriminative inhibition of mammalian digestive lipases by 3-phenyl substituted 1,3,4-oxadiazol-2(3H)-ones. *Eur J Med Chem.* (2012) 58:452–63. doi: 10.1016/j.ejmech.2012.10.040
28. Byard RW, Musgrave I. Herbal medicines and forensic investigations. *Forensic Sci Med Pathol.* (2010) 6:81–2. doi: 10.1007/s12024-010-9157-x
29. Astell KJ, Mathai ML, Su XQ. A review on botanical species and chemical compounds with appetite suppressing properties for body weight control. *Plant Foods Hum Nutr.* (2013) 68:213–21. doi: 10.1007/s11130-013-0361-1
30. Olennikov DN, Chirikova NK, Vasilieva AG, Fedorov IA. LC-MS profile, gastrointestinal and gut microbiota stability and antioxidant activity of *Rhodiola rosea* herb metabolites: a comparative study with subterranean organs. *Antioxidants*. (2020) 9:526. doi: 10.3390/antiox9060526
31. Zhang Z, Jiang M, Wei X, Shi J, Geng Z, Yang S, et al. Rapid discovery of chemical constituents and absorbed components in rat serum after oral administration of Fuzi-Lizhong pill based on high-throughput HPLC-Q-TOF/MS analysis. *Chin Med.* (2019) 14:6. doi: 10.1186/s13020-019-0227-z
32. Hu Q, Tian Z-H, Wang H-N, Huang J, Wang F-Y, Zhao B, et al. Rational design and development of a novel and highly specific near-infrared fluorogenic substrate for sensing and imaging of human pancreatic lipase in living systems. *Sens Actuators B Chem*. (2021) 341:130033. doi: 10.1016/j.snb.2021.130033
33. Zhang Q, Zhao Y, Zhang M, Zhang Y, Ji H, Shen L. Recent advances in research on vine tea, a potential and functional herbal tea with dihydromyricetin and myricetin as major bioactive compounds. *J Pharm Anal.* (2021) 11:555–63. doi: 10.1016/j.jpha.2020.10.002
34. Xin H, Qi XY, Wu JJ, Wang XX, Li Y, Hong JY, et al. Assessment of the inhibition potential of Licochalcone A against human UDP-glucuronosyltransferases. *Food Chem Toxicol.* (2016) 90:112–22. doi: 10.1016/j.fct.2016.02.007
35. Lei W, Wang DD, Dou TY, Hou J, Feng L, Yin H, et al. Assessment of the inhibitory effects of pyrethroids against human carboxylesterases. *Toxicol Appl Pharmacol.* (2017) 321:48–56. doi: 10.1016/j.taap.2017.02.018
36. He W, Wu JJ, Ning J, Hou J, Xin H, He YQ, et al. Inhibition of human cytochrome P450 enzymes by licochalcone A, a naturally occurring constituent of licorice. *Toxicology in vitro.* (2015) 29:1569–76. doi: 10.1016/j.tiv.2015.06.014
37. Zhou QH, Zhu GH, Song YQ, Que YF, He QQ, Tu DZ, et al. Methylophiopogonanone A is a naturally occurring broad-spectrum inhibitor against human UDP-glucuronosyltransferases: Inhibition behaviours and implication in herb-drug interactions. *Basic Clin Pharmacol Toxicol.* (2021) 129:437–49. doi: 10.1111/bcpt.13651
38. Song YQ, Weng ZM, Dou TY, Finel M, Wang YQ, Ding LL, et al. Inhibition of human carboxylesterases by magnolol: kinetic analyses and mechanism. *Chem Biol Interact.* (2019) 308:339–49. doi: 10.1016/j.cbi.2019.06.003
39. Xu Y, Wang S, Hu Q, Gao S, Ma X, Zhang W, et al. CavityPlus: a web server for protein cavity detection with pharmacophore modelling, allosteric site identification and covalent ligand binding ability prediction. *Nucleic Acids Res.* (2018) 46:W374–w9. doi: 10.1093/nar/gky380
40. van Tilbeurgh H, Egloff MP, Martinez C, Rugani N, Verger R, Cambillau C. Interfacial activation of the lipase-procolipase complex by mixed micelles revealed by X-ray crystallography. *Nature.* (1993) 362:814–20. doi: 10.1038/362814a0
41. Burley SK, Berman HM, Kleywegt GJ, Markley JL, Nakamura H, Velankar S. Protein Data Bank (PDB): the Single Global Macromolecular Structure Archive. *Methods Mol Biol.* (2017) 1607:627–41. doi: 10.1007/978-1-4939-7000-1_26
42. Trott O, Olson AJ. AutoDock Vina: improving the speed and accuracy of docking with a new scoring function, efficient optimization, and multithreading. *J Comput Chem.* (2010) 31:455–61. doi: 10.1002/jcc.21334
43. Van Der Spoel D, Lindahl E, Hess B, Groenhof G, Mark AE, Berendsen HJ, et al. GROMACS fast, flexible, and free. *J Comput Chem.* (2005) 26:1701–18. doi: 10.1002/jcc.20291
44. Vangoori Y, Dakshinamoorthi A, Kavimani S. Prominent pancreatic lipase inhibition and free radical scavenging activity of a myristica fragrans ethanolic extract *in vitro*. Potential role in obesity treatment. *Maedica.* (2019) 14:254–9. doi: 10.26574/maedica.2019.14.3.254
45. Jang DS, Lee GY, Kim J, Lee YM, Kim JM, Kim YS, et al. A new pancreatic lipase inhibitor isolated from the roots of Actinidia arguta. *Arch Pharm Res.* (2008) 31:666–70. doi: 10.1007/s12272-001-1210-9
46. Almasri IM. Computational approaches for the discovery of natural pancreatic lipase inhibitors as antiobesity agents. *Future Med Chem.* (2020) 12:741–57. doi: 10.4155/fmc-2019-0284
47. Su H, Ruan YT Li Y, Chen JG, Yin ZP, Zhang QF. *In vitro* and *in vivo* inhibitory activity of taxifolin on three digestive enzymes. *Int J Biol Macromol.* (2020) 150:31–7. doi: 10.1016/j.ijbiomac.2020.02.027
48. Hermoso J, Pignol D, Kerfelec B, Crenon I, Chapus C, Fontecilla-Camps JC. Lipase activation by nonionic detergents. The crystal structure of the porcine

lipase-colipase-tetraethylene glycol monooctyl ether complex. *J Biol Chem.* (1996) 271:18007–16. doi: 10.1074/jbc.271.30.18007

49. Rani N, Vasudeva N, Sharma SK. Quality assessment and anti-obesity activity of Stellaria media (Linn.) Vill. *BMC Complement Altern Med*. (2012) 12:145. doi: 10.1186/1472-6882-12-145
50. McClendon KS, Riche DM, Uwaifo GI. Orlistat: current status in clinical therapeutics. *Expert Opin Drug Saf.* (2009) 8:727–44. doi: 10.1517/14740330903321485
51. Suleiman JB, Nna VU, Othman ZA, Zakaria Z, Bakar ABA, Mohamed M. Orlistat attenuates obesity-induced decline in steroidogenesis and spermatogenesis by up-regulating steroidogenic genes. *Andrology*. (2020) 8:1471–85. doi: 10.1111/andr.12824
52. Filippatos TD, Derdemezis CS, Gazi IF, Nakou ES, Mikhailidis DP, Elisaf MS. Orlistat-associated adverse effects and drug interactions: a critical review. *Drug safety*. (2008) 31:53–65. doi: 10.2165/00002018-200831010-00005
53. Shang A, Gan RY, Xu XY, Mao QQ, Zhang PZ Li HB. Effects and mechanisms of edible and medicinal plants on obesity: an updated review. *Crit Rev Food Sci Nutr*. (2021) 61:2061–77. doi: 10.1080/10408398.2020.1769548
54. Yuliana ND, Korthout H, Wijaya CH, Kim HK, Verpoorte R. Plant-derived food ingredients for stimulation of energy expenditure. *Crit Rev Food Sci Nutr.* (2014) 54:373–88. doi: 10.1080/10408398.2011.586739
55. Huang R, Zhang Y, Shen S, Zhi Z, Cheng H, Chen S, et al. Antioxidant and pancreatic lipase inhibitory effects of flavonoids from different citrus peel extracts: an *in vitro* study. *Food Chem.* (2020) 326:126785. doi: 10.1016/j.foodchem.2020.126785
56. Ying HZ, Zang JN, Deng LL, Wang ZY Yu CH. Pentamethylquercetin reduces fat deposition *via* Sirt1-mediated pathways in male obese mice induced by a high fat diet. *Food Chem Toxicol.* (2013) 62:463–9. doi: 10.1016/j.fct.2013.09.002
57. Fan L, Zhao X, Tong Q, Zhou X, Chen J, Xiong W, et al. Interactions of Dihydromyricetin, a Flavonoid from Vine Tea (*Ampelopsis grossedentata*) with Gut Microbiota. *J Food Sci.* (2018) 83:1444–53. doi: 10.1111/1750-3841.14128
58. Chinese Materia Medica. Shanghai: Shanghai Scientific & Technical Publishers (1999).
59. D'Andrea G. Quercetin: a flavonol with multifaceted therapeutic applications? *Fitoterapia*. (2015) 106:256–71. doi: 10.1016/j.fitote.2015.09.018
60. Liu L, Yin X, Wang X, Li X. Determination of dihydromyricetin in rat plasma by LC-MS/MS and its application to a pharmacokinetic study. *Pharm Biol.* (2017) 55:657–62. doi: 10.1080/13880209.2016.1266669
61. Fan L, Tong Q, Dong W, Yang G, Hou X, Xiong W, et al. Tissue distribution, excretion, and metabolic profile of dihydromyricetin, a flavonoid from vine tea (*Ampelopsis grossedentata*) after oral administration in rats. *J Agric Food Chem.* (2017) 65:4597–604. doi: 10.1021/acs.jafc.7b01155
62. Zheng XJ, Xiao H, Zeng Z, Sun ZW, Lei C, Dong JZ, et al. Composition and serum antioxidation of the main flavonoids from fermented vine tea (*Ampelopsis grossedentata*). *J Funct Foods.* (2014) 9:290–4. doi: 10.1016/j.jff.2014.04.028
63. Li H, Li Q, Liu Z, Yang K, Chen Z, Cheng Q, et al. The Versatile Effects of Dihydromyricetin in Health. *Evid Based Complement Alternat Med.* (2017) 2017:1053617. doi: 10.1155/2017/1053617

Conflict of Interest: The authors declare that the research was conducted in the absence of any commercial or financial relationships that could be construed as a potential conflict of interest.

frontiers | Frontiers in Nutrition

ORIGINAL RESEARCH
published: 14 April 2022
doi: 10.3389/fnut.2022.869528

Construction of a Microfluidic Platform With Core-Shell CdSSe@ZnS Quantum Dot-Encoded Superparamagnetic Iron Oxide Microspheres for Screening and Locating Matrix Metalloproteinase-2 Inhibitors From Fruits of *Rosa roxburghii*

Yi Tao, Meiling Pan, Fei Zhu, Qing Liu and Ping Wang**

College of Pharmaceutical Science, Zhejiang University of Technology, Hangzhou, China

The microfluidic platform is a versatile tool for screening and locating bioactive molecules from functional foods. Here, a layer-by-layer assembly approach was used to fabricate core-shell CdSSe@ZnS quantum dot encoded superparamagnetic iron oxide microspheres, which served as a carrier for matrix metalloproteinase-2. The matrix metalloproteinase-2 camouflaged magnetic microspheres was further incorporated into a homemade microfluidic platform and incubated with extracts of fruits of *Rosa roxburghii*. The flow rate of the microfluidic platform was tuned. The major influencing parameters on ligand binding, such as dissociate solvents, incubation pH, ion strength, temperature, and incubation time were also optimized by using ellagic acid as a model compound. The specific binding ligands were sent for structure elucidation by mass spectrometry. The absolute recovery of ellagic acid ranged from 101.14 to 102.40% in the extract of *R. roxburghii* under the optimal extraction conditions. The linearity was pretty well in the range of 0.009–1.00 mg·ml^{-1} ($R^2 = 0.9995$). The limit of detection was 0.003 mg·ml^{-1}. The relative SDs of within-day and between-day precision were <1.91%. A total of thirteen ligands were screened out from fruits of *R. roxburghii*, which were validated for their inhibitory effect by enzyme assay. Of note, eleven new matrix metalloproteinase-2 inhibitors were identified, which may account for the antitumor effect of fruits of *R. roxburghii*.

Keywords: microfluidic, magnetic microspheres, *Rosa roxburghii*, matrix metalloproteinase-2, ligand fishing

OPEN ACCESS

Edited by:
Zhiqiang Wang,
Hebei University, China

Reviewed by:
Dong Zhu,
Nanjing University of Chinese Medicine, China
Yi Wang,
Zhejiang University, China

****Correspondence:***
Yi Tao
taoyi1985@zjut.edu.cn
Ping Wang
wangping45@zjut.edu.cn

Specialty section:
This article was submitted to Food Chemistry, a section of the journal Frontiers in Nutrition

Received: *04 February 2022*
Accepted: *14 March 2022*
Published: *14 April 2022*

Citation:
Tao Y, Pan M, Zhu F, Liu Q and Wang P (2022) Construction of a Microfluidic Platform With Core-Shell CdSSe@ZnS Quantum Dot-Encoded Superparamagnetic Iron Oxide Microspheres for Screening and Locating Matrix Metalloproteinase-2 Inhibitors From Fruits of Rosa roxburghii. Front. Nutr. 9:869528. doi: 10.3389/fnut.2022.869528

INTRODUCTION

Rosa roxburghii Tratt (RRT), which mainly grows in Guizhou province (1), has attracted intensive attention owing to its diverse biological properties such as antitumor (2, 3), antiatherogenic (4), antioxidant (5), antibrowning (6), hyperglycemic (7), radioprotection (8, 9), and so on. Recently, the fruits of RRT have been transformed into functional foods such as standardized juice and beverage products. Triterpenoids, phenolics, and polysaccharides were reported to be the major components of RRT fruits (10). Although many endeavors have shown that extracts of RRT fruits own excellent antitumor effects (11), the components which account for the antitumor property of RRT fruits remain unclear.

Ligand fishing is a feasible strategy for discovering bioactive components from the complex mixture of natural products (12). A series of nanomaterials have been used as support for the drug targets. For instance, Hsp 90α functionalized InP/ZnS quantum dots (QDs) embedded mesoporous nanoparticles were employed for ligand fishing from *Curcuma longa* L (13). Moreover, PTP1B displayed *Escherichia coli* cells can be used for ligand fishing from the extracts of *Rhodiola rosea* (14). Besides, magnetic microspheres (MSs) have recently been examined as a very useful material for ligand fishing (15, 16). The surface of MSs could be easily modified and coated with enzymes or proteins that enable them to bind to other biologically active compounds.

The rapid development of microfluidics technology (17) has promoted new innovations in the field of ligand fishing. For instance, a three-phase-laminar-flow-chip was developed for fishing antitumor ingredients by G-quadruplex recognition from *Macleaya cordata* seeds extracts (18, 19). Precise manipulation of fluids and MSs in a microfluidic chip will not only accelerate the speed of ligand fishing but also reduce the expenditure of the expensive target protein and other solvents. Importantly, microfluidic devices are one of the most promising platforms to mimic *in vivo* like conditions (20).

Quantum dots (QDs) are ideal candidate fluorophores for optical visualization because of their outstanding fluorescent properties. Herein, to visualize the flow of the MSs in the microfluidic channels, hydrophobic cadmium selenium sulfide/zinc sulfide (CdSSe/ZnS) QDs were first loaded onto the surface of magnetic polystyrene spheres via the modified layer-by-layer assembly. After that, the target protein was immobilized onto the polyethylenimine (PEI) modified surface of MS@QDs. As a showcase, matrix metallopeptidase 2 (MMP-2), which is highly expressed in the most of tumors, namely, breast, prostate, and bowel cancers (21), is selected as the target protein. The schematic of incorporation of the MS@PEI@QDs@PEI@MMP-2 into a homemade microfluidic platform for ligand fishing from RRT fruits is present in **Figure 1**. Briefly, MS@PEI@QDs@PEI@MMP-2 and extract of *R. roxburghii* were infused into the channel of the microfluidic chip and incubated for a period. Then, unspecific binding compounds were washed to the waste by using magnetic separation. The dissociated solvent was pumped into the channel to dissociate the MMP-2 binding ligands. The ligands were sent for UPLC-Q-TOF/MS analysis and validated by using an enzyme assay.

MATERIALS AND METHODS

Materials

The raw materials of *R. roxburghii* were collected from Guiyang County of Guizhou Province and authenticated by Prof. Ping Wang. Voucher specimens were stored in the Zhejiang University of Technology (No. RR2021041). Recombinant human matrix metalloproteinase-2 (expressed in HEK 293 cells), 1-(3-dimethyl-aminopropyl)-3-ethyl-carbodiimide (EDC), *N*-hydroxysuccinimide (NHS), and PEI (molecular weight: 750,000 Da) were purchased from Sigma Co. 2-(N-morpholino) ethanesulfonic acid (MES) was obtained from Shanghai Yien Chemical Technology Co. Oil-soluble core-shell CdSSe/ZnS QDs (5 $mg\cdot ml^{-1}$) with an emission wavelength at 594 nm and carboxyl terminated MSs (diameter: 5.53 μm and volume: 10 ml) were obtained from Hebei Langfei Biotechnology Co.

Standard substances, namely, ellagic acid, loganic acid, corilagin, oreganol A, kajiichigoside F_1, zebirioside O, niga-ichigoside F_1, and quadranoside VIII, were purchased from Weikeqi Bio-technology Co. Peduncloside and valerenic acid were obtained from Shanghai Yuanye Bio-Technology Co. Potentillanoside A was supplied by Shanghai Tauto Biotech Co. Medicagenic acid was obtained from Chengdu Biopurify Phytochemicals Co. Rosamultin and batimastat were purchased from MedChemExpress Co. Purities of all the reference compounds were >98%. ELISA kit for testing human matrix metalloproteinase-2 was obtained from Shanghai Easy Biotech Co. UPLC-grade acetonitrile was purchased from Merck Co. A 96-well microtiter plate was obtained from Corning Co.

Apparatus

The analytical apparatus included a JEM-1200EX transmission electron microscopy (NEC Co), a Scanning electron microscope (SEM, Hitachi S4800), a Confocal laser scanning microscopy (Zeiss Co.), an XPert PRO X-ray Diffractometer (PANalytical Co.), a PPMS-9 vibration sample magnetometer (Quantum Design Co.), a Jasco-4100 Fourier transform infrared spectroscopy (Jasco Co.), a Waters SYNAPT G2 quadrupole-ion mobility-time-of-flight mass spectrometry (Waters MS Technologies Co.), a PB-10 Sartorius pH meter (Sartorius Co.), a Tecan's Infinite 200 PRO system (Tecan Co.), and a Milli-Q Water Purification System (Millipore Co.).

Fabrication of Microfluidic Chips

The microfluidic chip was prepared by employing a standardized soft lithography technology (22, 23). Briefly, a new silicon wafer was rinsed with ethanol and dried with a stream of air. To prevent surface defects, forceps were used to handle the wafer. The wafer was transferred to a spin coater for 10 s at 600 rpm, followed by 30 s at 3,000 rpm, and then covered with a SU-2025 negative photoresist. Due to the photosensitivity of the photoresist, the room lights were turned off. After that, the photoresist-coated silicon wafer was transferred to a hot plate for "soft-bake" at 95°C for three min. Then, the photoresist coated silicon wafer was removed from the hot plate and allowed to cool for 1 min. A prefabricated mask with the desired pattern was placed on top of the photoresist-covered silicon wafer, which

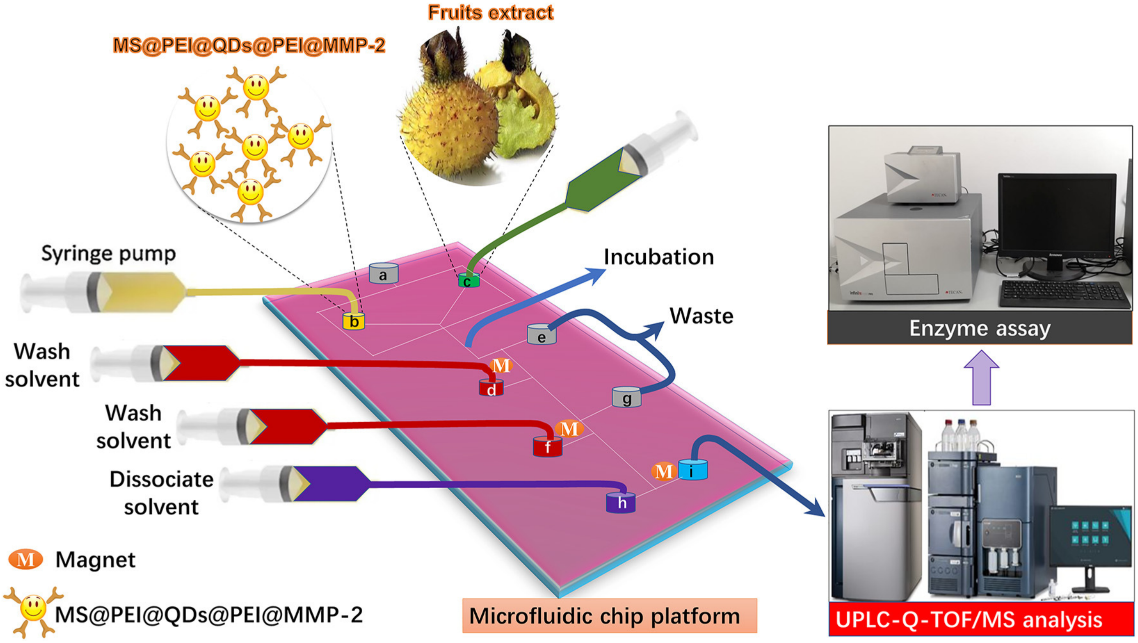

FIGURE 1 | Schematic of microfluidic chips-based matrix metalloproteinases inhibitors recognition system. MS@PEI@QDs@PEI@MMP-2 and extract of *Rosa roxburghii* were infused into the channel of the microfluidic chip and incubated for a period. Then, unspecific binding compounds were washed to the waste by using magnetic separation. The dissociated solvent was pumped into the channel to dissociate the MMP-2 binding ligands. The ligands were sent for UPLC-Q-TOF/MS analysis and validated by using an enzyme assay.

was then exposed to ultraviolet irradiation (350–450 nm) for 20 s. Subsequently, the silicon wafer was transferred to the hot plate for "hard-bake" at 110°C for six min. The room lights were turned on. The silicon wafer was carefully rinsed with a SU-8 photoresist developer three times and then rinsed with ethanol and air-dried. After that, polydimethylsiloxane (PDMS) elastomer solution and curing agent were mixed in a 10:1 weight ratio and then centrifuged at 900 rpm for 5 min to remove air bubbles. PDMS was poured onto the patterned silicon wafer in Petri dish and cured overnight at room temperature to form a complementary elastomeric stamp. Finally, PDMS was carefully removed from the silicon wafer. A razor edge was used to cut the stamp to the desired size. The homemade microfluidic chip is shown in **Supplementary Figure 1**. The width and height of the channels in the chip were 400 and 100 µm, respectively.

Preparation of MS@PEI@QDs@PEI@MMP-2

First, 600 µl aliquots of MSs were pipetted into a centrifuge tube, and the supernatant was removed by magnetic separation. The MS was further washed with MES buffer solution (10 mM, pH = 5) three times, and the supernatant was abandoned. A freshly prepared carbodiimide (EDC) solution (3 $g{\cdot}l^{-1}$) and PEI solution (80 $g{\cdot}l^{-1}$) were added to the MS successively, vortexed, and ultrasonically dispersed. After rotating for 3 h, the supernatant of the mixture solution was removed by magnetic separation. The remaining PEI-modified MS was washed 3 times with ultrapure water.

Second, 3 mg of MS@PEI was transferred to a centrifuge tube and washed with ethanol three times. Then, 1 ml aliquot of the CdSSe/ZnS QDs solution in chloroform/n-butanol (volume ratio, 1:20) was added into the centrifuge tube, vortexed, and rotated in the dark for 30 min. After that, the supernatant was removed by magnetic separation. Finally, MS@PEI@QDs were obtained and washed with ethanol 3 times and dispersed in ultrapure water.

Third, 1 ml aliquot of PEI solution (9 $g{\cdot}l^{-1}$) was prepared and added to the MS@PEI@QDs. The mixture solution was vortexed and then rotated in the dark for 30 min. The supernatant was removed by magnetic separation. Subsequently, MS@PEI@QDs@PEI was washed with ultrapure water three times. A total of 4 ml EDC (1 $mg{\cdot}ml^{-1}$) and 10 ml NHS (1 $mg{\cdot}ml^{-1}$) solution were added to 1 ml matrix metalloproteinase-2 solution, and reacted for 30 min to activate the carboxylic acid groups of matrix metalloproteinase-2. After that, this solution was rapidly added into 1.0 ml MS@PEI@QDs@PEI solution and agitated for 12 h to obtain MS@PEI@ QDs@PEI@MMP-2.

Characterization of MS@PEI@QDs@PEI@MMP-2

The surface of blank MS and modified MS were characterized by using transmission electron microscopy (TEM) and Fourier transform infrared spectroscopy. Magnetization was recorded at room temperature in a vibration sample magnetometer. The crystalline structure of MSs was identified by using a powder X-ray diffractometer. Confocal laser scanning microscopy was used to visualize the distribution of MS@PEI@QDs@PEI@MMP-2.

Experiments with varying amounts of MS@PEI@QDs@PEI (50, 100, 150, 200, and 250 µl) and a constant amount of matrix metalloproteinase-2 (200 μg) were carried out to investigate the amount of protein efficiently immobilized on the MS. Samples of the supernatants were withdrawn and analyzed for remaining protein by using the Bradford method and the calibration curve was prepared using solutions of bovine serum albumin. The protein immobilized on the MS was determined.

Optimization Conditions for Microfluidic Chip System-Based Ligand Fishing

All ligand fishing experiments were performed on the microfluidic chip system. The microfluidic chip system consisted of six modules, namely, a microscope stand, a light-emitting diode surface light source, a charge-coupled device (CCD) camera, a temperature controller, an automated x-y-z translation stage (Wuhan Mesovision Biotechnology Co.) for controlling the movement of the microfluidic chip, and four syringe pumps (Baoding Lange Constant Current Pump Co.). Before use, the microfluidic chip was first treated with 1% tween 80 in n-hexadecane (v/v) through port **a** to make the whole chip surface hydrophobic. A well-known matrix metalloproteinase-2 inhibitor, ellagic acid (24), was employed to select the best experimental conditions. Under the monitoring of the top-view CCD camera, MS@PEI@QDs@PEI@MMP-2 were infused into the upper left port **b**, whereas extract of *R. roxburghii* was infused into upper right port **c** at an appropriate flow rate to allow the solution to meet the MS@PEI@QDs@PEI @MMP-2 at the junction. The mixture was incubated in the channel for a period. Then, 500 μl aliquots of wash solvent (PBS buffer) were infused into the port **d**. At the turning point, a small ring magnet trapped the MS@PEI@QDs@PEI@MMP-2. Unspecific binding ligands were eluted to the waste port **e**. Again, 500 μl aliquots of wash solvent (PBS buffer) were infused into the port **f** and unspecific binding ligands were eluted to the waste port **g**. Finally, dissociate solvent was infused into the port **h,** the binding ligands were collected at port **i** and then sent for UPLC-Q-TOF/MS analysis.

Several parameters were investigated to optimize the screening conditions. At first, flow rates of the pump (10, 30, 50, 70, 90, and 120 μl/min) were investigated for optimization of the washing procedure. Second, different dissociation solvent was interrogated including methanol-water (10, 30, 50, 70, and 90%, v/v) and acetonitrile-water (10, 30, 50, 70, and 90%, v/v). Third, a gradient pH (pH 5.6, 6.2, 6.8, 7.4, and 8.0) and a gradient concentration (10, 50, 100, 250, and 500 mM, pH 7.4) of phosphate buffers were applied to study the effect of pH and ion strength of the incubation solution. Finally, incubation temperature (25, 30, 37, 45, and 50°C) and incubation time (10, 20, 30, 40, and 50 min) were also investigated for optimization of the screening procedure.

Validation of Microfluidic Chip System-Based Ligand Fishing Method

The ligand fishing was performed as described above. The specificity of the method was corroborated by detecting the interference of negative compound (loganic acid, 0.1 mg·ml^{-1}) at the retention times of the positive compound (ellagic acid, 0.1 mg·ml^{-1}). To obtain denatured MS@PEI@QDs@PEI@MMP-2, the prepared MS@PEI@QDs@PEI@MMP-2 was boiled in 100°C water for 10 min. The linearity was analyzed by plotting the peak area of the ellagic acid against a series of concentrations (0.009–1.00 mg·ml^{-1}). The lower limit of quantification was determined as the analytical concentration at an S/N ratio of 10. The intra- and interday precisions of the method were performed by repeated analyzing standard samples ($n = 6$) on the same day or on three consecutive days. The repeatability was interrogated by analyzing the same sample six times. Stability study was carried out with sample solution at 0, 2, 4, 8, 16, and 24 h. The recovery of the method was carried out by analyzing the peak area of ellagic acid (low, medium, and high concentration) spiked extract of *R. roxburghii* and the peak area of ellagic acid in the routine extract of *R. roxburghii*. The analysis was performed on an ACQUITY UPLC HSS T3 analytical column (1.8 μm, 100 × 2.1 mm i.d.). 0.1% Formic acid-water (A) and methanol (B) were selected as the mobile phase at a flow rate of 0.3 ml/min. The UV spectra were monitored at 254 nm. The injection volume was set to 2 μl.

Ligand Fishing From Extracts of *Rosa roxburghii*

The dried fruits of *R. roxburghii* were first ground into powder and sieved (60 mesh). After that, 5.0 g of powder was weighed and ultrasonicated in 50 ml of 70% ethanol-water for 30 min. The extraction was carried out two times. The extracts were combined and evaporated under a vacuum. Ligand fishing was performed according to the procedure as described above. The dissociated ligands were analyzed by using UPLC-Q-TOF/MS. The chromatographic separation was carried out on an ACQUITY UPLC HSS T3 analytical column (1.8 μm, 100 × 2.1 mm i.d.) with the column temperature set at 30°C. The mobile phase consisted of water containing 0.1% (v:v) formic acid (A) and methanol (B). A gradient program was used according to the following profile: 0–15 min, 5–55%B; 15–30 min, 55–95%B; 30–32 min, 95–100%B; and 32–35 min, 100–5%. The flow rate was 0.3 ml/min, and the injection volume was 2 μl. The UV spectra were recorded from 190 to 400 nm while the chromatogram was acquired at 254 nm. The acquisition parameters for mass spectrometry analyzes were as below: collision gas, ultrahigh-purity helium (He); nebulizing gas, high purity nitrogen (N_2); ion source temperature 120°C; cone voltage −30 V; desolvent gas flow rate 800 l/h; desolvation temperature 350°C; and mass range recorded *m/z* 50–1,500. Mass data analysis was performed by using MassLynx software (version 4.1, Waters MS Technologies Co).

Matrix Metalloproteinase-2 Inhibitory Assay

The inhibitory effects of binding ligands were evaluated as below. Batimastat served as a positive control. Test components were dissolved in the buffer to yield a gradient of concentrations between 1 and 200 μM. A total of 50 μl of test components and 100 μl of the enzyme solution were added to a 96-well plate and incubated for 30 min at 37°C. Afterward, the solution in the 96-well plate was discarded. The plate was dried on water adsorbing

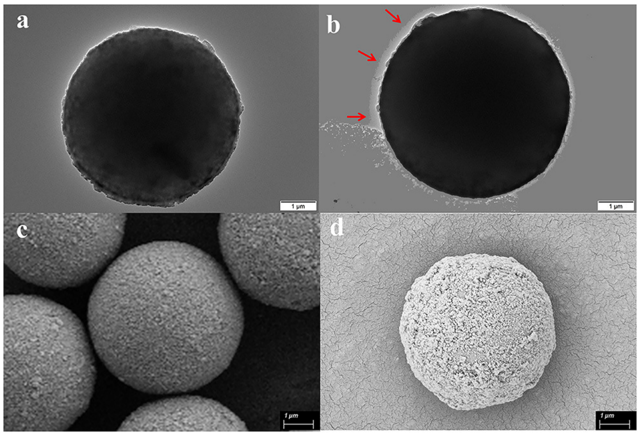

FIGURE 2 | Characterization of magnetic microspheres and MS@PEI@QDs@PEI @MMP-2. **(a)** TEM image of blank magnetic microspheres. **(b)** TEM image of MS@PEI@QDs@PEI@MMP-2. **(c)** The SEM picture of blank magnetic microspheres. **(d)** The SEM picture of MS@PEI@QDs@PEI@MMP-2.

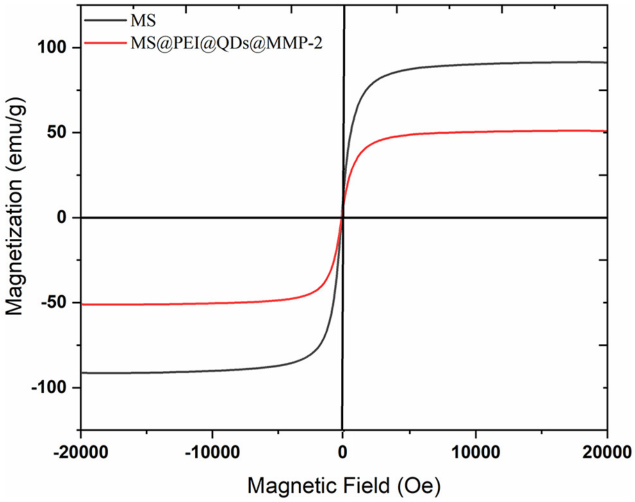

FIGURE 3 | Magnetization curves of blank magnetic microspheres (black line) and MS@PEI@QDs @PEI@MMP-2 (red line).

paper. A total of 200 μl of wash solution was added to each well and incubated for 30 s. Again, the solution in the 96-well plate was abandoned. The plate was dried on water adsorbing paper. This step was carried out five times. A total of 50 μl aliquots of solution A and 50 μl aliquots of solution B were added to each well and kept in a dark place for 15 min. As a result, 50 μl aliquots of stopping solution were pipetted into each well. The plate was monitored at the absorbance of 450 nm by using an automatic microplate reader.

Molecular Docking

The chemical structures of the ligands were imported into ChemBio3D Ultra 14.0 for energy minimization and saved in mol2 format. The minimum root-mean-square gradient was set to 0.001. The optimized small molecules are imported into AutodockTools-1.5.6 for hydrogenation, calculating the charge, assigning the charge, setting the rotatable bond, and saving it as "pdbqt" format. The protein structure of MMP-2 (PDB ID: 1CK7) was downloaded from the PDB database. Pymol 2.3.0 software was used to remove crystal water and original ligands. AutoDock Vina 1.1.2 was employed for docking, MMP-2-related parameters are set as below: center_x = 59.511, center_y = 96.28, and center_z = 147.189; search space: size_x: 126, size_y: 126, and size_z: 126 (the spacing between each grid point is 0.375Å), exhaustiveness: 10, and other parameters are default settings.

RESULTS AND DISCUSSION

Morphological Characterization

As is shown in **Figure 1**, the successful immobilization of matrix metalloproteinase-2 onto the MS@PEI@QDs@PEI was clearly revealed from the TEM images of the MSs before (**Figure 2A**) and after conjugation (**Figure 2B**). Scanning electron microscope images also showed that the surface of MSs was covered with a white layer (**Figures 2C,D**). FT-IR analysis provides direct proof for the immobilization of MMP-2 onto the MS@PEI@QDs@PEI. As is displayed in **Supplementary Figure 2**, the appearance of the C–N stretching band at (1,089.52 cm^{-1}) showed that the conjugation took place in a covalent manner through an amide linkage.

As is displayed in **Supplementary Figure 3**, the surface of the original MS shows a weak negative charge (−2.18 mV). After being modified with PEI, the surface potential becomes positive (+73.38 mV), indicating PEI was successfully attached to the MS surface. After loading the CdSSe/ZnS QDs, the positive potential of the MS@PEI@QDs surface was reduced (+68.67 mV), which is ascribed to that some of the amine groups are coordinated with CdSSe/ZnS QDs. When the PEI molecules were further adsorbed onto the surface of the MS@PEI@QDs, the zeta potential of MS@PEI@QDs@PEI surface was restored to a higher level (71.03 mV), revealing the surface of the MS@PEI@QDs@PEI is rich in amine functional groups. The loading of MMP-2 onto the surface lead to the drop in the zeta potential (53.99 mV), due to the consumption of the amine group.

The main peaks of the X-ray diffraction (XRD) of the MSs (black line) match well with the standard magnetite Fe_3O_4 XRD spectrum are displayed in **Supplementary Figure 4**. The peaks at 25.04°, 38.6°, and 48.76° correspond to the XRD spectrum of CdSSe/ZnS. Magnetization curves of blank MS and MS@PEI@QDs@PEI@MMP-2 are shown in **Figure 3**. The maximum saturation magnetization (51.15 emu/g) of MS@PEI@QDs@PEI@MMP-2 is a little less than that (91.44 emu/g) of blank MSs. The amounts of MSs were varied to determine the optimal ratio for immobilization of matrix metalloproteinase-2. As is shown in **Supplementary Figure 5**, when 150 μl MSs per 100 μg matrix metalloproteinase-2 were arranged, the largest percentage of conjugated protein was achieved. Thus, a ratio of 150 μl MSs per 100 μg matrix metalloproteinase-2 was chosen for subsequent studies.

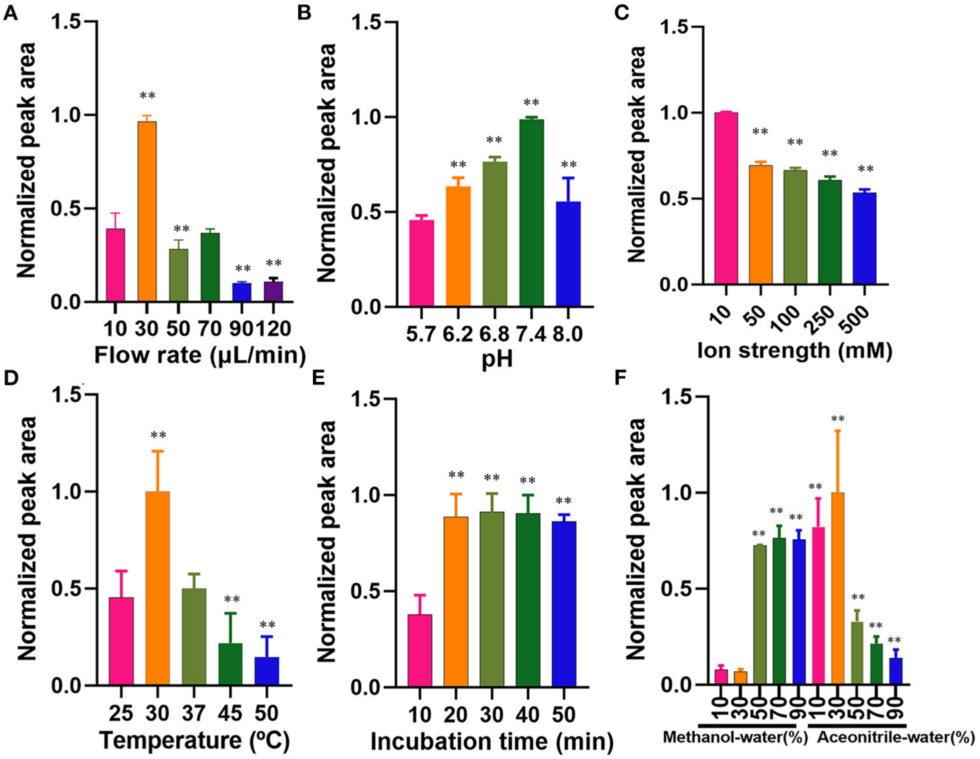

FIGURE 4 | Optimization of parameters affecting the microfluidic chip-based ligand screening system. **(A)** Flow rate, **(B)** pH profiles, **(C)** ionic strength profiles, **(D)** temperature profiles, **(E)** incubation time profiles, and **(F)** dissociated solvent. The symbol ** indicates $P < 0.05$ as compared with the first column.

Supplementary Figure 6 shows the confocal images of the obtained MS@PEI@QDs@PEI@MMP-2. It can be seen that there is a uniform red circle on the surface. The color halo further validated that the CdSSe/ZnS QDs were successfully loaded on the MS surface and were uniformly distributed on the MS surface. Meanwhile, the MS@PEI@QDs@PEI@MMP-2 were uniformly dispersed without obvious agglomeration, indicating that they have good dispersibility in an aqueous solution.

Optimization of Screening Condition

The flow rate of the microfluidic chip-based ligand fishing system is of great importance for the binding between the ligand and matrix metalloproteinase-2. As is presented in **Figure 4A**, a flow rate of 30 μl/min was the most suitable rate for ligand fishing. Non-covalent interaction between ligand and matrix metalloproteinase-2 is mainly driven by electrostatic interactions, the ionic strength and pH are of great importance to the interaction. As is shown in **Figure 4B**, the increase of pH from 5.7 to 7.4 led to an obvious decrease in the peak area of ellagic acid. Further increasing the pH value to 8.0 resulted in the drop of the peak area of ellagic acid. The optimal pH for the incubation is 7.4. The effect of ionic strength was investigated over a broad range of PBS concentrations (10–500 mM). As is displayed in **Figure 4C**, excessive PBS led to a significant decrease in binding between ellagic acid and MS@PEI@QDs@PEI @MMP-2. Thus, a PBS concentration of 10 mM was selected for the next experiment.

The incubation temperature was also investigated by varying temperatures ranging from 25 to 50°C. As is shown in **Figure 4D**, 30°C may be the suitable temperature for the incubation. Kato et al. (25) found that the reaction temperature was 37°C for human matrix metalloproteinase-2. In our experiment, the shift of 30–37°C suggested a significantly decreased binding efficiency. As is displayed in **Figure 4E**, an incubation time of 20 min was sufficient for the interaction between matrix metalloproteinase-2 and ellagic acid. Increasing the incubation time from 20 to 50 min exerted no significant effect on binding efficiency. Therefore, the incubation temperature and time were set to 30°C and 20 min.

The washing step plays a crucial role in ligand fishing. Different proportions of acetonitrile-water and methanol-water (10, 30, 50, 70, and 90% v/v), were arranged as denature solvents and investigated. The data of wash solvent is present in **Figure 4F**. The denaturation effect of 30% (v/v) acetonitrile-water was the best and was thus assigned as the denaturing solvent.

Method Validation

To investigate the specificity of the method, both positive control ellagic acid and negative control loganic acid were selected. As is presented in **Supplementary Figures 7A,B**, only the peak of

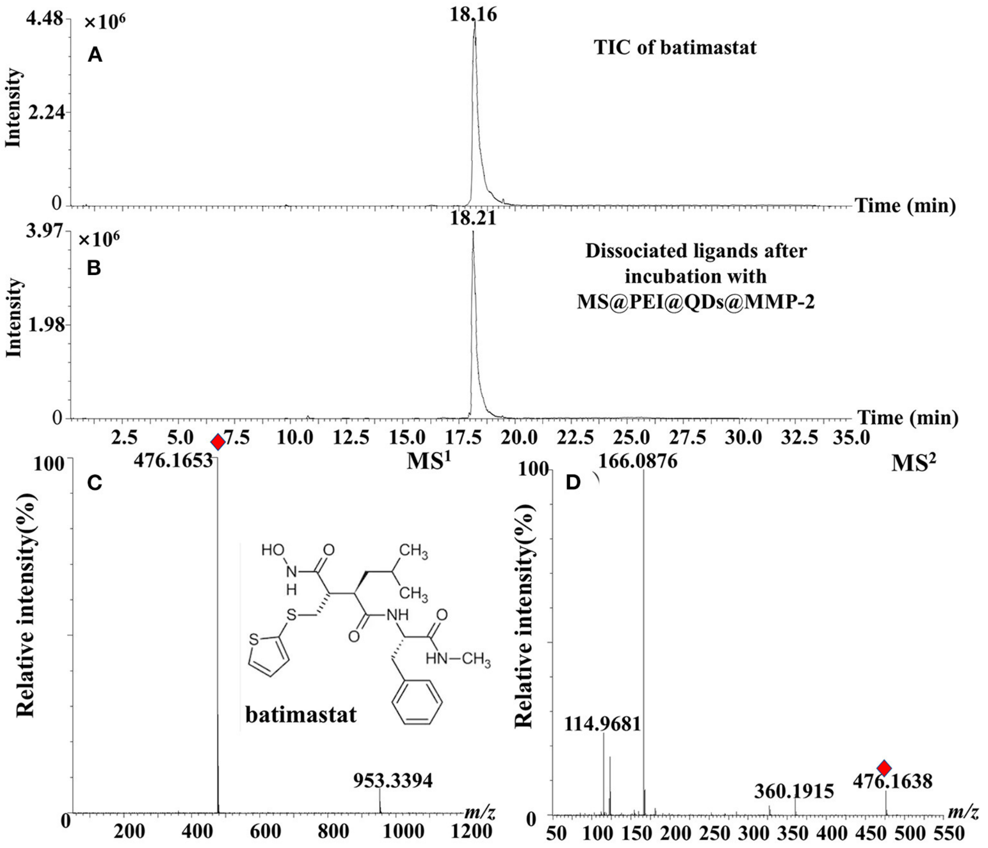

FIGURE 5 | TIC chromatograms of **(A)** batimastat, **(B)** dissociated solution after incubation with MS@PEI@QDs@PEI@MMP-2, **(C)** MS^1 chromatogram, and **(D)** MS^2 chromatogram of batimastat.

ellagic acid was observed after ligand fishing. No interference of the negative control loganic acid was observed. The method showed good specificity.

The calibration curve of ellagic acid showed good linearity in the range of 0.009–1.00 mg·ml^{-1} ($R^2 = 0.9995$). The limit of detection and limit of quantification of ellagic acid was determined to be 0.003 mg·ml^{-1} and from 0.009 mg·ml^{-1}. The relative SD (RSD) values of intraday and interday precisions were <1.91%. The RSD values of stability of ellagic acid were determined to be 2.53%. As is displayed in **Supplementary Table 1**, the average recoveries of ellagic acid were from 101.14 to 102.40% with RSD values from 1.21 to 2.13% for *R. roxburghii*. The RSD% values of repeatability of the method were no more than 2.98%. Moreover, the positive control batimastat was employed to interrogate the method. As is present in **Figures 5A,B**, the peak of batimastat was observed in the dissociated solution after microfluidic chip-based ligand fishing. The MS^1 and MS^2 information of batimastat (see **Figures 5C,D**) was in agreement with that of the literature (26). The extraction yield of batimastat was calculated as 76.6%. Overall, the developed microfluidic chip-based ligand fishing method was sensitive and robust.

Ligands Fishing From Extracts of *Rosa roxburghii*

Figure 6A shows the total ion chromatograms of the crude extract of *R. roxburghii*, while **Figure 6B** presents the dissociated ligands after incubation with MS@PEI@QDs@PEI@MMP-2. To exclude the non-specific binding, the TIC of dissociated solution after incubation with denatured MS@PEI@QDs@PEI@MMP-2 is presented in **Figure 6C**. It can be seen that none of the compounds were bound to the denatured MS@PEI@QDs@PEI@MMP-2. Detailed chemical information of the fourteen ligands is listed in **Table 1**. The structures of thirteen ligands (see **Supplementary Figure 8**) were elucidated by analyzing and comparing their retention times, UV data, and MS data with those of standard compounds. The compound corresponding to peaks 4 showed a parent ion at *m/z* 437.1101 [M-H]$^-$ and a daughter ion at *m/z* 300.9981 in negative MS^2 mode. In comparison with standard substance and the literature (27), peaks 4 was deduced as oreganol A. Peak 6 at the retention time of 8.63 min showed an [M-H]$^-$ ion at *m/z* 633 and major fragment ions at 301 [M-H-332]$^-$, were consistent with the loss of gallic acid and one glucose group, bonded to hexahydroxydiphenoyl group unit. Compared with the literature (28) and standard compound, peak 6 was unambiguously

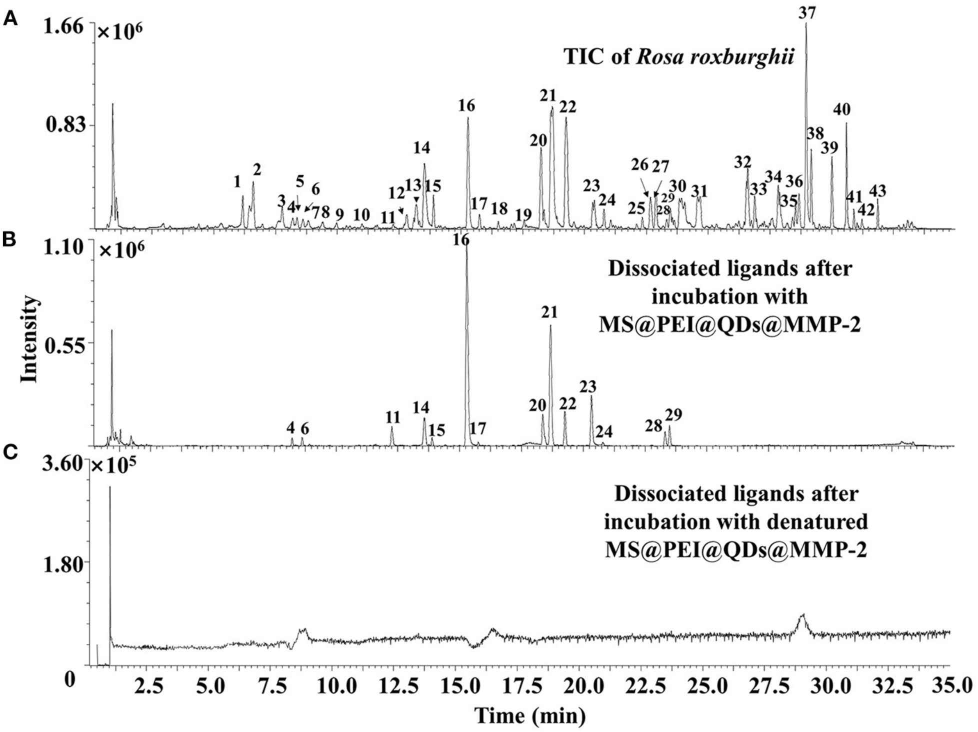

FIGURE 6 | TIC of **(A)** crude extract of *Rosa roxburghii* and **(B)** dissociated MMP-2 binding ligands after incubation with MS@PEI@QDs@PEI@MMP-2 or **(C)** denatured MS@PEI@QDs@PEI@MMP-2.

TABLE 1 | Chromatographic and mass characteristics of MMP-2 binding ligands.

No.	t_R (min)	MS^2	Formula	ESI-MS(-)		Identification
				Measured mass $[M-H]^-$ or $[M+HCOO]^-$	Error (ppm)	
4	8.22	**300.9981**	$C_{20}H_{22}O_{11}$	437.1110	5.9	Oreganol A
6	8.63	**301.0006**	$C_{27}H_{22}O_{18}$	633.0767	6.2	Corilagin
11	12.25	451.3176, **301.0107**	$C_{24}H_{50}O_{10}$	497.3368	8.4	—
14	13.53	**283.9986,** 229.0143	$C_{14}H_6O_8$	300.9991	2.3	Ellagic acid
15	13.87	301.0062, **271.0983**	$C_{21}H_{28}O_9$	423.1655	0.0	—
16	15.28	**677.4960**, 451.3290	$C_{37}H_{58}O_{11}$	723.5026	−4.3	Zebirioside O
17	15.75	**503.3400**	$C_{36}H_{58}O_{11}$	711.4001	−5.8	Niga-ichigoside F_1
20	18.25	**487.3368**	$C_{36}H_{58}O_{10}$	695.3994	−1.9	Peduncloside
21	18.68	**487.3402**	$C_{36}H_{58}O_{10}$	695.3974	3.7	Rosamultin
22	19.25	**487.3430**	$C_{36}H_{58}O_{10}$	695.3992	2.2	Kajiichigoside F_1
23	20.32	**485.3228**, 309.1722	$C_{36}H_{56}O_{10}$	693.3849	−0.1	Potentillanoside A
24	20.67	647.3819, **485.3219**	$C_{36}H_{56}O_{10}$	693.3844	−0.9	Quadranoside VIII
28	23.30	184.9697, **112.9872**	$C_{15}H_{22}O_2$	233.1545	1.3	Valerenic acid
29	23.49	**483.3058**, 465.2987	$C_{30}H_{46}O_6$	501.3221	1.0	Medicagenic acid

The bold values indicate the abundance of the ion is the largest.

identified as corilagin. The classification of compounds into ellagic acid or quercetin-based conjugates was made based on typical for these structures fragments ions appearing in MS/MS spectra. Fragment ions at *m/z* 283 $[M-H-H_2O]^-$ and 229 $[M-H-CO_2-CO]^-$, which were formed from precursor ion at *m/z* 301, suggested the presence of ellagic acid. Compared with standard compounds and the literature (29), peak 14 was unambiguously assigned as ellagic acid.

Peak 16 showed an $[M+HCOO]^-$ ion at m/z 723 and produced fragment ion at m/z 677 $[M–H]^-$ and m/z 485 in negative MS^2 mode. Compared with standard and the literature (30), peak 16 was deduced as zebirioside O. The $[M-162-46-H]^-$ ion in the MS^2 spectrum of peaks 17, 20, 21, 22, 23, and 24 corresponding to the presence of glucose group in the compounds. The formula of the six compounds was determined to be $C_{36}H_{58}O_{11}$, $C_{36}H_{58}O_{10}$, and $C_{36}H_{56}O_{10}$, indicating their structures were similar. Compared with the pieces of literature (31–36) and standard substances, peaks 17, 20, 21, 22, 23, and 24 were tentatively identified as niga-ichigoside F_1, peduncloside, rosamultin, kajiichigoside F_1, potentillanoside A, and quadranoside VIII, respectively. The formula of peaks 28 and 29 was calculated as $C_{15}H_{22}O_2$ and $C_{30}H_{46}O_6$. The two peaks were plausibly assigned as valerenic acid and medicagenic acid as compared with standards and the literature (37).

Matrix Metalloproteinase-2 Inhibitory Assay

A total of twelve binding ligands were evaluated for their inhibitory activities against matrix metalloproteinase-2 by using the conventional inhibitory assay. The IC_{50} value of batimastat was determined to be 4.58 nM, which was consistent with the literature (38). The assay data of binding ligands are shown in **Table 2**. The MMP-2 inhibitory activities of the twelve ligands were decreased as follows: niga-ichigoside F_1, rosamultin, kajiichigoside F_1, zebirioside O, peduncloside, potentillanoside A, quadranoside VIII, corilagin, oreganol A, ellagic acid, medicagenic acid, and valerenic acid. Except for ellagic acid, the matrix metalloproteinase-2 inhibitory effects of the other eleven ligands were reported for the first time.

TABLE 2 | Inhibitory effects of MMP-2 binding ligands.

No.	Compound	IC_{50} ± SD(μM)	Affinity (kcal/mol)
4	Oreganol A	30.83 ± 2.13	−8.3
6	Corilagin	28.56 ± 2.83	−9.6
14	Ellagic acid	37.80 ± 1.96	−9.0
16	Zebirioside O	23.19 ± 4.49	−8.4
17	Niga-ichigoside F_1	20.12 ± 1.55	−7.9
20	Peduncloside	23.24 ± 2.53	−8.6
21	Rosamultin	20.68 ± 2.06	−9.7
22	Kajiichigoside F_1	22.04 ± 2.15	−9.4
23	Potentillanoside A	25.54 ± 3.01	−8.1
24	Quadranoside VIII	25.88 ± 5.66	−8.3
28	Valerenic acid	82.49 ± 8.87	−7.1
29	Medicogenic acid	64.07 ± 13.60	−8.4
Control	Batimastat	4.58 ± 0.44 nM	–

Molecular Docking

Three-dimensional pictures of the best-docked conformation of MMP2-rosamultin, MMP2-corilagin, and MMP2-kajiichigoside F1 complexes were presented in **Supplementary Figure 9**. The binding affinity between rosamultin and MMP2 protein is determined to be −9.7 kcal/mol, which proves to have a good binding effect. Rosamultin interacts with the MMP-2 protein by forming hydrogen bonds with MET-373, CYS-390, PHE-512, ALA-510, ASP-188, and LYS-372, the lengths of which are 2.7, 2.8, 3.0, 2.9, 3.1, and 3.1 Å, respectively. Moreover, the binding affinity between corilagin and MMP-2 is −9.6 kcal/mol. Corilagin interacts with the MMP-2 protein through the formation of hydrogen bonds with VAL-107, TYR-110, LYS-62, PRO-183, HIS-193, and GLY-103, the lengths of which are 3.0, 2.9, 2.7, 3.0, 3.6, 2.8, and 2.8 Å. Furthermore, the binding affinity between kajiichigoside-F1 and MMP-2 protein is −9.4 kcal/mol. Kajiichigoside-F1 interacts with the MMP2 protein through the formation of hydrogen bonds with THR-511, ALA-510, SER-546, MET-373, CYS-390, and ASP-188, the lengths of which are 3.0, 2.9, 3.2, 2.7, 2.7, and 3.0 Å, respectively.

Comparisons With Previous Ligand Fishing Methods

Several ligand fishing methods have been reported, namely, monolithic column coated with white blood cell membranes (39), Hsp 90α functionalized InP/ZnS QDs embedded mesoporous nanoparticles (13), porcine pancreatic lipase immobilized organic framework UiO-66-NH_2 (40), and so on. A comparison between the previous ligand fishing method and this work was displayed in **Table 3**. Compared with the traditional ligand fishing method, this method takes less time and effectively

TABLE 3 | A comparison between the previous ligand fishing method and this work.

Method	Monolithic column -based method	Quantum dots embedded mesoporous nanoparticles -based method	Metal-organic framework base method	Microfluidic chip-based method
Consumption of organic solvent	AIBN, GMA, EDMA, cyclohexanol and dodecanol	TEOS, CTAB, TMB, APS, Glutaraldehyde	$ZrCl_4$, ATA, HAc, HCl, DMF	EDC, NHS, PEI
Consumption of time	Several days	Several days	Several days	Two days
Environmentally friendly	No	No	No	Yes
Cost	Expensive	Moderate	Moderate	Cheap
Enzyme function	Function	Function	Function	Function
Reference	(39)	(13)	(40)	This work

reduces the target protein and solvent expenditure. However, the microfluidic-based ligand fishing system also has certain limitations. For instance, the oil phase (n-hexadecane) will freeze at a low temperature, which will lead to the blockage of the chip pipeline, thereby affecting the ligand fishing result. Therefore, the temperature control system should be used to ensure the accuracy of the experimental results. Our results showed that this microfluidic-based ligand fishing method can be effectively applied to screen for bioactive ingredients from natural products.

CONCLUSION

In this article, a rapid microfluidic chip-based ligand fishing platform for discovering matrix metalloproteinase-2 inhibitors from *R. roxburghii* was presented. Six parameters were investigated to effectively optimize the ligand fishing procedure. A total of eleven new matrix metalloproteinase-2 inhibitors were discovered from the extract of *R. roxburghii*. These inhibitors may contribute to the antitumor effect of *R. roxburghii*. The proposed microfluidic chip-based ligand fishing method offers a good alternative to other screening assays and will pave the way for high-throughput screening from natural products.

DATA AVAILABILITY STATEMENT

The original contributions presented in the study are included in the article/**Supplementary Material**, further inquiries can be directed to the corresponding authors.

AUTHOR CONTRIBUTIONS

YT contributed to writing, reviewing, editing, funding acquisition, and project administration. MP performed methodology, validation, formal analysis, investigation, and data curation. FZ was involved in writing original draft preparation. QL was involved in formal analysis. PW did the conceptualization and funding acquisition. All authors contributed to the article and approved the submitted version.

FUNDING

Financial support was gratefully acknowledged from the National Natural Science Foundation for the Youth (No. 81703701) and the Natural Science Foundation of Zhejiang Province (No. Y21H280036).

ACKNOWLEDGMENTS

The authors would like to thank the reviewers for their invaluable suggestions that helped improve the manuscript.

SUPPLEMENTARY MATERIAL

The Supplementary Material for this article can be found online at: https://www.frontiersin.org/articles/10.3389/fnut.2022.869528/full#supplementary-material

Supplementary Figure 1 | Homemade microfluidic system and microfluidic chip.

Supplementary Figure 2 | FT-IR of magnetic microspheres with different coats.

Supplementary Figure 3 | Zeta potential values of magnetic microspheres with different coats.

Supplementary Figure 4 | XRD images of magnetic microspheres and MS@PEI@QDs@PEI@ MMP-2.

Supplementary Figure 5 | Effect of amount of magnetic microspheres on the percentage of conjugated MMP-2.

Supplementary Figure 6 | Confocal image of MS@PEI@QDs@PEI@MMP-2.

Supplementary Figure 7 | Specificity of the microfluidic-based screening system. 3.85 min: loganic acid, 6.35 min: ellagic acid.

Supplementary Figure 8 | Chemical structures of MMP-2 binding ligands.

Supplementary Figure 9 | 3D pictures of the best-docked conformation of MMP2-rosamultin, MMP2-corilagin, and MMP2-kajiichigoside F1 complexes.

REFERENCES

1. Li H, Fang W, Wang Z, Chen Y. Physicochemical, biological properties, and flavour profile of *Rosa roxburghii* Tratt, *Pyracantha fortuneana*, and *Rosa laevigata* Michx fruits: a comprehensive review. *Food Chem.* (2022) 366:130509. doi: 10.1016/j.foodchem.2021.130509
2. Liu W, Li SY, Huang XE, Cui JJ, Zhao T, Zhang H. Inhibition of tumor growth *in vitro* by a combination of extracts from *Rosa roxburghii* Tratt and *Fagopyrum cymosum*, *Asian Pac J Cancer Prev.* (2012) 13:2409–14. doi: 10.7314/APJCP.2012.13.5.2409
3. Chen Y, Liu ZJ, Liu J, Liu LK, Zhang ES, Li WL. Inhibition of metastasis and invasion of ovarian cancer cells by crude polysaccharides from *rosa roxburghii* tratt *in vitro*. *Asian Pac J Cancer Prev.* (2014) 15:10351–4. doi: 10.7314/APJCP.2014.15.23.10351
4. Zhang C, Liu X, Qiang H, Li K, Wang J, Chen D, et al. Inhibitory effects of *rosa roxburghii* tratt juice on *in vitro* oxidative modification of low density lipoprotein and on the macrophage growth and cellular cholesteryl ester accumulation induced by oxidized low density lipoprotein. *Clin Chim Acta.* (2001) 313:37–43. doi: 10.1016/S0009-8981(01)00647-7
5. Wang H, Li Y, Ren Z, Cong Z, Chen M, Shi L, et al. Optimization of the microwave-assisted enzymatic extraction of *Rosa roxburghii* Tratt. polysaccharides using response surface methodology and its antioxidant and α-d-glucosidase inhibitory activity. *Int J Biol Macromol.* (2018) 112:473–82. doi: 10.1016/j.ijbiomac.2018.02.003
6. Yu K, Zhou L, Sun Y, Zeng Z, Chen H, Liu J, et al. Anti-browning effect of *Rosa roxburghii* on apple juice and identification of polyphenol oxidase inhibitors. *Food Chem.* (2021) 359:129855. doi: 10.1016/j.foodchem.2021.129855
7. Wang L, Chen C, Zhang B, Huang Q, Fu X, Li C. Structural characterization of a novel acidic polysaccharide from *Rosa roxburghii* Tratt fruit and its α-glucosidase inhibitory activity. *Food Funct.* (2018) 9:3974–85. doi: 10.1039/C8FO00561C
8. Xu P, Cai X, Zhang W, Li Y, Qiu P, Lu D, et al. Flavonoids of *Rosa roxburghii* Tratt exhibit radioprotection and anti-apoptosis properties via the Bcl-2(Ca(2+))/Caspase-3/PARP-1 pathway. *Apoptosis.* (2016) 21:1125–43. doi: 10.1007/s10495-016-1270-1
9. Xu SJ, Zhang F, Wang LJ, Hao MH, Yang XJ, Li NN, et al. Flavonoids of *Rosa roxburghii* Tratt offers protection against radiation induced apoptosis and inflammation in mouse thymus. *Apoptosis.* (2018) 23:470–83. doi: 10.1007/s10495-018-1466-7

10. Liu M-H, Zhang Q, Zhang Y-H, Lu X-Y, Fu W-M, He J-Y. Chemical analysis of dietary constituents in *Rosa roxburghii* and Rosa sterilis Fruits. *Molecules.* (2016) 21:1204. doi: 10.3390/molecules21091204
11. Wang L-T, Lv M-J, An J-Y, Fan X-H, Dong M-Z, Zhang S-D, et al. Botanical characteristics, phytochemistry and related biological activities of *Rosa roxburghii* Tratt fruit, and its potential use in functional foods: a review. *Food Funct.* (2021) 12:1432–51. doi: 10.1039/D0FO02603D
12. Zhuo R, Liu H, Liu N, Wang Y. Ligand fishing: a remarkable strategy for discovering bioactive compounds from complex mixture of natural products. *Molecules.* (2016) 21:1516. doi: 10.3390/molecules21111516
13. Hu Y, Fu A, Miao Z, Zhang X, Wang T, Kang A, et al. Fluorescent ligand fishing combination with in-situ imaging and characterizing to screen Hsp 90 inhibitors from Curcuma longa L. based on InP/ZnS quantum dots embedded mesoporous nanoparticles. *Talanta.* (2018) 178:258–67. doi: 10.1016/j.talanta.2017.09.035
14. Yuan YC, Bai XL, Liu YM, Tang XY, Yuan H, Liao X. Ligand fishing based on cell surface display of enzymes for inhibitor screening, *Anal Chim Acta.* (2021) 1156:338359. doi: 10.1016/j.aca.2021.338359
15. Tao Y, Yan J, Cai B. Lable-free bio-affinity mass spectrometry for screening and locating bioactive molecules. *Mass Spectrom Rev.* (2021) 40:53–71. doi: 10.1002/mas.21613
16. Trindade Ximenes IA, de Oliveira PCO, Wegermann CA, de Moraes MC. Magnetic particles for enzyme immobilization: a versatile support for ligand screening. *J Pharm Biomed Anal.* (2021) 204:114286. doi: 10.1016/j.jpba.2021.114286
17. Wei Y, Zhu Y, Fang Q. Nanoliter quantitative high-throughput screening with large-scale tunable gradients based on a microfluidic droplet robot under unilateral dispersion mode. *Anal Chem.* (2019) 91:4995–5003. doi: 10.1021/acs.analchem.8b04564
18. Cai Q, Meng J, Ge Y, Gao Y, Zeng Y, Li H, et al. Fishing antitumor ingredients by G-quadruplex affinity from herbal extract on a three-phase-laminar-flow microfluidic chip, *Talanta.* (2020) 220:121368. doi: 10.1016/j.talanta.2020.121368
19. Gao Y, Peng H, Li L, Wang F, Meng J, Huang H, et al. Screening of high-efficiency and low-toxicity antitumor active components in Macleaya cordata seeds based on the competitive effect of drugs on double targets by a new laminar flow chip. *Analyst.* (2021) 146:4934–44. doi: 10.1039/D1AN00754H
20. Carvalho MR, Truckenmuller R, Reis RL, Oliveira JM. Biomaterials and microfluidics for drug discovery and development. *Adv Exp Med Biol.* (2020) 1230:121–35. doi: 10.1007/978-3-030-36588-2_8
21. Zhang X, Miao Z, Hu Y, Yang X, Tang Y, Zhu D. Programmed microcapsule-type matrix metalloproteinase-2 (MMP-2)-responsive nanosensor for *in situ* monitoring of intracellular MMP-2. *Sensor Actuat B Chem.* (2018) 273:511–18. doi: 10.1016/j.snb.2018.06.083
22. Christoffersson J, Mandenius CF. Fabrication of a microfluidic cell culture device using photolithographic and soft lithographic techniques. *Methods Mol Biol.* (2019) 1994:227–33. doi: 10.1007/978-1-4939-9477-9_21
23. Kipper S, Frolov L, Guy O, Pellach M, Glick Y, Malichi A, et al. Control and automation of multilayered integrated microfluidic device fabrication. *Lab Chip.* (2017) 17:557–66. doi: 10.1039/C6LC01534D
24. Huang ST, Wang CY, Yang RC, Wu HT, Yang SH, Cheng YC, et al. Ellagic acid, the active compound of Phyllanthus urinaria, exerts *in vivo* anti-angiogenic effect and inhibits MMP-2 activity. *Evid Based Complement Alternat Med.* (2011) 2011:215035. doi: 10.1093/ecam/nep207
25. Kato MT, Bolanho A, Zarella BL, Salo T, Tjäderhane L, Buzalaf MA. Sodium fluoride inhibits MMP-2 and MMP-9. *J Dent Res.* (2014) 93:74–7. doi: 10.1177/0022034513511820
26. Fingleton B, Menon R, Carter KJ, Overstreet PD, Hachey DL, Matrisian LM, et al. Proteinase activity in human and murine saliva as a biomarker for proteinase inhibitor efficacy. *Clin Cancer Res.* (2004) 10:7865–74. doi: 10.1158/1078-0432.CCR-04-1252
27. Zengin G, Cvetanović A, Gašić U, Dragićević M, Stupar A, Uysal A, et al. UHPLC-LTQ OrbiTrap MS analysis and biological properties of *Origanum vulgare* subsp. *viridulum* obtained by different extraction methods. *Ind Crops Prod.* (2020) 154:112747. doi: 10.1016/j.indcrop.2020.112747
28. Song XC, Canellas E, Dreolin N, Nerin C, Goshawk J. Discovery and characterization of phenolic compounds in Bearberry (*Arctostaphylos uva-ursi*) leaves using liquid chromatography-ion mobility-high-resolution mass spectrometry. *J Agric Food Chem.* (2021) 69:10856–68. doi: 10.1021/acs.jafc.1c02845
29. Huang D, Li C, Chen Q, Xie X, Fu X, Chen C, et al. Identification of polyphenols from *Rosa roxburghii* Tratt pomace and evaluation of *in vitro* and *in vivo* antioxidant activity. *Food Chem.* (2021) 377:131922. doi: 10.1016/j.foodchem.2021.131922
30. Zebiri I, Gratia A, Nuzillard JM, Haddad M, Cabanillas B, Harakat D, et al. New oleanane saponins from the roots of Dendrobangia boliviana identified by LC-SPE-NMR. *Magn Reson Chem.* (2017) 55:1036–44. doi: 10.1002/mrc.4619
31. Zhang AL, Ye Q, Li BG, Qi HY, Zhang GL. Phenolic and triterpene glycosides from the stems of Ilex litseaefolia. *J Nat Prod.* (2005) 68:1531–5. doi: 10.1021/np050285z
32. Wu L, Kang A, Shan C, Chai C, Zhou Z, Lin Y, et al. LC-Q-TOF/MS-oriented systemic metabolism study of pedunculoside with in vitro and in vivo biotransformation, *J Pharm Biomed Anal.* (2019) 175:112762. doi: 10.1016/j.jpba.2019.07.010
33. Wu YS, Shi L, Liu XG, Li W, Wang R, Huang S, et al. Chemical profiling of Callicarpa nudiflora and its effective compounds identification by compound-target network analysis. *J Pharm Biomed Anal.* (2020) 182:113110. doi: 10.1016/j.jpba.2020.113110
34. Pan H, Nie S, Kou P, Wang L, Wang Z, liu Z, et al. An enhanced extraction and enrichment phytochemicals from *Rosa roxburghii* Tratt leaves with ultrasound-assist CO_2-based switchable-solvent and extraction mechanism study. *J Mol Liq.* (2021) 337:116591. doi: 10.1016/j.molliq.2021.116591
35. Morikawa T, Ninomiya K, Imura K, Yamaguchi T, Akagi Y, Yoshikawa M, et al. Hepatoprotective triterpenes from traditional Tibetan medicine Potentilla anserine. *Phytochemistry.* (2014) 102:169–81. doi: 10.1016/j.phytochem.2014.03.002
36. Li W, Fu H, Bai H, Sasaki T, Kato H, Koike K. Triterpenoid saponins from Rubus ellipticus var. *obcordatus. J Nat Prod.* (2009) 72:1755–60. doi: 10.1021/np900237a
37. Liu SB, Lu SW, Sun H, Zhang AH, Wang H, Wei WF, et al. Deciphering the Q-markers of nourishing kidney-yin of Cortex Phellodendri amurense from ZhibaiDihuang pill based on Chinmedomics strategy. *Phytomedicine.* (2021) 91:153690. doi: 10.1016/j.phymed.2021.153690
38. Botos I, Scapozza L, Zhang D, Liotta LA, Meyer EF. Batimastat, a potent matrix mealloproteinase inhibitor, exhibits an unexpected mode of binding, *Proc Natl Acad Sci U S A.* (1996) 93:2749–54. doi: 10.1073/pnas.93.7.2749
39. Zhang F, Jiang Y, Jiao P, Li S, Tang C. Ligand fishing via a monolithic column coated with white blood cell membranes: a useful technique for screening active compounds in Astractylodes lancea. *J Chromatogr A.* (2021) 1656:462544. doi: 10.1016/j.chroma.2021.462544
40. Chen X, Xue S, Lin Y, Luo J, Kong L. Immobilization of porcine pancreatic lipase onto a metal-organic framework, PPL@MOF: a new platform for efficient ligand discovery from natural herbs. *Anal Chim Acta.* (2020) 1099:94–102. doi: 10.1016/j.aca.2019.11.042

Conflict of Interest: The authors declare that the research was conducted in the absence of any commercial or financial relationships that could be construed as a potential conflict of interest.

frontiers | Frontiers in Nutrition

ORIGINAL RESEARCH
published: 18 April 2022
doi: 10.3389/fnut.2022.862773

Characterization of Tyrosinase Inhibitors in *Dryopteris crassirhizoma* Rhizome Using a Combination of High-Speed Counter-Current Chromatography, Affinity-Based Ultrafiltration, and Liquid Chromatography–Tandem Mass Spectrometry

Zhiqiang Wang[1]*, Ning Wang[1], Dandan Han[1] and Hongyuan Yan[1,2]

[1] Key Laboratory of Public Health Safety of Hebei Province, School of Public Health, Hebei University, Baoding, China, [2] Key Laboratory of Medicinal Chemistry and Molecular Diagnosis of Ministry of Education, College of Pharmaceutical Sciences, Hebei University, Baoding, China

OPEN ACCESS

Edited by:
Sandrina A. Heleno,
Polytechnic Institute of Bragança
(IPB), Portugal

Reviewed by:
Ricardo Calhelha,
Centro de Investigação de Montanha
(CIMO), Portugal
Chunpeng Wan,
Jiangxi Agricultural University, China

****Correspondence:***
Zhiqiang Wang
wangzq2017@hbu.edu.cn

Specialty section:
This article was submitted to
Food Chemistry,
a section of the journal
Frontiers in Nutrition

Received: *26 January 2022*
Accepted: *21 March 2022*
Published: *18 April 2022*

Citation:
Wang Z, Wang N, Han D and Yan H (2022) Characterization of Tyrosinase Inhibitors in Dryopteris crassirhizoma Rhizome Using a Combination of High-Speed Counter-Current Chromatography, Affinity-Based Ultrafiltration, and Liquid Chromatography–Tandem Mass Spectrometry.
Front. Nutr. 9:862773.
doi: 10.3389/fnut.2022.862773

Dryopteris crassirhizoma rhizome (DCR) inhibits melanin production in B16F10 melanoma cells and tyrosinase activity. The melanin content and tyrosinase activity of DCR-treated zebrafish embryos were determined to evaluate the *in vivo* inhibitory effect of DCR on melanogenesis. Moreover, an off-line hyphenated method combining the high-speed counter-current chromatography, affinity-based ultrafiltration, and liquid chromatography–tandem mass spectrometry was used to identify and characterize the DCR compounds with tyrosinase inhibitory activity. Our results indicated that DCR significantly decreased the melanin content and tyrosinase activity in zebrafish embryos in a dose-dependent manner; moreover, 22 compounds in DCR presented tyrosinase inhibitory activity. *In silico* molecular docking prediction data indicated that the 22 compounds in DCR can form stable conformations in the active site pocket of tyrosinase.

Keywords: tyrosinase, *Dryopteris crassirhizoma*, affinity-based ultrafiltration, melanin content, zebrafish

INTRODUCTION

Melanin is a naturally occurring skin pigment that protects the human body against ultraviolet (UV) radiation damage (1). Recently, melanin biosynthesis has attracted considerable attention because of the increasing occurrence of melanomas, freckles, chloasma, and senile spots caused by skin hyperpigmentation (2–4). Tyrosinase, which is the primary monooxygenase during melanin synthesis, converts tyrosine into dopquinone *via* 3-dihydroxyphenylalanine as an intermediate

---

Abbreviations: DCR, *Dryopteris crassirhizoma* rhizome; EtOAc, ethyl acetate; hpf, hours post-fertilization; HPLC, high-performance liquid chromatography; HSCCC, high-speed countercurrent chromatography; LC–MS/MS, liquid chromatography–tandem mass spectrometry; *n*-BuOH, *n*-butanol; PBS, phosphate-buffered saline; UV, ultraviolet.

through a two-step catalytic process (5, 6). Therefore, numerous tyrosinase inhibitors have been developed to decrease the melanin synthesis rate and diminish hyperpigmentation. Nevertheless, the weak *in vivo* activity of tyrosinase inhibitors and safety concerns associated with them have hindered their practical use (7). Recently, the use of functional foods has gained popularity as consumers are paying an increasing attention to diet and health. Therefore, the development of safe functional foods that can effectively inhibit tyrosinase activity and melanogenesis has attracted considerable attention.

Pteridophyta plants, commonly known as ferns, have historically provided many health benefits to humans and have been used as food, teas, and herbal medicines by the Chinese, Indians, and Native Americans since ancient times. However, even though these plants are appreciated for their esthetic and medicinal properties, their potential applications and economic value are still underestimated (8). The rhizome of *Dryopteris crassirhizoma* Nakai, which is a perennial herbaceous fern species belonging to the *Dryopteridaceae* family, has been used to treat viral diseases (9, 10). Previous studies have demonstrated that *D. crassirhizoma* rhizome (DCR) significantly inhibited melanin production in B16F10 melanoma cells and also inhibited tyrosinase activity (11, 12). These findings suggested that DCR is a natural tyrosinase inhibitor that can be used as a functional food ingredient. However, the inhibitory effect of DCR on melanogenesis *in vivo* has not yet been investigated. Moreover, the DCR compounds with tyrosinase inhibitory activity should be identified and characterized.

Owing to the complex chemical composition of natural product extracts and high structural diversity of their components, the identification of biologically active compounds using bioassay-guided isolation is laborious (13). Recently, affinity-based ultrafiltration hyphenated with liquid chromatography–tandem mass spectrometry (LC–MS/MS) has been used for the *in situ* identification of bioactive compounds in natural product extracts (14, 15). However, the detection of the minor bioactive compounds captured by proteins *via* affinity-based ultrafiltration using LC–MS/MS is challenging because the significant differences in extracts composition cause the signals of the major components to mask those of the minor components (16). High-speed countercurrent chromatography (HSCCC) is a separation method that uses liquid–liquid partition without a solid phase. HSCCC does not entail irreversible adsorption. Therefore, despite the similar polarities of the minor and major components, the minor components of extracts can be enriched from the major components without loss using the differences in partition coefficients (17, 18). Consequently, the combination of HSCCC, affinity-based ultrafiltration, and LC–MS/MS can be a promising method for the identification of bioactive compounds from natural products.

Therefore, in this study, the melanin content and tyrosinase activity of zebrafish embryos were investigated to assess the effect of DCR on melanogenesis *in vivo*. Moreover, the tyrosinase inhibitors in DCR were identified and characterized using a combination of HSCCC, ultrafiltration, and LC–MS/MS.

MATERIALS AND METHODS

Reagents

Arbutin, dimethyl sulfoxide, L-tyrosine, and mushroom tyrosinase were provided by Sigma-Aldrich (St. Louis, MO, United States). Tricaine, embryo culture medium, methylcellulose, and lytic buffer were supplied by Shandong Yixiyue Biotechnology Co., Ltd. (Weifang, China). Phosphate-buffered saline (PBS; pH 7.2) was obtained from Gibco (Waltham, MA, United States). Dipotassium hydrogen phosphate, potassium dihydrogen phosphate, and NaOH were acquired from Aladdin (Shanghai, China). All the organic solvents were supplied by Concord Technology (Tianjin, China). A Milli-Q water purification system (Millipore, Billerica, MA, United States) was used to obtain ultrapure water (18.2 MΩ cm), which was used for all the experiments.

Preparation of the *Dryopteris crassirhizoma* Rhizome Extract

Dryopteris crassirhizoma rhizome (voucher WLL-2018-03) was provided by Yiyuan Chinese Herb Medicine Co., Ltd. (Anguo, Hebei, China) in August 2018 and stored at the College of Public Health, Hebei University. Dried ground DCR (10 g) was extracted in triplicate with 100 ml of a 90% methanol aqueous solution over 24 h, and 1.59 g of solid extract powder was obtained after filtration, concentration, and lyophilization.

Tyrosinase Assay

Mixtures of DCR extract samples with different concentrations, L-tyrosine (0.3 mM), and mushroom tyrosinase (50 units/ml) were incubated in PBS at 25°C, and their absorbances were recorded at 450 nm after 30 min. Arbutin, which was the positive control, was used as the reference compound. The tyrosinase inhibition values were calculated as follows:

$$\text{Inhibition}\,(\%) = [1-(A-B)/(C-D)] \times 100\%,$$

where A is the absorbance of the reaction system comprising the DCR extract sample and tyrosinase, B is the absorbance of the reaction system comprising only the DCR extract sample, C is the absorbance of the reaction system comprising only tyrosinase, and D is the absorbance of the reaction mixture without DCR extract samples and tyrosinase.

Zebrafish Maintenance and Breeding

A pair of healthy broodstock zebrafish was placed in an incubator equipped with a barrier, which was used to separate the male and female zebrafish overnight prior to mating. The barrier was removed the next morning, and light was used to stimulate the broodstock zebrafish to spawn. Then, 4 h post-fertilization (hpf), the zebrafish embryos were cultured with DCR (10, 50, and 100 μg/ml in embryo culture medium), arbutin (10, 50, and 100 μg/ml in embryo culture medium), or embryo culture medium in 96-well plates at 28°C under 14/10 h light/dark cycles. Each group comprised 60 embryos, and the corresponding culture media were changed daily. A stereomicroscope was used to record the melanin changes in the zebrafish embryos 72 hpf.

Determination of Tyrosinase Activity of Zebrafish

After treatment, 50 zebrafish embryos from each group were homogenized in the PBS using a tissue homogenizer, and the homogenates were centrifuged. The supernatant of each group was collected and used to determine the tyrosinase activity of the group. After protein concentration was normalized, the diluted supernatants containing tyrosinase (160 μl) and L-tyrosine solution (40 μl) were mixed and incubated at 37°C. After 1 h, 450 nm UV light was used to determine the absorbance of each mixture, and the tyrosinase inhibition values were calculated as follows:

$$\text{Inhibition (\%)} = (1 - A/A_0) \times 100\%,$$

where A is the absorbance of L-tyrosine incubated with the supernatant obtained from the zebrafish embryos treated with DCR or arbutin and A_0 is the absorbance of L-tyrosine incubated with the supernatant obtained from the zebrafish embryos treated with embryo culture medium.

Assessment of Melanin Content of Zebrafish

To assess the melanin content of each group of zebrafish, the melanin precipitate from each group was collected and suspended in 400 μl NaOH (1 M). Next, 490 nm UV light was used to evaluate the dissolved melanin content, and the relative melanin content was calculated as follows:

$$\text{Melanin content} = A/A_0 \times 100\%,$$

where A is the absorbance of the melanin samples obtained from the zebrafish embryos treated with DCR or arbutin and A_0 is the absorbance of the melanin samples obtained from the zebrafish embryos treated with embryo culture medium only.

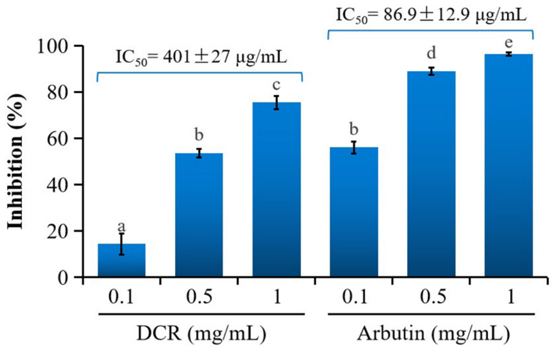

FIGURE 1 | Inhibitory activity of *Dryopteris crassirhizoma* rhizome (DCR) on mushroom tyrosinase. IC_{50} is the concentration of the sample with a mushroom tyrosinase inhibitory activity of 50%. Different lower case letters indicate significant differences ($p < 0.05$).

High-Speed Countercurrent Chromatography Separation

A TBE-300C HSCCC instrument (Tauto Biotechnique Company, Shanghai, China) equipped with an Isolera FLASH purification system (Biotage, Uppsala, Sweden) was used for separation. Before separation, 300 ml of the stationary phase was pumped into the coiled column and subsequently rotated at 400 rpm. After equilibrium was reached, 20 ml of the DCR extract solution was injected, and a series of mobile phases was delivered into the coil in the tail-to-head mode. A mixture of *n*-butanol (*n*-BuOH) and water [1:10 (v/v)] was used as the stationary phase. The injected DCR extract was dissolved in a mixture of ethyl acetate (EtOAc), n-BuOH, and water [1:1:10, (v/v/v)] to achieve a concentration of 25 mg/ml. A list of mobile phases is presented in **Figure 6**. Chromatograms were recorded at a wavelength of 254 nm.

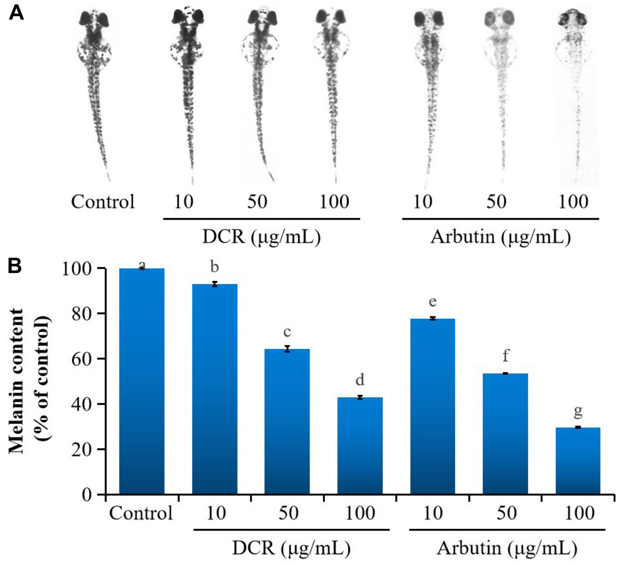

FIGURE 2 | The effect of *Dryopteris crassirhizoma* rhizome (DCR) on **(A)** melanogenesis in zebrafish embryos and **(B)** melanin content of zebrafish embryos. Different lower case letters indicate significant differences ($p < 0.05$).

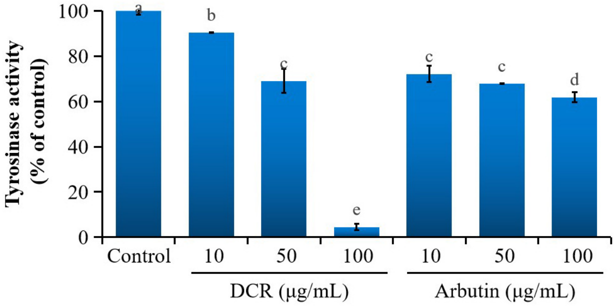

FIGURE 3 | The effect of *Dryopteris crassirhizoma* rhizome (DCR) on the tyrosinase activity of zebrafish embryos. Different lower case letters indicate significant differences ($p < 0.05$).

Affinity-Based Ultrafiltration

A mixture of DCR extract solution (0.1 mg/ml) and tyrosinase (100 units/ml) was incubated at 37°C for 30 min and subsequently centrifuged using a Microcon YM-10 centrifugal filter unit (Millipore, Billerica, MA, United States) at 10,000 × *g* for 30 min. A control group without tyrosinase was analyzed in parallel. The ultrafiltrates were collected for subsequent LC–MS/MS analysis.

Liquid Chromatography–Tandem Mass Spectrometry Analysis

An UltiMate 3000 high-performance liquid chromatography (HPLC) system (Thermo Fisher Scientific, Waltham, MA, United States) equipped with a Q Exactive Orbitrap mass spectrometer (Thermo Fisher Scientific, Waltham, MA, United States) was used for LC–MS/MS analysis. An Eclipse SB-C18 Rapid Resolution column (150 mm length, 4.6 mm ID, and 3.5 μm particle size; Agilent, Santa Clara, CA, United States) was used for separation. The sample's injection volume and flow rate were 10 μl and 1 mg/ml, respectively. The elution gradient program was as follows: 0–8 min, 5–20% B; 8–25 min, 20–30% B; 25–60 min, 30–100% B; 60–67 min, 100% B; 67–70 min, 100–5% B; 70–80 min, 5% B; and the mobile phases comprised 0.1% formic acid in water (A) and methanol (B). The eluent was monitored at 254 nm. Peak identification was performed in the negative mode, and the electrospray ionization source conditions were set as follows: sheath gas flow rate: 45 arb, auxiliary gas flow rate: 15 arb, capillary temperature: 320°C, full mass resolution: 70,000, MS/MS resolution: 17,500, collision energy: 20/40/60 eV in the normalized collision energy model, and spray voltage: −3.1kV.

In silico Docking

In silico docking was performed using the Surflex-Dock program version (Tripos, St. Louis, MO, United States), and the crystal structure of tyrosinase (2Y9X) was retrieved from the RCSB Protein Data Bank. Prior to docking, the macromolecules and small molecules were prepared, including structural file retrieval, water molecule removal, non-protein atom removal, structural defect correction, and molecular energy minimization. The "thresh" and "bloat" parameters of the docking protocol were set to be 0.5 and 1, respectively. The PyMOL (Schrödinger, New York, NY, United States) and LigPlot software (EMBL-EBI, Cambridge, United Kingdom) were used for data visualization.

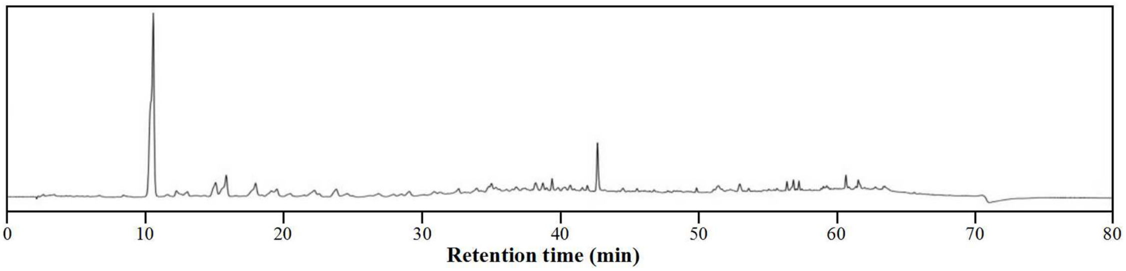

FIGURE 4 | High-performance liquid chromatography (HPLC) profile of the *Dryopteris crassirhizoma* rhizome (DCR).

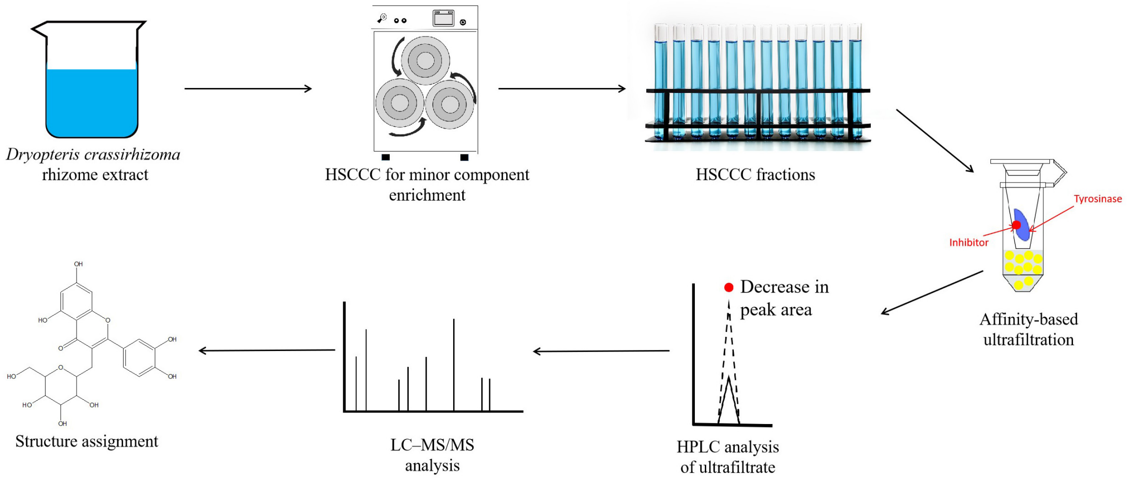

FIGURE 5 | Schematic of the hyphenated method used to identify and characterize the tyrosinase inhibiting compounds in *Dryopteris crassirhizoma* rhizome (DCR). Here, HSCCC, LC–MS/MS, and HPLC denote high-speed counter-current chromatography, liquid chromatography–tandem mass spectrometry, and high-performance liquid chromatography, respectively.

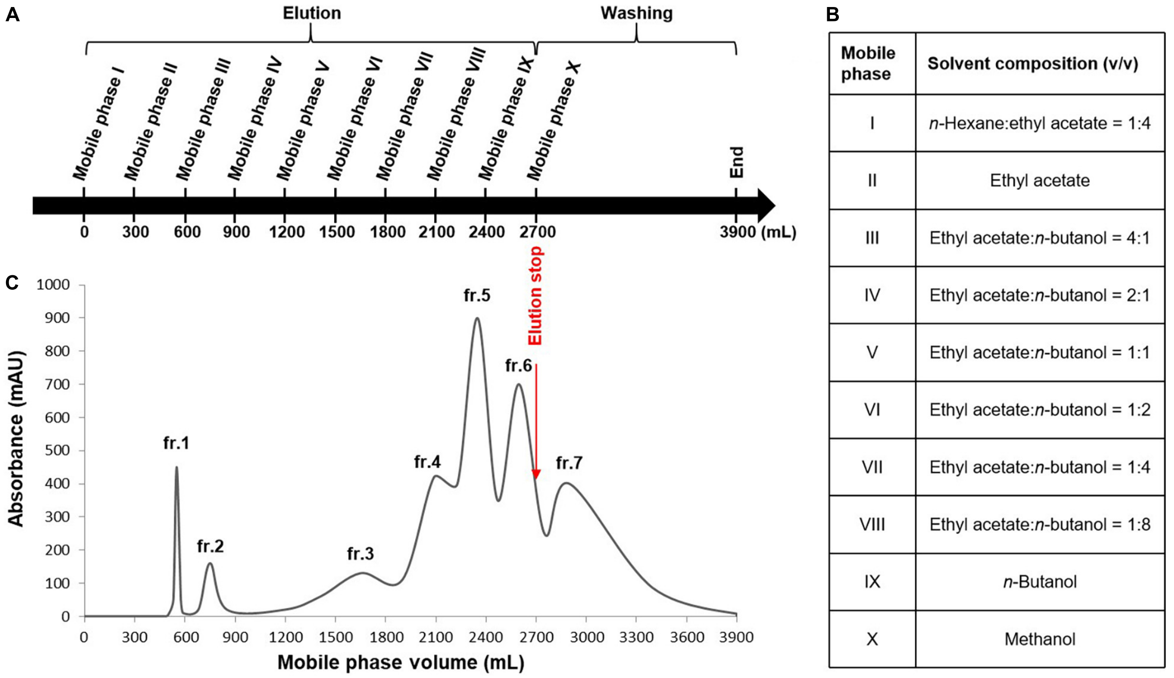

Mobile phase	Solvent composition (v/v)
I	*n*-Hexane:ethyl acetate = 1:4
II	Ethyl acetate
III	Ethyl acetate:*n*-butanol = 4:1
IV	Ethyl acetate:*n*-butanol = 2:1
V	Ethyl acetate:*n*-butanol = 1:1
VI	Ethyl acetate:*n*-butanol = 1:2
VII	Ethyl acetate:*n*-butanol = 1:4
VIII	Ethyl acetate:*n*-butanol = 1:8
IX	*n*-Butanol
X	Methanol

FIGURE 6 | Stepwise high-speed counter-current chromatography (HSCCC) for the enrichment of the minor components in the *Dryopteris crassirhizoma* rhizome (DCR) extract. **(A)** HSCCC elution and washing steps. **(B)** Mobile phases of the solvent system. **(C)** HSCCC profile. Stationary phase: water–*n*-butanol [1:10 (v/v)], flow rate: 4 ml/min, rotation speed: 400 rpm, mode: tail-to-head.

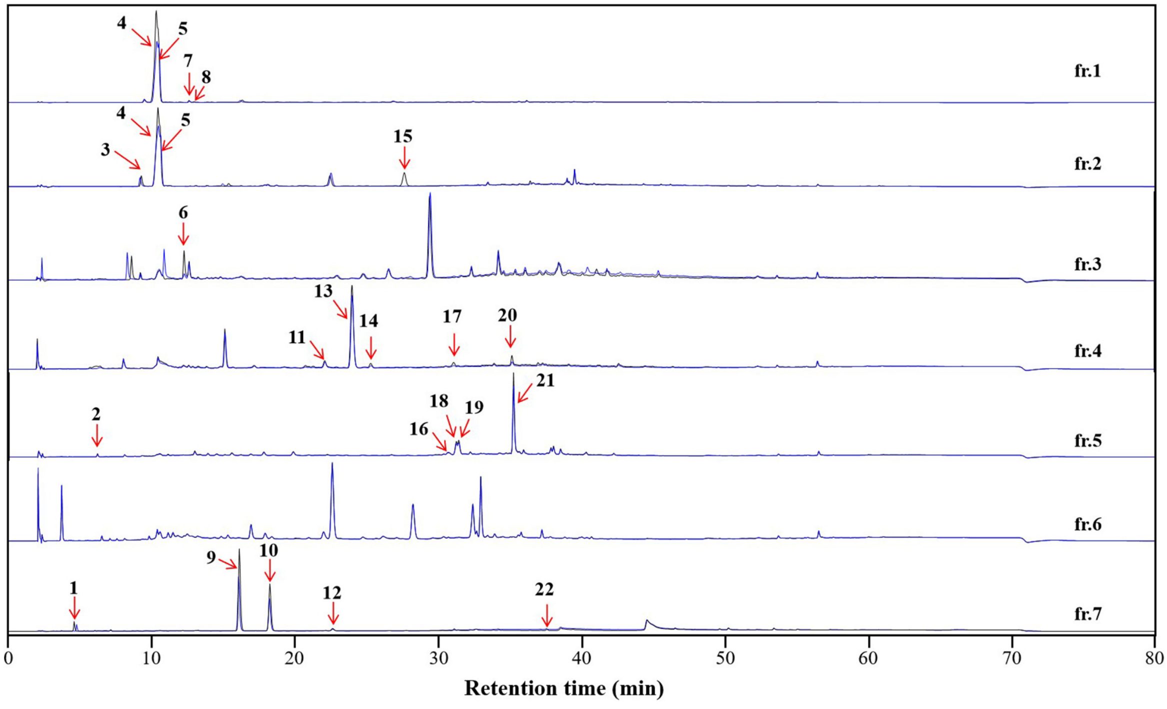

FIGURE 7 | The affinity-based ultrafiltration chromatograms of the high-speed counter-current chromatography (HSCCC) fractions of the *Dryopteris crassirhizoma* rhizome (DCR) extract. The blue and black lines indicate fractions incubated with and without tyrosinase, respectively. The numbered peaks correspond to tyrosinase inhibitors.

Statistical Analysis

All experiments were performed at least in triplicate, and the results are expressed as means ± standard deviations (SDs). Data analysis was performed using the SPSS software (IBM, Armonk, NY, United States). The mean values were compared using Student's unpaired t-test or one-way analysis of variance (ANOVA), and statistical significance was set at $p < 0.05$.

RESULTS AND DISCUSSION

Tyrosinase Inhibitory Activity of *Dryopteris crassirhizoma* Rhizome

The inhibitory effects of various concentrations of the DCR extracts on mushroom tyrosinase were tested *in vitro*. The DCR extracts considerably inhibited mushroom tyrosinase, and the inhibitions of the samples with DCR extract concentrations of 0.1, 0.5, and 1 mg/ml were 14.32, 53.61, and 75.47%, respectively (**Figure 1**). The half-maximal inhibitory concentration (IC_{50}) of the DCR extract for tyrosinase was 401 μg/ml. Experiments were performed using arbutin as the reference compound. The inhibitions of arbutin samples with concentrations of 0.1, 0.5, and 1 mg/ml were 56.03, 88.90, and 96.45%, respectively, and the IC_{50} of arbutin was 86.9 μg/ml. The tyrosinase inhibitory activity of DCR was considerable yet lower than that of arbutin, as confirmed by the aforementioned experimental results and previously reported data (11, 12).

Effect of *Dryopteris crassirhizoma* Rhizome on Melanogenesis in Zebrafish Embryos

Mushroom tyrosinase has been commonly used to assess the tyrosinase inhibitory activity related to the melanogenesis inhibition of traditional medicinal plants and food items (19). However, the effect of DCR on melanogenesis *in vivo* remains unclear. Zebrafish embryos present significant physiological

TABLE 1 | Tyrosinase inhibitors in the *Dryopteris crassirhizoma* rhizome (DCR) extract identified using liquid chromatography–tandem mass (LC–MS/MS) in the negative ion mode.

No.	Retention time (min)	[M-H]$^-$ (*m/z*)	MS/MS (*m/z*)	Formula	Mass error (mDa)	DBE[a]	Annotation
1	4.6	129.0548	114.9896; 111.0448	$C_6H_9O_3$	−0.4	2.5	4-Methyl-2-oxovaleric
2	6.1	152.0348	134.0238; 109.0276	$C_7H_6O_3N$	0.0	5.5	4-Aminosalicylic acid
3	9.2	181.0492	166.0517; 153.0260; 139.0379	$C_{12}H_9N_2$	−27.4	9.5	Harmane
4	10.4	153.0186	109.0077	$C_7H_5O_4$	−0.2	5.5	2,3-Dihydroxybenzoic acid
5	10.5	109.0288		$C_6H_5O_2$	−0.2	4.5	Catechol
6	12.2	194.0252	152.0467; 137.0226; 108.0213	$C_9H_8O_4N$	−20.1	6.5	2-Hydroxyhippurate
7	12.5	353.1316	165.0155; 139.0400; 121.0199	$C_{21}H_{21}O_5$	−7.3	11.5	5,7-Dihydroxy-2-(4-methoxyphenyl)-6-(3-methylbut-2-enyl)-2,3-dihydrochromen-4-one
8	12.9	137.0236	121.0316; 108.0220	$C_7H_5O_3$	−0.3	5.5	Salicylic acid
9	16.1	353.0865	233.0445; 205.0502	$C_{16}H_{17}O_9$	−0.8	8.5	Isobiflorin
10	18.2	353.0866	233.0444; 205.0495	$C_{16}H_{17}O_9$	−0.7	8.5	Biflorin
11	22.0	379.0689	335.0701; 162.0837	$C_{14}H_7O_4N_{10}$	3.7	16.5	(E)-1-(2-azido-3-nitrophenyl)-*N*-[(E)-(2-azido-3-nitrophenyl) methylideneamino]methanimine
12	22.6	367.0649	191.0335; 113.0234	$C_{16}H_{15}O_{10}$	1.6	9.5	2-Oxo-7-[(2S,3R,4S,5S,6R)-3,4,5-trihydroxy-6-(hydroxymethyl)oxan-2-yl]oxychromene-3-carboxylic acid
13	24.0	191.0361	160.8393	$C_{10}H_6O_4$	1.7	7.5	7-Hydroxy-6-methoxychromen-2-one
14	25.2	347.0768	303.0868; 259.0960	$C_{17}H_{15}O_8$	0.1	10.5	Asterric acid
15	27.6	345.0525	285.0398; 219.0288; 191.0335; 177.0183; 149.0234; 125.0235; 109.0285	$C_{12}H_{17}O_6N_4S$	−34.4	6.5	Oryzalin
16	30.6	261.0757	233.0810; 204.0418	$C_{14}H_{13}O_5$	−0.6	8.5	3-(2,3-Dihydroxy-5-methylphenoxy)-5-methylbenzene-1,2-diol
17	31.0	175.0366	129.0320	$C_{10}H_7O_3$	−2.9	7.5	4-Methylumbelliferone
18	31.1	463.0878	287.0544; 113.0225	$C_{21}H_{19}O_{12}$	0.1	12.5	Quercetin-3-*O*-glucoside
19	31.2	447.0935	327.0496	$C_{21}H_{19}O_{11}$	0.8	12.5	Kaempferol 7-*O*-glucoside
20	35.1	447.0923	285.0391	$C_{21}H_{19}O_{11}$	−0.4	12.5	Kaempferol 3-*O*-glucoside
21	35.1	461.0710	285.0395	$C_{21}H_{17}O_{12}$	−1.0	13.5	Kaempferol 3-*O*-glucuronide
22	37.5	533.1864	41.31438; 251.0912	$C_{23}H_{33}O_{14}$	−0.6	7.5	Dryopteroside

[a] *DBE, double bond equivalency.*

and genetic similarities with mammals. Moreover, pigmentation experiments using zebrafish require simple protocols (20). Therefore, zebrafish embryos have been increasingly used as *in vivo* test models, replacing mice and other animal models for phenotype-based melanogenesis inhibition studies. Consequently, the effect of DCR on melanogenesis inhibition was investigated using zebrafish embryos. The pigmentation of zebrafish larvae exposed to DCR or arbutin at 72 hpf decreased in a dose-dependent manner and was lighter than that of the control larvae. The melanin contents of the zebrafish larvae treated with DCR extracts with concentrations of 10, 50, and 100 μg/ml were 92.95, 64.34, and 42.85%, respectively, of the melanin content of the control group, whereas those of the zebrafish larvae treated with the arbutin concentrations of 10, 50, and 100 μg/ml were 77.73, 53.47, and 29.63%, respectively, of the melanin content of the control group (**Figure 2**). Moreover, no abnormalities were

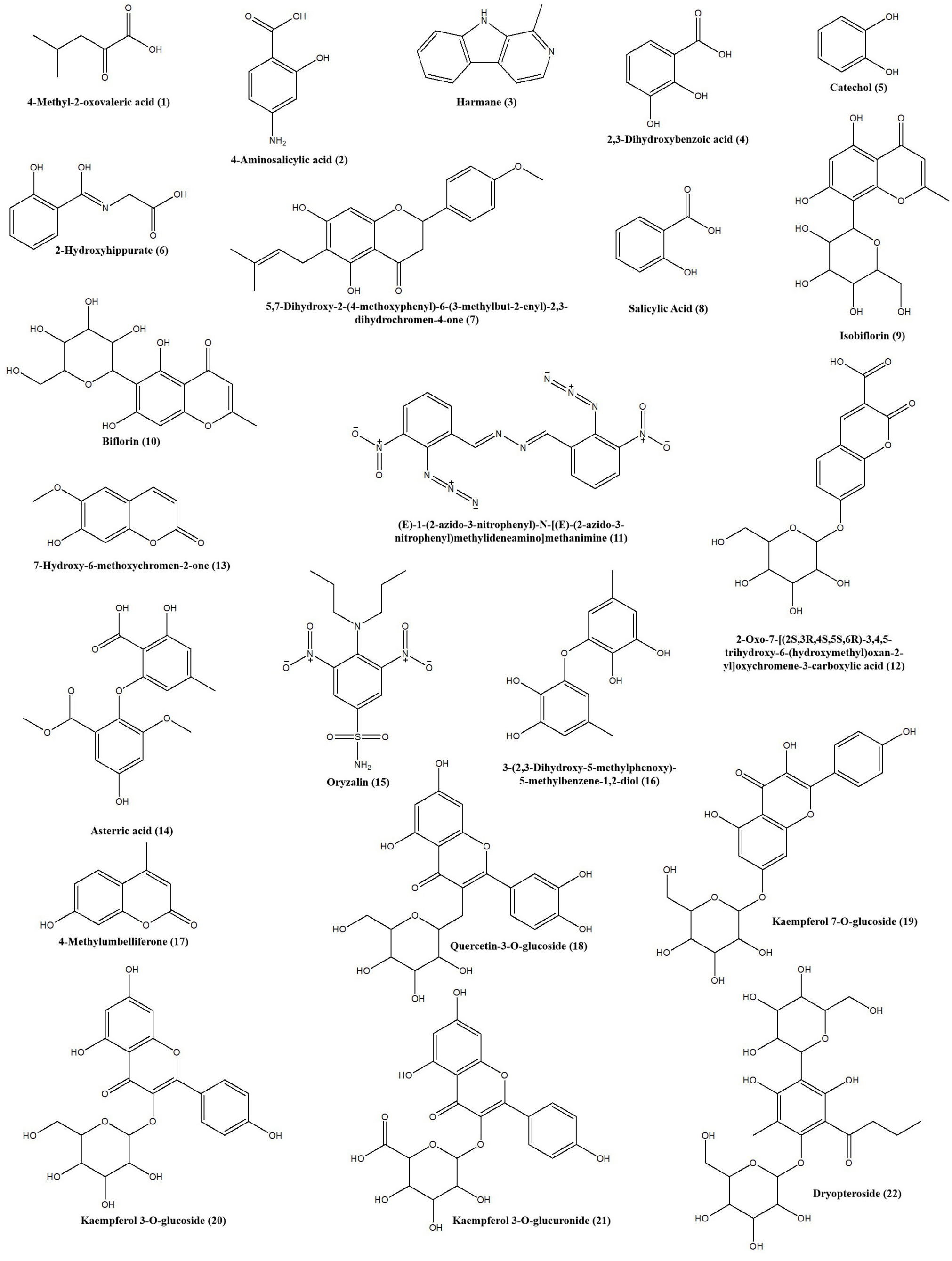

4-Methyl-2-oxovaleric acid (1)
4-Aminosalicylic acid (2)
Harmane (3)
2,3-Dihydroxybenzoic acid (4)
Catechol (5)
2-Hydroxyhippurate (6)
5,7-Dihydroxy-2-(4-methoxyphenyl)-6-(3-methylbut-2-enyl)-2,3-dihydrochromen-4-one (7)
Salicylic Acid (8)
Isobiflorin (9)
Biflorin (10)
(E)-1-(2-azido-3-nitrophenyl)-N-[(E)-(2-azido-3-nitrophenyl)methylideneamino]methanimine (11)
2-Oxo-7-[(2S,3R,4S,5S,6R)-3,4,5-trihydroxy-6-(hydroxymethyl)oxan-2-yl]oxychromene-3-carboxylic acid (12)
7-Hydroxy-6-methoxychromen-2-one (13)
Asterric acid (14)
Oryzalin (15)
3-(2,3-Dihydroxy-5-methylphenoxy)-5-methylbenzene-1,2-diol (16)
4-Methylumbelliferone (17)
Quercetin-3-O-glucoside (18)
Kaempferol 7-O-glucoside (19)
Kaempferol 3-O-glucoside (20)
Kaempferol 3-O-glucuronide (21)
Dryopteroside (22)

FIGURE 8 | Structures of the tyrosinase inhibitors in the *Dryopteris crassirhizoma* rhizome (DCR) extract.

TABLE 2 | Docking scores and predicted interactions between the 22 *Dryopteris crassirhizoma* rhizome (DCR) compounds with tyrosinase inhibitory activity and tyrosinase.

No.	Compounds	Hydrogen bonds	Hydrophobic interactions	Crash score	Polar score	D-score	PMF score	G-score	Chem score	C-score
1	4-Methyl-2-oxovaleric	Copper, His61, His85	Glu256, His259, Asn260, His263, Ala286	−1.04	1.85	−76.68	−71.85	−111.67	−14.85	4.64
2	4-Aminosalicylic acid	Copper, His61, Asn260	His85, His259, His263, Met280, Gly281, Ala286, Phe292	−1.52	2.89	−88.74	−76.79	−133.92	−22.01	4.51
3	Harmane	–	His61, His85, His244, Glu256, His259, Asn260, His263, Met280, Ser282, Val283, Ala286	−1.29	0	−114.57	−66.35	−174.07	−21.81	3.82
4	2,3-Dihydroxybenzoic acid	Met280	His61, His85, His259, Asn260, His263, Phe264, Gly281, Ser282, Val283, Ala286	−0.54	0.81	−90.81	−53.50	−127.26	−12.80	3.06
5	Catechol	–	Gly281, Phe264, Met280, His259, His263, Asn260	−0.36	2.12	−66.08	−21.31	−105.08	−16.52	4.11
6	2-Hydroxyhippurate	–	His259, Asn260, His263, Phe264, Met280, Gly281, Ser282, Val283, Ala286	−0.48	2.15	−97.06	−24.56	−106.02	−14.72	5.87
7	5,7-Dihydroxy-2-(4-methoxyphenyl)-6-(3-methylbut-2-enyl)-2,3-dihydrochromen-4-one	–	His61, His85, His259, Asn260, His263, Phe264, Gly281, Ser282, Val283, Ala286	−1.11	0.33	−132.01	−44.81	−164.31	−17.90	4.08
8	Salicylic acid	–	His61, His85, His259, Asn260, His263, Phe264, Met280, Gly281, Ser282, Val283, Als286,	−0.51	0.79	−76.61	−39.99	−116.19	−13.76	3.25
9	Isobiflorin	Coppers, Met280, Gly281	His61, His85, Phe90, His244, Glu256, His259, Asn260, His263, Phe264, Ser282, Val283, Ala286, Phe292	−3.92	4.18	−189.90	−105.66	−230.55	−28.35	5.05
10	Biflorin	Coppers, His259, His263, Met280	His61, His85, His244, Val248, Asn260, Phe264, Gly281, Ser282, Val283, Ala286	−2.23	3.94	−176.80	−102.67	−177.34	−20.85	6.72
11	(E)-1-(2-azido-3-nitrophenyl)-*N*-[(E)-(2-azido-3-nitrophenyl)methylidene amino]methanimine	Als246, Met280	His85, Gly86, His244, Val248, Asn260, His263, Phe264, Val283, Ala286, Glu322	−0.83	2.08	−108.83	−81.52	−164.28	−19.91	4.32
12	2-Oxo-7-[(2S,3R,4S,5S,6R)-3,4,5-trihydroxy-6-(hydroxymethyl)oxan-2-yl]oxychromene-3-carboxylic acid	Coppers, His61, His85	Phe90, Val248, His259, Asn260, His263, Phe264, Met280, Gly281, Ser282, Val283, Ala286	−2.99	2.43	−152.21	−120.32	−186.86	−17.16	4.89
13	7-Hydroxy-6-methoxychromen-2-one	Copper, His61, Asn260	His85, His244, Glu256, His259, His263, Val283, Ala286, Phe292	−0.75	2.97	−118.80	−103.76	−115.82	−23.66	4.72
14	Asterric acid	Coppers, Glu256, His259, His263	His61, His85, Phe90, His244, Val248, Asn260, Phe264, Met280, Gly281, Ser282, Val283	−4.09	3.32	−169.85	−104.25	−209.54	−24.69	4.76
15	Oryzalin	Gly281	His85, Asn260, His263, Phe264, Met280, Ser282, Val283	−3.59	1.66	−135.64	−34.37	−209.64	−20.05	3.86
16	3-(2,3-Dihydroxy-5-methylphenoxy)-5-methylbenzene-1,2-diol	His244	His61, His85, His259, Asn260, His263, Phe264, Met280, Gly281, Als286,	−1.23	3.05	−138.85	−58.11	−172.59	−22.26	6.54
17	4-Methylumbelliferone	Copper, His61	His85, Glu256, His259, Asn260, His263, Phe264, Met280, Gly281, Val283, Phe292	−0.88	1.89	−109.82	−77.08	−130.26	−23.36	4.46
18	Quercetin-3-*O*-glucoside	Coppers, His61, His85, His94, Met280	His244, Val248, His259, Asn260, His263, Phe264, Arg268, Pro277, Gly281, Ser282, Val283, Ala286, His296	−3.00	2.46	−170.51	−121.99	−215.29	−24.17	4.19

(Continued)

TABLE 2 | (Continued)

No.	Compounds	Hydrogen bonds	Hydrophobic interactions	Crash score	Polar score	D-score	PMF score	G-score	Chem score	C-score
19	Kaempferol 7-*O*-glucoside	Coppers, His244, His259, His263, Met280,	His85, Asn260, Phe264, Gly281, Ser282, Val283, Pro284, Ala286	−1.51	3.97	−166.57	−121.68	−106.86	−20.38	6.79
20	Kaempferol 3-*O*-glucoside	Coppers, His61, His85, Arg268, Met280, Ser282, Val283	Val248, His259, Asn260, His263, Phe264, Gly281, Pro284, Ala286	−3.45	3.93	−163.03	−108.03	−131.90	−23.34	4.49
21	Kaempferol 3-*O*-glucuronide	Copper, His61, His85, Arg268, Met280	Val248, His259, Asn260, His263, Phe264, Pro277, Gly281, Ser282, Val283, Ala286	−2.50	3.04	−169.61	−120.77	−152.54	−23.33	5.05
22	Dryopteroside	Coppers, His61, His85, Met280, Ser282, Val283	His244, Val248, His259, Asn260, His263, Phe264, Gly281, Pro284, Ala286	−3.32	3.56	−211.41	−116.56	−216.75	−14.49	6.88
	Arbutin	Copper, His61, His94, Glu256, Asn260, His296	His85, His244, Val248, His259, His263, Phe264, Val283, Ala286, Phe292	−2.02	3.35	−148.86	−109.69	−175.31	−18.62	4.83

observed in the morphologies of the DCR- and arbutin-treated zebrafish larvae. These results suggested that the DCR extract inhibited melanogenesis *in vivo*.

To further determine whether melanogenesis inhibition in zebrafish embryos correlated with tyrosinase inhibition, the tyrosinase activity in zebrafish embryos was investigated. Treatment with DCR and arbutin considerably decreased the tyrosinase activity in zebrafish embryos at 72 hpf. The tyrosinase activities of the zebrafish embryos treated with DCR extracts at the concentrations of 10, 50, and 100 μg/ml were 90.34, 69.08, and 4.51%, respectively, of the tyrosinase activity of the control group, whereas those of the zebrafish treated with the arbutin concentrations of 10, 50, and 100 μg/ml were 72.14, 67.79, and 61.84%, respectively, of the tyrosinase activity of the control group (**Figure 3**). These results suggested that the DCR extract inhibited melanin synthesis *via* tyrosinase inhibition, thereby lowering pigmentation; moreover, these findings indicated that the DCR extract contained tyrosinase inhibitors.

Characterization of the Tyrosinase Inhibitors in *Dryopteris crassirhizoma* Rhizome

To characterize the composition of the biologically active components of plant extracts, isolation is typically performed prior to evaluation or application. However, isolating biologically active components from DCR extracts is challenging because of the complex chemical composition of DCR (**Figure 4**). Alternatively, to characterize the tyrosinase inhibitors in DCR, an off-line hyphenation method combining HSCCC, affinity-based ultrafiltration, and LC–MS/MS was used in this study. A stepwise HSCCC was initially performed to enrich the minor components in DCR, and then, affinity-based ultrafiltration was conducted to identify potential tyrosinase inhibitors in DCR. Lastly, the structures of the potential tyrosinase inhibitors in DCR were determined using LC–MS/MS (**Figure 5**).

An appropriate liquid phase comprising two immiscible liquids that satisfy the golden rules proposed by Ito is typically required for HSCCC separation (21). The HSCCC procedure was adopted because assessing the numerous solvent systems and comparing the partition coefficients of the components using HPLC or thin-layer chromatography is time-consuming. Moreover, the separation of compounds with similar partition coefficients is restricted by the low resolution of HSCCC. Stepwise HSCCC separation was performed to maximize the enrichment of the minor components in the primary components of the complex extracts and simplify solvent system selection. In this study, nine mobile phases of the n-hexane–EtOAc–n-BuOH–water solvent system with a wide polarity range were used without calculating the partition coefficients of the components (**Figure 6**). After mobile phase elution, the residual stationary phase in the coil was washed with methanol. Lastly, seven fractions were obtained, and their HPLC profiles are presented in **Figure 7**. The experimental data indicated that the primary components in DCR were collected in fractions 1 and 2, whereas the minor components were enriched in fractions 3–7.

To characterize the tyrosinase inhibitors in DCR, the obtained HSCCC fractions were further analyzed *via* ultrafiltration combined with LC–MS/MS (22). The HPLC peak areas of the 22 compounds separated from DCR decreased, indicating their tyrosinase-inhibiting potentials. The structures of the 22 compounds, namely, 4-methyl-2-oxovaleric acid (**1**), 4-aminosalicylic acid (**2**), harmane (**3**), 2,3-dihydroxybenzoic acid (**4**), catechol (**5**), 2-hydroxyhippurate (**6**), 5,7-dihydroxy-2-(4-methoxyphenyl)-6-(3-methylbut-2-enyl)-2,3-dihydrochromen-4-one (**7**), salicylic acid (**8**), isobiflorin (**9**), biflorin, (**10**), (E)-1-(2-azido-3-nitrophenyl)-*N*-[(E)-(2-azido-3-nitrophenyl)methylideneamino]methanimine (**11**), 2-oxo-7-[(2S,3R,4S,5S,6R)-3,4,5-trihydroxy-6-(hydroxymethyl) oxan-2-yl]oxychromene-3-carboxylic acid (**12**), 7-hydroxy-6-methoxychromen-2-one (**13**), asterric acid (**14**), oryzalin (**15**), 3-(2,3-dihydroxy-5-methylphenoxy)-5-methylbenzene-1,2-diol (**16**), 4-methylumbelliferone (**17**), quercetin-3-O-glucoside (**18**), kaempferol 7-O-glucoside (**19**), kaempferol 3-O-glucoside (**20**), kaempferol 3-O-glucuronide (**21**), and dryopteroside (**22**), which are illustrated in **Figure 7**, were assigned by matching the precursors and MS/MS m/z values of the compounds with those compiled in libraries and comparing the data with references (**Table 1** and **Figure 8**).

Molecular Docking Prediction

The isolation of minor and trace compounds from complex extracts is laborious (23). Therefore, molecular docking analysis was performed to rapidly confirm the binding mechanisms of the identified compounds to tyrosinase, and the results are presented in **Table 2** and **Supplementary Figures 1–23**. Each of the binuclear copper atoms of tyrosinase is bonded to three histidine residues and plays a critical role in catalytic reactions (24). We hypothesized that the interactions between **3**, **5**, **6**, **7**, and **8** and the amino acid residues of tyrosinase were hydrophobic, whereas the other 17 compounds interacted with tyrosinase *via* hydrogen bonding and hydrophobic interactions. In particular, **4**, **11**, **15**, and **16** formed hydrogen bonds with the amino acid residues of tyrosinase and did not interact with the copper atoms; **1**, **2**, **13**, **17**, and **21** formed hydrogen bonds with one copper atom and several amino acid residues; and **9**, **10**, **12**, **14**, **18–20**, and **22** formed hydrogen bonds with two copper atoms and several amino acid residues. The binding stabilities toward and affinities for tyrosinase of the 22 compounds were assessed using crash, polar, chem, G-, D-, potential mean force, and C-scores (**Table 2**). Specifically, the crash scores reflected the incorrect penetration of the ligand in the active site pocket of tyrosinase; the polar scores reflected the ligand region; the D-scores were calculated using the charges and van der Waals interactions between proteins and ligands; the potential mean force scores indicated the Helmholtz free energies for the protein–ligand atom interactions; the G-scores were derived by evaluating the internal energies of hydrogen-bonding, protein–ligand, and ligand–ligand interactions; and the chem scores described the points where hydrogen-bonding, lipophilic contact, and rotational entropy changed. Each scoring method was used for different purposes, and the individual scores could not comprehensively evaluate the ligand–tyrosinase interactions. Therefore, the C-scores were calculated by combining the crash, polar, chem, G-, D-, and potential mean force scores, and the results were used to comprehensively assess the ligand affinity (25). The C-scores decreased as follows: **22** (6.88) > **19** (6.79) > **10** (6.72) > **16** (6.54) > **6** (5.87) > **9** (5.05) > **21** (5.05) > **12** (4.89) > **14** (4.76) > **13** (4.72) > **1** (4.64) > **2** (4.51) > **20** (4.49) > **17** (4.46) > **11** (4.32) > **18** (4.19) > **5** (4.11) > **7** (4.08) > **15** (3.86) > **3** (3.82) > **8** (3.25) > **4** (3.06). Arbutin, which is a known tyrosinase inhibitor, forms hydrogen bonds with one of the copper atoms and the His61, His94, Glu256, Asn260, and His296 residues of tyrosinase, and its C-score was 4.83. These results indicate that the 22 compounds formed stable conformations in the active site pocket of tyrosinase. Among the 22 compounds, **8** and **21** have been reported as tyrosinase inhibitors (26, 27), whereas **4** and **5** have been reported as tyrosinase substrates (28, 29). The rest of the 22 compounds have not been reported to interact with tyrosinase. Kubo et al. (30) reported that **18** and **20** were not tyrosinase inhibitors or substrates. However, Ohguchi et al. (31) demonstrated that **18** considerably inhibited the production of melanin in mouse B16 melanoma cells by suppressing tyrosinase expression. The inhibitory effects of the 22 compounds will be investigated in a future study.

CONCLUSION

In this study, the inhibitory activity of DCR on mushroom tyrosinase was assessed, and the effect of DCR on melanogenesis in zebrafish embryos was evaluated. Our results demonstrated that DCR could serve as an effective tyrosinase inhibitor and significantly decreased the melanin content and tyrosinase activity in zebrafish embryos. An offline hyphenated method comprising HSCCC, affinity-based ultrafiltration, and LC–MS/MS was used to identify and characterize the 22 DCR compounds with tyrosinase inhibitory activity. Lastly, *in silico* molecular docking was performed to rapidly evaluate the binding mechanisms of the 22 compounds on tyrosinase, and our results indicated that the compounds formed stable conformations in the active site pocket of tyrosinase.

DATA AVAILABILITY STATEMENT

The original contributions presented in the study are included in the article/**Supplementary Material**, further inquiries can be directed to the corresponding author.

ETHICS STATEMENT

All animal experiments were performed in accordance with the guidelines and approval of the Institutional Animal Care and Use Committee (IACUC) of Hebei University (IACUC-20180051). Written informed consent was obtained from the owners for the participation of their animals in this study.

AUTHOR CONTRIBUTIONS

ZW: conceptualization, writing the original draft preparation, project administration, and funding acquisition. HY: conceptualization, writing, reviewing, editing, and funding acquisition. NW: methodology and investigation. DH: writing, reviewing, and editing. All authors contributed to the article and approved the submitted version.

FUNDING

This work was supported by the National Natural Science Foundation of China (81803401 and 82073605), the Natural Science Foundation of Hebei Province (H2019201186), China Postdoctoral Science Foundation (2019M651057), the Interdisciplinary Project of Hebei University (DXK202014), and the Medical Science Foundation of Hebei University (2020A01).

SUPPLEMENTARY MATERIAL

The Supplementary Material for this article can be found online at: https://www.frontiersin.org/articles/10.3389/fnut.2022.862773/full#supplementary-material

REFERENCES

1. Brenner M, Hearing VJ. The protective role of melanin against UV damage in human skin. *Photochem Photobiol.* (2008) 84:539–49. doi: 10.1111/j.1751-1097.2007.00226.x
2. Cestari TF, Dantas LP, Boza JC. Acquired hyperpigmentations. *An Bras Dermatol.* (2014) 89:11–25. doi: 10.1590/abd1806-4841.20142353
3. Nouveau S, Agrawal D, Kohli M, Bernerd F, Misra N, Nayak CS. Skin hyperpigmentation in Indian population: insights and best practicle. *Indian J Dermatol.* (2016) 61:487–95. doi: 10.4103/0019-5154.190103
4. Dorga S, Sarangal R. Pigmentary disorders: an insight. *Pigment Int.* (2014) 1:5–7. doi: 10.4103/2349-5847.135429
5. Sanchez-Ferrer A, Rodriguez-Lopez JN, Garcia-Canovas F, Garcia-Carmona F. Tyrosinase: a comprehensive review of its mechanism. *Biochim Biophys Acta.* (1995) 1247:1–11. doi: 10.1016/0167-4838(94)00204-t
6. Ortiz-Ruiz CV, Maria-Solano MA, Garcia-Molina MDM, Varon R, Tudela J, Tomas V, et al. Kinetic characterization of substrate-analogous inhibitors of tyrosinase. *IUBMB Life.* (2015) 67:757–67. doi: 10.1002/iub.1432
7. Zolghadri S, Bahrami A, Khan MTH, Munoz-Munoz J, Garcia-Molina F, Garcia-Canovas F, et al. A comprehensive review on tyrosinase inhibitors. *J Enzym Inhib Med Chem.* (2019) 34:279–309. doi: 10.1080/14756366.2018.1545767
8. Lee CH, Shin SL. Functional activities of ferns for human health. In: Kumar A, Fernández H, Revilla M editors. *Working with Ferns*. New York, NY: Springer (2011). p. 347–59. doi: 10.1007/978-1-4419-7162-3_24
9. Gao ZP, Ali Z, Zhao JP, Qiao L, Lei HM, Lu YR, et al. Phytochemical investigation of the rhizomes of Dryopteris crassirhizoma. *Phytochem Lett.* (2008) 1:188–90. doi: 10.1016/j.phytol.2008.09.005
10. Lee SM, Na MK, Na RB, Min BS, Lee HK. Antioxidant activity of two phloroglucinol derivatives from Dryopteris crassirhizoma. *Biol Pharm Bull.* (2003) 26:1354–6. doi: 10.1248/bpb.26.1354
11. Pham VC, Kim O, Lee JH, Min BS, Kim JA. Inhibitory effects of phloroglucinols from the roots of Dryopteris crassirhizoma on melanogenesis. *Phytochem Lett.* (2017) 21:51–6. doi: 10.1016/j.phytol.2017.05.022
12. Lee KT, Kim BJ, Kim JH. Biological screening of 100 plant extracts for cosmetic use (I): inhibitory activities of tyrosinase and DOPA auto-oxidation. *Int J Cosmetic Sci.* (1997) 19:291–8. doi: 10.1046/j.1467-2494.1997.171725.x
13. Wang Z, Hwang SH, Lim SS. Characterization of DHDP, a novel aldose reductase inhibitor isolated from Lysimachia christinae. *J Funct Foods.* (2017) 37:241–8. doi: 10.1016/j.jff.2017.07.057
14. Wang Z, Zhang Y, Yan H. *In situ* net fishing α-glucosidase inhibitors from evening primrose (Oenothera biennis) defatted seeds by combination of LC-MS/MS, molecular networking, affinity-based ultrafiltration, and molecular docking. *Food Funct.* (2022) 13:2545–58. doi: 10.1039/d1fo03975j
15. Chen G, Guo M. Rapid screening for ?-glucosidase inhibitors from Gymnemasylvestre by affinity ultrafiltration-HPLC-MS. *Front Pharmacol.* (2017) 8:228. doi: 10.3389/fphar.2017.00228
16. Wang Z, Hwang SH, Lim SS. Comprehensive profiling of minor tyrosinase inhibitors from Gastrodia elata using an off-line hyphenation of ultrafiltration, high-speed countercurrent chromatography, and high-performance liquid chromatography. *J Chromatogr A.* (2017) 1529:63–71. doi: 10.1016/j.chroma.2017.11.008
17. Rodríguez-Rivera MP, Lugo-Cervantes E, Winterhalter P, Jerz G. Metabolite profiling of polyphenols in peels of Citrus limetta Risso by combination of preparative high-speed countercurrent chromatography and LC-ESI-MS/MS. *Food Chem.* (2014) 158:139–52. doi: 10.1016/j.foodchem.2014.02.077
18. Liu JL, Wang XY, Zhang LL, Fang MJ, Wu YL, Wu Z, et al. Two-dimensional countercurrent chromatography×high performance liquid chromatography with heart-cutting and stop-and-go techniques for preparative isolation of coumarin derivatives from Peucedanum praeruptorum Dunn. *J Chromatogr A.* (2014) 1374:156–63. doi: 10.1016/j.chroma.2014.11.053
19. Mayr F, Sturm S, Ganzera M, Waltenberger B, Martens S, Schwaiger S, et al. Mushroom tyrosinase-based enzyme inhibition assay are not suitable for bioactivity-guided fractionation of extracts. *J Nat Prod.* (2019) 82:136–47. doi: 10.1021/acs.jnatprod.8b00847
20. Choi TY, Kim JH, Ko DH, Kim CH, Hwang JS, Ahn S, et al. Zebrafish as a new model for phenotype-based screening of melanogenic regulatory compounds. *Pigm Cell Res.* (2007) 20:120–7. doi: 10.1111/j.1600-0749.2007.00365.x
21. Ito Y. Golden rules and pitfalls in selecting optimum conditions for high-speed counter-current chromatography. *J Chromatogr A.* (2005) 1065:145–68. doi: 10.1016/j.chroma.2004.12.044
22. Wang Z, Hwang SH, Huang B, Lim SS. Identification of tyrosinase specific inhibitors from Xanthium strumarium fruit extract using ultrafiltration-high performance liquid chromatography. *J Chromatogr B.* (2015) 1002:319–28. doi: 10.1016/j.jchromb.2015.08.030
23. Wu B, Song HP, Zhou X, Liu XG, Gao W, Dong X, et al. Screening of minor bioactive compounds from herbal medicines by *in silico* docking and the trace peak exposure methods. *J Chromatogr A.* (2016) 1436:91–9. doi: 10.1016/j.chroma.2016.01.062
24. Fujieda N, Umakoshi K, Ochi Y, Nishikawa Y, Yanagisawa S, Kubo M, et al. Copper-oxygen dynamics in the tyrosinase mechanism. *Angew Chem.* (2020) 132:13487–92. doi: 10.1002/anie.202004733
25. Ragunathan A, Malathi K, Ramaiah S, Anbarasu A. FtsA as a cidal target for Staphylococcus aureus: molecular docking and dynamics studies. *J Cell Biochem.* (2019) 120:7751–8. doi: 10.1002/jcb.28049
26. Zhang JP, Chen QX, Song KK, Xie JJ. Inhibitory effects of salicylic acid family compounds on the diphenolase activity of mushroom tyrosinase. *Food Chem.* (2006) 95:579–84. doi: 10.1016/j.foodchem.2005.01.042
27. Quispe YNG, Hwang SH, Wang Z, Lim SS. Screening of Peruvian medicinal plants for tyrosinase inhibitory properties: identification of tyrosinase inhibitors in Hypericum laricifolium Juss. *Molecules.* (2017) 22:402. doi: 10.3390/molecules22030402
28. Xie JJ, Song KK, Qiu L, He Q, Huang H, Chen QX. Inhibitory effects of substrate analogues on enzyme activity and substrate specificities of mushroom tyrosinase. *Food Chem.* (2007) 103:1075–9. doi: 10.1016/j.foodchem.2006.04.030
29. Nedellec Y, Gondran C, Gory K, Mc Murtry S, Agostini P, Elmazria O, et al. Microcapsule-based biosensor containing catechol for the reagent-free inhibitive detection of benzoic acid by tyrosinase. *Biosens Bioelectron.* (2021) 180:113137. doi: 10.1016/j.bios.2021.113137
30. Kubo I, Kinst-Hori I, Chaudhuri SK, Kubo Y, Sánchez Y, Ogura T. Flavonols from Heterotheca inuloides: tyrosinase inhibitory activity and structural criteria. *Bioorgan Med Chem.* (2000) 8:1749–55. doi: 10.1016/s0968-0896(00)00102-4
31. Ohguchi K, Nakajima C, Oyama M, Iinuma M, Itoh T, Akao Y, et al. Inhibitory effects of flavonoid glycosides isolated from the peel of Japanese persimmon (Diospyros kaki 'Fuyu') on melanin biosynthesis. *Biol Pharm Bull.* (2010) 33:122–4. doi: 10.1248/bpb.33.122

Conflict of Interest: The authors declare that the research was conducted in the absence of any commercial or financial relationships that could be construed as a potential conflict of interest.

frontiers | Frontiers in Nutrition

ORIGINAL RESEARCH
published: 25 April 2022
doi: 10.3389/fnut.2022.865077

Evaluation and Screening of Hypoglycemic Activity of Total Ginsenosides GBE-5 Fraction From *Panax Ginseng* Berry Based on UHPLC–MS Metabolomics

Heyu Wang*[1,2], *Yu Tong*[1], *Anqi Wang*[1], *Ying Li*[1], *Bofan Lu*[1], *Hui Li*[1], *Lili Jiao*[1] and *Wei Wu*[1]

[1] Jilin Ginseng Academy, Changchun University of Chinese Medicine, Changchun, China, [2] School of Pharmacy, Jilin Medical University, Jilin, China

Objective: Ginseng berry (GB) was the mature fruit of medicinal and edible herb, *Panax ginseng* C.A. Meyer, with significant hypoglycemic effect. Ginsenoside was the main hypoglycemic active component of GB. Evaluating and screening the effective components of GB was of great significance to further develop its hypoglycemic effect.

Methods: The polar fractions of ginseng berry extract (GBE) were separated by a solvent extraction, and identified by ultra-high performance liquid chromatography–high-resolution mass spectrometry (UHPLC–MS). The insulin resistance model of HepG2 cells was established, and the hypoglycemic active fraction in GBE polar fractions were screened *in vitro*. Rat model of type 2 diabetes mellitus (T2DM) was established to verify the hypoglycemic effect of the GBE active fraction. The metabolomic study based on UHPLC–MS was used to analyze the differential metabolites in the serum of T2DM rats after 30 days of intervention with hypoglycemic active GBE fraction. The kyoto encyclopedia of genes and genomes (KEGG) metabolic pathway enrichment analysis was used to study the main metabolic pathways involved in the regulation of hypoglycemic active parts of GBE.

Results: It was found that GBE-5 fraction had better hypoglycemic activity than other GBE polar fractions *in vitro* cell hypoglycemic activity screening experiment. After 30 days of treatment, the fasting blood glucose value of T2DM rats decreased significantly by 34.75%, indicating that it had significant hypoglycemic effect. Eighteen differential metabolites enriched in KEGG metabolic pathway were screened and identified in the rat serum from T2DM *vs.* GBE-5 group, and the metabolic pathways mainly involved in regulation include arachidonic acid (AA) metabolism, linoleic acid (LA) metabolism, unsaturated fatty acid biosynthesis, and ferroptosis.

Conclusions: The hypoglycemic effect of GBE-5 fraction was better than that of total ginsenoside of GB. The AA metabolism, LA metabolism, unsaturated fatty acid biosynthesis, and ferroptosis were the potential metabolic pathways for GBE-5 fraction to exert hypoglycemic regulation.

Keywords: ginseng berry, ginsenoside, UHPLC-MS, metabolomics, type 2 diabetes mellitus

Edited by:
Mingquan Guo,
Wuhan Botanical Garden (CAS), China

Reviewed by:
Jian-Lin Wu,
Macau University of Science and Technology, Hong Kong SAR, China
Haixia Chen,
Tianjin University, China

****Correspondence:***
Wei Wu
weiwu_ccucm@126.com

Specialty section:
This article was submitted to Food Chemistry, a section of the journal Frontiers in Nutrition

Received: *29 January 2022*
Accepted: *16 March 2022*
Published: *25 April 2022*

Citation:
Wang H, Tong Y, Wang A, Li Y, Lu B, Li H, Jiao L and Wu W (2022) Evaluation and Screening of Hypoglycemic Activity of Total Ginsenosides GBE-5 Fraction From Panax Ginseng Berry Based on UHPLC–MS Metabolomics. Front. Nutr. 9:865077. doi: 10.3389/fnut.2022.865077

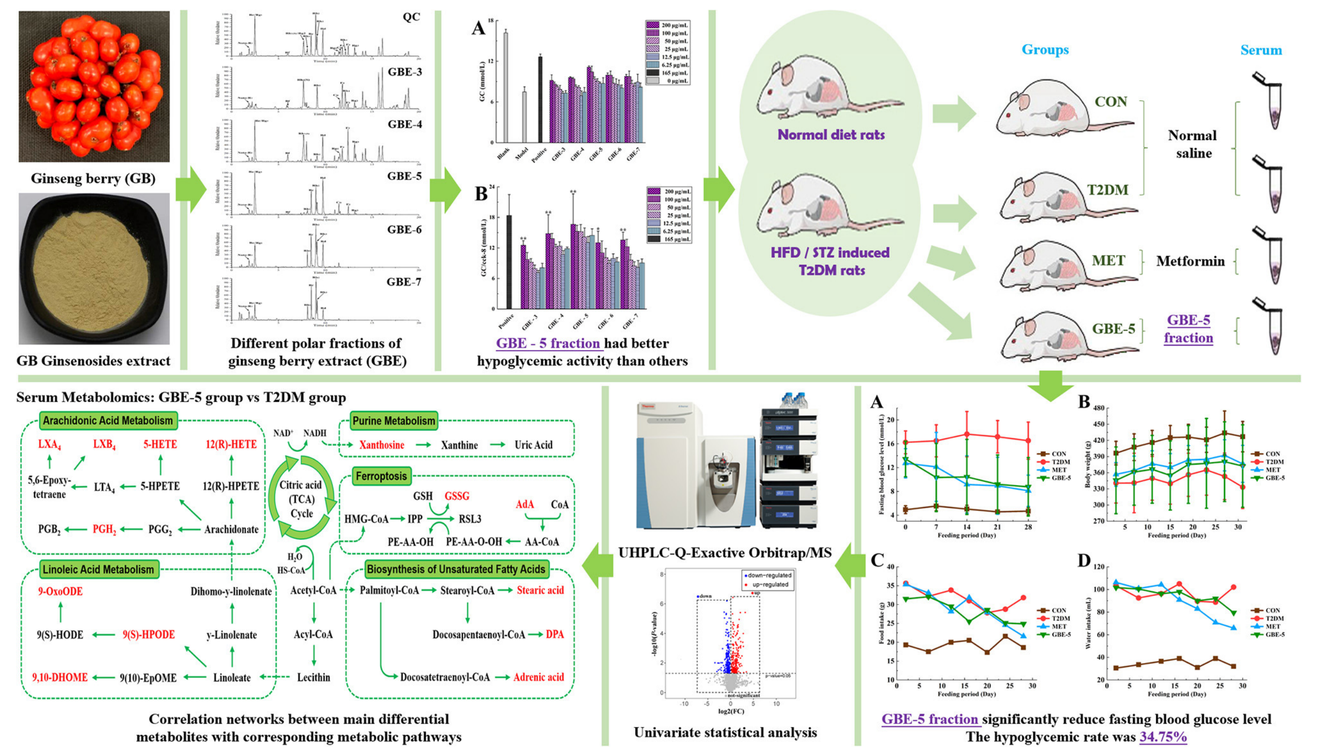

GRAPHICAL ABSTRACT | The main experimental process of this study.

INTRODUCTION

Ginseng (*Panax ginseng* C.A. Meyer), a perennial herb in the genus *Panax* of the Araliaceae family, has been used as herbal medicine, functional food, or dietary supplement in Asian countries for thousands of years, which was the globally top-selling herbal product (1). As a natural plant-based supplement, ginseng has gradually developed many ginseng-based foods, such as ginseng beverage, ginseng tea, ginseng sugar, and ginseng honey tablets (2). Ginseng berry (GB) was the mature fruit of *P. ginseng*, which could be harvested from the year of fourth of the ginseng planting (3). The main active component of GB were ginsenosides, which had anti-cancer, anti-oxidant, anti-inflammatory, immune modulation, hypoglycemic, and anti-diabetic effects (4–10). The content of ginsenosides in GB was more abundant than that in ginseng root (3); therefore, it has shown a stronger effect in anti-diabetic (2), which has been developed as a clinical drug for treatment and improvement of type 2 diabetes mellitus (T2DM) and its complications, such as Zhenyuan capsule, the main ingredient was GB total ginsenosides extract, had good hypoglycemic and hypolipidemic effects (11).

The research showed that the content of ginsenoside in GB was 4–10 times that of ginseng root (12), and the content of ginsenoside Re was 7–30 times that of ginseng root (13). It was reported that the content of ginsenoside Re in GB accounts for 85% of the total ginsenosides (11), which meant that ginsenoside Re may be the main active component of GB. In previous studies, the hypoglycemic activity of total ginsenosides extract of GB was verified (7), it was found that GB could significantly reduce the fasting blood glucose in T2DM rats, and the hypoglycemic rate was 27.35%. Further research on ginsenoside Re found that although Re was the main component of GB, its hypoglycemic rate was lower than GB, which was 21.97% (14), indicated that the hypoglycemic effect of GBE was not caused by a single component, but by multiple active components acting on multiple targets so as to play the role of reducing blood glucose. In general, the latest research on the hypoglycemic effects of ginseng and American ginseng mainly focused on total saponins (7, 15) or single ginsenoside (14, 16, 17), while there were few studies on hypoglycemic combination components. Among the reported hypoglycemic mechanisms of ginseng, relevant studies mainly focused on the level of cell signal transduction pathway, while there were few studies based on the mechanism of metabolic pathway. Therefore, it was necessary to screen the pharmacodynamic material basis of hypoglycemic effect in GB in order to further develop and utilize its excellent hypoglycemic activity.

Type 2 diabetes mellitus was mainly caused by insulin resistance or insufficient insulin secretion (18), ginsenosides could promote insulin secretion, increased insulin sensitivity, and reduced blood glucose concentration, but will not increase the risk of hypoglycemia (19). In the study of diabetes, the T2DM rats induced by high-fat and high-sucrose (HFD) diet combined with streptozotocin (STZ) was usually used as experimental

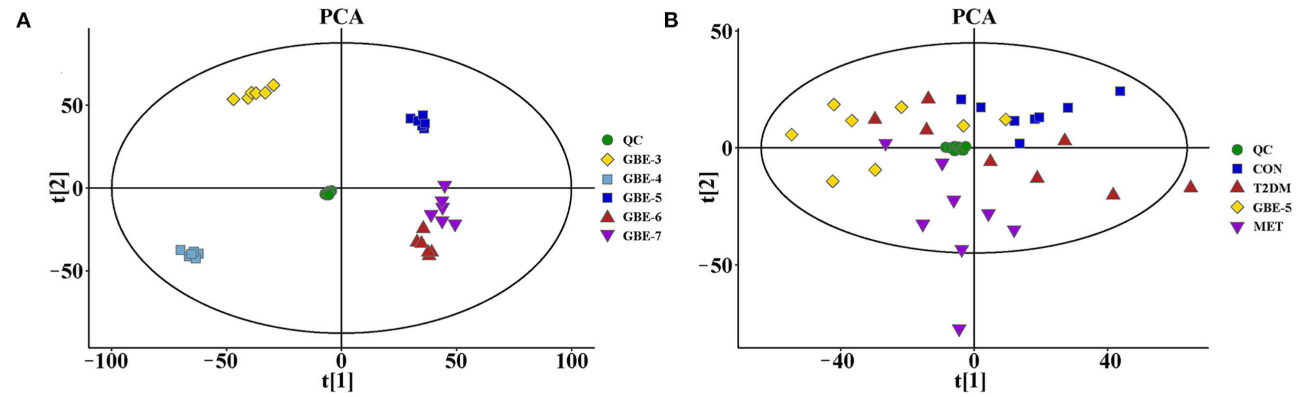

FIGURE 1 | The principal component analysis (PCA) score plots of GBE fractions **(A)** and rat serum samples **(B)**.

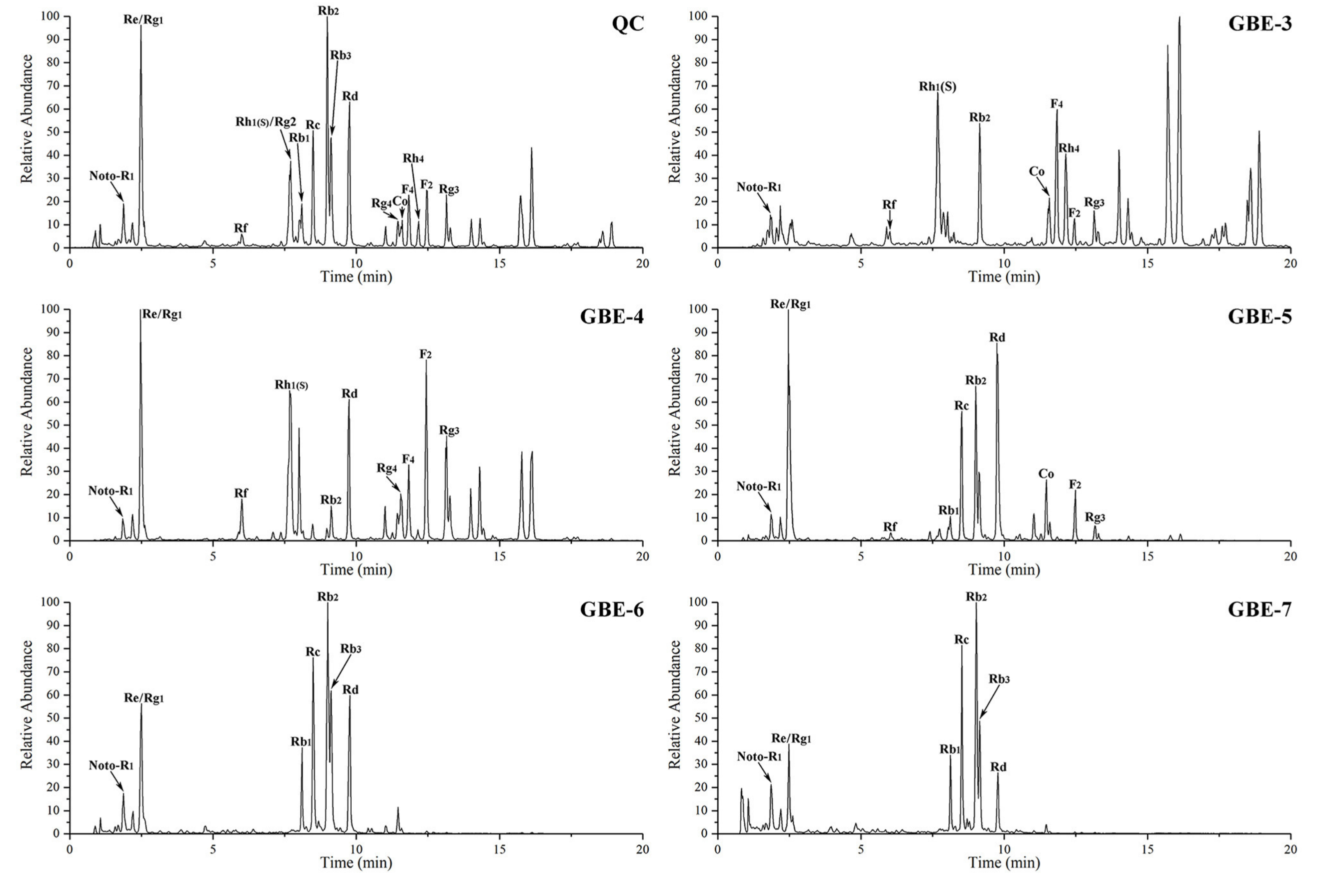

FIGURE 2 | The UHPLC–MS TIC of GBE fraction.

animal models *in vivo*, and the STZ destroyed rat islet β-cell to simulate the state of insufficient insulin secretion (20, 21). It was stated that HepG2 was a popular hepatic cell line, its surface contained high-affinity insulin receptor, which could meet the requirements of typical insulin receptor (22), and *in vitro*, the HepG2 human hepatoma cells were usually used to establish insulin resistance model to simulate insulin resistance in the patients with diabetics. There were three main modeling methods of HepG2 cell insulin resistance model, high-glucose induced cell insulin resistance model, high-concentration insulin induced cell insulin resistance model, and fatty acid (palmitic acid) induced cell insulin resistance model (23). In recent years, scholars often use fatty acid method for relevant experimental research (24), and compared with other modeling methods, it has more reliable characteristics.

In this study, cell model activity screening combined with metabolomics was used to explore the active components of GB total ginsenosides, which had good hypoglycemic activity. As shown in **Graphical Abstract**, the polar segmentation of the total ginsenosides GBE was separated by organic solvent extraction, and the insulin resistance model of HepG2 cells was established, and the hypoglycemic active fraction of GBE was screened *in vitro*, then the hypoglycemic activity was verified by T2DM rat model. The univariate statistical analysis based on UHPLC–MS was used to screen the differential metabolites in rat serum after 30 days of intervention. Combined with the enrichment analysis of KEGG metabolic pathway, the potential targets of hypoglycemic active fraction of GBE were explored.

MATERIALS AND METHODS

Material and Reagents

The *P. ginseng* berry was purchased from Ji-An (Jilin, China) in June 2019, the botanical identification was undertaken by Professor L. Jiao, and the voucher specimen (No. 20190002) was kept at the Jilin Ginseng Academy, Changchun University of Chinese Medicine, China. Ginseng berry total ginsenosides extract was prepared according to the literature method (7). Also, HepG2 human hepatoma cell line was purchased from Shanghai Institute of Biochemistry and Cell Biology, Chinese Academy of Sciences (Shanghai, China).

Petroleum ether, ethyl ether, ethyl acetate–ethyl ether and *n*-butanol were purchased from Beijing chemical works (AR, Beijing, China). Sodium hydroxide (NaOH) was purchased from Tianjin Xintong Chemical Co., Ltd (AR, Tianjin, China). Streptozotocin was purchased from Sigma chemical Co. (St. Louis, MO, USA). Citric acid and sodium citrate were purchased from Beijing Taibo Chemical Co., Ltd. (Beijing, China). Notoginsenoside R_1, Ginsenoside Rg_1, Re, Rf, Rb_1, Rc, Rb_2, Rb_3, Rd, F_2, Rg_3 (purity $\geq$ 98%) were purchased from the National Institutes for Food and Drug Control (Beijing, China). The UHPLC-grade acetonitrile and formic acid were purchased from Fisher Scientific (Waltham, MA, USA). Ultrapure water was filtered using a Milli-Q device (Millipore, Milford, MA, USA). Cell Counting Kit-8 (CCK-8) was purchased from Dojindo Chemical Co. (Dojindo, Kumamoto, Japan). Bovine serum albumin (BSA) was purchased from Shanghai Yuanye Bio-Technology Co., Ltd (Shanghai, China). Glucose assay kit were obtained from Nanjing Jiancheng Biotech. Co., Ltd. (Nanjing, China).

Preparation of Different Polar Fractions of Ginseng Berry Extract

Weighed 30 g of total ginsenoside from ginseng berry extract (GBE), added 300 ml of distilled water and dissolved in 60°C water bath, placed it in 1,000 ml separatory funnel, and added different organic reagents to extract it in turn. First, petroleum ether was added and extracted for 3 times, 300 ml each time, after combination, ginseng berry extraction I (GBE-1) was obtained. Added ethyl ether solution, extracted 3 times, with the volume of 300 ml each time, and combined to obtain ginseng berry extraction II (GBE-2). Added ethyl acetate–ethyl ether (3:2, v/v) solvent and extracted for 3 times. The addition volumes were 300, 200, and 150 ml, respectively. The extraction of ginseng berry extraction III (GBE-3) was obtained by merging the extraction layers. Added ethyl acetate-*n*-butanol (4:1, v/v) solvent for extraction for 3 times, and the added volumes were 300, 200, and 150, respectively. After merging extraction layers, the extraction of ginseng berry extraction IV (GBE-4) was obtained. Add ethyl acetate-*n*-butanol (10:9, v/v) solvent, extracted for 3 times, with the volume of 300, 200, and 150 ml, respectively, and combined to obtain the extraction of ginseng berry extraction V (GBE-5). Also, *N*-butanol was added for extraction for 3 times, and each time, the volume was the same as that of the remaining aqueous solution. After the combination, the extraction of ginseng berry extraction VI (GBE-6) was obtained. Finally, the GBE-6 fraction was back extracted with distilled water for 3 times, and the amount of each time was 1/2 of the volume of *n*-butanol. After converged, the ginseng berry stripping VII (GBE-7) was obtained. Weighed 6 parts of GBE, extracted 6 times in parallel with the above method, concentrated each extraction layer under reduced pressure, and froze dry to obtain the corresponding polar fractions; GBE-1 and GBE-2 fractions were liposoluble constituents, which were not used in subsequent experiments.

Screening of Hypoglycemic Activity of HepG2 Cell Insulin Resistance Model

Cell Culture

The HepG2 cells were cultured in RPMI 1640 completed medium (SH30809-01, Hyclone, Logan, UT, USA), containing 10% fetal bovine serum (FBS, Gibco, Grand Island, NY, USA) and 1% penicillin-streptomycin (BBI life Sciences, Shanghai, China) in a 5% CO_2 humidified atmosphere at 37°C. Took the cells in logarithmic growth period for the experiment.

Effects of GBE Fractions on HepG2 Cells Proliferation

The HepG2 cells (5×10^4 cells·ml^{-1}) were seeded in 96-well cell culture plates,100 μl per hole, and cultured in 5% CO_2 incubator at 37°C for 24 h. Then they are divided into 3 groups: Blank group, control group (CON group), and experimental groups. The blank group had only completed medium without cells and

TABLE 1 | The effects of four concentrations of PA on glucose consumption of HepG2 cells.

Groups	Contents	GC(mmol·L^{-1})
Blank group	Only complete medium	14.635 ± 0.775
Normal group	HepG2 cell	5.274 ± 0.369
Model group	HepG2 cell added 1.0 mmol·L^{-1} PA	0.858 ± 0.615*
	HepG2 cell added 0.75 mmol·L^{-1} PA	0.992 ± 0.226*
	HepG2 cell added 0.5 mmol·L^{-1} PA	1.244 ± 0.549*
	HepG2 cell added 0.25 mmol·L^{-1} PA	1.526 ± 0.863*

Data was expressed as mean ± SD. $^{*}p < 0.01$ vs. normal group.

drugs, the CON group was normal cultured cells by completed medium without drugs, and experimental groups were normal cultured cells added with GB extraction fractions GBE-3, GBE-4, GBE-5, GBE−6, and GBE-7, respectively, which also dissolved in the completed medium. The concentrations of each fraction were 1,000, 500, 250, 125, 62.5, and 36.25 $\mu g \cdot ml^{-1}$, respectively. All groups and fractions set six multiple holes with 100 μl per hole. All complete medium contained 0.1% dimethyl sulfoxide (DMSO). Then cultured for 24 h, and the medium was sucked out, add another 100 μl basal-medium as well as 10 μl CCK-8 solution to each hole, incubated for another 2 h, and then determined the absorbance value at 450 nm.

Establishment of Insulin Resistance Model of HepG2 Cells

The insulin resistance model of HepG2 cells was established by palmitic acid (PA, Solarbio, Beijing, China). A 100 $mmol \cdot L^{-1}$ palmitic acid (PA) solution was prepared with absolute ethanol; 0.1 mol L^{-1} NaOH solution and 10% BSA solution were prepared with ultrapure water. Mixed the PA solution with NaOH solution (1:1 v/v) by water bath at 70°C for 30 min, the mixed solution was then mixed with 10% BSA solution (1:19 v/v), vortex for 30 s, and water bath at 55°C for 15 min to prepare PA working fluid (2.5 $mmol \cdot L^{-1}$). Diluted the PA working fluid with complete medium at the concentrations of 1, 0.75, 0.5, and 0.25 $mmol \cdot L^{-1}$, respectively, and filtered. HepG2 cells (5×10^4 $cells \cdot ml^{-1}$, dissolved in completed medium) were seeded in 96-well microtiter plates, and set up the following three groups: Blank group (only complete medium), normal group (cells with complete medium), and model group, respectively. The model group was added with concentrations of 1, 0.75, 0.5, and 0.25 $mmol \cdot L^{-1}$ PA working fluid, respectively. Also, six multiple holes were set with 100 μl per hole in every groups. After incubation at 37°C for 24 h, sucked out the culture-medium of each group, washed it with phosphate buffered saline (PBS, Gibco, Carlsbad, CA, USA) for 3 times, and added 100 μl basal-medium in each group, continued to cultivate for 24 h; then detected the glucose content in the medium, and calculated the glucose consumption (GC) of cells in each group.

Effects of GBE Fractions on Glucose Consumption in Cells Model

The HepG2 cells (5×10^4 $cells \cdot ml^{-1}$) were seeded on 96-well cell culture plates with 100 μl per hole. Set up a blank group (only blank group had no cells), a normal group, a model group, a positive group, and an experimental group, with six multiple holes in each group. Discarded the original medium, continued to add complete medium to the blank group and normal group, and add 0.25 $mmol \cdot L^{-1}$ PA working fluid to the model group, positive group, and experimental group, 100 μl per hole in each group. Then, cells were incubated for 24 h to establish the insulin resistance model of HepG2 cells. After the experimental model was established, the medium of each group was sucked out and washed with PBS for 3 times. Then the blank group, normal group, and model group were added with complete medium which had no drugs. The positive group was added with 165 $\mu g \cdot ml^{-1}$ concentration of metformin which dissolved in complete medium. The experimental group was added with complete medium containing the GB extracted fractions GBE-3, GBE-4, GBE-5, GBE−6, and GBE-7, the concentrations of each extracted fraction were 200, 100, 50, 25, 12.5, and 6.25 $\mu g \cdot ml^{-1}$, respectively. Every medium contained 0.1% DMSO. Each group was incubated for another 24 h, then the medium was discarded, washed with PBS for 3 times, add 100 μl basal-medium in each group, incubated again in 5% CO_2 incubator at 37°C for 24 h. Then the glucose content in each group were measured. Cell GC = Glucose content of blank group – Glucose content of corresponding group.

Cell Viability Assay

After the glucose content of each group was detected, 10 μl CCK-8 reagent was added to each well of 96-well cell culture plates, which was then cultured for 2 h, and the absorbance value at 450 nm was measured to calculate the cell survival rate. The cell survival rate = $[(A - C)/(B - C)] \times 100\%$, where A was the absorbance value of the experimental group, B was the absorbance value of the normal group, and C was the absorbance value of the blank group.

Animal Experiments

Animal Feeding and Grouping

A 7-week-old adult male Wistar rats (weighing 190 ± 10 g) were supplied by the Experimental Animal Center of Jilin University (Changchun, Jilin, China). All rat experimental procedures were performed in accordance with the Regulations for the Administration of Affairs Concerning Experimental Animals approved by the State Council of People's Republic of China. Rats were raised in a standard SPF barrier environment. The conditions were constant temperature of 23 ± 2°C, relative humidity of 40–80%, alternating day and night light cycle of 6:00 a.m. to 6:00 p.m., and the rats were free to eat and drink. After 7 days of environmental adaptation, 8 rats were randomly selected as the CON group, which was fed with ordinary diet during the whole experiment. The other rats were fed with HFD, which were consisting of 10.0% lard, 20.0% sucrose, 2.5% cholesterol, 1.0% sodium cholate, and 66.5% pulverized standard rat pellet (7). After 8 weeks of HFD feeding, the rats were intraperitoneally injected with freshly prepared STZ (40 $mg \cdot kg^{-1}$ b.w.) dissolved in citric acid buffer (0.1 $mol \cdot L^{-1}$, pH 4.3–4.5). The rats in CON group were only injected with citric acid buffer. After 7 days, fasting blood glucose was measured after fasting for 12 h. The blood glucose value ≥ 7.8 mmol L^{-1}, accompanied by symptom of polyuria and polydipsia, was regarded as successfully established T2DM rats. Also, 24 T2DM rats were randomly divided into three groups ($n = 8$), including GBE-5 group, which was fed HFD diet, and intragastrically administered with 200 $mg \cdot kg^{-1}$ (b.w.) ginseng berry GBE-5 fraction dissolved in saline once daily. The metformin (MET) group was fed with HFD diet, and intragastrically administered metformin dissolved in saline once daily, with a therapeutic dose of 100 mg $\cdot kg^{-1}$ (b. w.). The T2DM group was fed with HFD diet and intragastrically administered with saline once daily. The CON group was fed with normal diet and intragastrically administered with saline once daily. The blood glucose value of rats after fasting for 12 h was measured every 7 days; the body weight (b.w.), food consumption, and water consumption within 24 h were measured every 4 days.

Serum Sample Collection and Preparation

After 30 days of continuous intervention, the rats fasted for 12 h, and were anesthetized by intraperitoneal injection of 10% chloral hydrate (3 ml/kg b. w.) for 15 min, and blood was collected from the abdominal aorta of the rats. After the plasma was left at room temperature for 60 min, centrifuged at 3,000*g* and 4°C for 15 min, it was immediately put into liquid nitrogen and finally stored in the refrigerator at −80°C. The serum samples were thawed at 4°C before analysis, and 250 μl of serum mixed with 750 μl chromatographic methanol (1:3 v/v, 4°C), vortex for 30 s, and then centrifuged at 12,000 rpm for 15 min at 4°C. Take the supernatant, blow dry with nitrogen, add 1.0 l of ultrapure water for re-dissolution (4°C), vortex for 15 s, centrifuged again at 12,000 rpm for 15 min at 4°C, and the supernatant was filtered through 0.22 μm membrane filter before UHPLC–MS detection.

UHPLC-MS Analysis

An analysis was performed using UHPLC-ESI-Q-Exactive Orbitrap/MS system. The UHPLC was equipped with UltiMate 3000 system (Thermo Fisher Scientific, Dionex, Sunnyvale, CA, USA) coupled with Golden C_{18} column (2.1 × 50 mm, 1.9 μm, Thermo Fisher Scientific, San Jose, CA, USA) maintained at 35°C. The automatic sampler and sample chamber temperature was 4°C, sample injection volume was 2.0 μl, the flow rate was 0.3 ml/min, the mobile

TABLE 2 | The effect of GBE fractions on GC of insulin resistant HepG2 cells.

Groups	Drug Dosage (μg·ml^{-1})	GC(mmol·L^{-1})	CCK-8 (A 450)	GC/CCK-8(mmol·L^{-1})
Blank group	0	16.187 ± 0.517	-	-
Normal group	0	14.323 ± 0.379	1.021 ± 0.077	14.111 ± 1.090*
Model group	0	7.487 ± 0.755	0.914 ± 0.041	7.707 ± 0.983$^{\blacktriangle}$
Positive group	165	12.646 ± 0.417	0.731 ± 0.195	18.375 ± 4.113
GBE-3 fraction	200	9.185 ± 0.808	0.735 ± 0.058	12.526 ± 0.890**
	100	8.662 ± 0.269	0.902 ± 0.087	9.727 ± 1.361
	50	8.258 ± 0.224	0.904 ± 0.083	9.192 ± 0.692
	25	7.849 ± 0.590	0.994 ± 0.086	7.934 ± 0.699
	12.5	7.255 ± 0.303	1.020 ± 0.071	7.136 ± 0.438
	6.25	7.319 ± 0.342	0.913 ± 0.097	8.103 ± 0.876
GBE-4 fraction	200	9.596 ± 0.128	0.701 ± 0.212	14.800 ± 3.725**
	100	9.410 ± 0.189	0.685 ± 0.057	13.817 ± 1.030
	50	8.264 ± 0.254	0.677 ± 0.033	12.223 ± 0.463
	25	8.143 ± 0.260	0.663 ± 0.061	12.359 ± 0.848
	12.5	6.897 ± 0.730	0.649 ± 0.090	10.689 ± 0.787
	6.25	7.454 ± 0.679	0.629 ± 0.056	11.853 ± 0.322
GBE-5 fraction	200	11.135 ± 0.184	0.769 ± 0.292	16.637 ± 5.986**
	100	10.437 ± 0.846	0.688 ± 0.072	15.248 ± 1.202
	50	9.381 ± 0.324	0.622 ± 0.055	15.204 ± 1.398
	25	9.060 ± 0.368	0.649 ± 0.081	14.163 ± 1.755
	12.5	8.708 ± 0.213	0.674 ± 0.072	13.039 ± 1.207
	6.25	8.747 ± 0.830	0.607 ± 0.053	14.458 ± 1.290
GBE-6 fraction	200	9.955 ± 0.314	0.790 ± 0.145	13.011 ± 2.278*
	100	9.943 ± 0.608	0.964 ± 0.288	11.013 ± 2.349
	50	8.769 ± 0.827	0.903 ± 0.209	10.078 ± 1.811
	25	8.635 ± 0.784	0.965 ± 0.115	8.995 ± 0.557
	12.5	8.482 ± 0.744	0.859 ± 0.078	9.918 ± 0.921
	6.25	8.059 ± 0.446	0.882 ± 0.124	9.250 ± 0.850
GBE-7 fraction	200	9.778 ± 0.282	0.730 ± 0.081	13.553 ± 1.545**
	100	9.754 ± 0.808	0.802 ± 0.056	12.233 ± 1.458
	50	8.700 ± 0.492	0.916 ± 0.109	9.619 ± 1.135
	25	8.337 ± 0.460	0.991 ± 0.100	8.480 ± 0.799
	12.5	8.920 ± 1.168	1.103 ± 0.123	8.174 ± 1.350
	6.25	8.206 ± 0.583	0.907 ± 0.025	9.061 ± 0.784

Data was expressed as mean ± SD. $^{*}p < 0.05$ *vs. model group.* $^{**}p < 0.01$ *vs. model group.* $^{\blacktriangle}p < 0.01$ *vs. GBE-5 fraction group.*

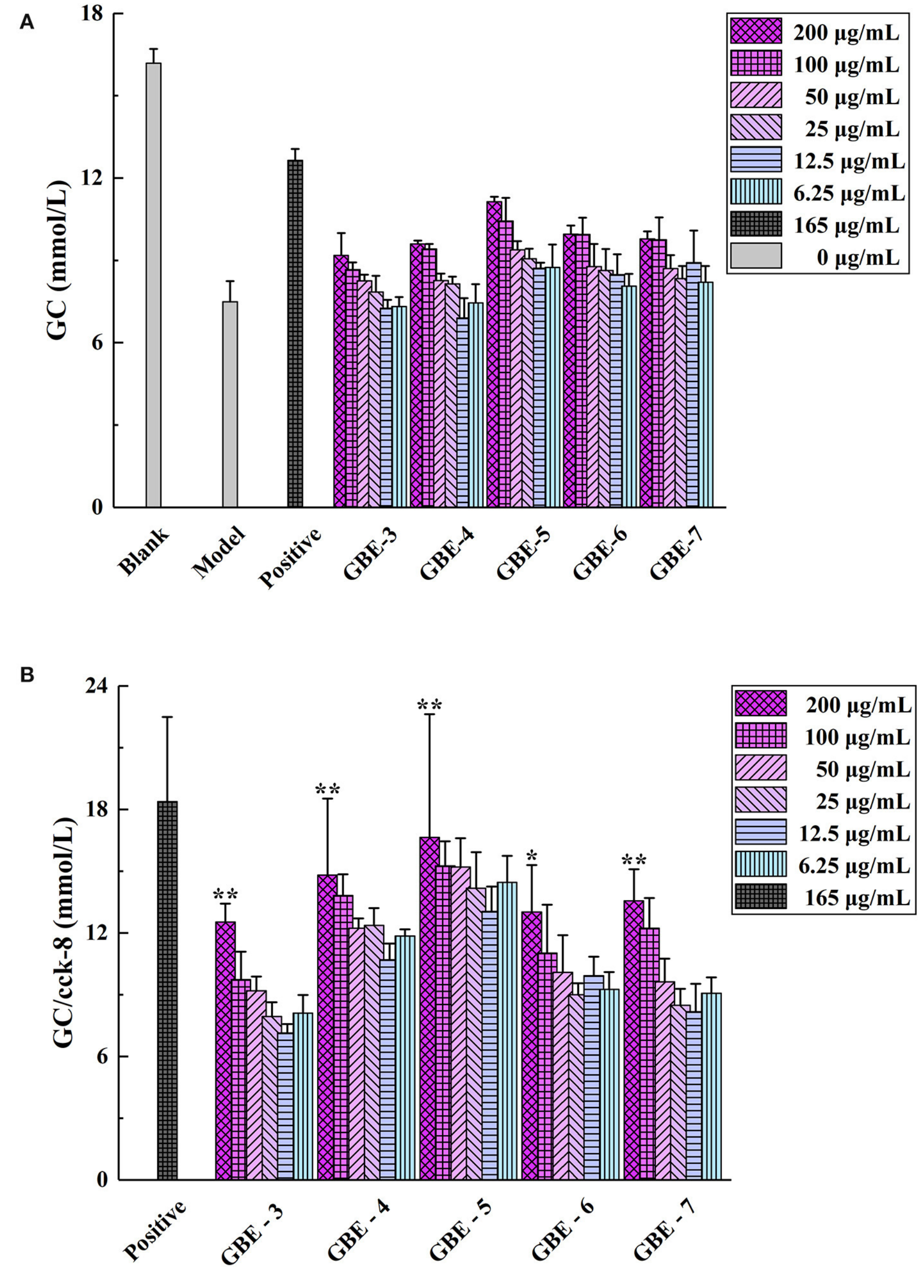

FIGURE 3 | (A) Cell GC and **(B)** GC/Cell survival rate (CCK-8). *$p < 0.05$ vs. model group, ** $p < 0.01$ vs. model group.

phase A was 0.1% formic acid in water, and phase B was 100% acetonitrile. The chromatographic conditions of rat serum were: 0–1 min, 3% phase B, 1–16 min, 3–70% phase B, 16–18 min, 70% phase B, 18–25 min, 70–90% phase B, 25–26 min, 90–100% phase B, 26–30 min, 100% phase B. The chromatographic conditions of GBE fractions were: 0–20 min, 25–65% phase B, 20–25 min, 65–100% phase B, 25–30 min, 100% phase B.

The MS detection was performed on Q-Exactive orbitrap MS (Thermo Fisher Scientific, USA), for which the source parameters were set as follows: Sweep gas flow was 0.175 Mpa, sheath gas flow was 6.125 Mpa, and auxiliary gas flow was 2.625 Mpa. The capillary temperature was 320°C, the capillary voltage was 3.5 kV, and the auxiliary gas heater temperature was 350°C. The electrospray ionization source in both positive (ESI+, pos) and negative (ESI–, neg) ion modes was used, and the scanning range were m/z 66.7 ∼ 1,000 (rat serum) and m/z 133.4 ∼ 2,000 (GBE fractions). The scan mode was Full MS with dd-MS^2, Top $N = 8$, of which the resolution was 17,500 (date dependent-MS^2) and 70,000 (Full

TABLE 3 | Identification of compounds in GBE-5 fraction from ginseng berry total ginsenosides.

No.	Compounds	Formula	Accurate mass (m/z)	Measured mass (m/z)	Adducts	MS^2 fragment ions (Mass accuracy < 10 ppm)
1	Notoginsenoside R_1	$C_{47}H_{80}O_{18}$	932.5345	931.5268	$[M\text{-}H]^-$	781.4741, 751.4636, 637.4318, 619.4213, 149.0450
2	Ginsenoside Rg_1	$C_{42}H_{72}O_{14}$	800.4922	845.4904	$[M+FA\text{-}H]^-$	781.4753, 637.4319,619.4216,457.3685, 179.0559
3	Ginsenoside Re	$C_{48}H_{82}O_{18}$	946.5501	991.5483	$[M+FA\text{-}H]^-$	781.4740, 637.4319, 619.4215, 279.1085, 163.0612
4	Ginsenoside Rf	$C_{42}H_{72}O_{14}$	800.4922	799.4846	$[M\text{-}H]^-$	619.4213, 475.3792, 457.3685, 295.1032, 179.0569
5	Ginsenoside Rb_1	$C_{54}H_{92}O_{23}$	1108.6029	1107.5953	$[M\text{-}H]^-$	945.5426, 783.4899, 691.4426, 341.1086, 179.0553
6	Ginsenoside Rc	$C_{53}H_{90}O_{22}$	1078.5924	1077.5856	$[M\text{-}H]^-$	969.5436, 897.5224, 735.4696, 179.0571, 56.9989
7	Ginsenoside Rb_2	$C_{53}H_{90}O_{22}$	1078.5924	1077.5853	$[M\text{-}H]^-$	897.5228, 753.4799, 645.4387, 149.0466, 131.0351
8	Ginsenoside Rb_3	$C_{53}H_{90}O_{22}$	1078.5924	1077.5846	$[M\text{-}H]^-$	945.5089, 621.4128, 293.0719, 149.0389, 83.4633
9	Ginsenoside Rd	$C_{48}H_{82}O_{18}$	946.5501	991.5485	$[M+FA\text{-}H]^-$	783.4883, 621.4351, 529.3881, 295.1021
10	Ginsenoside F_2	$C_{42}H_{72}O_{13}$	784.4973	783.4898	$[M\text{-}H]^-$	621.4358, 603.4253, 529.3887, 499.3779, 149.0463
11	Ginsenoside Rg_3	$C_{42}H_{72}O_{13}$	784.4973	783.4893	$[M\text{-}H]^-$	603.4257, 459.3846, 441.3746, 179.0567

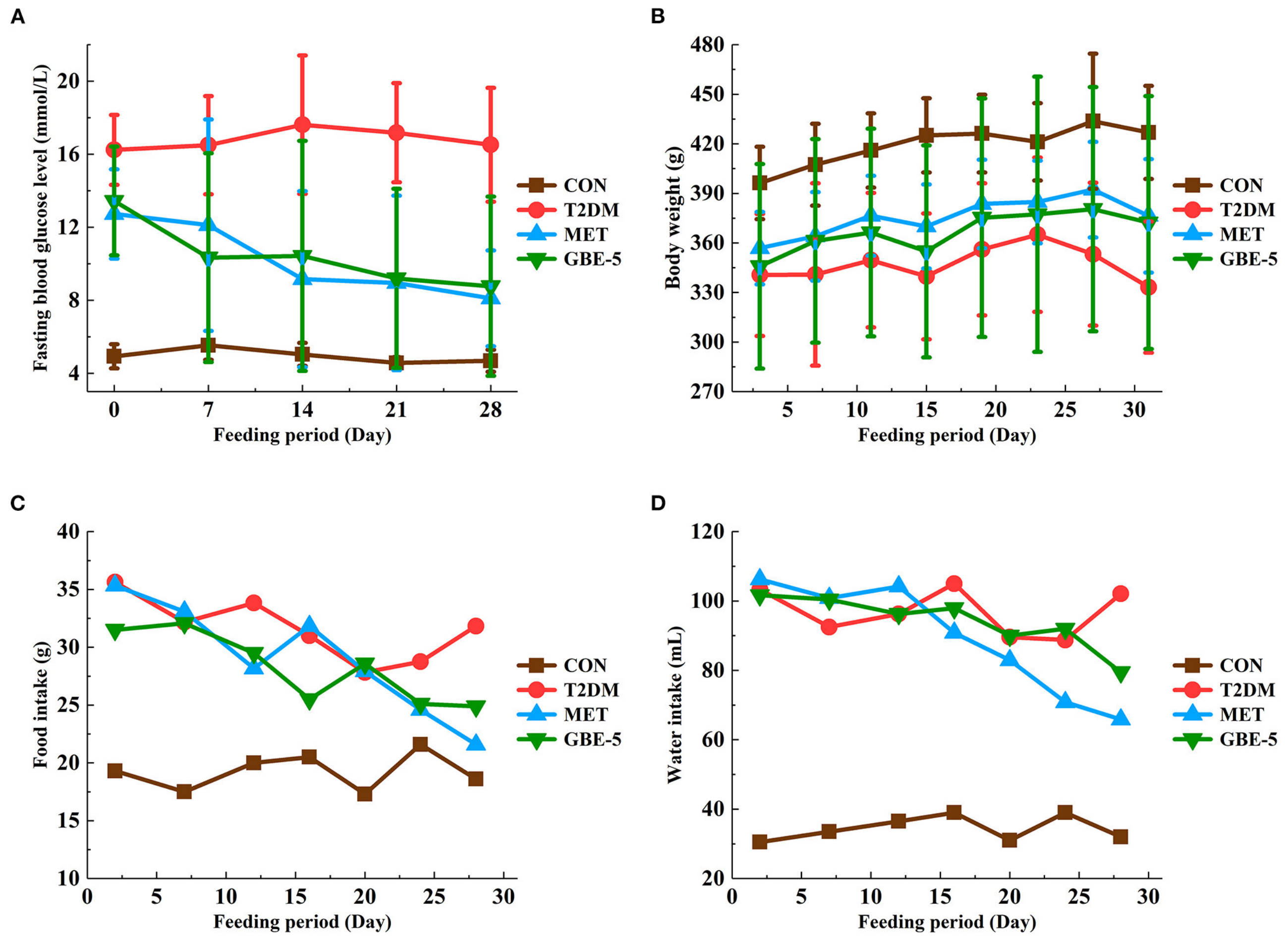

FIGURE 4 | The effect of GBE-5 fraction on the fasting blood glucose level **(A)**, body weight **(B)**, food **(C)**, and water **(D)** intake in T2DM rats.

MS), respectively, and the collision energy was 10, 20, and 40%, when it was dd-MS^2 mode. The instrument was able to meet the quality accuracy of pos/neg and MS/MS^2 cycling. Our selected acquisition mode improved the efficiency of acquisition, and also met the requirements of the established secondary MS^2 identification efficiency. The data were recorded and analyzed using the Xcalibur software (Version 2.2.42, Thermo Fisher Scientific, USA).

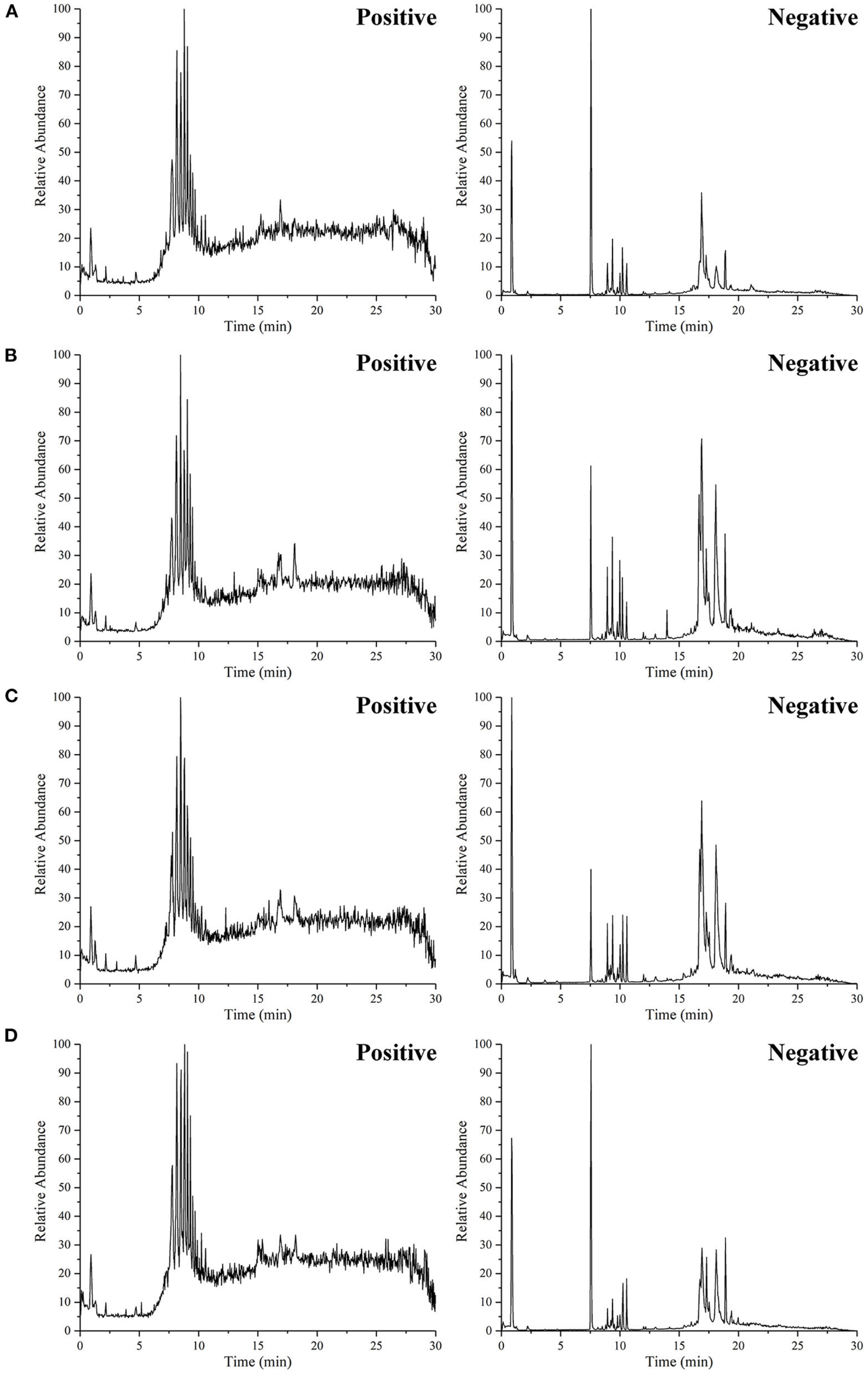

FIGURE 5 | The representative UHPLC–MS TIC of serum from the CON group **(A)**, T2DM group **(B)**, MET group **(C)**, and GBE-5 fraction group **(D)**; the TIC on the left side was positive modes and the right side was negative modes, respectively.

Quality Control Sample Preparation

To test the stability and reproducibility of the system, quality control (QC) samples of rat serum and GBE fractions were prepared, respectively. Took a small part of the same volume from all samples, mixed it and treated it according to the treatment method of corresponding samples to obtain QC samples of rat serum and GBE fractions, respectively. Before the experiment, QC samples were tested 6 times to balance the UHPLC–MS analysis system, and then QC samples and blank samples (75% acetonitrile in water) were tested once between every 6 samples in the sample detection sequence.

Multivariate Data Processing and Analysis

The raw data of rat serum was obtained from Dionex^{TM}, Chromeleon^{TM} 6.8, and Thermo Xcalibur, which was then imported into Progenesis QI v 2.3 software (Newcastle, UK) and used for deconvolution, calibrate the retention time (RT), peak alignment, and normalization. Combined the positive and negative ion data into a data matrix and saved as Excel file, which was then imported to the R programming language software (Ropls package v3.6.2) for the principal components analysis (PCA), and observed the overall distribution of each sample and the stability of the UHPLC–MS analysis process. Univariate statistical analysis was carried out by Stats software package, and ggplot2 package was used to get the volcano plot, which could visualize the *p*-value and the fold change (FC) value. Metabolite meeting $p < 0.05$ as well as FC ≥ 1.5 or FC ≤ 0.67 was usually considered to be differential metabolites.

Differential Metabolites Identification and Pathway Analysis

Metabolomics databases such as human metabolome database (HMDB) (http://www.hmdb.ca/), Lipidmaps v2.3 (http://www.lipidmaps.org), and METLIN (https://metlin.scripps.edu/) were screened and identified the matched metabolites, when the product ion mass spectra and MS/MS fragment ion suited with the structural information in the databases. The KEGG (https://www.kegg.jp/) database was used for metabolic pathway enrichment analysis of potential differential metabolites.

RESULTS AND DISCUSSION

Analysis of GBE Fractions by UHPLC–MS

The PCA Analysis

In order to verify the stability and reliability of the UHPLC-MS and acquired data, PCA analysis was carried out on GBE fractions and its QC samples. As shown in **Figure 1A**, it could be observed that QC samples showed a good aggregation state in the PCA score plot and approached the coordinate origin, indicating that the experimental condition was in a stable state during the data collection.

Analysis of the GB Extract Fractions by UHPLC–MS

The total ion chromatograms (TIC) of the GBE fractions obtained by UHPLC–MS were shown in **Figure 2**, in which both were in negative ion mode (ESI-), and the ion peaks in the spectrum were well separated, indicating that the corresponding chromatographic and MS conditions were suitable for samples determination. As the polarity of the seven reagents (or mixed reagents) used in the extraction segmentation process increased in turn, the polarity was petroleum ether < ethyl ether < ethyl acetate–ethyl ether (3:2, v/v) < ethyl acetate-*n*-butanol (4:1, v/v) < ethyl acetate-*n*-butanol (10:9, v/v) < *n*-butanol < distilled water, respectively. Therefore, the polarity of the corresponding extraction fractions GBE-1 to GBE-7 also increased in turn, which could be seen from the TIC that the RT (min) of the active components in GBE-3 to GBE-7 fraction gradually moved to the left (GBE-1 and 2 fractions were discarded), indicating that the polarity of the main active components of each fraction gradually increased, suggesting that the solvent extraction method could segmented the GBE well. Weighed 30 g of GBE, respectively; prepared the extract fractions in parallel for 6 times; and dried them to constant weight. The final average weight of each fraction was 0.51 ± 0.03 g for GBE-3, 6.05 ± 0.08 g for GBE-4, 12.31 ± 0.18 g for GBE-5, 5.76 ± 0.16 g for GBE-6, and 1.37 ± 0.09 g for GBE-7 fraction, respectively. It could be seen that the main active components of GBE were concentrated in GBE-4 to GBE-6 fractions. The main component of GBE-4 was 20(*S*)-protopanaxatriol, while the main component of GBE-5 and GBE-6 was 20(*S*)-protopanaxadiol. The result was expressed as mean ± SD.

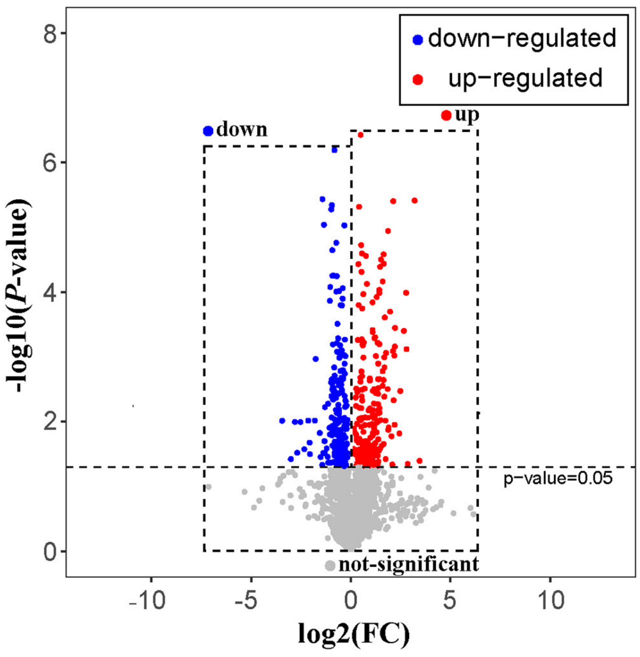

FIGURE 6 | The volcano plot of T2DM vs. GBE-5 fraction group.

Screening of Hypoglycemic Active Fraction From GBE

Effects of GBE Fractions on the Proliferation of HepG2 Cells

The effect of GBE concentration on HepG2 cell proliferation was investigated, it was found that when the drug concentration was $\geq$ 250 μmol·L^{-1}, the cell survival rate of the experimental group was generally less than 50%. Therefore, the administration concentration of cells should be less than 250 μmol·L^{-1}. Since six different administration concentrations were set for each fraction of GBE, the final concentrations were set as 200, 100, 50, 25, 12.5, and 6.25 μmol·L^{-1}.

The Result of HepG2 Cells Insulin Resistance Model Establishment

The HepG2 insulin resistance model was established by PA. It was found that when the concentrations of PA were 1, 0.75, 0.5, and 0.25 mmol·L^{-1}, the GC of each model group was significantly lower than that of the normal group ($p < 0.01$), indicating that the HepG2 insulin resistance model was successfully established by PA at each concentration, which was shown in **Table 1**. Considering the effect of PA concentration on HepG2 cell survival, the smallest PA concentration (0.25 mmol·L^{-1}) was selected for modeling, which was also consistent with that reported in the literature (23, 24).

Effects of GBE Fractions on GC in Insulin Resistance Model

The screening results of hypoglycemic activity of GBE fractions were shown in **Table 2**. It was found that the GC of the cells in the model group was significantly lower than that in the normal group ($p < 0.01$), indicating that the model of insulin resistance of HepG2 cells was successfully established. The GC of GBE fractions in the experimental group were significantly higher than ($p < 0.05$) or very significantly higher than ($p < 0.01$) the model group, suggesting that the drug intervention could improve the GC of HepG2 cell insulin resistance model. The cell GC of the blank group, model group, positive group, and experimental group was shown in **Figure 3A**. The ratio of GC to cell survival rate (CCK-8) was calculated to eliminate the influence of the number of cells in the group on the GC of each group. The calculation results were shown in **Figure 3B**. It was found that GBE-5 fraction has better hypoglycemic activity than other extraction fractions, but the hypoglycemic effect was worse than that of the positive group ($p > 0.05$). The main components of GBE-5 fraction were putatively identified by the accurate mass measurement and MS^2 fragment ions obtained by UHPLC–MS, as well as the database searching. The molecular MS error of all identified metabolites was less than 10 ppm. The compounds of GBE-5 were final identified by comparing the RT, accurate mass, and MS/MS spectra of authentic standards. The analyzed data were shown in **Table 3**.

Anti-diabetic Effects of GBE-5 Fraction in T2DM Rats

A rat model of T2DM induced by HFD and STZ was used to study the hypoglycemic effect of GBE-5 fraction. At the end of the 30-days experiment, it was found that GBE-5 fraction could significantly reduce the fasting blood glucose level in T2DM rats, and decreased from 13.44 ± 2.99 mmol·L^{-1} to 8.77 ± 4.91 mmol·L^{-1} ($p < 0.05$), as shown in **Figure 4**, food and water intake decreased in MET group and GBE-5 group, and there was no significant difference in body weight among the groups ($p > 0.05$). In the previous studies, it was found that total ginsenosides of GB could reduce the fasting blood glucose of rats by 27.35% (7). On the premise of the same drug dosage and treatment time, the fasting blood glucose of GBE-5 fraction which derived from GB total ginsenosides decreased significantly by 34.75% after 30 days of intervention in T2DM rats, indicating that the hypoglycemic effect of GBE-5 fraction was better than that of total ginsenosides of GB.

Serum Metabolic Profiling by UHPLC–MS

The positive and negative TIC of rat serum samples collected by UHPLC–MS was shown in **Figure 5**, in which A was CON group, B was T2DM group, C was MET group, and D was GBE-5 group. The ion peaks in the spectrum were well separated, indicating that the UHPLC–MS conditions in this experiment were suitable for sample determination.

Univariate Statistical Analysis

The rat serum and its QC samples were analyzed by PCA, as shown in **Figure 1B**, the QC samples showed a good aggregation state and closed to the coordinate origin, indicating that the acquisition instrument was in a stable state during data collection. Univariate statistical analysis based on UHPLC–MS data was used to screen the differential metabolites in rat serum after the 30-days intervention of GBE-5 fraction. Univariate analysis often used the FC value to represent the regulation multiple of metabolites between the two comparison groups. It was generally considered that compounds with FC value $\geq$ 1.5 or $\leq$ 0.67 and $p < 0.05$ were the differential metabolites between groups, which could be visualized by volcano plot, as shown in **Figure 6**, the red dots represented the significantly up-regulated differential metabolites ($\log_2$FC > 0, $p < 0.05$), the blue dots represented the significantly down-regulated differential metabolites ($\log_2$FC < 0, $p < 0.05$), and the gray dots represented the metabolites with no significant regulation ($p > 0.05$).

Identification of Metabolites and KEGG Pathway Enrichment Analysis

The RT, accurate mass spectra and MS/MS spectra of the differential compounds screened by univariate statistical analysis were imported into the metabolomics database, the data information of the standard in the database was compared, the mass error of all metabolites was less than 10 ppm, so the compounds were qualitatively identified. There were 66 compounds screened as differential metabolites in the GBE-5 *vs*. T2DM group. Then the KEGG online database was

TABLE 4 | The identification results of differential metabolites in T2DM vs. GBE-5 fraction group in serum.

No.	Mode	Metabolite	Formula	Adduct	t_R/min	Measured m/z	MS^2 fragment ions	Error (ppm)	FC	*p*
1	Pos	Metanephrine	$C_{10}H_{15}NO_3$	$[M+K]^+$	0.85	236.0676	180.1017, 149.0595, 125.0595	−3.9	1.71	0.00003
2	Pos	L-Proline	$C_5H_9NO_2$	$[M+Na]^+$	1.02	138.0527	98.0608, 87.0456, 70.0659	1.3	2.17	0.00335
3	Neg	12(*R*)-HETE	$C_{20}H_{32}O_3$	$[M-H]^-$	17.29	319.2266	275.2368, 179.1066, 111.1168	−2.6	2.88	0.00003
4	Neg	5-HETE	$C_{20}H_{32}O_3$	$[M-H_2O-H]^-$	18.84	301.2164	301.2160, 257.2261, 87.0438	−2.7	1.75	0.03753
5	Neg	9(*S*)-HPODE	$C_{18}H_{32}O_4$	$[M-H]^-$	15.96	311.2220	277.2165, 233.2267, 169.1226	−2.4	3.23	0.00102
6	Neg	9,10-DHOME	$C_{18}H_{34}O_4$	$[M-H]^-$	15.21	313.2378	295.2273, 251.2375, 171.1021	−2.1	2.15	0.00041
7	Neg	9-OxoODE	$C_{18}H_{30}O_3$	$[M-H]^-$	16.14	293.2118	275.2012, 249.2220, 185.1179	−1.4	2.41	0.00097
8	Neg	ADA	$C_{22}H_{36}O_2$	$[M-H]^-$	20.22	331.2632	313.2527, 287.2734, 271.2421	−3.2	1.70	0.01985
9	Neg	Dihydroneopterin triphosphate	$C_9H_{16}N_5O_{13}P_3$	$[M-H]^-$	16.91	493.9876	408.9601, 238.8909, 158.9246	−1.4	1.68	0.03974
10	Neg	DPA	$C_{22}H_{34}O_2$	$[M-H]^-$	19.96	329.2475	311.2369, 269.2264	−3.3	2.27	0.00316
11	Neg	Lipoxin A_4	$C_{20}H_{32}O_5$	$[M-H]^-$	14.71	351.2163	333.2057, 217.1583, 115.0387	−3.1	2.82	0.00948
12	Neg	Lipoxin B_4	$C_{20}H_{32}O_5$	$[M-H]^-$	14.94	351.2162	315.1951, 203.1063, 129.0906	−4.1	2.07	0.02378
13	Neg	LysoSM(d18:1)	$C_{23}H_{50}N_2O_5P^+$	$[M-H_2O-H]^-$	19.10	446.3280	124.9996, 104.1068	0.1	2.07	0.03470
14	Neg	GSSG	$C_{20}H_{32}N_6O_{12}S_2$	$[M-H_2O-H]^-$	14.09	593.1366	352.0662, 306.0785, 242.0801	4.0	1.67	0.02512
15	Neg	PGH_2	$C_{20}H_{32}O_5$	$[M-H]^-$	13.05	351.2163	333.2057, 225.1118, 99.0801	−4.0	2.47	0.01466
16	Neg	Stearic acid	$C_{18}H_{36}O_2$	$[M-H]^-$	20.74	283.2637	265.2526, 239.2734, 155.1795	−1.9	2.05	0.03708
17	Neg	Testosterone	$C_{19}H_{28}O_2$	$[M-H]^-$	13.22	287.2013	231.1746, 189.1276, 135.0807	−1.3	2.08	0.05293
18	Neg	Xanthosine	$C_{10}H_{12}N_4O_6$	$[M-H]^-$	1.97	283.0679	151.0251, 133.0145, 108.0193	−1.7	1.85	0.03535

TABLE 5 | Enriched KEGG pathway of differential metabolites in T2DM vs. GBE-5 fraction group.

No.	Metabolite	Compound ID	KEGG	Annotation
1	Metanephrine	HMDB0004063	C05588	Tyrosine metabolism
2	L-Proline	HMDB0000162	C00148	Protein digestion and absorption/Arginine and proline metabolism
3	12(*R*)-HETE	HMDB0062287	C14822	AA metabolism
4	5-HETE	HMDB0011134	C04805	AA metabolism
5	9(*S*)-HPODE	HMDB0006940	C14827	LA metabolism
6	9,10-DHOME	HMDB0004704	C14828	LA metabolism
7	9-OxoODE	HMDB0004669	C14766	LA metabolism
8	ADA	HMDB0002226	C16527	Ferroptosis/Biosynthesis of unsaturated fatty acids
9	Dihydroneopterin triphosphate	HMDB0000980	C04895	Folate biosynthesis
10	DPA	HMDB0006528	C16513	Biosynthesis of unsaturated fatty acids
11	Lipoxin A_4	HMDB0004385	C06314	AA metabolism /Toxoplasmosis
12	Lipoxin B_4	HMDB0005082	C06315	AA metabolism
13	LysoSM (d18:1)	HMDB0006482	C03640	Sphingolipid metabolism
14	GSSG	HMDB0003337	C00127	Ferroptosis /Thyroid hormone synthesis/Glutathione metabolism
15	PGH_2	HMDB0001381	C00427	AA metabolism /Oxytocin signaling pathway/Platelet activation /Retrograde endocannabinoid signaling
16	Stearic acid	HMDB0000827	C01530	Biosynthesis of unsaturated fatty acids /Fatty acid biosynthesis
17	Testosterone	HMDB0000234	C00535	Endocrine resistance /Prostate cancer
18	Xanthosine	HMDB0000299	C01762	Caffeine metabolism

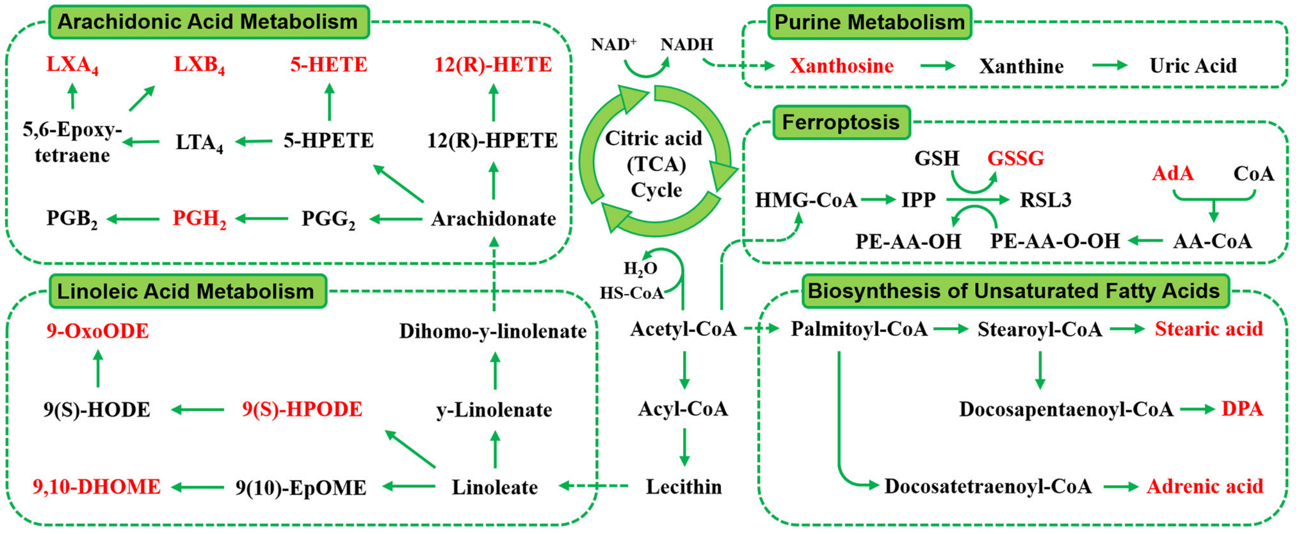

FIGURE 7 | The correlation networks between main differential metabolites with corresponding metabolic pathways.

used to pathway enrichment analysis, a total of 18 differential metabolites could be enriched in the KEGG metabolic pathway. The differential metabolites information and metabolic pathway enrichment results were shown in **Tables 4**, **5**, respectively. It was found that the four main metabolic pathways involved in regulation maybe the potential regulatory mechanism for the anti-diabetic effect of the GBE-5 fraction. Among them, five differential metabolites: 12(*R*)-HETE, 5-HETE, Lipoxin A4, Lipoxin B4, and PGH2 were involved in AA metabolism, three differential metabolites: 9(*S*)-HPODE, 9,10-DHOME, and 9-OxoODE were involved in linoleic acid (LA) metabolism, three differential metabolites: Adrenic acid (AdA), docosapentaenoic acid (DPA), and stearic acid were involved in the biosynthesis of unsaturated fatty acids, and two differential metabolites: Oxidized glutathione (GSSG) and AdA were involved in ferroptosis. These metabolic pathways were all widely linked to

T2DM, and the correlation networks of differential metabolites mentioned discussed was shown in **Figure 7**.

The metabolism of AA, LA, and biosynthesis of unsaturated fatty acids belongs to lipid metabolism. The LA was a kind of unsaturated fatty acids, due to the substantial increase in vegetable oils consumption, the intake of LA also increased greatly, and dietary fatty acids were responsible for the development and occurrence of many chronic diseases, such as obesity and diabetes (25). The LA was the direct precursor of AA) the conversion efficiency of LA into AA in human body was low, they were linked through metabolism. It was reported that AA and LA could be used as predictive markers for gestational diabetes mellitus (26), AA and its derivatives played a key role in the occurrence and development of obesity and T2DM, and played a diverse and partly contrasting roles in the pathogenesis of T2DM. Therefore, the study of AA as well as LA metabolism may help to identify novel targets for the treatment of T2DM and its associated complications (27).

Wang et al. (28) used proteomics to study the differential abundant proteins associated with diabetes in hamster liver. Combined with enrichment analysis of KEGG pathway, found that AA metabolism, LA metabolism, and bile acid (BA) metabolism in diabetic hamsters were affected. Our previous study had also found that GB exerted anti-diabetic effect by regulating AA and BA metabolism (7). However, in this study, the GBE-5 fraction was not involved in the regulation of BA metabolism pathway, which suggested that the screened GBE-5 fraction may not contained all of the GB active substances with anti-diabetic activity. Although the *in vivo* hypoglycemic activity experimental result of GBE-5 showed that its hypoglycemic effect was better than GB and other GBE fractions, the segmentation of GB by polar extraction method had its limitations, which cannot effectively collect all the pharmacodynamic material bases in GB. In the next experiment, the combination could be carried out according to the actual content of several main ginsenosides in GB, and then a hypoglycemic drug composed of ginsenoside monomer compounds could be found through *in vitro* hypoglycemic activity screening and *in vivo* hypoglycemic activity verification, which had more efficient hypoglycemic activity and could be used to replace the original total ginsenoside extract. It was conducive to drug quality control as well as modern development of hypoglycemic effect of GB.

Ferroptosis was a new programmed cell death mode, which different from apoptosis and autophagy. Its main mechanism was that under the action of divalent iron or lipoxygenase, unsaturated fatty acids on cell membrane produce lipid peroxidation, and then induced cell death (29). It was reported that pancreatic iron deposition will occur during the development of T2DM, which will lead to pancreatic β-cells dysfunction and death. The inhibition of pancreatic iron deposition and pancreatic β-cells ferroptosis had a beneficial regulatory effect on T2DM, indicating that ferroptosis was closely related to the occurrence and development of T2DM, and its internal relationship with T2DM was worthy of further study (30).

CONCLUSIONS

In the present study, the total ginsenosides extract of GB was extracted by organic solvent extraction, and 5 extraction fractions of GB with different polarity were obtained. The insulin resistance model of HepG2 cells was established, and the hypoglycemic active fraction of five extracted fractions were screened *in vitro*. It was found that GBE-5 fraction had better hypoglycemic activity than other fractions, which was the hypoglycemic active fraction of GBE. The main components of GBE-5 fraction were found to be ginsenoside Rg_1, Re, Rc, Rd, Rb_1, Rb_2, Rb_3, and Rg_3. The T2DM rat model induced by HFD/STZ was established, and the hypoglycemic activity of ginsenoside GBE-5 was evaluated. It was found that ginsenoside GBE-5 had significant hypoglycemic activity, the fasting blood glucose decreased from 13.44 ± 2.99 mmol·L^{-1} to 8.77 ± 4.91 mmol·L^{-1} ($p < 0.05$), and the blood glucose decreased significantly by 34.75%, the hypoglycemic effect was better than the total ginsenosides extract of GB (the hypoglycemic rate was 27.35 %). Univariate statistical analysis based on UHPLC–MS was used to screen the metabolites with different contents in the serum of rats after 30 days of intervention. Combined with the enrichment analysis of KEGG metabolic pathway, 18 differential metabolites that could be enriched into KEGG metabolic pathway were screened and identified in serum of T2DM *vs.* GBE-5 group. The metabolic pathways involved in regulation mainly include AA metabolism, LA metabolism, biosynthesis of unsaturated fatty acids and ferroptosis, which were potential targets for hypoglycemic activity of GBE-5 fraction of GB. In this study, the GBE-5 active fraction and its main hypoglycemic mechanism were studied, which will lay a foundation for the further development and utilization of *P. ginseng* berry as health functional food or dietary supplement.

DATA AVAILABILITY STATEMENT

The original contributions presented in the study are included in the article/supplementary material, further inquiries can be directed to the corresponding author/s.

ETHICS STATEMENT

The animal study was reviewed and approved by the Institutional Animal Care and Use Committee (IACUC) of the Changchun University of Chinese Medicine with the permit code CPCCUCM IACUC 2019-009.

AUTHOR CONTRIBUTIONS

This study was designed by WW and HW. The sample collection, detection, and data curation were done by HW, YT, and AW. The data analysis and interpretation were exercised by WW, HW, and YL. The software, supervision, and validation were dealt by HW, HL, LJ, and BL. The writing of original draft was carried out by HW. Writing-review and editing and final approval of the published version were done by WW. All authors read and approved the final manuscript.

FUNDING

This research work was supported by Jilin Scientific and Technological Development Program (No. 20200301049RQ) and National College Students Innovation and Entrepreneurship Training Program (202110199015).

REFERENCES

1. Ichim MC, Boer HJD. A review of authenticity and authentication of commercial ginseng herbal medicines and food supplements. *Front Pharmacol.* (2021) 11:612071. doi: 10.3389/fphar.2020.612071
2. Guo M, Shao S, Wang D, Zhao D, Wang M. Recent progress in polysaccharides from *Panaxginseng* C. *A Meyer Food Funct.* (2021) 12:494–518. doi: 10.1039/D0FO01896A
3. Byun J, Kim SK, Ban JY. Anti-inflammatory and anti-oxidant effects of Korean ginseng berry extract in LPS-Activated RA W2647 macrophages. *Am J Chin Med.* (2021) 49:719–35. doi: 10.1142/S0192415X21500336
4. Wang CZ, Hou L, Wan JY, Yao H, Yuan J, Zeng J, et al. Ginseng berry polysaccharides on inflammation-associated colon cancer: inhibiting T-cell differentiation, promoting apoptosis, and enhancing the effects of 5-fluorouracil. *J Ginseng Res.* (2020) 44:282–90. doi: 10.1016/j.jgr.2018.12.010
5. Lee MY, Seo HS, Singh D, Lee SJ, Lee CH. Unraveling dynamic metabolomes underlying different maturation stages of berries harvested from *Panax ginseng*. *J Ginseng Res.* (2020) 44:413–23. doi: 10.1016/j.jgr.2019.02.002
6. Wang CZ, Wan C, Luo Y, Zhang CF, Zhang QH, Chen L, et al. Ginseng berry concentrate prevents colon cancer via cell cycle, apoptosis regulation, and inflammation-linked Th17 cell differentiation. *J Physiol Pharmacol.* (2021) 72:225–37. doi: 10.26402/jpp.2021.2.08
7. Wang H, Huang R, Li H, Jiao L, Liu S, Wu W. Serum metabolomic analysis of the anti-diabetic effect of Ginseng berry in type II diabetic rats based on ultra high-performance liquid chromatography-high resolution mass spectrometry. *J Pharm Biomed Anal.* (2021) 196:113897. doi: 10.1016/j.jpba.2021.113897
8. Choi SR, Lee MY, Reddy CK, Lee SJ, Lee CH. Evaluation of metabolite profiles of ginseng berry pomace obtained after different pressure treatments and their correlation with the antioxidant activity. *Molecules.* (2021) 26:284. doi: 10.3390/molecules26020284
9. Xu XY Yi ES, Kang CH, Liu Y, Lee YG,Choi HS, et al. Whitening and inhibiting NF-kB-mediated inflammation properties of the biotransformed green ginseng berry of new cultivar K[[sb]]1[[/s]],ginsenoside Rg^2 enriched, on B16 and LPS-stimulated RAW2647 cells. *J Ginseng Res.* (2021) 45:631–41. doi: 10.1016/j.jgr.2021.02.007
10. Nam JH, Choi J, Monmai C, Rod IW, Jang AY, You S, et al. Immune-enhancing effects of crude polysaccharides from Korean ginseng berries on spleens of mice with cyclophosphamide-induced immunosuppression. *J Microbiol Biotechnol.* (2021) 32. doi: 10.4014/jmb.2110.10021
11. Qiao Y, Zhang J, Liu Y, Liang Z, Wang Y, Zheng W, et al. Efficacy and safety of zhenyuan capsule for coronary heart disease with abnormal glucose and lipid metabolism: study protocol for a randomized, double-blind, parallel-controlled, multicenter clinical trial. *Evid Based Complement Alternat Med.* (2018) 1716430. doi: 10.1155/2018/1716430
12. Park JE, Kim H, Kim J, Choi SJ, Ham J, Nho CW, et al. A comparative study of ginseng berry production in a vertical farm and an open field. *Ind Crop Prod.* (2019) 140:111612. doi: 10.1016/j.indcrop.2019.111612
13. Joo KM, Lee JH, Jeon HY, Park CW, Hong DK, Jeong HJ, et al. Pharmacokinetic study of ginsenoside Re with pure ginsenoside Re and ginseng berry extracts in mouse using ultra performance liquid chromatography/mass spectrometric method. *J Pharmaceut Biomed.* (2010) 51:278–83. doi: 10.1016/j.jpba.2009.08.013
14. Wang H, Teng Y, Li S, Li Y, Li H, Jiao L, et al. UHPLC-MS-based serum and urine metabolomics reveals the anti-diabetic mechanism of ginsenoside re in type 2 diabetic rats. *Molecules.* (2021) 26:6657. doi: 10.3390/molecules26216657
15. Liu Z, Qu CY Li LX, Wang YF Li W, Wang CZ, et al. Hypoglycemic and hypolipidemic effects of malonyl ginsenosides from american ginseng (Panax quinquefolius L) on type 2 diabetic mice ACS. *Omega.* (2021) 6:33652–64. doi: 10.1021/acsomega.1c04656
16. Zhu Y, Yang H, Deng J, Fan D. Ginsenoside Rg5 Improves Insulin Resistance and Mitochondrial Biogenesis of Liver via Regulation of the Sirt1/PGC-1α Signaling Pathway in db/db Mice. *J Agric Food Chem.* (2021) 69:8428–39. doi: 10.1021/acs.jafc.1c02476
17. Wei Y, Yang H, Zhu C, Deng J, Fan D. Ginsenoside Rg5 relieves type 2 diabetes by improving hepatic insulin resistance in db/db mice. *J Funct Foods.* (2020) 71:104014. doi: 10.1016/j.jff.2020.104014
18. Park SY, Gautier JF, Chon S. Assessment of insulin secretion and insulin resistance in human. *Diabetes Metab J.* (2021) 45:641–54. doi: 10.4093/dmj.2021.0220
19. Jovanovski E, Duvnjal LS, Komishon A, Yeung FRA, Sievenpiper JL, Zurbau A, et al. Effect of coadministration of enriched Korean Red Ginseng (*Panaxginseng*) and American ginseng (*Panax quinquefolius* L) on cardio metabolic outcomes in type-2 diabetes: A randomized controlled trial. *J Ginseng Res.* (2021) 45:546–54. doi: 10.1016/j.jgr.2019.11.005
20. Pandey S, Dvorakova MC. Future perspective of diabetic animal models. *Endocr Metab Immune Disord Drug Targets.* (2020) 20:25–38. doi: 10.2174/1871530319666190626143832
21. Noshahr ZS, Salmani H, Rad AK, Sahebkar A. Animal models of diabetes-associated renal injury. *J Diabetes Res.* (2020) 9416419. doi: 10.1155/2020/9416419
22. Arzumanian VA, Kiseleva OI, Poverennaya EV. The curious case of the HepG2 cell line: 40 years of expertise. *Int J Mol Sci.* (2021) 22:13135. doi: 10.3390/ijms222313135
23. Zhao H, Shu L, Huang W, Song G, Ma H. Resveratrol affects hepatic gluconeogenesis via histone deacetylase 4. *Diabetes Metab Syndr Obes.* (2019) 12:401–11. doi: 10.2147/DMSO.S198830
24. Malik SA, Acharya JD, Mehendale NK, Kamat SS, Ghaskadbi SS. Pterostilbene reverses palmitic acid mediated insulin resistance in HepG2 cells by reducing oxidative stress and triglyceride accumulation. *Free Radic Res.* (2019) 53:815–27. doi: 10.1080/10715762.2019.1635252
25. Burns JL, Nakamura MT, Ma DWL. Differentiating the biological effects of linoleic acid from arachidonic acid in health and disease. *Prostag Leukotr Ess.* (2018) 135:1–4. doi: 10.1016/j.plefa.2018.05.004
26. Szczuko M, Kikut J, Komorniak N, Bilicki J, Celewicz Z, Zietek M. The role of arachidonic and linoleic acid derivatives in pathological pregnancies and the human reproduction process. *Int J Mol Sci.* (2020) 21:9628. doi: 10.3390/ijms21249628
27. Sonnweber T, Pizzini A, Nairz M, Weiss G, Tancevski I. Arachidonic acid metabolites in cardiovascular and metabolic diseases. *Int J Mol Sci.* (2018) 19:3285. doi: 10.3390/ijms19113285
28. Wang W, Shi Z, Zhang R, Yu J, Wang C, Hou J, et al. Liver proteomics analysis reveals abnormal metabolism of bile acid

and arachidonic acid in Chinese hamsters with type 2 diabetes mellitus. *J Proteomics.* (2021) 239:104186. doi: 10.1016/j.jprot.2021.104186

29. Hirschhorn T, Stockwell BR. The development of the concept of ferroptosis. *Free Radic Biol Med.* (2019) 133:130–43. doi: 10.1016/j.freeradbiomed.2018.09.043
30. Li D, Jiang C, Mei G, Zhao Y, Chen L, Liu J, et al. Quercetin alleviates ferroptosis of pancreatic cells in type 2 diabetes. *Nutrients.* (2020) 12:2954. doi: 10.3390/nu12102954

Conflict of Interest: The authors declare that the research was conducted in the absence of any commercial or financial relationships that could be construed as a potential conflict of interest.

frontiers | Frontiers in Nutrition

ORIGINAL RESEARCH
published: 25 April 2022
doi: 10.3389/fnut.2022.851972

EGCG Inhibits Proliferation and Induces Apoptosis Through Downregulation of SIRT1 in Nasopharyngeal Carcinoma Cells

Shisheng Jiang[1†], Chaoming Huang[1†], Guodong Zheng[1], Wei Yi[1], Bo Wu[1], Junyuan Tang[1], Xiawen Liu[1], Biyun Huang[1], Dan Wu[1], Tingdong Yan[2*], Mingxi Li[3], Chunpeng Wan[3*] and Yi Cai[1*]

[1] Key Laboratory of Molecular Target & Clinical Pharmacology, The State & NMPA Key Laboratory of Respiratory Disease, School of Pharmaceutical Sciences, Fifth Affiliated Hospital, Guangzhou Medical University, Guangzhou, China, [2] School of Pharmacy, Nantong University, Nantong, China, [3] Research Center of Tea and Tea Culture, College of Agronomy, Jiangxi Agricultural University, Nanchang, China

Edited by:
Zhiqiang Wang,
Hebei University, China

Reviewed by:
Yuan Li,
Nanjing Medical University, China
Zhenhua Hu,
Institute of Molecular and Cell Biology
(A*STAR), Singapore

***Correspondence:**
Yi Cai
yicaisysu@163.com
Tingdong Yan
tingdong.yan@ntu.edu.cn
Chunpeng Wan
chunpengwan@jxau.edu.cn

† These authors have contributed equally to this work

Specialty section:
This article was submitted to
Food Chemistry,
a section of the journal
Frontiers in Nutrition

Received: 10 January 2022
Accepted: 14 March 2022
Published: 25 April 2022

Citation:
Jiang S, Huang C, Zheng G, Yi W, Wu B, Tang J, Liu X, Huang B, Wu D, Yan T, Li M, Wan C and Cai Y (2022) EGCG Inhibits Proliferation and Induces Apoptosis Through Downregulation of SIRT1 in Nasopharyngeal Carcinoma Cells. Front. Nutr. 9:851972. doi: 10.3389/fnut.2022.851972

Epigallocatechin-3-gallate (EGCG), a frequently studied catechin in green tea, has been shown involved in the anti-proliferation and apoptosis of human nasopharyngeal carcinoma (NPC) cells. However, the underlying molecular mechanism of the apoptotic effects of EGCG has not been fully investigated. Recent literature emphasized the importance of Sirtuin 1 (SIRT1), an NAD^+-dependent protein deacetylase, in regulating cellular stress responses, survival, and organismal lifespan. Herein, the study showed that EGCG could significantly inhibit cell proliferation and promote apoptosis of 2 NPC (CNE-2 and 5-8F) cell lines. Moreover, it was also found that SIRT1 is down-regulated by EGCG, and the SIRT1-p53 signaling pathway participates in the effects of EGCG on CNE-2 and 5-8 F cells. Taken together, the findings of this study provided evidence that EGCG could inhibit the growth of NPC cell lines and is linked with the inhibition of the SIRT1-p53 signaling pathway, suggesting the therapeutic potential of EGCG in human NPC.

Keywords: EGCG, nasopharyngeal carcinoma, SIRT1, p53, apoptosis

INTRODUCTION

Nasopharyngeal carcinoma (NPC) is a malignant tumor with a high incidence rate in the Southeast Asia and Southern China (1, 2). Currently, radiotherapy combined with chemotherapy is routinely used to control early disease progression. Due to the insidious location of NPC and lack of obvious early symptoms, over 70% of NPC patients present with locally advanced or metastatic lesions at the time of diagnosis (3). The effect of radiotherapy alone is unsatisfactory, so adjuvant chemotherapy is essential. As first-line chemotherapeutic drugs for NPC, cisplatin, and paclitaxel can significantly improve NPC's therapeutic efficacy. But the larger doses of cytotoxic drugs often lead to severe toxic side effects by inducing cancer multi-drug resistance and, hence, are declared the main treatment failures (4). Therefore, it is necessary to find high-efficacy with lower toxicity chemotherapeutic agents to improve the patients' clinical efficacy and high survivorship.

Natural products have historically contributed to pharmacotherapy, especially for cancer and infectious diseases (5, 6). (-)-Epigallocatechin-3-gallate (EGCG), is a polyphenolic component extracted from green tea, has been demonstrated to exhibit a variety of health benefits such as anti-tumor, anti-oxidant, anti-inflammatory, cardiovascular protection, and neuroprotection (7, 8). The recent studies revealed that EGCG inhibited proliferation and improved the sensitization of NPC cells to radiotherapy, which suggested the therapeutic potential of EGCG on NPCs (9, 10). However, little is known about potential targets for EGCG-induced inhibition in NPC cells.

SIRT1 is a prominent and extensively studied member of the sirtuins family of the mammalian class III histone deacetylases heavily implicated in healthspan and aging (11). The vast literature demonstrated that SIRT1 expression increased in most human cancers, especially, prostate cancer, primary colon cancer, acute myeloid leukemia, and squamous epithelial cell carcinoma (12). Studies have also reported that the expression levels of SIRT1 are linked with cancer invasion/metastasis and drug resistance, which in turn affect the prognosis of cancers (13). Recently, literature has focused that SIRT1 can promote the proliferation, migration, and lipid metabolism in NPC cells, suggesting that SIRT1 is an attractive target to treat NPCs (14). However, it is not known whether the SIRT1-dependent signaling pathway participates in the effect of EGCG on NPC cells. Therefore, this study aimed to investigate the effect of EGCG on the growth of NPC (CNE-2 and 5-8F) cell lines and determine whether the SIRT1 signaling is involved in this phenomenon or not.

REGENTS AND METHODS

Reagents

Human NPC cell lines (CNE-2 and 5-8F) were purchased from cell bank of the Chinese Academy of Sciences (Shanghai, China). RPMI 1,640 medium and fetal bovine serum (FBS) was purchased from Gibco (Logan, UT, USA). Rabbit anti-caspase 3 (#9,662), Rabbit anti-α-tubulin (#21,44S), Rabbit anti-Apaf-1 (#89,69S), Rabbit anti-caspase 9 (#95,08S), Rabbit anti-Acetyl-p53 (Lys382) (#25,25S), and Rabbit anti-SIRT1 (#2,493) were purchased from Cell Signaling Technology (Boston, MA, USA). EGCG (purity $> 95\%$) was purchased from Sigma Aldrich and dissolved in distilled water at 100 μM, and stored at −20°C until dilution before use. The cell counting kit 8 (CCK8) was purchased from DOJINDO (Japan). The terminal deoxynucleotidyl transferase (TDT)-mediated dUTP nick end labeling (TUNEL) assay kit was purchased from the Nanjing KeyGen Biotech Co., Ltd. (Nanjing, China). The BCA protein assay kit was purchased from Thermo Fisher Scientific (Chicago, IL). Super signal chemiluminescent substrate (ECL) was obtained from Thermo Scientific (Waltham, MA, USA).

Cell Culture

Cells (CNE-2 and 5-8F) were grown in RPMI-1640 culture medium supplemented with 10% FBS, 100 u/ml penicillin, and 100 mg/ml streptomycin at 37°C in humid incubator contains 95% air and 5% CO_2. The medium was changed every other day. When the culture reaches 70∼90% confluence, cells are subcultured at a split ratio of 1:3. Before treating with EGCG, cells were cultured in FBS-free for 12 h.

CCK-8 Analyses

Cells (CNE-2 and 5-8F) were seeded at 1×10^4/well in 96-well plates. After being cultured in a complete medium for 24 h, the cells changed to an FBS-free medium for another 12 h at 37°C. Then, the cells were treated with EGCG at the indicated concentration (0, 10, 20, and 40 μm) or with 40 μm after overexpression of SIRT1 for 24 h. A total of 10 μl of CCK-8 solution was added to each well and incubated for another 1 h, followed by reading the absorbance at 450 nm using a Multi-Volume Spectrophotometer system (BioTek Instruments, Inc., USA).

Real-Time PCR

Total RNA from CNE-2 cells was extracted with TRIzol. cDNA was generated using the PrimeScript^{TM} RT reagent kit (Takara Bio Inc., Japan). The mRNA expression levels were measured using a quantitative PCR Kit (Takara Biotechnology) by the iCycler iQ system (Bio-Rad). Amplification conditions were 15 min at 95°C, followed by 40 cycles of 30 s at 95°C, 1 min at 55°C, and 30 s at 72°C. Human-specific primers (**Supplementary Table S1**) for Bax, Bcl-2, and GAPDH were synthesized by Invitrogen. The GAPDH was used as endogenous control. Each PCR amplification was performed in triplicate.

TUNEL Assay

TUNEL analyses were performed as described previously (15). Cells were fixed with 4% formaldehyde in PBS at room temperature for 30 min. After two washes in PBS, the cells were permeabilized using 0.2% TritonX-100 in PBS for 5 min. Then, the cells were labeled with Biotinylated dUTP and TDT enzymes in a humidified box at 37°C for 1 h, followed by incubation with streptavidin-fluorescein for 30 min. Finally, cells were counterstained with 4',6-diamidino-2-phenylindole (DAPI) at room temperature for 10 min before observation under a microscope. Cells were only labeled as being TUNEL positive and expressed as a percentage of the total nuclei.

Western Blot Analysis

Western blot assays were performed as described previously (16). Total protein was exacted from CNE-2 or 5-8F cells using RIPA lysis buffer, and the protein concentration was evaluated using a BCA protein assay kit (Thermo Fisher Scientific). The same amount of protein (20 μg per lane) was separated by SDS-PAGE gel electrophoresis and then transferred to the PVDF membrane (Millipore). After blocking 5% nonfat milk, the membranes were incubated with primary antibodies overnight at 4°C. Next, membranes were incubated with appropriate horseradish peroxidase (HRP)-labeled second antibodies for 1 h at room temperature. At last, the blotted membranes were visualized by the enhanced chemiluminescent (ECL) method, and molecular band intensity was determined by densitometry. α-tubulin was used as endogenous control. The intensities of the blots were quantified by densitometry using the image lab analysis system and NIH image J software.

SIRT1 Histone Deacetylase Activity Assay

The histone deacetylase activity assay was performed as described previously (16). Total proteins, extracted from CNE-2 or 5-8F cells, were immunoprecipitated with anti-SIRT1 antibody and protein G agarose beads (Pierce). After incubation overnight at 4°C, the precipitates were transferred into a new tube. The reaction was carried out by mixing 15 μl of precipitates and 35 μl reaction mixture (20 μM fluorosubstrate peptide, 800 μM NAD, 0.25 mAU/ml lysylendopeptidase, 1 μm trichostatin A and 50 mM Tris-HCl) according to the manufacturer's instructions (CycLex, Ina). Then, the intensity of fluorescence was detected by microtiter plate fluorometer (excitation filter: 490 ± 10 nm, emission filter: 530 ± 15 nm) and normalized by the protein concentration.

Plasmid Transfection and RNA Interference

For SIRT1 overexpression and RNA interference, CNE-2 and 5-8F cell lines were transfected with flag-empty, flag-SIRT1, siSIRT1, and negative control siRNA, respectively, using Lipofectamine 2000 (Invitrogen) according to the procedure described in our previous study (17). At 48 h after transfection, real-time PCR, western blotting, and fluorometric assay kit were used to evaluate the transfection efficiency. A total of three different duplex siRNAs (**Supplementary Table S2**) for SIRT1 (siSIRT1-1, siSIRT1-2, and siSIRT1-3) and negative control siRNA were purchased from Genepharma (Shanghai, PR China).

Molecular Docking

According to a previous study, the molecular docking was carried out using Discovery Studio 3.1. The crystal structure of SIRT1 was obtained from the Protein Data Bank (PDB ID: 4KXQ). We first used the protein preparation wizard to deal with the protein structure and reassigned the bone orders. Then, we minimized the sampled hydrogens to fine tune the hydrogen-bonding network. Finally, a restrained minimization was conducted by applying the CHARMm force field. In addition, EGCG was processed through increasing explicit hydrogen atoms and using the CHARMm force field and geometry optimization with the prepared ligands module of Discovery Studio 3.1. The docking grid was generated with its center set to the native ligand, and the grid size was set similarly (the search grid of binding site was identified as center x: 32.225016, center y: −16.502403, and center z: 9.395139 with the radius of 10.297739). After completing the aforementioned preparatory work, EGCG was performed to docking at the extra precision (XP) level.

Statistical Analysis

Data are presented as mean ± standard error (SE). Statistical analyses between two groups were performed by unpaired Student's *t*-test. Differences among groups were tested by one-way ANOVA. In all the cases, differences were considered statistically significant with $P < 0.05$.

RESULTS

Effect of EGCG on Proliferation and Apoptosis of NPC Cell Lines

To investigate the effect of EGCG on the proliferation of NPC cell lines, CNE-2 and 5-8F cells were incubated with various concentrations of EGCG at different times. And the cell viability was assessed by CCK8 assay. As shown in **Figures 1A–D**, EGCG inhibited NPC cell lines (CNE-2 and 5-8F) viability in a dose- and time-dependent manner. We further tested the proliferation kinetics of NPC cells and showed that EGCG treatment could significantly inhibit cell proliferation in CNE-2 and 5-8F cell lines (**Figures 1E,F**). Then, we detected the effect of EGCG on the apoptosis of NPC cells. As shown in **Figures 1G–J**, EGCG-induced apoptosis in NPC cell lines. Meanwhile, EGCG caused caspase-3 cleavage (**Figures 2A–C**). Moreover, EGCG also resulted in a dose-dependent increase in the Bax/Bcl-2 ratio that favors apoptosis in NPC cell lines (CNE-2 and 5-8F) (**Figures 2D–I**).

Effect of EGCG on Expression and Activity of SIRT1 in NPC Cell Lines

Previous studies have demonstrated that SIRT1 activation promoted NPC cells' proliferation, migration, and lipid metabolism. It indicated that SIRT1 might participate in the effect of EGCG on NPC cell lines. To elucidate the potential molecular mechanisms of EGCG on NPC cells *in vitro*, we checked the protein level of SIRT1. As shown in **Figures 3A–D**, EGCG could inhibit the protein expression of SIRT1 in a time- and dose-dependent manner. Then, we further assessed the histone deacetylase activity of SIRT1 and found that EGCG inhibited the enzyme activity of SIRT1 in NPC cell lines (**Figures 3E–H**).

SIRT1 Participate in the Regulation of EGCG on Proliferation and Apoptosis in NPC Cell Lines

To examine the role of SIRT1 in EGCG-induced apoptosis, cells were transfected with SIRT1. Overexpression of SIRT1 significantly increased the expression and activity of SIRT1 in CNE-2 and 5-8F cells (**Supplementary Figure S1**). Then, we checked the cell viability and apoptosis in NPC cell lines. As shown in **Figures 4A–F**, EGCG treatment inhibited the proliferation and induced apoptosis in CNE-2 and 5-8F cells, which could be attenuated by preincubation with SIRT1 overexpression. Moreover, when SIRT1 was overexpressed, EGCG failed to increase the Bax/Bcl-2 ratio (**Figures 4G,H**) and caspase-3 cleavage (**Figures 4I,J**). Then, we tested the effect of SIRT1 siRNA interference on proliferation and apoptosis of NPC cells induced by EGCG. When the cells were transfected with siSIRT1, the expression and activity of SIRT1 were decreased significantly (**Supplementary Figure S2**). We further measured the cell viability and apoptosis in NPC cell lines. As shown in **Figure 5**, knockdown of SIRT1 aggravated the cell proliferation inhibition and apoptosis in NPC cell lines (**Figures 5A–F**), as

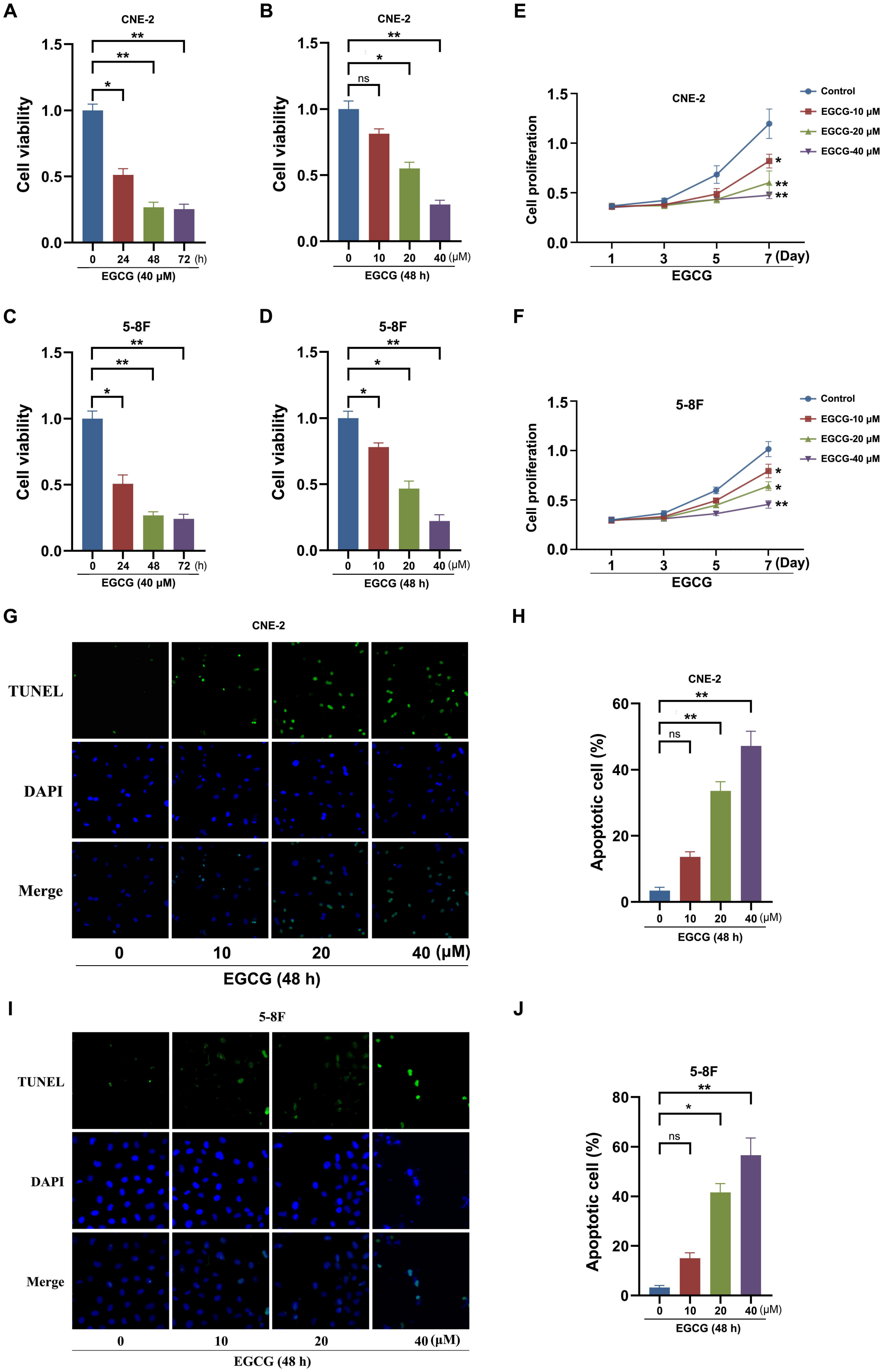

FIGURE 1 | Effect of EGCG on proliferation and apoptosis of NPC cell lines. CNE-2 and 5-8F cells were treated with various concentrations of EGCG for 48 h or with 40 μM EGCG for indicated time points. The cell viability **(A–D)** and proliferation kinetics **(E,F)** were detected by CCK8 assay. Cells were treated with various concentrations of EGCG for 48 h. **(G–J)** The cell apoptosis was detected by tunnel assay. *$P < 0.05$ and **$P < 0.01$ vs. the group without treatment, $n = 5$. ns = no significance which means no statistical difference.

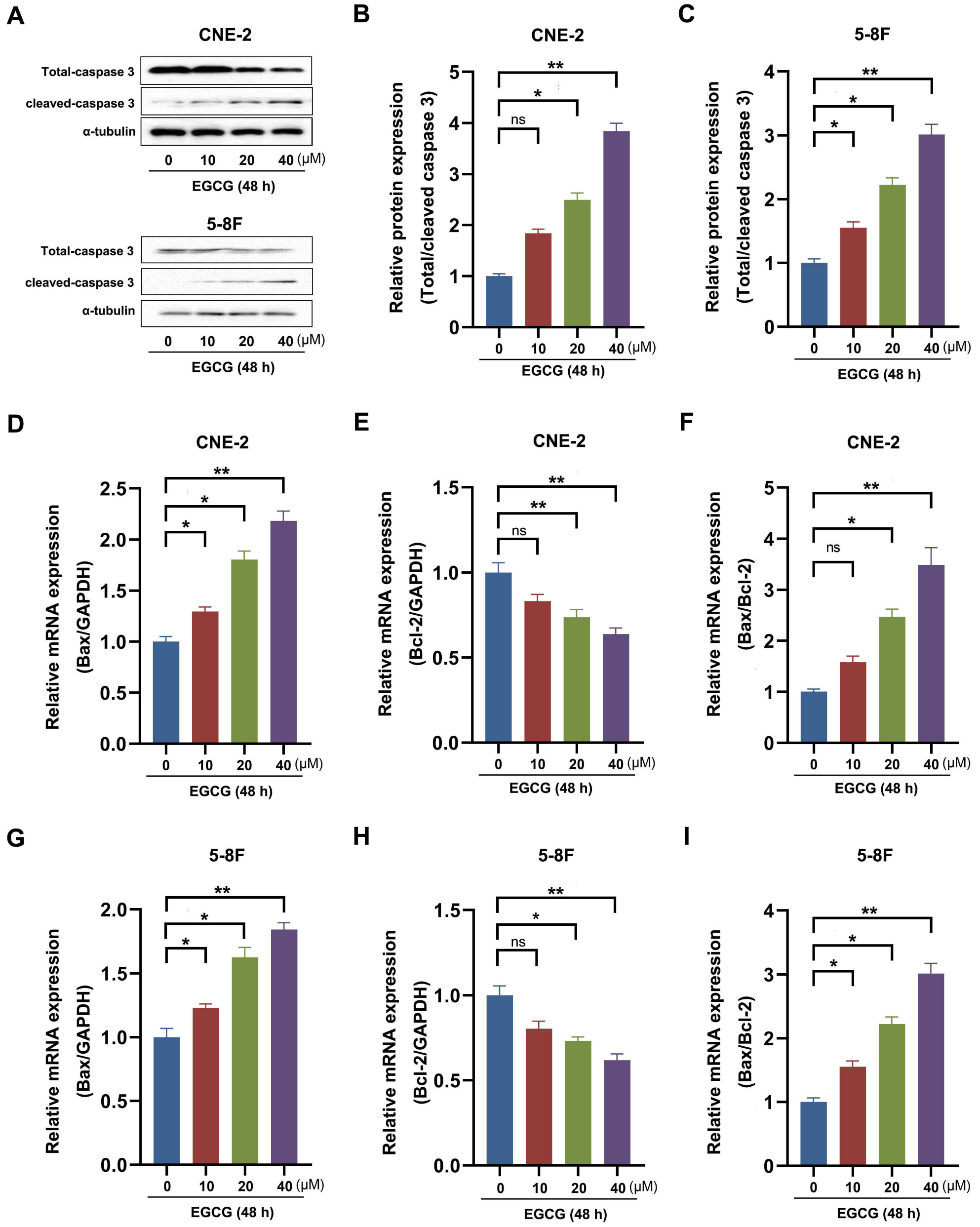

FIGURE 2 | Effect of EGCG on apoptosis-related genes expression in NPC cell lines. CNE-2 and 5-8F cells were treated with various concentrations of EGCG for 48 h. **(A–C)** The protein expression of caspase 3 was analyzed by Western Blotting. **(D–I)** The mRNA expression of Bax and Bcl-2 was determined by real-time PCR. $^*P < 0.05$ and $^{**}P < 0.01$ vs. the group without treatment, $n = 5$. ns = no significance which means no statistical difference.

well as the Bax/Bcl-2 ratio (**Figures 5G,H**) and caspase 3 cleavage (**Figures 5I,J**).

Effect of EGCG on p53-Dependent Apoptotic Pathways in NPC Cell Lines

Previous studies showed that SIRT1 might deacetylate p53, thereby inverting p53-mediated cell growth arrest and apoptosis in many cancer cells (18). So, the effect of EGCG on p53-dependent apoptotic pathways in the NPC cells was studied. As shown in **Figure 6**, EGCG treatment could significantly increase the protein expression of Ac-p53, Apaf-1, and cleaved-caspase 9, which could be attenuated by preincubation with SIRT1 overexpression. However, the knockdown of SIRT1 aggravated the level of these proteins in CNE-2 (**Figures 6A–D**) and 5-8F (**Figures 6E–H**) cells. These results suggested that SIRT1 may

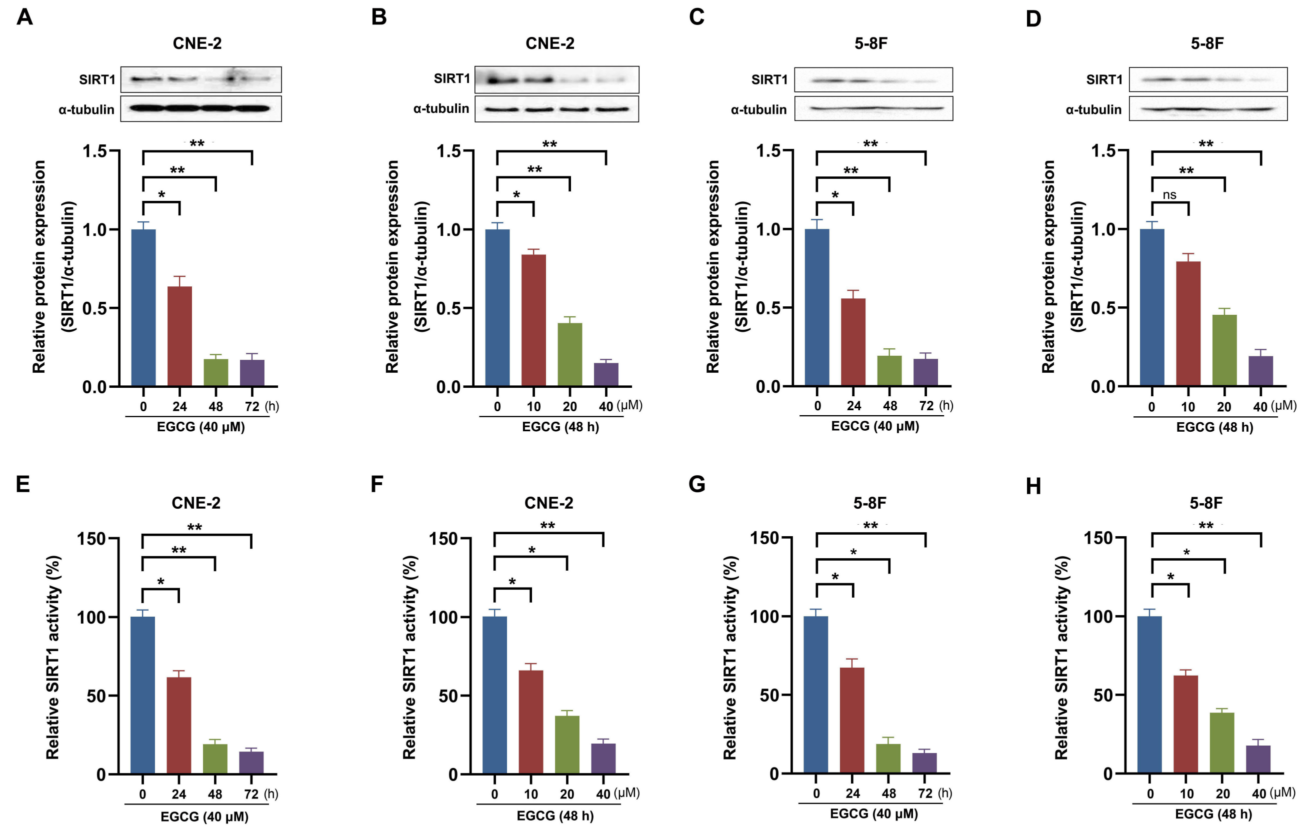

FIGURE 3 | Effect of EGCG on expression and activity of SIRT1 in NPC cell lines. CNE-2 and 5-8F cells were treated with various concentrations of EGCG for 48 h or with 40 μM EGCG for indicated time points. The protein expression **(A–D)** and deacetylase activity **(E–H)** of SIRT1 were detected by Western Blotting and deacetylase fluorometric assay kit, respectively. *$P < 0.05$ and **$P < 0.01$ vs. the group without treatment, $n = 5$. ns = no significance which means no statistical difference.

participate in the effect of EGCG on the protein expression of p53-dependent apoptotic pathways.

Molecular Docking Study Analyzed the Interaction Between EGCG With SIRT1

To investigate the mechanism by which EGCG-inhibited SIRT1, molecular docking was performed using Discovery Studio 3.1 software. We first obtained the SIRT1 crystal structures from the Protein Data Bank (PDB: 4KXQ) (**Figure 7A**). As shown in **Figure 7B,** the binging mode of EGCG and crystal structure of SIRT1 showed that EGCG enters the pocket of SIRT1 by seven hydrogen bonds, which turns out to be ARG-466 (1.9 Å), ASN-465 (2.4 Å), GLU-467 (2.3 Å), SER-442 (2.4 Å), SER-441 (1.9 Å), ARG-274 (1.8 Å), and GLY-263 (2.4 Å). ARG-274 and ARG-466 have been reported as the critical amino acids affecting SIRT1 activity, which suggested the regulatory effect of EGCG on the deacetylase activity of SIRT1 may be related to its interaction with SIRT1.

DISCUSSION

Nasopharyngeal carcinoma is the most prevalent malignant tumor in China, characterized by insidious location, lack of obvious early symptoms, and poor specificity (19–21). Currently, radiotherapy combined with chemotherapies is considered the standard treatment for NPCs (22). However, NPC patients often have a poor prognosis following treatment due to specific toxicities and drug resistance against chemotherapeutic drugs (23). Hence, it is urgent to exploit highly efficient and low-toxicity anticancer drugs combined with radiotherapy to improve the therapeutic effect of NPC.

Epidemiological studies have shown that the consumption of green tea is inversely associated with the incidence of certain cancers, and long-term consumption of green tea may reduce the risk of developing cancer and metastasis (24, 25). Green tea contains polyphenolic compounds, including flavanols, flavanonols, flavonoids, and phenolic acids accounting for almost 30% of the dry weight of green tea leaves. Most of the polyphenols in green tea are flavanols commonly known as catechins (26). EGCG, the major catechins in green tea, shows multiple biological activities such as antibacterial, antiviral, cardiovascular protection, and antiangiogenesis (7). Currently, the anti-cancer potential of EGCG has gained much attention on a global scale. Studies have shown that EGCG may intervene in the occurrence and development of cancers by inhibiting cell proliferation, inducing apoptosis, interference in cellular

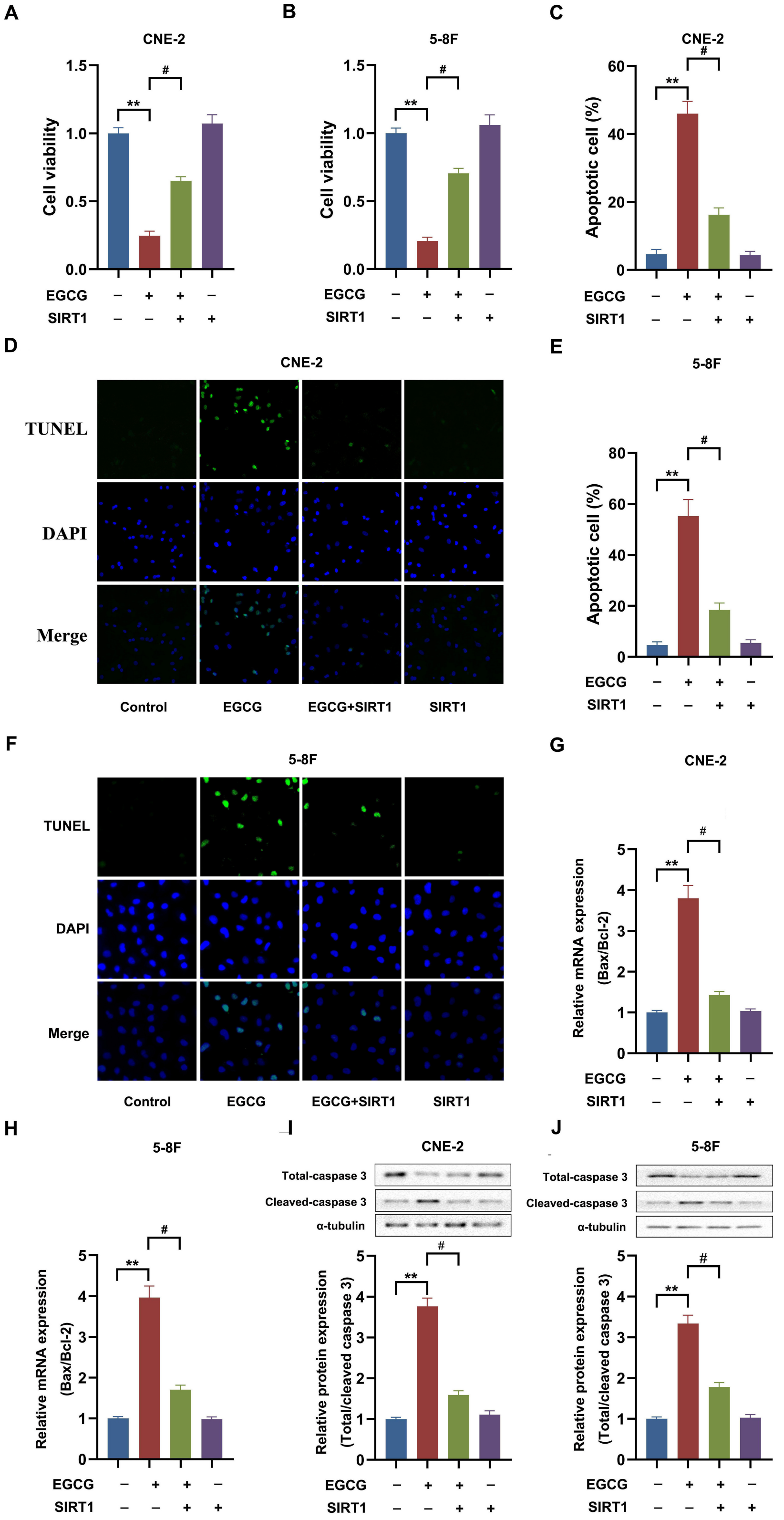

FIGURE 4 | SIRT1 overexpression ameliorated the effect of EGCG on proliferation and apoptosis in NPC cell lines. Cells transfected with or without SIRT1 were treated with 40 μM EGCG for 48 h. **(A,B)** The cell viability was detected by CCK8 assay. **(C–F)** The cell apoptosis was detected by tunnel assay. **(G,H)** The mRNA expression of Bax and Bcl-2 were determined by real-time PCR. **(I,J)** The protein expression of caspase 3 was analyzed by Western Blotting. $^{**}P < 0.01$ *vs.* the group without treatment, $^{\#}P < 0.05$ vs. the group without treatment with EGCG alone, $n = 5$.

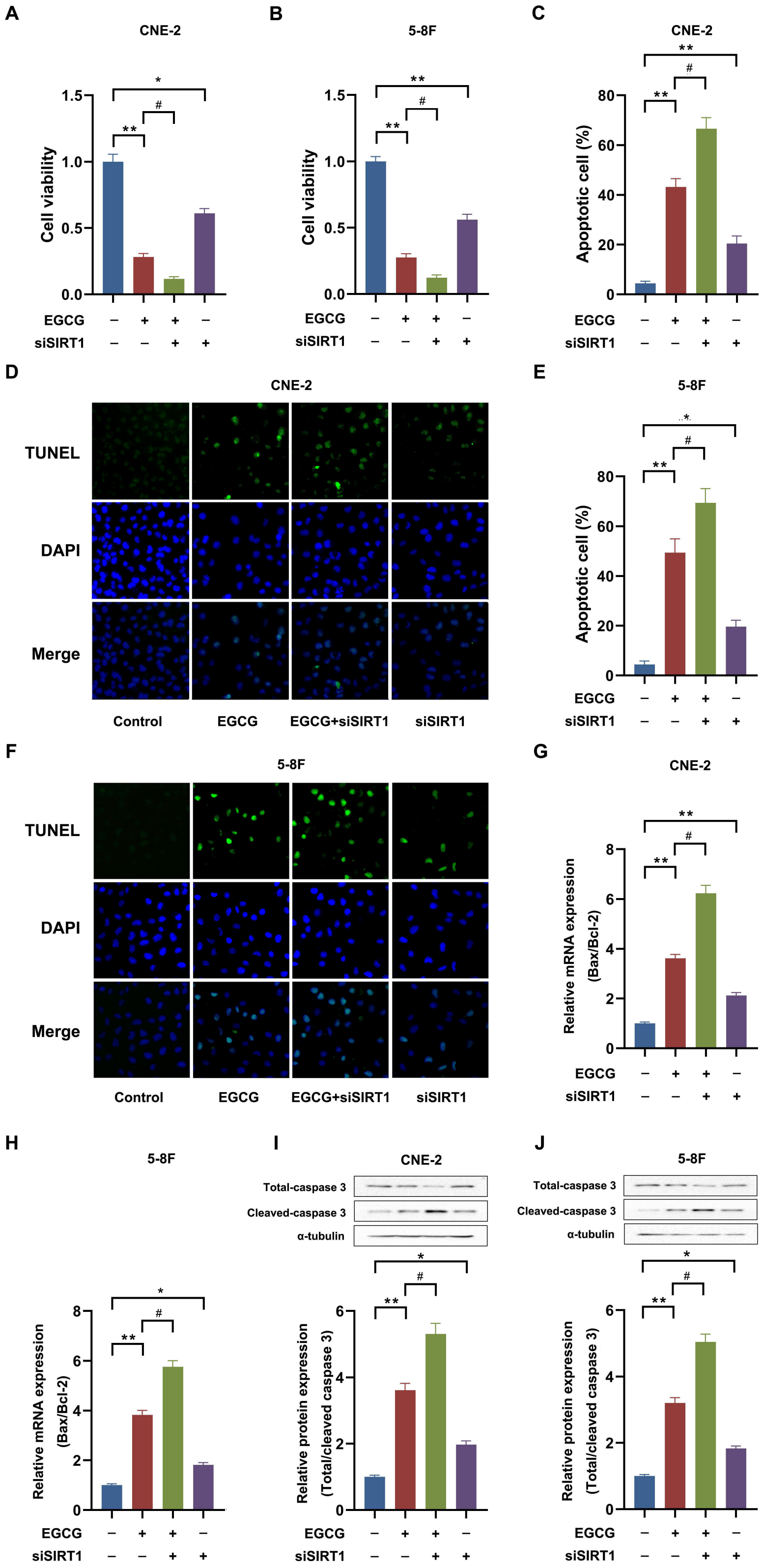

FIGURE 5 | SIRT1 knockdown aggregated the effect of EGCG on proliferation and apoptosis in NPC cell lines. Cells transfected with or without siSIRT1 were treated with 40 μM EGCG for 48 h. **(A,B)** The cell viability was detected by CCK8 assay. **(C–F)** The cell apoptosis was detected by tunnel assay. **(G,H)** The mRNA expression of Bax and Bcl-2 were determined by real-time PCR. **(I,J)** The protein expression of caspase 3 was analyzed by Western Blotting. $^*P < 0.05$ and $^{**}P < 0.01$ *vs.* the group without treatment, $^{\#}P < 0.05$ vs. the group without treatment with EGCG alone, $n = 5$.

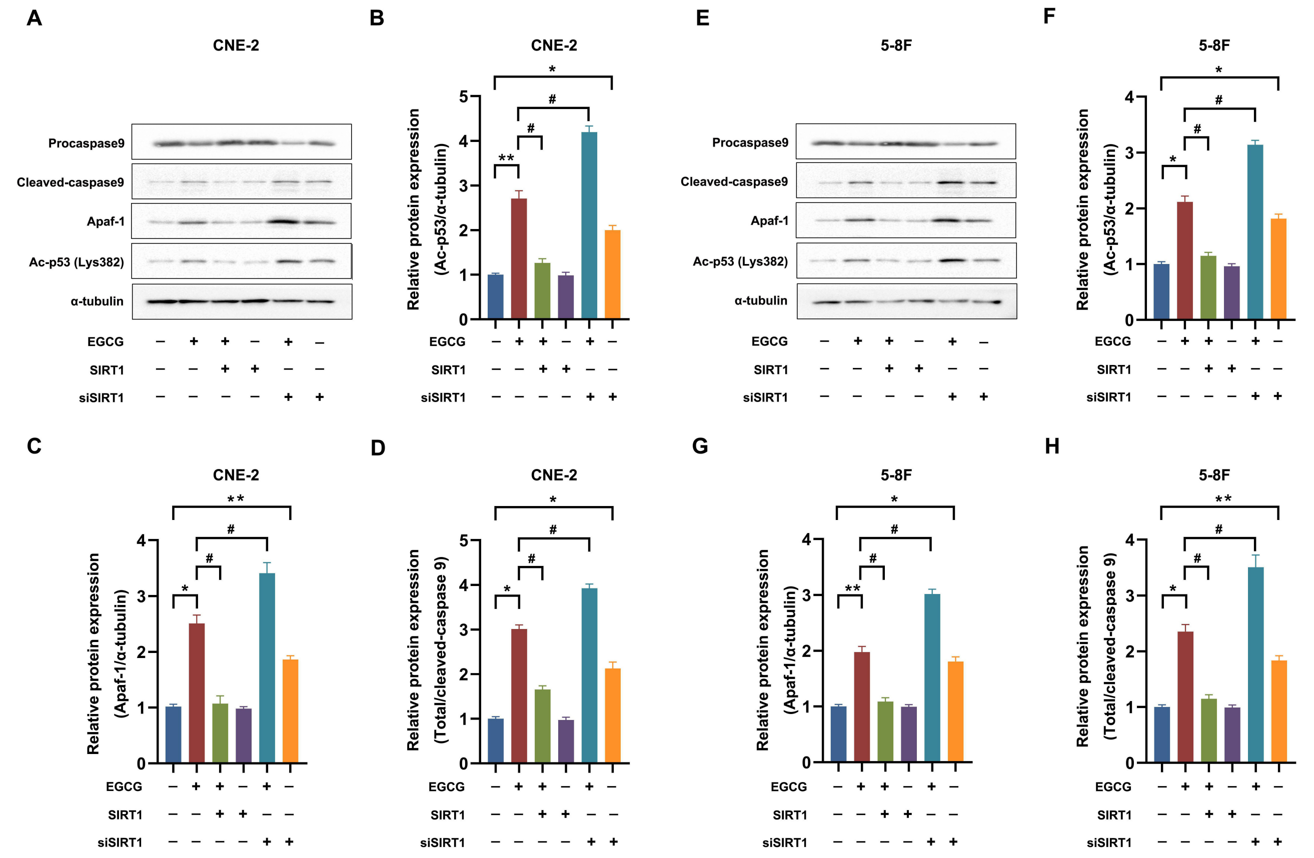

FIGURE 6 | Effect of EGCG on p53-dependent apoptotic pathways in NPC Cell Lines. Cells transfected with or without SIRT1/siSIRT1 were treated with 40 μM EGCG for 48 h. The protein expression of Ac-p53, Apaf-1, and caspase 9 was detected by Western Blotting in CNE-2 **(A–D)** and 5-8F **(E–H)** cell lines. *$P < 0.05$ and **$P < 0.01$ vs. the group without treatment, $^{\#}P < 0.05$ *vs.* the group without treatment with EGCG alone, $n = 5$.

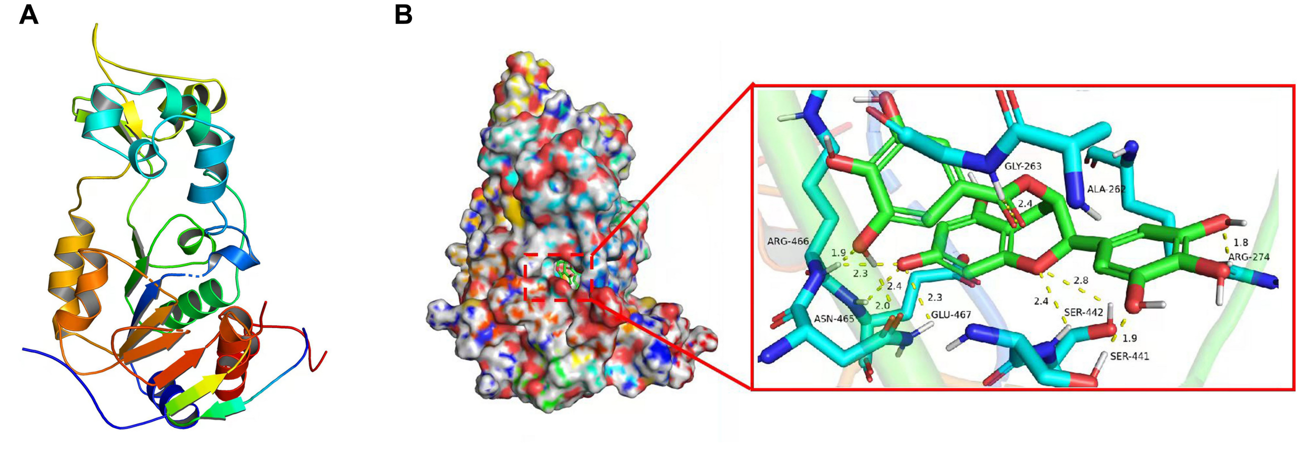

FIGURE 7 | EGCG was docked to the SIRT1 protein structure. **(A)** The protein structure of SIRT1. **(B)** Molecular docking between EGCG and SIRT1.

metabolism, inhibiting oncogene expression, and inhibiting tumor neovascularization (27). In a clinical study on subjects given EGCG at a single dose of 1,600 mg or 800 mg a day for 1 month, no obvious toxicity or side effects were seen except mild gastrointestinal reactions (28, 29). However, some animal studies reported the adverse effects linked with the consumption of high doses of EGCG. Moreover, an oral administration of 2,000 mg/kg, e.g., Teavigo, to rats resulted in about 80% mortalities, and histological analysis revealed hemorrhagic lesions in the stomach and intestine (30). In addition, high oral doses of EGCG (2,000 mg/kg) have also been reported to induce hepatotoxicity *in vivo* mice models (31). Despite this, the high doses of EGCG used in these articles have far exceeded the conventional doses used in animals and humans, suggesting the safety of EGCG. The EGCG significantly inhibited proliferation by inducing apoptosis in NPC cells. These results indicated that EGCG might be a potential chemotherapeutic agent for the treatment of NPCs. However, the exact molecular mechanism of EGCG-mediated inhibition of proliferation in NPC cells is not well elucidated.

A recent study has shown that EGCG could inhibit the proliferation of the nasopharyngeal CNE-1 cell line by inhibiting NF-κB nuclear translocation and EGFR phosphorylation (32). Moreover, EGCG has also been reported to inhibit the migration of the HONE-1 cell line by inhibiting the expression of MMP-2 (33). In addition, EGCG also inhibits NPC cells' invasion by regulating miRNA-296 (34). However, the mechanism of EGCG regulating the proliferation of NPC cells is still poorly known; hence, it is necessary to explore the precise molecular mechanism of EGCG inhibition of nasopharyngeal carcinoma cell growth. Sirtuins are a family of NAD^+-dependent deacetylases involved in the multiple biological processes, including cell survival, DNA damage/repair, life span, and aging (35). There are seven different sirtuins in mammals, namely, SIRT1-SIRT7 (36). Recently, the sirtuin family has attracted much attention in cancer research, as they play an essential role in the onset and progression of cancer (37). SIRT1, the most extensively characterized family member, has also been demonstrated to be involved in cancer progression (38, 39). However, SIRT1 can function as both a tumor promoter and tumor suppressor simultaneously, depending on the immediate microenvironment (40). On the one hand, SIRT1 inhibits tumor formation by inhibiting tumor promoters such as NF-κB and c-Myc (41, 42). Furthermore, SIRT1 may suppress tumor cell apoptosis by inhibiting tumor suppressor genes such as P53, FOXO1, and FOXO3 (43, 44). Among them, the first discovered non-histone target of SIRT1, the p53 is suggested to play a central role in SIRT1-mediated functions in tumorigenesis (18). SIRT1 physically interacts with p53 and deacetylates p53 K382, inhibiting p53 activity, thus enabling cells to bypass p53-mediated apoptosis help the cells survive (43). In both of the NPC (CNE-2 and 5-8F) cell lines, the expression of SIRT1 were significantly increased compared with normal nasopharyngeal epithelial cells NP69, and SIRT1 overexpression could promote the proliferation and migration of NPC cells (14). In addition, SIRT1 is a direct target of miR-34a, and overexpression of miR-34a could increase the radiotherapy sensitivity of nasopharyngeal CNE-1 cells by inhibiting SIRT1 (45). These results suggest that SIRT1 plays a vital role in the developing and progression of NPCs. However, whether EGCG inhibits NPC cells' proliferation by regulating SIRT1 has not been reported. Herein, it is demonstrated for the first time that EGCG could inhibit protein expression and enzyme activity of SIRT1 in CNE-2 and 5-8F cells in a dose-dependent manner. Further studies showed that SIRT1-p53 signaling participated in the effect of EGCG on NPC cells.

Although it was also found that EGCG induces apoptosis in NPC cells through SIRT1 inhibition, however, whether SIRT1 acts as an oncogene or tumor suppressor may depend on the stages of tumor development or upstream and downstream regulators. In some cases, whether activation of SIRT1 also could inhibit the growth of NPC cells is still worth exploring. Moreover, initially, the inhibitory effect of EGCG on SIRT1 was not specific and displayed different modalities of regulation in different cell lines. The research showed that EGCG inhibits homocysteine-induced oxidative damage in endothelial cells by activating the

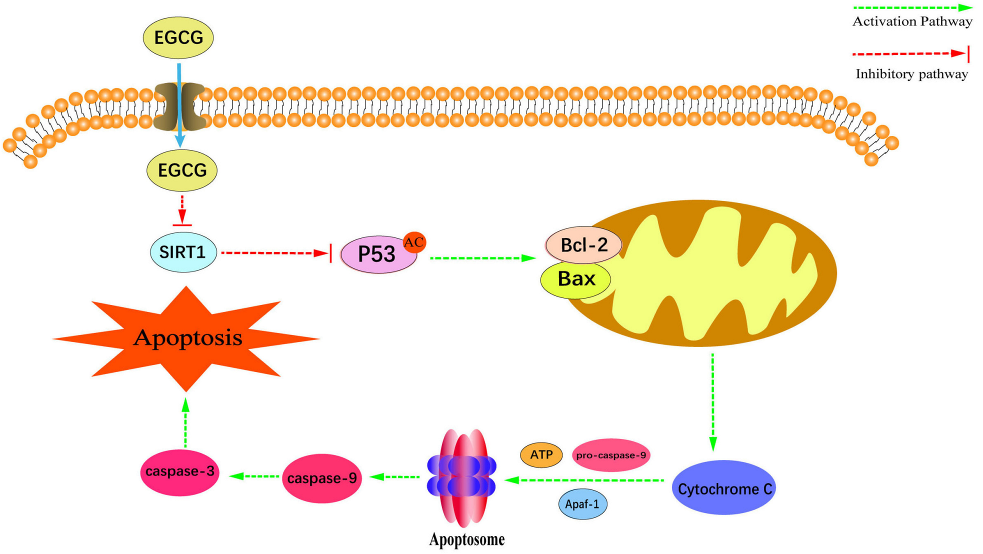

FIGURE 8 | Schematic diagram of the proposed mechanisms of EGCG-induced apoptosis and anti-proliferation in NPC cell lines.

SIRT1/AMPK pathway (46). The study also demonstrated that EGCG inhibits hepatic cholesterol synthesis by targeting SREBP-2 through modulation of the SIRT1/FOXO1 signaling pathway (47). Our previous work showed that EGCG inhibited the growth of H9C2 cardiomyocytes by suppressing the expression of SIRT1 (15). In this study, we are the pioneers to report that EGCG-induced apoptosis in nasopharyngeal carcinoma CNE-2 cells by inhibiting the expression and activity of SIRT1. In addition to SIRT1, EGCG also affected other Sirtuin family proteins. For example, previous EGCG could regulate senescence and anti-SASP *via* SIRT3 in 3T3-L1 Preadipocytes (48). Moreover, previously we reported that EGCG increased SIRT6 activity by affecting the level of NAD (16). The regulatory role of EGCG on other members of the Sirtuins family needs to be further investigated.

How does EGCG carry out its inhibitory regulatory role on the expression of SIRT1 or not? Following the literature, it is shown that the regulation mode of SIRT1 by EGCG remained variable in the different cell lines. It was demonstrated that EGCG could activate SIRT1 in endothelial cells (46), while our previous study also showed that EGCG could inhibit SIRT1 expression in H9C2 cardiomyocytes (15). This work demonstrated that EGCG inhibited proliferation and induced apoptosis in NPC CNE-2 cells by downregulating SIRT1. However, the specific molecular mechanism by which EGCG regulates SIRT1 expression in NPC cells is still unknown. To clarify the regulatory mechanism of EGCG on SIRT1, at first, the effect of EGCG on the mRNA expression of SIRT1 was examined, and no impact on the mRNA level of SIRT1 was observed, suggesting that EGCG does not inhibit the expression and activity of SIRT1 at the transcriptional level (**Supplementary Figure S3**). Therefore, the interaction between EGCG and SIRT1 using a molecular docking approach to clarify EGCG was the only molecule to bind directly to SIRT1 (**Figure 7**). However, the interaction between EGCG and SIRT1 needs to be further justified through surface plasmon resonance (SPR) methods. Moreover, whether the binding of EGCG to SIRT1 affects the expression and activity of SIRT1 needs to be further investigated.

In conclusion, this study has demonstrated for the first time that EGCG could activate the mitochondrial apoptotic pathway by inhibiting the SIRT1-p53 signaling pathway and finally inducing the apoptosis in human NPC cell lines (**Figure 8**). Our study further elucidated the critical role of SIRT1 in the occurrence and development of NPC, which provided the necessary experimental data and theoretical basis for the application of EGCG in the prevention and treatment of NPCs.

DATA AVAILABILITY STATEMENT

The original contributions presented in the study are included in the article/supplementary material, further inquiries can be directed to the corresponding authors.

AUTHOR CONTRIBUTIONS

SJ: investigation, data analysis, and writing—original draft. CH: investigation and writing—original draft. GZ, WY, BW, JT, and ML: resources and investigation. XL and BH: investigation. DW: data analysis. TY: funding acquisition, resources, and supervision. CW: writing—review and editing. YC: funding acquisition, conceptualization, supervision, resources, and writing—review and editing. All authors have read and agreed to the final manuscript draft.

FUNDING

This work was supported by grants from the National Natural Science Foundation of China (Nos. 31972889 and 81300085), the Natural Science of Guangdong Province (No. 2017A030313571), and the High-level University Construction Fund of Guangdong Province (Nos. 06-410-2107240 and 06-410-2107244).

ACKNOWLEDGMENTS

We thank Muhammad Farrukh Nisar (Cholistan University of Veterinary & Animal Sciences) for his linguistic assistance in preparing this manuscript.

SUPPLEMENTARY MATERIAL

The Supplementary Material for this article can be found online at: https://www.frontiersin.org/articles/10.3389/fnut.2022.851972/full#supplementary-material

REFERENCES

1. Nakanishi Y, Wakisaka N, Kondo S, Endo K, Sugimoto H, Hatano M, et al. Progression of understanding for the role of Epstein-Barr virus and management of nasopharyngeal carcinoma. *Cancer Metastasis Rev.* (2017) 36:435–47. doi: 10.1007/s10555-017-9693-x
2. Wu L, Li C, Pan L. Nasopharyngeal carcinoma: a review of current updates. *Exp Ther Med.* (2018) 15:3687–92. doi: 10.3892/etm.2018.5878
3. Zhu J, Duan B, Shi H, Li Y, Ai P, Tian J, et al. Comparison of GP and TPF induction chemotherapy for locally advanced nasopharyngeal carcinoma. *Oral Oncol.* (2019) 97:37–43. doi: 10.1016/j.oraloncology.2019.08.001
4. Ke LR, Xia WX, Qiu WZ, Huang XJ Yu YH, Liang H, et al. A phase II trial of induction NAB-paclitaxel and cisplatin followed by concurrent chemoradiotherapy in patients with locally advanced nasopharyngeal carcinoma. *Oral Oncol.* (2017) 70:7–13. doi: 10.1016/j.oraloncology.2017.04.018
5. Sibley CH. Infectious diseases. Understanding artemisinin resistance. *Science.* (2015) 347:373–4. doi: 10.1126/science.aaa4102
6. Romano A, Martel F. The Role of EGCG in Breast Cancer Prevention and Therapy. *Mini Rev Med Chem.* (2021) 21:883–98. doi: 10.2174/1389557520999201211194445
7. Chakrawarti L, Agrawal R, Dang S, Gupta S, Gabrani R. Therapeutic effects of EGCG: a patent review. *Expert Opin Ther Pat.* (2016) 26:907–16. doi: 10.1080/13543776.2016.1203419
8. Negri A, Naponelli V, Rizzi F, Bettuzzi S. Molecular Targets of Epigallocatechin-Gallate (EGCG): a Special Focus on Signal Transduction and Cancer. *Nutrients.* (2018) 10:1936. doi: 10.3390/nu10121936

9. Fang CY, Wu CC, Hsu HY, Chuang HY, Huang SY, Tsai CH, et al. EGCG inhibits proliferation, invasiveness and tumor growth by up-regulation of adhesion molecules, suppression of gelatinases activity, and induction of apoptosis in nasopharyngeal carcinoma cells. *Int J Mol Sci.* (2015) 16:2530–58. doi: 10.3390/ijms16022530
10. Chen J, Zhang F, Ren X, Wang Y, Huang W, Zhang J, et al. Targeting fatty acid synthase sensitizes human nasopharyngeal carcinoma cells to radiation via downregulating frizzled class receptor 10. *Cancer Biol Med.* (2020) 17:740–52. doi: 10.20892/j.issn.2095-3941.2020.0219
11. Tang BL. Sirt1 and the Mitochondria. *Mol Cells.* (2016) 39:87–95. doi: 10.14348/molcells.2016.2318
12. Lin Z, Fang D. The Roles of SIRT1 in Cancer. *Genes Cancer.* (2013) 4:97–104. doi: 10.1177/1947601912475079
13. Wang Z, Chen W. Emerging Roles of SIRT1 in Cancer Drug Resistance. *Genes Cancer.* (2013) 4:82–90. doi: 10.1177/1947601912473826
14. Yin HM, He X, Shan Y, Zhai HX, Zhang KW, Xia T, et al. Research of SIRT1 on promoting the proliferation, migration and lipid metabolism of nasopharyngeal carcinoma. *Zhonghua Er Bi Yan Hou Tou Jing Wai Ke Za Zhi.* (2020) 55:934–43. doi: 10.3760/cma.j.cn115330-20200727-00626
15. Cai Y, Zhao L, Qin Y, He Y. High dose of epigallocatechin-3-gallate inhibits proliferation and induces apoptosis of H9C2 cardiomyocytes through down-regulation of SIRT1. *Pharmazie.* (2015) 70:12–6. doi: 10.1691/ph.2015.4717
16. Cai Y, Yu SS, He Y, Bi XY, Gao S, Yan TD, et al. EGCG inhibits pressure overload-induced cardiac hypertrophy via the PSMB5/Nmnat2/SIRT6-dependent signalling pathways. *Acta Physiol (Oxf).* (2021) 231:e13602. doi: 10.1111/apha.13602
17. Cai Y, Yu SS, Chen SR, Pi RB, Gao S, Li H, et al. Nmnat2 protects cardiomyocytes from hypertrophy via activation of SIRT6. *FEBS Lett.* (2012) 586:866–74. doi: 10.1016/j.febslet.2012.02.014
18. Yi J, Luo J. SIRT1 and p53, effect on cancer, senescence and beyond. *Biochim Biophys Acta.* (2010) 1804:1684–9. doi: 10.1016/j.bbapap.2010.05.002
19. Lee AW, Sze WM, Au JS, Leung SF, Leung TW, Chua DT, et al. Treatment results for nasopharyngeal carcinoma in the modern era: the Hong Kong experience. *Int J Radiat Oncol Biol Phys.* (2005) 61:1107–16. doi: 10.1016/j.ijrobp.2004.07.702
20. Shi L, Xiao R, Wang M, Zhang M, Weng N, Zhao X, et al. MicroRNA3423p suppresses proliferation and invasion of nasopharyngeal carcinoma cells by directly targeting Cdc42. *Oncol Rep.* (2018) 40:2750–7. doi: 10.3892/or.2018.6642
21. Torre LA, Bray F, Siegel RL, Ferlay J, Lortet-Tieulent J, Jemal A. Global cancer statistics, 2012. *CA Cancer J Clin.* (2015) 65:87–108. doi: 10.3322/caac.21262
22. Wei Z, Zhang Z, Luo J, Li N, Peng X. Induction chemotherapy plus IMRT alone versus induction chemotherapy plus IMRT-based concurrent chemoradiotherapy in locoregionally advanced nasopharyngeal carcinoma: a retrospective cohort study. *J Cancer Res Clin Oncol.* (2019) 145:1857–64. doi: 10.1007/s00432-019-02925-z
23. Lee AW, Ma BB, Ng WT, Chan AT. Management of Nasopharyngeal Carcinoma: Current Practice and Future Perspective. *J Clin Oncol.* (2015) 33:3356–64. doi: 10.1200/JCO.2015.60.9347
24. Yang CS, Wang X, Lu G, Picinich SC. Cancer prevention by tea: animal studies, molecular mechanisms and human relevance. *Nat Rev Cancer.* (2009) 9:429–39. doi: 10.1038/nrc2641
25. Yuan JM, Sun C, Butler LM. Tea and cancer prevention: epidemiological studies. *Pharmacol Res.* (2011) 64:123–35. doi: 10.1016/j.phrs.2011.03.002
26. Yan Z, Zhong Y, Duan Y, Chen Q, Li F. Antioxidant mechanism of tea polyphenols and its impact on health benefits. *Anim Nutr.* (2020) 6:115–23. doi: 10.1016/j.aninu.2020.01.001
27. Wang YQ, Lu JL, Liang YR, Li QS. Suppressive Effects of EGCG on Cervical Cancer. *Molecules.* (2018) 23:2334. doi: 10.3390/molecules23092334
28. Ullmann U, Haller J, Decourt JP, Girault N, Girault J, Richard-Caudron AS, et al. A single ascending dose study of epigallocatechin gallate in healthy volunteers. *J Int Med Res.* (2003) 31:88–101. doi: 10.1177/147323000303100205
29. Chow HH, Cai Y, Hakim IA, Crowell JA, Shahi F, Brooks CA, et al. Pharmacokinetics and safety of green tea polyphenols after multiple-dose administration of epigallocatechin gallate and polyphenon E in healthy individuals. *Clin Cancer Res.* (2003) 9:3312–9.
30. Isbrucker RA, Edwards JA, Wolz E, Davidovich A, Bausch J. Safety studies on epigallocatechin gallate (EGCG) preparations. Part 2: dermal, acute and short-term toxicity studies. *Food Chem Toxicol.* (2006) 44:636–50. doi: 10.1016/j.fct.2005.11.003
31. Lambert JD, Kennett MJ, Sang S, Reuhl KR, Ju J, Yang CS. Hepatotoxicity of high oral dose (-)-epigallocatechin-3-gallate in mice. *Food Chem Toxicol.* (2010) 48:409–16. doi: 10.1016/j.fct.2009.10.030
32. Yan Z, Yong-Guang T, Fei-Jun L, Fa-Qing T, Min T, Ya C. Interference effect of epigallocatechin-3-gallate on targets of nuclear factor kappaB signal transduction pathways activated by EB virus encoded latent membrane protein 1. *Int J Biochem Cell Biol.* (2004) 36:1473–81. doi: 10.1016/j.biocel.2003.10.024
33. Ho HC, Huang CC, Lu YT, Yeh CM, Ho YT, Yang SF, et al. Epigallocatechin-3-gallate inhibits migration of human nasopharyngeal carcinoma cells by repressing MMP-2 expression. *J Cell Physiol.* (2019) 234:20915–24. doi: 10.1002/jcp.28696
34. Lin CH, Wang HH, Chen TH, Chiang MC, Hung PH, Chen YJ. Involvement of MicroRNA-296 in the Inhibitory Effect of Epigallocatechin Gallate against the Migratory Properties of Anoikis-Resistant Nasopharyngeal Carcinoma Cells. *Cancers (Basel).* (2020) 12:973. doi: 10.3390/cancers12040973
35. Zhang GZ, Deng YJ, Xie QQ, Ren EH, Ma ZJ, He XG, et al. Sirtuins and intervertebral disc degeneration: Roles in inflammation, oxidative stress, and mitochondrial function. *Clin Chim Acta.* (2020) 508:33–42. doi: 10.1016/j.cca.2020.04.016
36. Mei Z, Zhang X, Yi J, Huang J, He J, Tao Y. Sirtuins in metabolism, DNA repair and cancer. *J Exp Clin Cancer Res.* (2016) 35:182. doi: 10.1186/s13046-016-0461-5
37. Edatt L, Poyyakkara A, Raji GR, Ramachandran V, Shankar SS, Kumar VBS. Role of Sirtuins in Tumor Angiogenesis. *Front Oncol.* (2019) 9:1516. doi: 10.3389/fonc.2019.01516
38. Choupani J, Mansoori Derakhshan S, Bayat S, Alivand MR, Shekari Khaniani M. Narrower insight to SIRT1 role in cancer: a potential therapeutic target to control epithelial-mesenchymal transition in cancer cells. *J Cell Physiol.* (2018) 233:4443–57. doi: 10.1002/jcp.26302
39. Jiao F, Gong Z. The Beneficial Roles of SIRT1 in Neuroinflammation-Related Diseases. *Oxid Med Cell Longev.* (2020) 2020:6782872. doi: 10.1155/2020/6782872
40. Alves-Fernandes DK, Jasiulionis MG. The Role of SIRT1 on DNA Damage Response and Epigenetic Alterations in Cancer. *Int J Mol Sci.* (2019) 20:3153. doi: 10.3390/ijms20133153
41. Brandl L, Kirstein N, Neumann J, Sendelhofert A, Vieth M, Kirchner T, et al. The c-MYC/NAMPT/SIRT1 feedback loop is activated in early classical and serrated route colorectal cancer and represents a therapeutic target. *Med Oncol.* (2018) 36:5. doi: 10.1007/s12032-018-1225-1
42. Yang Q, Wang B, Gao W, Huang SY, Liu ZF, Li WJ, et al. SIRT1 Is Downregulated in Gastric Cancer and Leads to G(1)-phase Arrest via NF-kappa B/Cyclin D1 Signaling. *Mol Cancer Res.* (2013) 11:1497–507. doi: 10.1158/1541-7786.MCR-13-0214
43. Ong ALC, Ramasamy TS. Role of Sirtuin1-p53 regulatory axis in aging, cancer and cellular reprogramming. *Ageing Res Rev.* (2018) 43:64–80. doi: 10.1016/j.arr.2018.02.004
44. Yang H, Bi Y, Xue L, Wang J, Lu Y, Zhang Z, et al. Multifaceted Modulation of SIRT1 in Cancer and Inflammation. *Crit Rev Oncog.* (2015) 20:49–64. doi: 10.1615/CritRevOncog.2014012374
45. Liu Y, Li Q, Liang H, Xiang M, Tang D, Huang M, et al. MiR-34a Regulates Nasopharyngeal Carcinoma Radiosensitivity by Targeting SIRT1. *Technol Cancer Res Treat.* (2020) 19:1–10. doi: 10.1177/1533033820940424
46. Pai PY, Chou WC, Chan SH, Wu SY, Chen HI, Li CW, et al. Epigallocatechin Gallate Reduces Homocysteine-Caused Oxidative Damages through Modulation SIRT1/AMPK Pathway in Endothelial Cells. *Am J Chin Med.* (2021) 49:113–29. doi: 10.1142/S0192415X21500063
47. Li Y, Wu S. Epigallocatechin gallate suppresses hepatic cholesterol synthesis by targeting SREBP-2 through SIRT1/FOXO1 signaling pathway. *Mol Cell Biochem.* (2018) 448:175–85. doi: 10.1007/s11010-018-3324-x
48. Lilja S, Oldenburg J, Pointner A, Dewald L, Lerch M, Hippe B, et al. Epigallocatechin Gallate Effectively Affects Senescence and Anti-SASP via SIRT3 in 3T3-L1 Preadipocytes in Comparison with Other Bioactive Substances. *Oxid Med Cell Longev.* (2020) 2020:4793125. doi: 10.1155/2020/4793125

Conflict of Interest: The authors declare that the research was conducted in the absence of any commercial or financial relationships that could be construed as a potential conflict of interest.

frontiers | Frontiers in Nutrition

ORIGINAL RESEARCH
published: 27 April 2022
doi: 10.3389/fnut.2022.865070

Studies on Bioactive Components of Red Ginseng by UHPLC-MS and Its Effect on Lipid Metabolism of Type 2 Diabetes Mellitus

*Rensong Huang, Meng Zhang, Yu Tong, Yaran Teng, Hui Li and Wei Wu**

Changchun University of Chinese Medicine, Jilin Ginseng Academy, Changchun, China

Objectives: Red ginseng is a processed product of *Panax ginseng* C.A. Meyer, which is one of the widely used medicinal and edible herbs for the treatment of type 2 diabetes mellitus (T2DM). Ginsenosides are its main pharmacologically active ingredient. This study aims to clarify the material basis of total ginsenosides of red ginseng (RGW) and verify the activity of RGW in treating lipid metabolism disorders caused by T2DM.

Methods: An ultrahigh performance liquid chromatography coupled with quadrupole time of flight mass spectrometry (UHPLC-Q-TOF-MS) technology was applied to quantitatively analyze RGW. A T2DM rat model was established to verify the activity of RGW in treating lipid metabolism disorders caused by diabetes. First, the changes in diabetes-related parameters were observed, then the biochemical parameters of the rat serum and liver were measured, and finally, the pathological sections of the rat liver were observed, and the content of short-chain fatty acids in stools was measured. The *in vitro* activity of RGW was verified by fatty degenerated HepG2 cells.

Results: A total of 10 ginsenosides were identified and quantitatively analyzed in RGW. Experimental results demonstrated that RGW can improve lipid metabolism disorders. RGW significantly reduced the fasting blood glucose and TG and TC levels in T2DM rats, and hepatic steatosis was significantly ameliorated. *In vitro* experiments by RGW treatment also significantly attenuated lipid deposition in HepG2 cells. RGW upregulated the content of 5 short-chain fatty acids in rat stools, which are related to lipid oxidation and liver gluconeogenesis.

Conclusion: The total RGW were quantitatively analyzed by UHPLC-MS, and its effect on lipid metabolism of T2DM was studied. The experiment demonstrated that red ginseng can regulate lipid metabolism and improve lipid deposition, which provides a promising development for red ginseng as a functional food.

Keywords: red ginseng, UHPLC-MS, type 2 diabetes mellitus, lipid metabolism, short-chain fatty acids

Edited by:
Mingquan Guo,
Wuhan Botanical Garden (CAS),
China

Reviewed by:
Na Li,
Macau University of Science
and Technology, Macao SAR, China
Guilin Chen,
Wuhan Botanical Garden (CAS),
China

****Correspondence:***
Wei Wu
weiwu_ccucm@126.com

Specialty section:
This article was submitted to
Food Chemistry,
a section of the journal
Frontiers in Nutrition

Received: *29 January 2022*
Accepted: *25 March 2022*
Published: *27 April 2022*

Citation:
Huang R, Zhang M, Tong Y,
Teng Y, Li H and Wu W (2022) Studies
on Bioactive Components of Red
Ginseng by UHPLC-MS and Its Effect
on Lipid Metabolism of Type 2
Diabetes Mellitus.
Front. Nutr. 9:865070.
doi: 10.3389/fnut.2022.865070

INTRODUCTION

Panax ginseng C.A. Meyer was used as an herbal or tonic food in Eastern Asia for a long time (1), and recently, was approved by the Ministry of Health of the People's Republic of China as a new food resource that can be used in the healthcare sector. Several studies have been conducted to elucidate its bioactive components as well as its pharmacological actions, considering its health-related benefits in daily life as a nutritional product. Specifically, red ginseng (Ginseng Radix et Rhizoma Rubra; RG), which has a "warming effect" and is used in Chinese medicine to "boost yang" and replenish vital essence, is a thermally processed ginseng product that is obtained by steaming fresh ginseng at a certain temperature followed by drying (2). Furthermore, RG extract is widely used in healthcare (3), and its current product forms primarily include natural roots, powder, tablets, tea, extracts, and beverages. Furthermore, the biotransformation and health benefits of ginseng and RGW, and their application in dairy products have also been reported (4). In particular, lactic acid bacteria-fermented RG, with lipid-lowering activity, has been used as a health food in China. It has also been observed that RG contains high amounts of ginsenosides, which are bioactive components with various pharmacological effects. Furthermore, studies involving diabetic animal models and cells have shown that ginsenosides exert antidiabetic effects by regulating the production and secretion of insulin and improving glucose and lipid metabolism as well as inflammation (5). Using LC-MS, ginsenosides have been identified from ginseng and its related processed products such as protopanaxatriol (PPT), protopanaxadiol (PPD), and oleanolic acid based on the structure of the aglycone skeleton (6). Additionally, these ginsenosides show a wide range of biological activities owing to their species diversity and different chemical structures. Thus, to ensure the quality, safety, and efficacy of ginseng and related products, it is often necessary to monitor the constituent active ingredients. In this regard, LC-MS/MS analysis techniques are of great significance. Studies with a focus on the overall as well as the multi-target effects of ginseng have also been conducted by monitoring the multiple bioactive components of ginseng (7, 8), and LC-MS/MS has also been successfully applied in the identification of ginsenosides in ginseng, white ginseng, and RGW extracts (9). In a previous study, non-targeted metabolomics based on UPLC-MS/MS was developed to elucidate the different mechanisms of action of American ginseng traits in human systems (10).

Type 2 diabetes mellitus, which induces a continuous increase in blood glucose levels and increases the risks associated with different syndromes (e.g., diabetic nephropathy, diabetic eye disease, and diabetic cardiomyopathy), is a chronic metabolic disease that is mainly caused by insufficient insulin secretion or insulin resistance (11, 12). In addition to abnormal glucose metabolism, McGarry reported that lipid metabolism disorders also play an important role in the development of T2DM metabolic disorders (13). Specifically, lipid metabolism disorders, which have an important relationship with various major diseases in the human body, represent one of the main classes of clinical manifestations of T2DM (14). Reportedly, obesity is a trigger for insulin resistance. This is because excessive fat accumulation can lead to abnormal glucose metabolism, which can then impair the metabolic functioning of multiple organs, including adipose tissue and the surrounding organs, thereby aggravating the disease (15). Excessive fat accumulation will also lead to abnormal changes in lipid-related biochemical indicators such as triglyceride (TG) and total cholesterol (TC). Therefore, regulating

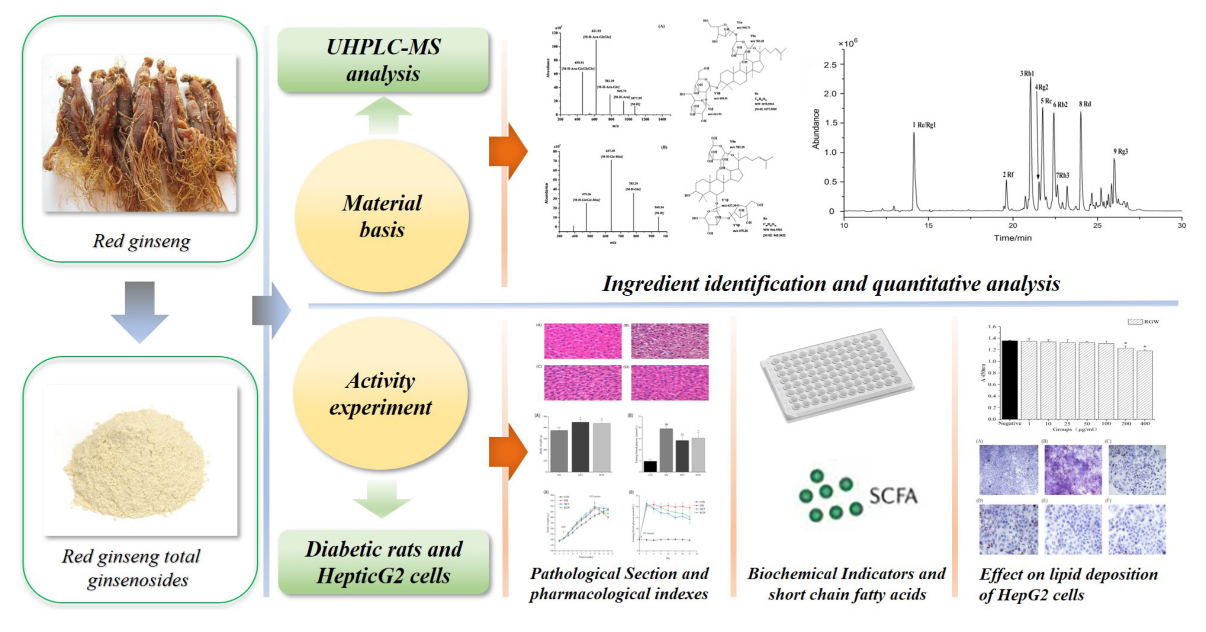

GRAPHICAL ABSTRACT | Studies on bioactive components of red ginseng by UHPLC-MS and its effect on lipid metabolism of type 2 diabetes mellitus.

lipid metabolic disorders is of great practical significance in the prevention and treatment of T2DM. Currently, the main drugs for T2DM treatment are insulin and oral hypoglycemic agents (16, 17). They have potential side effects (18, 19). Thus, the use of natural products as alternative anti-T2DM agents has attracted extensive attention over the years. Some natural products, such as ginsenosides, have been studied for their hypoglycemic activity and effects on the treatment of diabetes (20–22). In particular, ginsenoside Rg1 protects mice against streptozotocin (STZ)-induced type 1 diabetes by modulating the NLRP3 and Keap1/Nrf2/HO-1 pathways (23). Furthermore, ginsenoside Rk3 ameliorates insulin resistance, prevents inflammation, and improves lipid accumulation and gluconeogenesis in HFD/STZ-induced T2DM mice *via* the AMPK/Akt signaling pathway (24), and ginsenoside Re can reduce blood glucose levels, increase insulin levels, improve lipid metabolism, and reduce endothelial cell dysfunction by modulating the p38 MAPK, ERK1/2, and JNK signaling pathways to produce antidiabetic effects (25). Furthermore, ginsenoside Rg3 administered before islet transplantation enhances islet cell function and attenuates cytokine-induced injury (26). Previous studies have also shown that ginsenoside Rg2 treatment can significantly reduce TG and TC levels in oleic acid and palmitic acid (OA&PA)-induced mouse primary hepatocytes, and this was also confirmed by Oil Red O staining (27). The current studies on the pharmacological activities of ginsenosides mostly focus on monomer compounds, thus, exploring the antidiabetic activity of the ginsenosides in RGW for multiple target functions can be of great significance. Studies have also shown that short-chain fatty acids (SCFAs) are closely related to diabetes in that they improve insulin resistance and pancreatic damage while attenuating the inflammatory responses caused by diabetes (28). At the same time, it can also increase the expression of G protein-coupled receptor 43 mRNA in the colon and increase the levels of hormones GLP-1 and Peptide YY, thereby repairing glucose intolerance in type 2 diabetic mice (29).

In this study, in the first place, UHPLC-Q-TOF-MS was used to quantitatively analyze the total ginsenosides in RG (RGW) for quality control. Furthermore, the effects of RGW on lipid metabolism disorders caused by T2DM from three aspects were comprehensively studied: *in vivo*, *in vitro*, and metabolites. Specifically, a T2DM rat model was established to verify the ability of RGW to treat lipid metabolism disorders caused by diabetes. Thereafter, diabetes-related parameters of rats were studied, and biochemical indicators in rat serum, as well as hepatic and short-chain fatty acid contents in stool samples from the rats, were measured. *In vitro* experiments were also performed using fatty degenerated HepG2 cells to verify the activity of RGW, and pathological sections of the liver were also observed.

MATERIALS AND METHODS

Plant Material and Reagents

The *P. ginseng* used in this study was purchased from Ji An (Jilin, China) in June 2020 and was processed at our laboratory to obtain RG. The preparation method for RG was as follows: cleaned fresh ginseng was placed in a steaming box, the temperature was increased to 100°C within 60 min, and steaming was continued for 3 h; then, the ginseng sample was cooled and taken out. The steamed ginseng samples were dried in an oven at 50°C to obtain RG. Botanical identification was undertaken by Professor L. Jiao, and the voucher specimen (No. 20200005) was kept at the Jilin Ginseng Academy, Changchun University of Chinese Medicine, China.

The red ginseng was soaked overnight in a given volume of distilled water. Eight times the volume of distilled water was added, and the extraction was performed four times at 80°C for 1 h. The extracts obtained were combined and centrifuged. The resulting supernatant was then concentrated to the appropriate volume in a water bath at 60°C. Extraction was performed on the concentrated supernatant three times using n-butanol, and the n-butanol layer was collected. Then the n-butanol layer was evaporated to dryness, dissolved by adding an appropriate volume of DW, and freeze-dried to obtain RGW.

Furthermore, ginsenoside standards Re, Rg1, Rf, Rb1, Rg2, Rc, Rb2, Rb3, Rd, and Rg3 were purchased from Shanghai Yuanye Bio-Technology Co., Ltd. (Shanghai, China), and STZ, 2-ethylbutyric acid, acetic acid, propionic acid, butyric acid, valeric acid, and isovaleric acid were purchased from Sigma Chemical Co. (St. Louis, MO, United States). Citric acid and sodium citrate were purchased from Beijing Taibo Chemical Co., Ltd. (Beijing, China), acetonitrile and chromatographically pure methanol (MeOH) were obtained from Fisher Scientific (Waltham, MA, United States), and a Milli-Q device (Millipore, Milford, MA, United States) was used to produce ultrapure water. Furthermore, commercial reagent kits for the determination of TC, TG, high-density lipoprotein (HDL-C), and low-density lipoprotein (LDL-C) levels were obtained from Nanjing Jiancheng Biotech. Co., Ltd. (Nanjing, China), while concentrated sulfuric acid and ether were purchased from Beijing Chemical Works (Beijing, China).

UHPLC-Q-TOF-MS Analysis

Total ginsenosides of red ginseng and the 10 reference compounds (1 mg each) were accurately weighed and dissolved in a 1-ml volumetric flask containing 80% chromatographic methanol. Thereafter, the resulting solutions were filtered through a 0.22-μm membrane filter, followed by UHPLC-MS analysis. The UHPLC-MS analysis of RGW was performed using a UHPLC-ESI-Q-TOF/MS system. Specifically, UHPLC was performed using an Agilent 1200SL RRLC system (Agilent Technologies; Waldbronn, Germany) coupled with an Agilent SB-C18 column (3.0 × 100 mm, 1.8 μm, 600 bar). The mobile phase consisted of 0.1% formic acid in water (solvent A) and acetonitrile (solvent B) eluted at 0.30 ml/min and the elution gradient was set as follows: 0–5 min, 19% B; 5–12 min, 19–28% B; 12–22 min, 28–40% B; 22–24 min, 40–85% B; 24–25 min, 85–19% B; and 25–30 min, 19% B. Each injection volume was set at 5.0 μl and the column temperature was maintained at 30°C. Mass spectrometric analysis was performed *via* Q-TOF mass spectrometry. Specifically, the electrospray ionization source in the negative (ESI-) ion mode, with a scanning range of m/z ∼200–3,000, was used. The MS source parameters were set as follows: drying gas flow rate, 10.0 L/min; vaporizer temperature, 350°C; nebulizer pressure, 255 kPa; capillary voltage, 3.5 kV; fragmentor voltage, 200 V; cone voltage, 65 V; and octopole RF voltage, 250 V. All data were acquired and analyzed using Mass Hunter Qualitative and Mass Profiler Professional (MPP, version B. 02.01, MHQ, version B.03.01, Agilent Technologies, Santa Clara, CA).

Validation of UHPLC-MS Method

Calibration Curves, Limits of Detection, and Quantification

To construct calibration curves, 1 mg/ml methanol stock solutions of the 10 reference compounds were diluted to the appropriate concentrations. Thereafter, six concentrations of the different solutions were analyzed in triplicate, and calibration curves were constructed by plotting the peak areas corresponding to the extracted ion current spectra against the analyte concentrations. Furthermore, suitable concentrations were injected into the UHPLC-MS system for analysis, and the limits of determination (LOD) and the limits of quantification (LOQ) under the prevailing conditions were determined at signal-to-noise (S/N) ratios of approximately 3 and 10, respectively.

Precision, Accuracy, and Stability

First, a precision experiment was performed. The method was tested for inter-day and intraday precision by analyzing the same sample six times a day on three separate days. The experimental results were expressed as relative standard deviation (RSD) values. Additionally, recovery tests were used to determine the accuracy of the method. Accurate amounts of 10 ginsenosides were added to the solution of a known concentration of the test substance. The average recoveries were calculated using the following formula: recovery (%) = (amount found-original amount)/amount spiked*100%. Samples were analyzed at 0, 2, 4, 6, 8, 10, 12, 16, and 24 h using an established method for stability assessment. Thus, the stability was expressed as the RSD values corresponding to the nine data points. Six samples were used for each experiment.

Animal Experiments

The animal experiments were approved by the Institutional Animal Care and Use Committee (IACUC) of Changchun University of Chinese Medicine (Approval number: CPCCUCM IACUC 2020-040). A total of 60 adult male Wistar rats were placed in an SPF barrier environment under standard environmental conditions (temperature, 25°C; relative humidity, 55 ± 5%) with unrestricted access to water and food. After 1 week of acclimatization, all the rats were randomly divided into four groups ($n = 15$), namely, the CON (healthy animals treated with DW), DM (T2DM animals treated with DW), MET (T2DM animals treated with metformin at 100 mg/kg/day), and RGW (T2DM animals treated with RGW at 100 mg/kg/day) groups. The CON group was fed with ordinary feed, while the other three groups were fed a high-fat diet (HFD) consisting of 18% lard, 20% sucrose, 3% egg yolk powder, and 59% pulverized normal rat feedstuff. After the HFD feeding for 8 weeks, the rats were fasted for 12 h but were free to drink. Rats in the CON group then received an intraperitoneal injection of citrate buffer, while those in the other three groups received an intraperitoneal injection of low-dose STZ solution (35 mg/kg) dissolved in sodium citrate buffer (0.1 mol/L, pH 4.3–4.5). A fasting blood glucose level $\geq$ 11.1 mmol/L indicated the successful establishment of the T2DM rat model. The RGW intervention process then lasted for 21 days, and the fasting glucose level in blood samples from the tail vein (approximately 0.3 μl each time) was tested at 3-day intervals. Furthermore, from the beginning of the experiment, changes in the body weights of the rats were also monitored once a week.

Sample Collection and Preparation

At the end of the treatment period, the rats in the four groups were anesthetized *via* the intraperitoneal injection of 3% pentobarbital sodium (0.3 ml/100 g body weight), and blood samples were collected from the abdominal aorta using a vacuum tube, while liver tissue samples were collected from the abdominal cavity. The stools were collected from the cecum. The collected blood samples were then centrifuged at 4,000 rpm for 10 min at 4°C, and the supernatant was collected into liquid nitrogen, snap-frozen, and finally stored at −80°C until analysis. The stored serum samples were thawed at 4°C. The levels of different lipids in the serum samples were measured, including TC, TG, HDL-C, and LDL-C. Simultaneously, some of the collected hepatic tissue samples were used to test TC, TG, HDL-C, and LDL-C using the kits, while the other part of the hepatic tissue samples was fixed with paraformaldehyde for more than 24 h and, thereafter, used for hematoxylin-eosin (H&E) staining.

Cell Line Culture and Cytotoxicity Assay

HepG2 cells were grown in DMEM containing 10% fetal bovine serum (FBS) and, thereafter, incubated at 37°C in a humidified atmosphere containing 5% CO_2. Cells were passaged at a ratio of 1:3, and in the logarithmic growth phase, they were collected and used for the cytotoxicity assay experiments. The *in vitro* cytotoxicity of RGW was analyzed using a CCK8 assay kit (30). Briefly, the HepG2 cell suspension (1×10^5 cells/ml) was inoculated into a 96-well cell culture plate at 100 μl per well, and after culturing for 24 h, the original medium was aspirated and different concentrations of the sample test solutions (0–400 μg/ml) were added to each well, and then incubated at 37°C for 72 h. Finally, 10 μl of CCK8 was added to each well 4 h before the end of the culturing process, and the optical density value was measured at 450 nm.

Induction of Lipid Accumulation in HepG2 Cells, Drug Treatment, and Oil Red O Staining

Inoculated HepG2 cells (5×10^5 cells/ml) were seeded into 6-well cell culture plates (2 ml/well). When the cells reached 10%–80% confluence, the culture medium was replaced with a serum-free medium and, after 12 h, oleic acid at different concentrations was

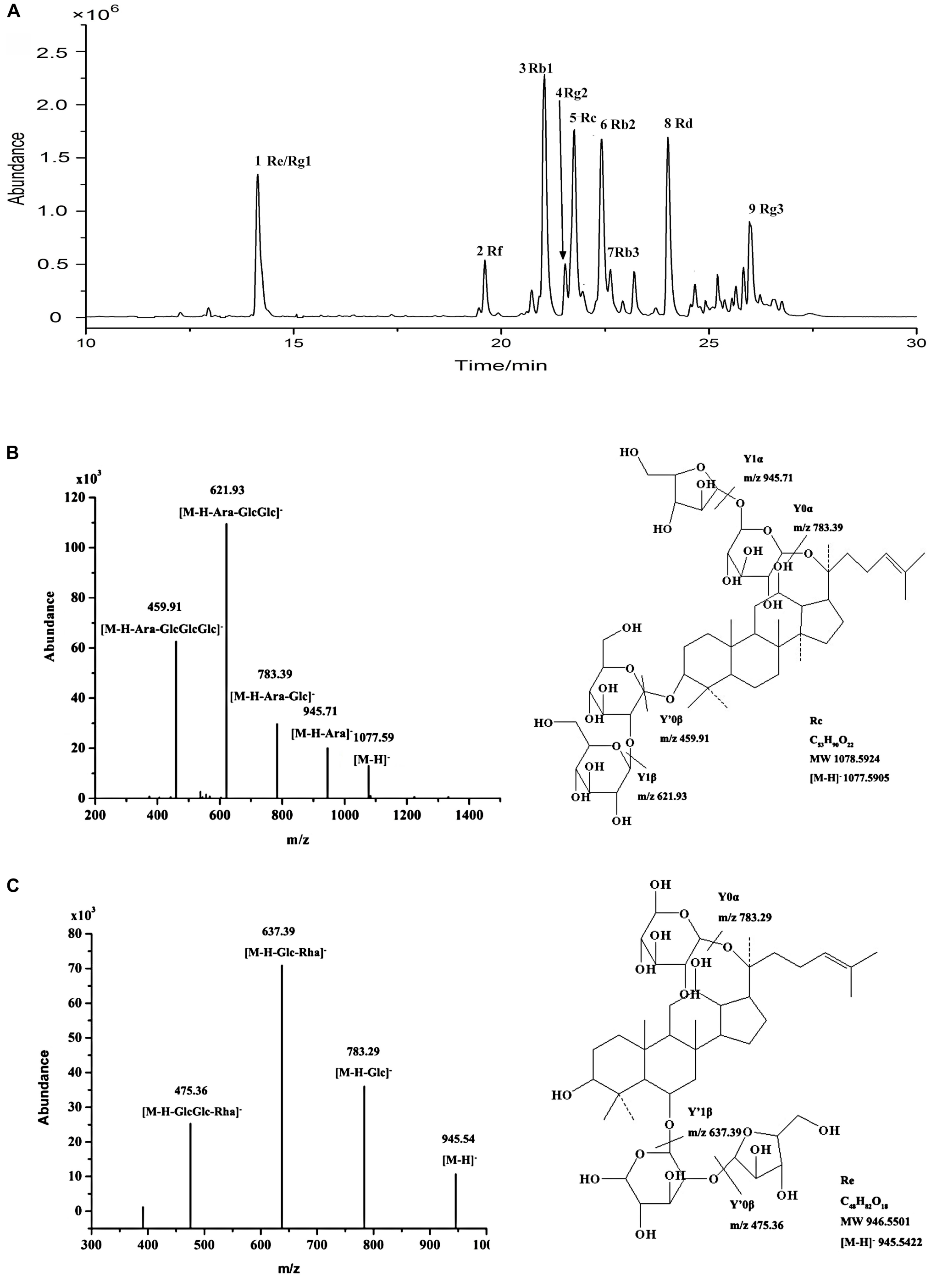

FIGURE 1 | (A) UHPLC-Q-TOF-MS TIC of total ginsenoside of red ginseng. **(B)** ESI-Q-TOF-MS/MS spectra of ginsenoside Rc in negative ion mode. **(C)** ESI-Q-TOF-MS/MS spectra of ginsenoside Re in negative ion mode.

added to induce the accumulation of intracellular lipids. Each concentration was repeated 3 times and incubated for 24 h.

Total ginsenosides of red ginseng were dissolved in the medium and assisted by adding 0.1% DMSO. The experiments at each concentration were performed in triplicate. Specifically, the cells were incubated with RGW at different concentrations (25, 50, and 100 μg/ml) for 24 h at 37°C; metformin (2 mM) was used as the positive control. Oil Red O staining was performed on treated HepG2 cells. The above cells were cultured in a 24-well culture plate with sterile coverslips, and the samples to be tested were added and cultured for 24 h. They were rinsed 3 times with PBS, fixed with paraformaldehyde for 30 min, rinsed with DW for 2 times, and stained with Oil Red O staining solution at room temperature for 30 min after rinsing, hematoxylin staining, and mounting. Finally, the results were observed under a microscope.

Determination of Short-Chain Fatty Acids by Gas Chromatography-Mass Spectrometry

2-Ethylbutyric acid was prepared as a 0.1 mmol/L ether solution as an internal standard solution, and acetic acid, propionic acid, butyric acid, isovaleric acid, and valeric acid were prepared as 0.1 mmol/L standard solutions, which were used to prepare a standard curve at different concentrations.

A precision experiment was conducted as follows: the determination of the same sample solution was repeated 12 times, and the RSD value was calculated. A stability experiment was conducted as follows: a sample of treated stool was taken and it was measured two times at 0, 2, 4, and 6 h to calculate the RSD value. The standard recovery experiment was conducted as follows: a sample of rat feces was chosen after measurement, weighing 9 portions of 30 mg each. According to the concentration of the standard acid reference substance added to them, they were divided into three groups: high, medium, and low, with 3 copies in each group. The ratio of the concentration of the standard acid reference substance added to the previously determined acid concentrations in the high, medium, and low groups was 1.2:1, 1:1, and 0.8:1.

Furthermore, an appropriate amount of rat stool was dissolved in DW, vortexed for 1 min, and then centrifuged at 10,000 rpm for 10 min. Thereafter, 50% sulfuric acid solution and the internal standard solution were added, followed by vertexing for 1 min, and then centrifuged at 10,000 rpm for 10 min. The mixture was incubated at 4°C for 30 min, and the supernatant was collected for GC analysis. Chromatographic separation was then performed on an FFAP capillary column (30 m × 0.25 mm × 0.25 μm) using helium (1.0 ml/min) as the carrier gas. At a split ratio of 10:1, 1 μl of the sample solution was injected into the GC system, with the injector temperature set at 230°C, which was obtained using the following protocol: the initial temperature was

TABLE 1 | Compounds identified from red ginseng (RGW).

			[M-H]$^-$			Fragment ions of [M-H]$^-$	
Peak	**Identity**	**Molecular formula**	**Measd mass**	**Calcd mass**	**Mass accuracy (ppm)**	**MS (m/z)**	**MS/MS fragment ions**
1	Re	$C_{48}H_{82}O_{18}$	945.5428	945.5422	−6.77	945.5[M-H]$^-$	783.29[M-H-Glc]$^-$ 637.39[M-H-Glc-Rha]$^-$ 475.36[M-H-GlcGlc-Rha]$^-$
1	Rg1	$C_{42}H_{72}O_{14}$	799.4849	799.4843	7.63	799.5[M-H]$^-$	637.33[M-H-Glc]$^-$ 475.99[M-H-GlcGlc]$^-$ 392.61[M-H-GlcGlc-C_6H_{12}]$^-$
2	Rf	$C_{42}H_{72}O_{14}$	799.5206	799.5148	7.25	799.3[M-H]$^-$	637.39[M-H-Glc]$^-$ 475.28[M-H-GlcGlc]$^-$ 391.17[M-H-GlcGlc-C_6H_{12}]$^-$
3	Rb1	$C_{54}H_{92}O_{23}$	1107.6048	1107.5951	8.76	1107.6[M-H]$^-$	945.49[M-H-Glc]$^-$ 783.36[M-H-GlcGlc]$^-$ 621.53[M-H-GlcGlcGlc]$^-$ 459.24[M-H-GlcGlcGlcGlc]$^-$
4	Rg2	$C_{42}H_{72}O_{13}$	783.4964	783.4894	8.93	783.6[M-H]$^-$	637.51[M-H-Rha]$^-$ 475.25[M-H-Rha-Glc]$^-$ 391.17[M-H-Rha-Glc-C_6H_{12}]$^-$
5	Rc	$C_{53}H_{90}O_{22}$	1077.5905	1077.5845	5.57	1077.5[M-H]$^-$	945.71[M-H-Ara]$^-$ 783.39[M-H-Ara-Glc]$^-$ 621.93[M-H-Ara-GlcGlc]$^-$ 459.91[M-H-Ara-GlcGlcGlc]$^-$
6	Rb2	$C_{53}H_{90}O_{22}$	1077.5883	1077.5845	3.53	1077.5[M-H]$^-$	945.65[M-H-Ara(p)]$^-$ 783.57[M-H-Ara-Glc]$^-$ 621.55[M-H-Ara-GlcGlc]$^-$
7	Rb3	$C_{53}H_{90}O_{22}$	1077.5830	1077.5845	4.18	1077.5[M-H]$^-$	945.62[M-H-Xyl]$^-$ 783.57[M-H-Xyl-Glc]$^-$ 621.53[M-H-Xyl-GlcGlc]$^-$ 293.18[XylGlc-H]$^-$ 149.04[Xyl-H]$^-$
8	Rd	$C_{48}H_{82}O_{18}$	945.5361	945.5422	−6.45	945.5[M-H]$^-$	783.46[M-H-Glc]$^-$ 621.52[M-H-GlcGlc]$^-$ 459.47[M-H-GlcGlcGlc]$^-$ 161.14[Glc-H]$^-$
9	Rg3	$C_{42}H_{72}O_{13}$	783.4957	783.4894	8.04	783.6[M-H]$^-$	621.70[M-H-Glc]$^-$ 459.50[M-H-Glc-Glc]$^-$

maintained at 40°C for 2 min, and the temperature was increased at a heating rate of 10°C/min to 200°C for 5 min. Furthermore, the injection volume, transfer line temperature, and ion source temperature were 1.0 μl, 230°C, and 250°C, respectively.

Statistical Analysis

All data have been tested for normality and were presented as mean ± SD and analyzed using Statistical Product and Service Solutions software (SPSS software). Student's *t*-tests were used to compare the differences between the two groups. One-way analysis of variance (ANOVA) followed by Tukey's multiple comparison test was used to compare more than two groups. $P < 0.05$ was considered to be statistically significant.

RESULTS

UHPLC-MS Analysis of Red Ginseng

Using optimal chromatographic and MS conditions, a total of 10 major ginsenosides were identified in the obtained RGW. The presence of the ginsenosides, Re, Rg1, Rf, Rb1, Rg2, Rc, Rb2, Rb3, Rd, and Rg3 (**Figure 1A**), was confirmed by comparing their molecular weights and MS/MS (**Figures 1B,C**). In the negative ion mode, the ginsenosides appeared as the deprotonated $[M\text{-}H]^-$ ion and $[M + HCOO]^-$ ion. Negative ion mode was chosen for the following experiments, as it gives a much clearer fragmentation pattern for structural identification. The characteristic fragment ions of ginsenoside are summarized in **Table 1**. The characteristic product ions of aglycone PPD (m/z 459) and PPT (m/z 475) are observed. The types of sugar substitution were determined as hexose (glucose), deoxyhexose (rhamnose), and fructose (arabinose, xylose) with different linkages (**Table 1**). The characteristic neutral losses of these sugar residues were 162 Da (hexose), 146 Da (deoxyhexose), and 132 Da (fructose), respectively. **Figures 1B,C** shows the MS/MS spectra of representative types of ginsenoside PPD (Rc) and PPT (Re) as examples. In **Figure 1B**, the fragment ion at m/z 945 is produced by the loss of an arabinose residue of 132 Da. The ion at m/z 783 is generated by the loss of one arabinose-glucose residue (162 + 132 Da). The fragment ion at m/z 621 ion is generated by the loss of arabinose-glucose residue (162 + 132 Da) and glucose residue (162 Da). The ion at m/z 459 is produced by the loss of glucose–arabinose residue (162 + 132 Da) and glucose-glucose residue (162 + 162 Da), which is the characteristic ion of PPD-type aglycone. In **Figure 1C**, the ion at m/z 783 is generated by the loss of one glucose residue (162 Da). The fragment ion at m/z 637 ion is generated by the loss of glucose residue (162 Da) and rhamnose residue (146 Da). The ion at m/z 475 is produced by the loss of glucose-rhamnose residue (162 + 146 Da) and glucose residue (162 Da), which is the characteristic ion of PPT-type aglycone. The identified ginsenosides are shown in **Table 1**, which indicates that the mass accuracy for quasi-molecular ions and fragment ions was < 10 ppm, indicating that the detected molecular weights of the quasi-molecular and fragment ions were well matched with the corresponding theoretical values. To validate the quantitative analytical method, the linearity, regression, and linear ranges of the 10 ginsenosides were determined using the developed UHPLC-MS method. As shown in **Table 2**, the data indicated a good linear relationship between the investigated compound concentrations and their peak areas within the test ranges ($R^2 > 0.9979$). Additionally, the overall RSD values of intraday and inter-day variations corresponding to the 10 ginsenosides were no more than 2.33% and 2.82%, respectively, and the results of our accuracy tests showed that the accuracy of the established method was also acceptable, with the overall spike recovery rates for the ginsenosides varying in the range from 98.75 to 105.23%. Regarding the stability of the method, the RSDs of the ten ginsenosides detected within 24 h were all below 2.23%. At signal-to-noise ratios (S/N) of 3 and 10, the lower limits of detection (LOD) and LOQ were less than 0.8 and 1.1 $ng{\cdot}ml^{-1}$, respectively. This validated LC-MS method was then applied for the quantitative determination of the 10 ginsenosides in RGW.

Pathological Characteristics of Diabetic Mice

After STZ administration, rats in the DM, MET, and RGW groups showed a significant increase in fasting blood glucose levels compared with those in the CON group (**Figure 2B**). Furthermore, STZ administration resulted in decreased body weight (**Figures 2A, 3A**), and symptoms of polydipsia, polyuria, and polyphagia were also observed. These findings demonstrate that the T2DM model was successfully established.

Hypoglycemic and Hyperlipidemia Effects of Red Ginseng in T2DM Rats

The obvious characteristics of diabetes are a relative decrease in body weight gain and an increase in blood glucose levels. As shown in **Figure 3A**, the body weights of all the rats increased steadily, and their blood glucose levels were normal. However, the growth rate of the rats in the CON group was slower. Conversely, after STZ administration, the body weight of all rats began to decrease, and their blood glucose levels increased significantly relative to the rats in the CON group. Additionally, rats in both the MET and RGW groups tended to show a decrease in weight after STZ administration. The effect of RGW on the fasting blood glucose level of the rats is shown in **Figure 3B**, from which it is evident that the blood glucose levels of rats in the MET and RGW groups decreased gradually after 3 weeks of treatment. However, rats in the DM group only showed a slight decrease in blood glucose levels. At the end of treatment period, rats in both the MET and RGW groups showed significant decreases in fasting blood glucose level from 21.45 ± 1.25 mmol/L down to 14.22 ± 2.06 mmol/L ($p < 0.01$) and 20.92 ± 1.92 mmol/L to 15.34 ± 2.53 mmol/L ($p < 0.05$), respectively.

The lipid biochemical parameters of the T2DM rats in the different groups after treatment for 21 days are shown in **Table 3**. From this table, it is evident that rats in the DM group showed abnormal lipid metabolism as indicated by the increases in TC, TG, and LDL-C levels ($p < 0.01$) and a decrease in HDL-C levels ($p < 0.01$). However, after RGW treatment, serum TG, TC, and LDL-C levels decreased significantly ($p < 0.01$), while the level of HDL-C increased significantly ($p < 0.01$). Furthermore, the hepatic biochemical indicators showed abnormal lipid

TABLE 2 | Calibration curves, accuracy, precision, and content for 10 ginsenosides (n = 6).

Ginsenosides	Calibration curve	R^2	Test range (μg)	Intra-day precision RSD (%)	Inter-day precision RSD (%)	Recovery (%)	RSD(%)	Content (mg/g)
Rb1	$y = 0.2822x + 0.2156$	0.9979	0.005–0.03	1.09	1.80	103.44	1.76	23.70 ± 0.08
Re	$y = 0.2239x + 0.0552$	0.9994	0.005–0.03	2.01	2.41	100.15	2.45	9.87 ± 0.32
Rf	$y = 0.3001x + 0.1582$	0.9982	0.005–0.03	2.09	2.06	98.89	1.88	8.01 ± 0.18
Rb2	$y = 0.2648x + 0.1572$	0.9990	0.005–0.03	1.75	0.99	105.23	2.25	6.78 ± 0.02
Rb3	$y = 0.3437x + 0.1589$	0.9992	0.005–0.03	2.14	2.12	101.20	1.87	2.59 ± 0.26
Rc	$y = 0.2419x + 0.2927$	0.9986	0.005–0.03	2.25	2.26	99.56	3.20	13.14 ± 0.07
Rd	$y = 0.2355x + 0.1748$	0.9992	0.005–0.03	2.33	2.57	102.50	1.23	9.46 ± 0.85
Rg3	$y = 0.152x + 0.2133$	0.9995	0.005–0.03	1.57	1.59	99.98	1.47	7.73 ± 0.47
Rg2	$y = 0.2829x + 0.1751$	0.9992	0.005–0.03	2.14	2.82	98.75	2.72	4.85 ± 0.39
Rg1	$y = 0.2788x + 0.0981$	0.9979	0.005–0.03	1.89	1.61	103.53	1.52	8.02 ± 1.21

Data were expressed as mean ± SD.

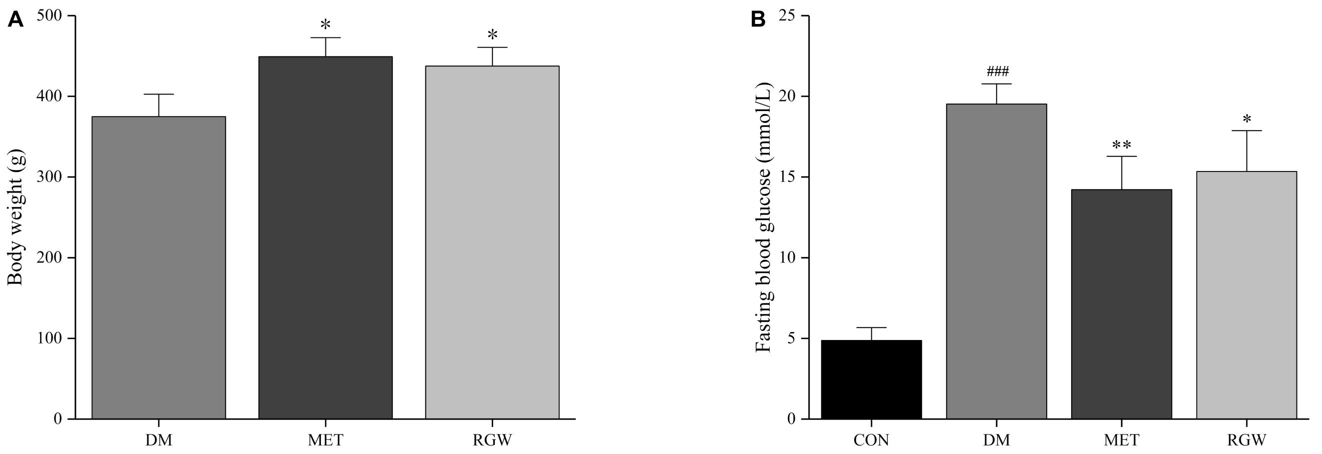

FIGURE 2 | Pathological characteristics of diabetic rats. **(A)** Body weight. **(B)** Fasting blood glucose. Data are expressed as mean ± SD. $^{*}p < 0.05$, $^{**}p < 0.01$ vs. DM; $^{###}p < 0.005$ vs. CON (n = 8).

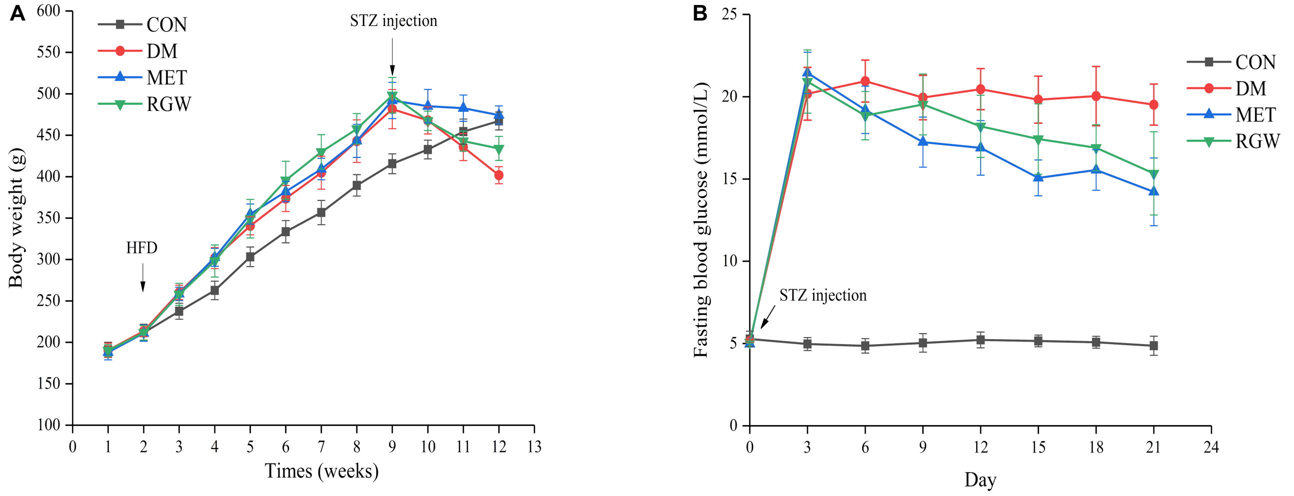

FIGURE 3 | Effects of RGW on body weight and fasting blood glucose in DM rats. **(A)** Body weight. **(B)** Fasting blood glucose. Data are expressed as mean ± SD (n = 8).

TABLE 3 | Serum biochemical parameters of rats in different groups after being treated for 21 days (*n* = 8).

Items	CON	DM	MET	RGW
HDL-C (mmol/ml)	1.00 ± 0.13	$0.65 \pm 0.10^{**}$	$1.29 \pm 0.24^{\#\#}$	$1.16 \pm 0.39^{\#\#}$
LDL-C (mmol/ml)	0.56 ± 0.16	$3.05 \pm 0.50^{**}$	$0.59 \pm 0.16^{\#\#}$	$0.90 \pm 0.54^{\#\#}$
TG (mmol/ml)	0.54 ± 0.11	$2.83 \pm 0.19^{**}$	$0.71 \pm 0.12^{\#\#}$	$1.64 \pm 0.65^{\#}$
TC (mmol/ml)	7.49 ± 0.85	$29.83 \pm 6.17^{**}$	$8.04 \pm 0.32^{\#\#}$	$9.07 \pm 3.31^{\#\#}$

Data was expressed as mean ± SD. $^{*}p < 0.05$, $^{**}p < 0.01$ *vs. CON;* $^{\#}p < 0.05$, $^{\#\#}p < 0.01$ *vs. DM.*

TABLE 4 | Hepatic biochemical parameters of rats in different groups after being treated for 21 days (*n* = 8).

Items	CON	DM	MET	RGW
HDL-C (mmol/ml)	0.27 ± 0.04	$0.08 \pm 0.01^{**}$	$0.27 \pm 0.05^{\#}$	$0.29 \pm 0.05^{\#\#}$
LDL-C (mmol/ml)	0.03 ± 0.01	$0.32 \pm 0.04^{**}$	$0.02 \pm 0.00^{\#}$	$0.04 \pm 0.01^{\#}$
TG (mmol/ml)	0.49 ± 0.11	0.48 ± 0.14	$0.35 \pm 0.03^{\#}$	0.47 ± 0.12
TC (mmol/ml)	0.12 ± 0.02	0.14 ± 0.04	0.12 ± 0.01	0.11 ± 0.03

Data was expressed as mean ± SD. $^{*}p < 0.05$, $^{**}p < 0.01$ *vs. CON;* $^{\#}p < 0.05$, $^{\#\#}p < 0.01$ *vs. DM.*

metabolism for rats in the DM group (**Table 4**). Further, hepatic tissues from rats in the RGW group also showed a significant increase in HDL-C ($p < 0.01$). The levels of TG and TC showed a downward trend, even though the decreases were not significant.

Pathological Changes in Hepatic Tissue of T2DM Rats

The histopathological characteristics of the hepatic tissue from each rat group were evaluated using H&E staining. The results thus obtained are shown in **Figure 4**, from which it is evident that in hepatic tissues from rats in the DM group, the cell arrangement was disordered (**Figure 4A**), with lipid droplet vacuoles of varying sizes and numbers present in the cytoplasm, and with most of the hepatocytes showing fatty degeneration (**Figure 4B**). But, after RGW treatment, the morphology of hepatic cells tended to be normal, and the size of fat droplets in the cells decreased significantly. Thus, RGW treatment almost completely reversed fatty degeneration in the hepatic cells (**Figure 4D**). Similar observations were made for the MET group.

Effect of Red Ginseng on Lipid Metabolism

Oleic acid-induced HepG2 cells in a high-fat model of HepG2 cells were used to test the effect of RGW on lipid metabolism. After RGW treatment, cell viability did not decrease significantly at doses of 100 μg/ml as shown in **Figure 5**, showing lower cytotoxicity. Therefore, the maximum RGW dose was set at 100 μg/ml. As a fat-soluble dye, Oil Red O can specifically bind to triglycerides in tissues and cells to dye fat cells red. Thus, it was used to study the effect of RGW on lipid accumulation in HepG2 cells (**Figure 6**). After 24 h of incubation with oleic acid, a large number of red lipid droplets were

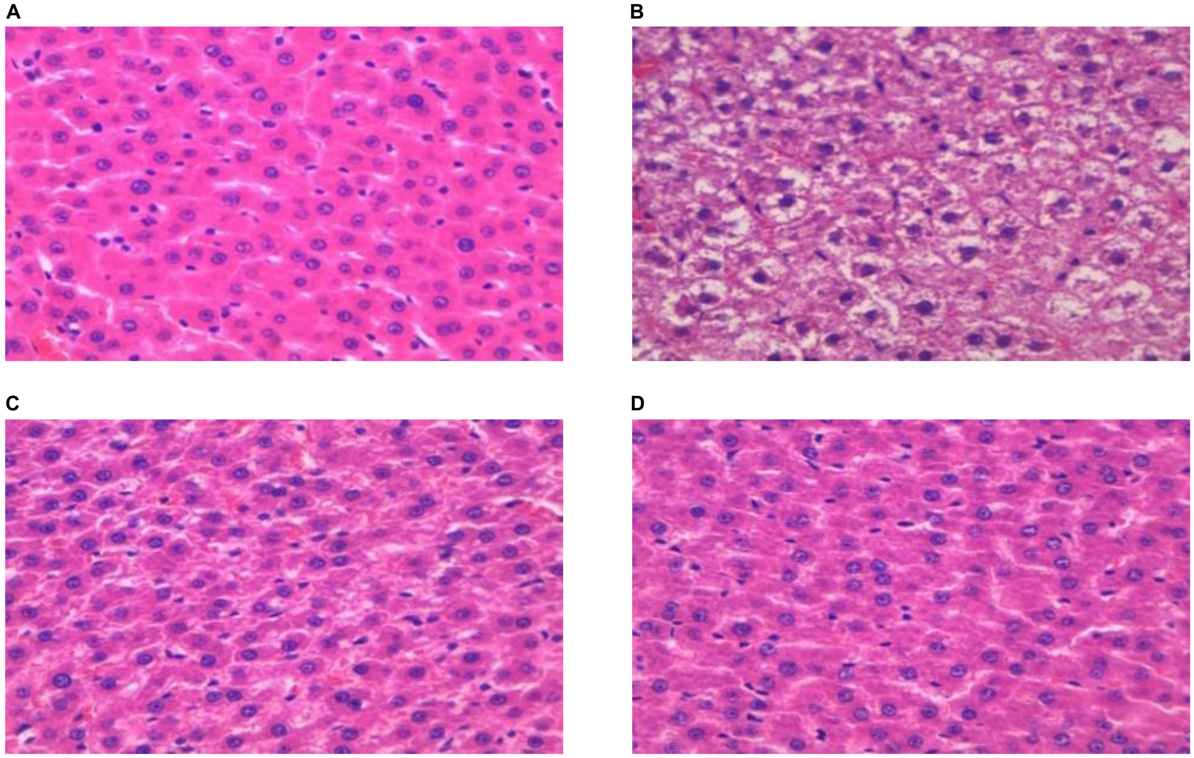

FIGURE 4 | H&E staining of the hepatic (400 ×). **(A)** CON; **(B)** DM; **(C)** MET; and **(D)** RGW.

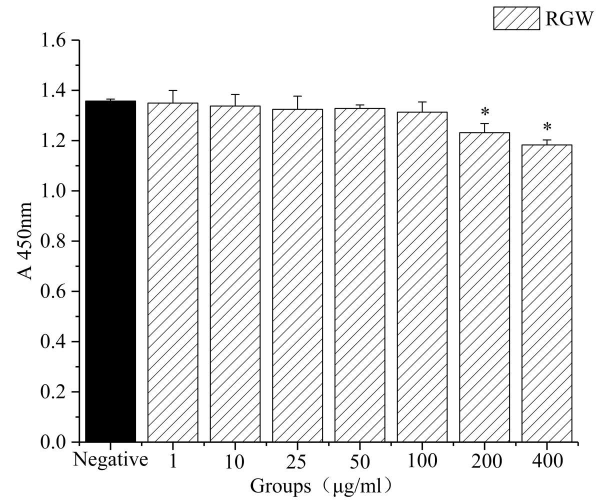

FIGURE 5 | Effect of RGW on HepG2 cells. $^*p < 0.05$ vs. negative.

observed in the cells, indicating that the lipid accumulation cell model had been successfully established. Our results further indicated that intracellular lipid accumulation decreased after RGW administration, and compared with the negative control group, the effect of the RGW treatment group was obvious, indicating that RGW could effectively inhibit lipid accumulation *in vitro*. Additionally, as the RGW dose increased, the sizes of the lipid droplets in the cells gradually decreased, and the inhibitory effect was more significant, highlighting an obvious dose-dependent manner.

Determination of Short-Chain Fatty Acids

To validate the quantitative analytical method, the linearity, regression, and linear ranges of the 5 SCFAs were determined using the developed gas chromatography-mass spectrometry (GC-MS) method. The data indicated a good linear relationship between the investigated compound concentrations and their peak areas within the test ranges ($R^2 > 0.9950$). Additionally, the overall RSD values of intraday and inter-day variations corresponding to the 5 SCFAs were no more than 3.66% and 3.72%, respectively, and the results of our accuracy tests showed that the accuracy of the established method was also acceptable, with the overall spike recovery rates for the five varying in the range from 92.44 to 113.95%. Regarding the stability of the method, the RSDs of the 5 SCFAs detected within 24 h were all below 4.04%. This validated GC-MS method was then applied for the quantitative determination of the 5 SCFAs.

As the end metabolites of the microbial fermentation of carbohydrates in the gut, SCFAs play an important role in lipid metabolism and participate in multiple lipid metabolism pathways. In this study, we examined the levels of five SCFAs based on the analysis of stool samples *via* GC-MS using the internal standard method. As shown in **Table 5**, compared with the CON group, the SCFA content of the stool samples from the rats in the DM group decreased significantly ($p < 0.01$). However, after RGW treatment, the levels of propionic acid, butyric acid, and isovaleric acid increased ($p < 0.05$). Those of acetic acid and valeric acid also increased, but the increases were not statistically significant.

DISCUSSION

In this study, a T2DM rat model was established to evaluate the regulatory effects of RGW on lipid metabolism disorders. The results demonstrated that RGW effectively improved lipid metabolism disorders caused by T2DM mainly through the lowering of blood lipids, reducing lipid deposition and increasing SCFAs levels.

Typical symptoms of T2DM include insulin resistance and abnormally elevated blood glucose levels. Particularly, insulin resistance plays a key role in the development of dyslipidemia in patients with T2DM, given that long-term insulin resistance in adipocytes leads to the increased production of free fatty acids, which in turn leads to an abnormal increase in TG levels (31). Our results showed that RGW treatment improved these parameters, leading to improved body weight as well as decreases in blood glucose and lipid levels during the intervention period. Thus, RGW has a regulatory effect on these metabolic disorders. Hyperglycemia is the main clinical manifestation of diabetes. This study showed that after 3 weeks of RGW treatment, rats in the DM group showed significant decreases in blood glucose levels, and those in the MET group showed a stronger hypoglycemic effect following this treatment. Thus, our experiments indicated that RGW has a good hypoglycemic effect, and this conclusion is consistent with those reported in some previous studies (32). Additionally, diabetes leads to the progressive accumulation of lipid metabolites, and the levels of TG, TC, LDL-C, and HDL-C are considered important biomarkers of hyperlipidemia (33). Our results confirmed that RGW showed a strong antihyperlipidemic effect by lowering TG, TC, and LDL-C levels while increasing HDL-C in T2DM rats.

The liver, as a central detoxifying organ of the body, plays a primary role in gluconeogenesis and lipogenesis regulation, and the abnormal physiological state of the liver is an important factor in the disorder of glucose and lipid metabolism (34). Experimental results indicated lipid deposition and cell degeneration in the liver of rats in the DM group, and this may have caused the abnormality of serum biochemical indicators. But owing to RGW treatment, this hepatic steatosis state was almost completely reversed. At the same time, the detection of liver biochemical indicators also verified this (**Table 4**). Lipid accumulation in the liver is caused by increased lipid acquisition and decreased lipid clearance. To verify how RGW ameliorated hepatic steatosis, experiments were performed using oleic acid-induced HepG2 cells. The experiments showed that the number of lipid droplets in HepG2 cells treated with 25, 50, and 100 μg/ml RGW decreased significantly, indicating that one of the reasons for the improvement in steatosis of hepatocytes may be a reduction in lipid deposition. Likewise, a study demonstrated that the reduction of hepatic steatosis leads to the recovery of liver function and the call-back of parameters related to lipid metabolism (35), which also confirmed our previous experimental results.

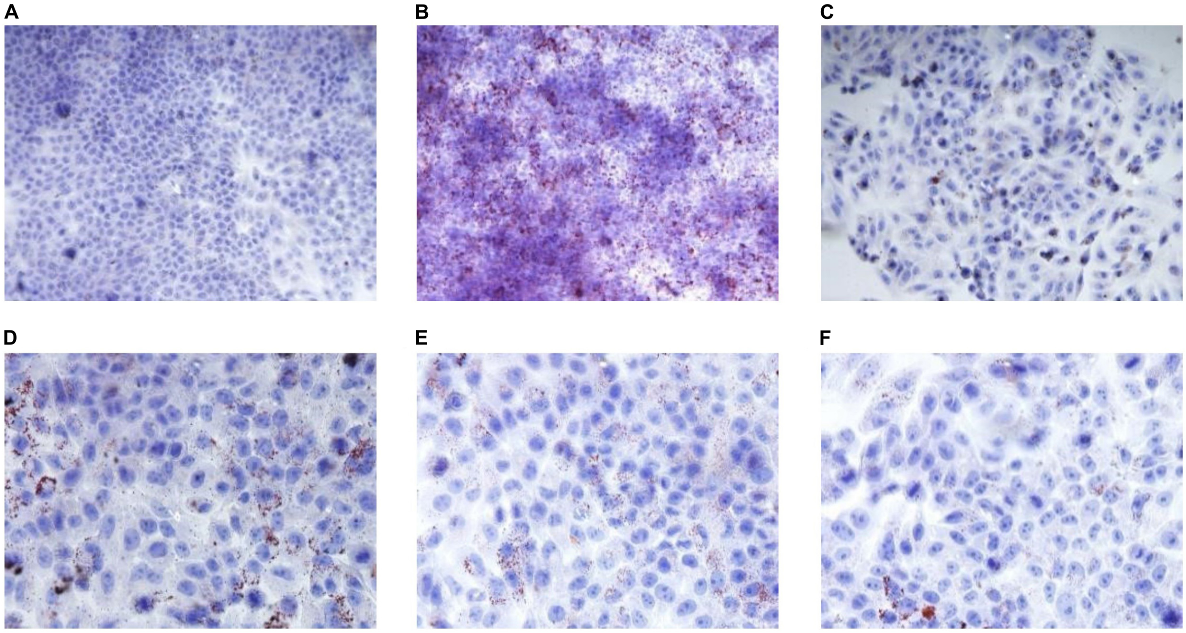

FIGURE 6 | Effect of RGW on lipid metabolism. **(A)** Blank; **(B)** negative; **(C)** positive; **(D)** RGW 25 μg/ml; **(E)** RGW 50 μg/ml; and **(F)** RGW 100 μg/ml.

TABLE 5 | The content of five short-chain fatty acids (SCFAs) in rat stools (*n* = 8).

Items	CON	DM	MET	RGW
Acetic acid (umol/l)	347.76 ± 29.86	$252.66 \pm 15.49^{**}$	$336.22 \pm 19.15^{\#}$	316.22 ± 22.79
Propionic acid (umol/l)	62.33 ± 7.40	$27.79 \pm 5.44^{**}$	$48.12 \pm 8.65^{\#\#}$	$51.16 \pm 9.82^{\#}$
Butyric acid (umol/l)	58.44 ± 15.86	$35.37 \pm 9.68^{**}$	$57.36 \pm 6.77^{\#\#}$	$43.38 \pm 4.40^{\#}$
Valeric acid (umol/l)	12.55 ± 2.09	$6.52 \pm 1.98^{**}$	$10.84 \pm 2.52^{\#\#}$	9.60 ± 1.42
Isovaleric acid (umol/l)	14.10 ± 4.13	$10.89 \pm 1.92^{**}$	$13.47 \pm 2.53^{\#\#}$	$13.00 \pm 0.74^{\#}$

Data was expressed as mean ± SD. $^{*}p < 0.05$, $^{**}p < 0.01$ *vs. CON;* $^{\#}p < 0.05$, $^{\#\#}p < 0.01$ *vs. DM.*

Short-chain fatty acids, which are produced *via* the fermentation of dietary fiber by gut microbiota, have beneficial health effects. However, their insufficient production is associated with T2DM and obesity (36). After 3 weeks of RGW intervention, increased SCFAs contents were observed. Reportedly, propionic acid and butyric acid contents are closely related to the incidence and prevention of T2DM. Administration of acetic acid has been shown to affect systemic lipolysis as well as intracellular lipolysis in adipocytes in *in vitro* and *in vivo* animal and human studies. (37). Additionally, G protein-coupled receptors (GPCRSs), which are SCFA receptors, including GPR43 and GPR41, play important roles in maintaining glucose and lipid metabolism. Specifically, GPR41 is activated by propionate to increase insulin sensitivity and maintain energy and glucose homeostasis, while GPR43 can be activated by acetate in white adipose tissue to modulate energy uptake and improve glucose and lipid metabolism (38). In addition to acting as signal molecules, SCFAs can also serve as energy substrates in adipocytes. Furthermore, in hepatocytes, acetate and butyrate are mainly involved in lipid biosynthesis, whereas propionate is primarily involved in gluconeogenesis, and in adipocytes, SCFAs may enter the adipogenic pathway after being absorbed and activated by short-chain coenzyme synthase (39). It has also been observed that propionate is an important factor that influences hepatic gluconeogenesis and lipid metabolism (40, 41). This study confirms the importance of propionate to inhibit hepatic lipogenesis and improve insulin sensitivity in high-fat diet-induced obesity (42). Another factor in the reversal of hepatocyte steatosis and lowering of blood glucose levels by RGW may be mediated in part by the effect of propionate on hepatic carbohydrate metabolism. Additionally, butyrate, which is the main energy source for colonic epithelium, can induce gluconeogenesis in the intestine, thereby improving glucose and energy homeostasis. Additionally, it can enhance fatty acid oxidation and energy consumption in the human body (43). Thus, the increase in butyrate content following RGW treatment may also be responsible for the decrease in blood lipid and glucose levels in diabetic rats.

In this study, the RGW were quantitatively analyzed using UHPLC-MS and its effect on the lipid metabolism of T2DM was studied. We observed that after 21 days of RGW treatment, all the diabetes-related parameters corresponding to the T2DM rats improved. Moreover, *in vitro* cell experiments demonstrated that RGW had a significant lipid deposition improvement effect. These experimental results provide a usable basis for functional food development for the treatment of diabetes. Additionally, our results imply that RGW, which is easy to obtain and has controllable quality, can be developed as a potential natural antidiabetic food for the prevention and treatment of obesity-related diabetes.

DATA AVAILABILITY STATEMENT

The original contributions presented in the study are included in the article/supplementary material, further inquiries can be directed to the corresponding author.

ETHICS STATEMENT

The animal experiment was approved by the Institutional Animal Care and Use Committee (IACUC) of Changchun University of Chinese Medicine.

AUTHOR CONTRIBUTIONS

RH: methodology, investigation, and original draft preparation. YTo, MZ, YTe, and HL: validation and software. WW: conceptualization, methodology, supervision, and funding acquisition. All authors contributed to the article and approved the submitted version.

FUNDING

This study was supported by the Jilin Provincial Department of Science and Technology (No. 20200301049RQ).

ACKNOWLEDGMENTS

We would like to thank Lili Jiao and Heyu Wang for their help with data acquisition and quality control of figures and tables.

REFERENCES

1. Sun HC, Seok WJ, Byung HL, Hyeon JK, Sung HH, Ho KK, et al. Ginseng pharmacology: a newparadigm based ongintonin-lysophosphatidic acidreceptor interactions. *Front Pharmacol.* (2015) 6:245. doi: 10.3389/fphar.2015.00245
2. Xie Y-Y, Luo D, Cheng Y-J, Ma J-F, Wang Y-M, Liang Q-L, et al. Steaming-induced chemical transformations and holistic quality assessment of red ginseng derived from *Panax ginseng* by means of HPLC-ESI-MS/MS(n)-based multicomponent quantification fingerprint. *J Agric Food Chem.* (2012) 6033:8213–24. doi: 10.1021/jf301116x
3. Kim M, Kim J, Moon S, Choi BY, Kim S, Jeon HS, et al. Korean Red ginseng improves astrocytic mitochondrial function by upregulating HO-1-mediated AMPKα-PGC-1α-ERRα circuit after traumatic brain injury. *Int J Mol Sci.* (2021) 2223:13081. doi: 10.3390/ijms222313081
4. Jung J, Lee NK, Paik HD. Bioconversion, health benefits, and application of ginseng and red ginseng in dairy products. *Food Sci Biotechnol.* (2017) 265:1155–68. doi: 10.1007/s10068-017-0159-2
5. Yuan HD, Kim JT, Kim SH, Chung SH. Ginseng and diabetes: the evidences from in vitro, animal and human studies. *J Gins Res.* (2012) 361:27–39. doi: 10.5142/jgr.2012.36.1.27
6. Wu W, Qin Q-J, Guo Y-Y, Sun J-H, Liu S-Y. Studies on the chemical transformation of 20(S)-protopanaxatriol (PPT)-type ginsenosides R(e), R(g2), and R(f) using rapid resolution liquid chromatography coupled with quadruple-time-of-flight mass spectrometry (RRLC-Q-TOF-MS). *J Agric Food Chem.* (2012) 6040:10007–14. doi: 10.1021/jf302638f
7. Yang Z, Dan W, Li Y, Zhou X, Liu T, Shi C, et al. Untargeted metabolomics analysis of the anti-diabetic effect of red ginseng extract in Type 2 diabetes mellitus rats based on UHPLC-MS/MS. *Biomed Pharmacother.* (2021) 146:112495. doi: 10.1016/j.biopha.2021.112495
8. Cho SS. Effects of Korean red ginseng extract and the conventional systemic therapeutics of atopic dermatitis in a murine model. *Nutrients.* (2021) 141:33. doi: 10.3390/nu14010133
9. Jo JJ, Cho PJ, Lee S. Simultaneous quantification of 13 ginsenosides by LC-MS/MS and its application in diverse ginseng extracts. *Mass Spectrom Lett* (2018) 92:41–5. doi: 10.5478/MSL.2018.9.2.41
10. Li M-M, Wang Y-K, Sheng Y-H, Huang X, Yue H, Liu S-Y. Application of UPLC-QTOF-MS non-targeted metabonomics in mechanism study of property differences of ginseng and American ginseng. *Chin J Chin Mater Med.* (2021) 4622:5930–5. doi: 10.19540/j.cnki.cjcmm.20210811.403
11. Yang J-R, Chen H-H, Nie Q-X, Huang X-J, Nie S-P. Dendrobium officinale polysaccharide ameliorates the liver metabolism disorders of type II diabetic rats. *Int J Biol Macromol.* (2020) 164:1939–48. doi: 10.1016/j.ijbiomac.2020.08.007
12. Dabelea D, Stafford JM, Mayerdavis EJ, D'Agostino R, Dolan L, Imperatore G, et al. Association of type 1 diabetes vs type 2 diabetes diagnosed during childhood and adolescence with complications during teenage years and young adulthood. *Jama.* (2011) 3178:825. doi: 10.1001/jama.2017.0686:
13. McGarry JD. Banting lecture 2001: dysregulation of fatty acid metabolism in the etiology of type 2 diabetes. *Diabetes.* (2002) 511:7–18. doi: 10.2337/diabetes.51.1.7
14. Jiao L-L, Li H, Li J-M, Bo L, Zhang X-Y, Wu W, et al. Study on structure characterization of pectin from the steamed ginseng and the inhibition activity of lipid accumulation in oleic acid-induced HepG2 cells. *Int J Biol Macromol.* (2020) 159:57–65. doi: 10.1016/j.ijbiomac.2020.04.167
15. Sun X, Chen L, Wu R, Zhang D, He Y. Association of thyroid hormone with body fat content and lipid metabolism in euthyroid male patients with type 2 diabetes mellitus: a cross-sectional study. *BMC Endocr Disord.* (2021) 211:241. doi: 10.1186/s12902-021-00903-6
16. Ishii H, Nakajima H, Kamei N, Niiya T, Hiyoshi T, Hiramori Y, et al. Quality-of-Life comparison of dapagliflozin versus dipeptidyl peptidase 4 inhibitors in patients with type 2 diabetes mellitus: a randomized controlled trial (J-BOND Study). *Diabetes Ther.* (2020) 1112:2959–77. doi: 10.1007/s13300-020-00941-8
17. Amori RE, Lau J, Pittas AG. Efficacy and safety of incretin therapy in type 2 diabetes: systematic review and meta-analysis. *Jama.* (2007) 2982:194–206. doi: 10.1001/jama.298.2.194
18. Gupta P, Bala M, Gupta S, Dua A, Dabur R, Injeti E, et al. Efficacy and risk profile of anti-diabetic therapies: conventional vs traditional drugs-a mechanistic revisit to understand their mode of action. *Pharmacol Res.* (2016) 113:636–74. doi: 10.1016/j.phrs.2016.09.029
19. Governa P, Baini G, Borgonetti V, Cettolin G, Giachetti D, Magnano AR, et al. Phytotherapy in the management of diabetes: a review. *Molecules.* (2018) 231:105. doi: 10.3390/molecules23010105
20. Shishtar E, Jovanovski E, Jenkins A, Vuksan V. Effects of Korean white ginseng (*Panax Ginseng* C.A. Meyer) on vascular and glycemic health in type 2 diabetes: results of a randomized, double blind, placebo-controlled, multiple-crossover, acute dose escalation trial. *Clin Nutr Res.* (2014) 32:89–97. doi: 10.7762/cnr.2014.3.2.89
21. Vuksan V, Sievenpiper JL, Koo VY, Francis T, Beljan-Zdravkovic U, Xu Z, et al. American ginseng (*Panax quinquefolius L*) reduces postprandial glycemia in nondiabetic subjects and subjects with type 2 diabetes mellitus. *Arch Intern Med.* (2000) 1607:1009–13. doi: 10.1001/archinte.160.7.1009
22. Shao JW, Jiang JL, Zou JJ, Yang MY, Jia L. Therapeutic potential of ginsenosides on diabetes: from hypoglycemic mechanism to clinical trials. *J Funct Foods* (2019) 64:103630. doi: 10.1016/j.jff.2019.103630

23. Gao Y, Li J-T, Chu S-F, Zhang Z, Chen N-H, Li L, et al. Ginsenoside Rg1 protects mice against streptozotocin-induced type 1 diabetic by modulating the NLRP3 and Keap1/Nrf2/HO-1 pathways. *Eur J Pharmacol.* (2020) 866:172801. doi: 10.1016/j.ejphar.2019.172801
24. Liu Y, Deng J-J, Fan D-D. Ginsenoside Rk3 ameliorates high-fat-diet/streptozocin induced type 2 diabetes mellitus in mice via the AMPK/Akt signaling pathway. *J Food Funct.* (2019) 105:2538–51. doi: 10.1039/c9fo00095j
25. Shi Y-W, Wan X-S, Shao N, Ye R-Y, Zhang N, Zhang Y-J. Protective and anti-angiopathy effects of ginsenoside Re against diabetes mellitus via the activation of p38 MAPK, ERK1/2 and JNK signaling. *Mol Med Rep.* (2016) 145:4849–56. doi: 10.3892/mmr.2016.5821
26. Kim SS, Jang HJ, Oh MY, Eom DW, Kang KS, Kim YJ, et al. Ginsenoside Rg3 enhances islet cell function and attenuates apoptosis in mouse islets. *Transpl P.* (2014) 464:1150–5. doi: 10.1016/j.transproceed.2013.12.028
27. Cheng B, Gao W-H, Wu X-J, Zheng M-X, Yu Y-Y, Song C-H, et al. Ginsenoside Rg2 ameliorates High-Fat Diet-induced metabolic disease through SIRT1. *J Agric Food Chem.* (2020) 68:4215–26. doi: 10.1021/acs.jafc.0c00833
28. Larasati RA, Harbuwono DS, Rahajeng E, Pradipta S, Nuraeni HS, Wibowo H. The role of butyrate on monocyte migration and inflammation response in patient with type 2 diabetes mellitus. *Biomedicines.* (2019) 74:74. doi: 10.3390/biomedicines7040074
29. Li K-K, Tian P-J, Wang S-D, Lei P, Qu L, Huang J-P, et al. Targeting gut microbiota *Lactobacillus* alleviated type 2 diabetes via inhibiting LPS secretion and activating GPR43 pathway. *J Food Funct.* (2017) 38:561–70. doi: 10.1016/j.jff.2017.09.049
30. Geng J, Wang Y-H, Zhang L, Wang R-Q, Li C, Sheng W-J, et al. The cajanine derivative LJ101019C regulates the proliferation and enhances the activity of NK cells via Kv1.3 channel-driven activation of the AKT/mTOR pathway. *Phytomedicine.* (2020) 66:153113. doi: 10.1016/j.phymed.2019.153113
31. Oza MJ, Kulkarni YA. Biochanin A improves insulin sensitivity and controlshyperglycemia in type 2 diabetes. *J Bio pharmaco.* (2018) 107:1119–27. doi: 10.1016/j.biopha.2018.08.073
32. Bang H, Kwak JH, Ahn HY, Shin DY, Lee JH. Korean red ginseng improves glucose control in subjects with impaired fasting glucose, impaired glucose tolerance, or newly diagnosed type 2 diabetes mellitus. *J Med Food.* (2014) 171:128–34. doi: 10.1089/jmf.2013.2889
33. Bibak B, Khalili M, Rajaei Z, Soukhtanloo M, Hadjzadeh M, Hayatdavoudi P. Effects of melatonin on biochemical factors and food and water consumption in diabetic rats. *Adv Biomed Res.* (2014) 3:173. doi: 10.4103/2277-9175.139191
34. Glaser F, John C, Engel B, Höh B, Weidemann S, Dieckhoff J, et al. Liver infiltrating Tcells regulate bile acid metabolism in experimental cholangitis. *J Hepatol.* (2019) 714:783–92. doi: 10.1016/j.jhep.2019.05.030
35. Xu MX, Tan J, Dong W, Zou BK, Teng XP, Zhu LC, et al. The E3 ubiquitin-protein ligase Trim31 alleviates non-alcoholic fatty liver disease by targeting Rhbdf2 in mouse hepatocytes. *Nat Commun.* (2022) 131:1052. doi: 10.1038/s41467-022-28641-w
36. Ju M-Z, Liu Y-Q, Li M-Y, Cheng M-J, Zhang Y, Deng G-Z, et al. Baicalin improves intestinal microecology and abnormal metabolism induced by high-fat diet. *Eur J Pharmacol.* (2019) 857:172457. doi: 10.1016/j.ejphar.2019.172457
37. Hernández MAG, Canfora EE, Jocken JWE, Blaak EE. The short-chain fatty acid acetate in body weight control and insulin sensitivity. *Nutrients.* (2019) 118:1943. doi: 10.3390/nu11081943
38. Kimura I, Ozawa K, Inoue D, Imamura T, Kimura K, Maeda T, et al. The gut microbiota suppresses insulin-mediated fat accumulation via the short-chain fatty acid receptor GPR43. *Nat Commun.* (2013) 4:1829.
39. Heimann E, Nyman M, Pålbrink AK, Lindkvist-Petersson K, Degerman E. Branched short-chain fatty acids modulate glucose and lipid metabolism in primary adipocytes. *Adipocyte.* (2016) 54:359–68. doi: 10.1080/21623945.2016.1252011
40. Chu HK, Duan Y, Yang L, Schnabl B. Small metabolites, possible big changes: a microbiota-centered view of non-alcoholic fatty liver disease. *Gut.* (2019) 682:359–70. doi: 10.1136/gutjnl-2018-316307
41. Louis P, Flint HJ. Diversity, metabolism and microbial ecology of butyrate-producing bacteria from the human large intestine. *FEMS Microbiol Lett.* (2009) 2941:1–8. doi: 10.1111/j.1574-6968.2009.01514.x
42. Weitkunat K, Schumann S, Nickel D, Kappo KA, Petzke KJ, Kipp AP, et al. Importance of propionate for the repression of hepatic lipogenesis and improvement of insulin sensitivity in high-fat diet-induced obesity. *Mol Nutr Food Res* (2016) 12:2611–21. doi: 10.1002/mnfr.201600305
43. Suzuki T, Yoshida S, Hara H. Physiological concentrations of short-chain fatty acids immediately suppress colonic epithelial permeability. *Br J Nutr.* (2008) 1002:297–305. doi: 10.1017/s0007114508888733

Conflict of Interest: The authors declare that the research was conducted in the absence of any commercial or financial relationships that could be construed as a potential conflict of interest.

frontiers | Frontiers in Nutrition

ORIGINAL RESEARCH
published: 10 May 2022
doi: 10.3389/fnut.2022.854882

Potential Anti-aging Components From *Moringa oleifera* Leaves Explored by Affinity Ultrafiltration With Multiple Drug Targets

Yongbing Xu [1,2,3,4]***, Guilin Chen*** [1,2,3,4] ***and Mingquan Guo*** [1,2,3,4]*

[1] Key Laboratory of Plant Germplasm Enhancement and Specialty Agriculture, Wuhan Botanical Garden, Chinese Academy of Sciences, Wuhan, China, [2] College of Life Sciences, University of Chinese Academy of Sciences, Beijing, China, [3] Sino-Africa Joint Research Center, Chinese Academy of Sciences, Wuhan, China, [4] Innovation Academy for Drug Discovery and Development, Chinese Academy of Sciences, Shanghai, China

Moringa oleifera (*M. oleifera*), widely used in tropical and subtropical regions, has been reported to possess good anti-aging benefits on skincare. However, the potential bioactive components responsible for its anti-aging effects, including anti-collagenase, anti-elastase, and anti-hyaluronidase activities, have not been clarified so far. In this study, *M. oleifera* leaf extracts were first conducted for anti-elastase and anti-collagenase activities *in vitro* by spectrophotometric and fluorometric assays, and the results revealed that they possessed good activities against skin aging-related enzymes. Then, multi-target bio-affinity ultrafiltration coupled to high-performance liquid chromatography-mass spectrometry (AUF-HPLC-MS) was applied to quickly screen anti-elastase, anti-collagenase, and anti-hyaluronidase ligands in *M. oleifera* leaf extracts. Meanwhile, 10, 8, and 14 phytochemicals were screened out as the potential anti-elastase, anti-collagenase, and anti-hyaluronidase ligands, respectively. Further confirmation of these potential bioactive components with anti-aging target enzymes was also implemented by molecule docking analysis. In conclusion, these results suggest that the *M. oleifera* leaves might be a very promising natural source of anti-aging agent for skincare, which can be further explored in the cosmetics and cosmeceutical industries combating aging and skin wrinkling.

Keywords: *Moringa oleifera*, anti-aging, affinity ultrafiltration, collagenase, elastase, hyaluronidase, LC-MS

Edited by:
Charalampos Proestos,
National and Kapodistrian University of Athens, Greece

Reviewed by:
Jian-lin Wu,
Macau University of Science and Technology, Macao SAR, China
Chunpeng Craig Wan,
Jiangxi Agricultural University, China

****Correspondence:***
Mingquan Guo
guomq@wbgcas.cn

Specialty section:
This article was submitted to Food Chemistry, a section of the journal Frontiers in Nutrition

Received: *14 January 2022*
Accepted: *11 April 2022*
Published: *10 May 2022*

Citation:
Xu Y, Chen G and Guo M (2022) Potential Anti-aging Components From Moringa oleifera Leaves Explored by Affinity Ultrafiltration With Multiple Drug Targets. Front. Nutr. 9:854882. doi: 10.3389/fnut.2022.854882

INTRODUCTION

Skin aging is one of the visible precursors of aging and mainly caused by oxidative stress and the enhanced activation of proteolytic enzymes, such as elastase, collagenase, and hyaluronidase, which belong to the matrix metalloproteinases (MMPs) (1). Hyaluronic acid performs multiple functions in the skin, including maintaining moisture and promoting the mechanical elasticity and flexibility of the skin. Moreover, elastin plays an important role in maintaining the elasticity of the skin. The degradation of elastin is the main reason for skin aging to produce sagging skin and fine wrinkles. In addition, collagen, which is widely found in the extracellular matrix, plays a pivotal role in maintaining the flexibility, strength, and elasticity of the skin (2). However, hyaluronidase, elastase, and collagenase could degrade hyaluronic acid, elastin, and collagen, respectively. Therefore, hyaluronidase, elastase, and collagenase inhibitors are potential bioactive ingredients since they have antiaging and anti-wrinkle activities on the skin.

Moringa oleifera (*M. oleifera*) is native to India, and it is widely planted and used in tropical and subtropical areas in recent decades, due to its high nutritive values in proteins, amino acids, fats, minerals, and vitamins (3). In contrast, the complex and diverse chemical components including flavonoids, phenolic acids, glucosinolates, and nitrile glycosides in *M. oleifera* lead to its numerous pharmacological activities, for example, antioxidant (4), anti-inflammatory (5), antibacterial (6), anticancer (7), hypoglycemic (8), and hypolipidemic (9) activities. Therefore, *M. oleifera* has received increasing attention in recent years. In the meantime, a large number of studies indicated that *M. oleifera* also possessed anti-aging properties. For instance, *M. oleifera* leaf extracts displayed anti-aging activity by improving oxidative stress resistance and nutrient-sensing pathways (10), extending the life span, and improving stress tolerance of *Caenorhabditis elegans* (11). Moreover, it was also found that the *M. oleifera* leaf extracts observably decreased age-related neurodegeneration in the old treated rat model (12), and its cream restored skin vitality and reduced skin aging (13). However, the specific bioactive ingredients in *M. oleifera* leaf extracts that contributed most to its conspicuous antiaging activity remain unexplored until now. Therefore, it is of great necessity to unravel the prominent anti-aging constituents in the *M. oleifera* leaves.

At present, an integrative strategy combining affinity ultrafiltration with LC-MS based on the interactions between small bioactive molecules and their correlative target enzymes was developed, which, thereafter, made the high-throughput screening and rapid identification of these bioactive components possible. For example, 7, 10, 6, and 7 components belonging to flavonoids and lignans in *Podophyllum sinense* were screened out as the potential Topo I, Topo II, COX-2, and ACE2 ligands, respectively (14). In addition, 10 and 14 potential bioactive constituents in *M. oleifera* leaf extracts showed high binding abilities to pancreatic lipase and α-glucosidase, respectively (15). Furthermore, 16 potential bioactive ligands targeting 5-LOX from Zi-shen pill extract were selected using the affinity ultrafiltration approach (16).

Until now, the antiaging activities of *M. oleifera* leaves, especially elastase and collagenase inhibitory activities, have not been reported yet. In this study, we aimed to explore the prominent anti-aging activities of *M. oleifera* leaves and screened out the correlated potential anti-aging multi-target components. To achieve this, the *in vitro* elastase and collagenase enzyme inhibitory assays were first conducted to evaluate the activities of *M. oleifera* leaf extracts. Then, affinity ultrafiltration coupled with LC-MS was employed to fish out the potential anti-aging components in *M. oleifera* leaves, and the subsequent verification was further implemented with molecule docking analysis. Overall, this study could provide molecular evidence for *M. oleifera* leaves as a natural source of anti-aging agents. At the same time, it will further facilitate its better application and development as a functional food or skincare product in the near future.

MATERIALS AND METHODS

Plant Materials

The fresh leaves of *M. oleifera* were collected from a farm in Machakos County, Kenya. The specimen was authenticated by Professor Guangwan Hu, a senior botanist of Wuhan Botanical Garden, Chinese Academy of Sciences, and stored in the herbarium of the Key Laboratory of Plant Germplasm Enhancement and Specialty Agriculture with the voucher specimen numbers (No. 2018001). The sun-dried leaves were packed in sealed polyethylene bags and stored in the refrigerator at 4°C until further use.

Chemicals and Reagents

The collagenase was supplied by Shanghai Yuanye Biotechnology Co., Ltd. (Shanghai, China). The elastase was obtained from Beijing Coolaber Technology Co., Ltd. (Beijing, China). The hyaluronidase from bovine testes and the fluorogenic MMP 2 substate (N-Succinyl-Ala-Ala-Ala-*p*-nitroanilide) were bought from Sigma-Aldrich (St Louis, MO, United States). The 10 kDa cutoff centrifugal ultrafiltration filters (YM-10) were purchased from Millipore Co., Ltd. (Bedford, MA, United States). The membranes (0.22 μm) were bought from Tianjin Jinteng Experiment Equipment Co., Ltd. (Tianjin, China). Epigallocatechin gallate was bought from Shanghai Meryer Chemical Technology Co., Ltd. (Shanghai, China). Acetonitrile (ACN) and formic acid (FA) of HPLC grade were purchased from TEDIA Company Inc. (Fairfield, Ohio, USA). The ultrapure water for LC-MS analysis and pure water for the sample process were prepared using the EPED water system (Nanjing EPED Technology Development Co., Ltd, Nanjing, China). All other chemicals were of analytical grade and supplied by Sinopharm Chemical Reagent Co., Ltd. (Shanghai, China), including methanol (MeOH), hydrochloric acid (HCl), sodium dihydrogen phosphate (NaH_2PO_4), dibasic sodium phosphate (Na_2HPO_4), and ascorbic acid.

Preparation of Sample Extracts

For the sample preparation, first, 100 g dried powders of *M. oleifera* leaves were accurately weighed, then soaked with 800 mL 90% ethanol overnight, and later extracted with ultrasound for 30 min. Then, the extracts were filtered, and the residues were re-extracted with 90% ethanol. Then, the above extraction process was repeated twice. After the extraction, the supernatants were combined and concentrated to dryness using a rotary evaporator under a vacuum. The dried extracts were deposited in the refrigerator prior to further use.

Determination of Collagenase Inhibitory Activity

The inhibitory activity of *M. oleifera* leaf extracts on collagenase was measured using a slightly modified spectrofluorimetric method described by Stavropoulou et al. (17). In brief, collagenase was added to Tris–HCl buffer (50 mM, pH 7.8) to obtain a concentration of 2 units/mL, and the fluorogenic metalloproteinase-2 (MMP2) substrate (MCA-Pro-Leu-Ala-Nva-DNP-Dap-Ala-Arg-NH2) was prepared at the concentration of 25 μM by being dissolved in buffer. Then, the samples (20 μL) were incubated at 37 °C with collagenase (20 μL) and Tris–HCl buffer (60 μL) in a black 96-well plate. After being kept in darkness for 15 min, the substrate solution (100 μL) was added to trigger the reaction, and the mixture solution was incubated at 37 °C for 30 min in darkness. Finally, the fluorescence values were recorded at the excitation wavelength of 320 nm and the emission wavelength of 405 nm using a multifunctional microplate reader (Tecan Infinite M200 PRO, TECAN, Männedorf, Switzerland). EGCG (6.25–200 μg/mL) was performed as the positive control, and all the samples were tested in triplicate. The inhibition rate of *M. oleifera* leaf extracts on collagenase was computed according to the following formula:

$$\textbf{Inhibition rate}\ (\%) = \frac{\mathbf{RFU_{100} - RFU_{sample}}}{\mathbf{RFU_{100}}} \times \mathbf{100}$$

where RFU_{100} is the fluorescence value of 100% enzyme activity control group, RFU_{sample} is the fluorescence value of the tested sample or positive control, and the half inhibitory concentration (IC_{50}) was acquired when the collagenase was inhibited by 50% under assay conditions.

Determination of Elastase Inhibitory Activity

The inhibitory activity of *M. oleifera* leaf extracts on elastase was determined using N-succinyl-Ala-Ala-Ala-*p*-nitroanilide as the substrate (18). In brief, 10 μL of sample solution was mixed with 90 μL of Tris–HCl buffer solution (50 mM, pH = 7.8) and 20 μL of elastase solution (0.5 units/μL), and the mixture solution was incubated for 15 min in a 96-well plate at 37 °C in darkness. Later, 80 μL of the substrate N-succinyl-Ala-Ala-Ala-*p*-nitroanilide (2 mM, dissolved in Tris–HCl buffer solution) was added to start the reaction. After incubation for 30 min at 37 °C in darkness, the absorbance was monitored at 405 nm. Meanwhile, ascorbic acid (0.125-2 mM) was used as the positive control, and each sample was tested in triplicate. The inhibitory activity of *M. oleifera* leaf extracts on elastase was expressed as 50% inhibitory concentration (IC_{50}). The inhibition rate was calculated according to the following formula:

$$\textbf{Inhibition rate}\ (\%) = (\mathbf{1} - \frac{\mathbf{Abs_{sample} - Abs_{sample-blank}}}{\mathbf{Abs_{control} - Abs_{control-blank}}}) \times \mathbf{100}$$

where Abs_{sample} is the absorbance of sample group with elastase, $Abs_{sample-blank}$ is the absorbance of sample group without elastase, $Abs_{control}$ is the absorbance of 100% elastase, and $Abs_{control-blank}$ is the absorbance of the reagent blank without elastase.

Affinity Ultrafiltration Procedures

The potential anti-aging components in *M. oleifera* leaves exhibiting different binding affinities with elastase, collagenase, and hyaluronidase were screened out by affinity ultrafiltration. The screening procedures were conducted according to our previous method with some modifications (15, 19), which mainly includes three major steps, namely, incubation, ultrafiltration, and analysis. In brief, the *M. oleifera* leaf extracts were weighed accurately and fully dissolved in Tris–HCl buffer solution (pH = 7.8, for elastase and collagenase) or PBS buffer solution (pH = 5.35, for hyaluronidase) at the final concentration of 8 mg/mL. Later, 100 μL of prepared sample solution was mixed with 20 μL of elastase (10 U), 40 μL of collagenase (2 U), or 40 μL of hyaluronidase (60 U) in a 1.5 mL EP tube and then incubated at 37 °C for 40 min in the water bath. At the same time, for the negative control group, the incubation conditions for the inactivated elastase, collagenase, or hyaluronidase, which was obtained in boiling water for 15 min, were the same as active enzymes. After incubation, the mixtures were ultra-filtrated through a 10 KD cutoff ultrafiltration membrane (Millipore, 0.5 mL) by centrifuging at 10,000 rpm for 10 min. Then, the membranes were eluted with 200 μL Tris–HCl or PBS buffer solutions 3 times to remove the unbound ligands. Subsequently, the ligands with specific bindings to elastase, collagenase, or hyaluronidase were released from the complexes by being incubated with 200 μL of 90% *(v/v)* MeOH-H_2O for 10 min at room temperature and followed by centrifugation at 10,000 rpm for 10 min. This step was repeated three times. Later, the filtrates above were collected and combined. Finally, they were dried using a nitrogen blower and then dissolved in 50 μL of methanol for the HPLC-UV-ESI-MS/MS analysis.

By comparing the varieties of peak areas in the chromatograms of active and inactive enzymes, specific bindings to elastase, collagenase, and hyaluronidase were defined with the binding degree (BD) using the following formula (20):

$$\textbf{Binding degree}\ (\%) = \left(\frac{\mathbf{A_a - A_b}}{\mathbf{A_a}}\right) \times \mathbf{100\%}$$

where A_a and A_b are the peak areas in the chromatograms of active and inactive elastase, collagenase and hyaluronidase enzymes, respectively. If the peak area in the active enzyme group is bigger than that in the inactive enzyme group, the compound is considered as potentially active ligands.

HPLC-UV/ESI-MS/MS Analysis

The HPLC-UV/ESI-MS/MS analysis was performed using a TSQ Quantum Access MAX mass spectrometer in the negative mode, which was connected with a Thermo Accela 600 series HPLC system (Thermo Fisher Scientific, San Jose, CA, USA). The chromatographic separation of samples was carried out using a Waters Symmetry RP-C18 column (250 mm × 4.6 mm, 5 μm) at 25 °C. The mobile phases consisted of 0.1% (*v/v*) formic acid–water (A) and acetonitrile (B). The HPLC elution procedures were optimized as follows: 0–30 min, 8–30% B; 30–40 min, 30–95% B. The injection volume of all the samples was 10 μL, the flow rate was set at 800 μL/min, and the wavelength was monitored at 280 nm. Moreover, the optimized parameters of the MS instrument were implemented as follows: capillary temperature of 350 °C; vaporizer temperature of 300 °C; spray voltage of 3,000 V; sheath gas (nitrogen, N_2) of 40 psi; auxiliary gas (N_2) of 10 psi; and mass range (*m/z*) of 100–1,500. The mass spectrum data were obtained in the full-scan and the data-dependent mode and analyzed by the Thermo Xcalibur ChemStation (Thermo Fisher Scientific).

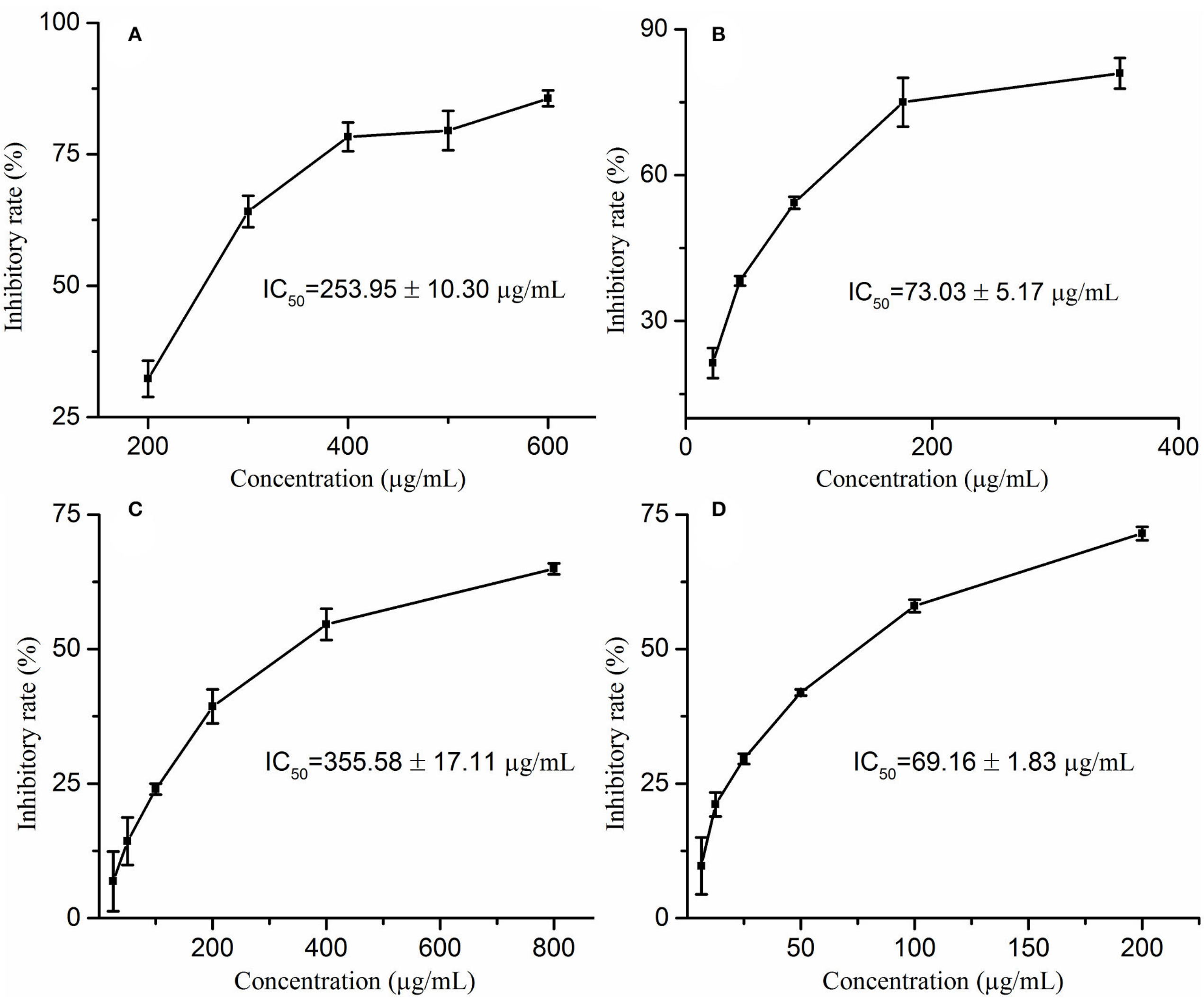

FIGURE 1 | The inhibitory rates of *Moringa oleifera* leaf extracts on elastase **(A)** and collagenase **(C)** as well as their corresponding positive drugs ascorbic acid **(B)** on elastase, EGCG **(D)** on collagenase.

Molecular Docking Analysis

Molecular docking analysis between potential ligands in *M. oleifera* leaf extracts and elastase, collagenase, and hyaluronidase were performed by the AutoDock Vina 1.5.6 and Discovery Studio 4.5 Client. The analytical steps generally consisted of the measurement of the binding modes between the proteins and the small ligands, assessment of the scoring system, and the calculation of docking results according to our previous study (15). In brief, the crystal structures of elastase (PDB: 1U4G), collagenase (PDB: 1CGL), and hyaluronidase (PDB: 1FCV) were downloaded from the RCSB Protein Data Bank (www.rcsb.org). The three-dimensional (3D) structures of the ligands with the lowest energies were obtained by ChemBio3D Ultra. Subsequently, the 3D structures of ligands and receptors were processed by removing the water molecules, adding the hydrogen atoms, calculating the charge, and so on by AutoDock Tools. Later, the docking active sites of elastase, collagenase, and hyaluronidase were obtained by Discovery Studio 4.5 Client. Thereinto, the coordinates of the active sites of elastase were (X: 17.554; Y: 28.659; Z: −4.625), collagenase (X: 23.679; Y: 44.947; Z: −8.569), and hyaluronidase (X: 4.447; Y: 29.902; Z: −9.110), respectively. Besides, the grid box was centered on the active sites of the receptors with a dimension size of 60 Å × 60 Å × 60 Å. Finally, molecular docking analysis between ligands and receptors was performed with 50 independent runs of the genetic algorithm by AutoDock Tools with other default parameters. In addition, EGCG was used as a positive control against collagenase and hyaluronidase enzymes, and ascorbic acid was applied as a positive drug against elastase enzyme.

Statistical Analysis

In this study, the half inhibitory concentration (IC_{50}) was calculated by nonlinear regression analysis and represented as

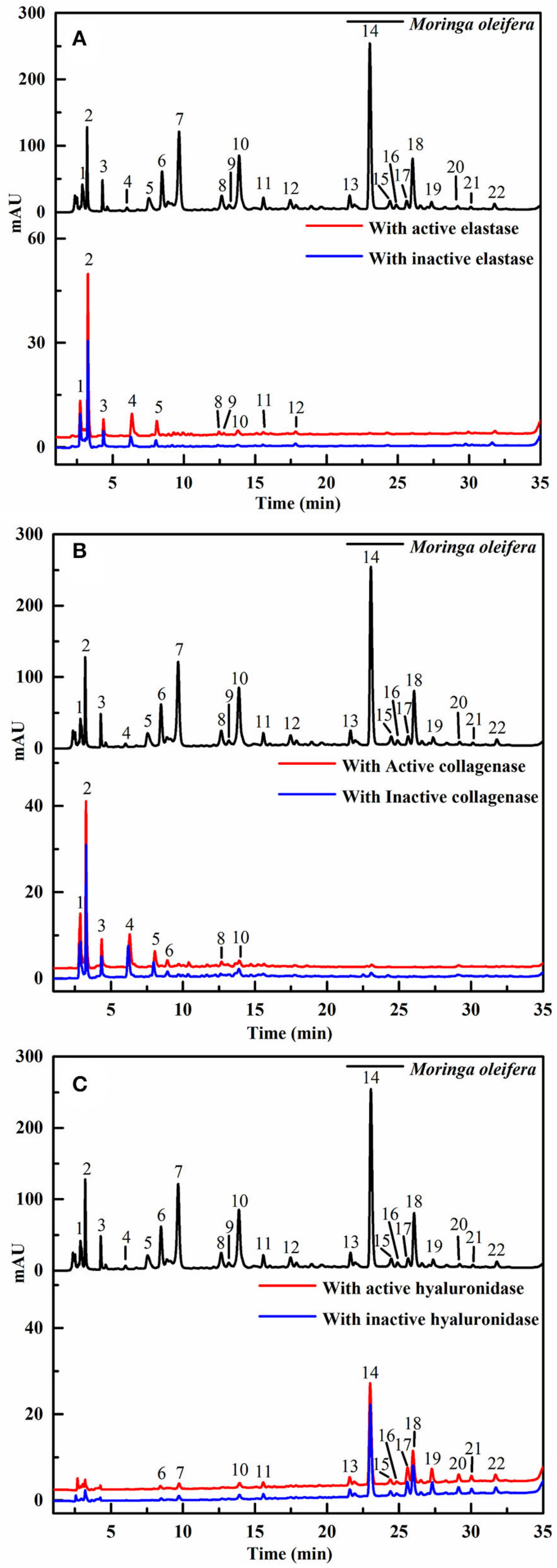

FIGURE 2 | The high-performance liquid chromatography (HPLC) profiles of the chemical components in *M. oleifera* were monitored after affinity

(Continued)

FIGURE 2 | ultrafiltration at 280 nm. The black line represents HPLC chromatograms of *M. oleifera* leaf extracts without ultrafiltration; the red line and blue line represent the leaf extract of *M. oleifera* with activated and inactivated elastase **(A)** collagenase **(B)** and hyaluronidase **(C)** respectively.

means ± standard deviation (SD) employed using SPSS 22.0 (IBM Corp., New York, USA).

RESULTS

In vitro Collagenase and Elastase Inhibitory Activities

Wrinkles are one of the characteristics of aging, and the degradation of elastin and collagen is the main cause of wrinkles. Moreover, elastase and collagenase play a pivotal role in the degradation of elastin and collagen, respectively. Therefore, exploring natural elastase and collagenase inhibitors has become one of the effective ways to delay aging. In this study, the anti-aging activities of *M. oleifera* leaf extracts were evaluated by determining the inhibitory activities against collagenase and elastase *in vitro*. On the one hand, this study reveals that *M. oleifera* leaf extracts exhibited a promising anti-collagenase effect in a concentration-dependent manner with a 50% inhibition value (IC_{50} value) at 355.58 ± 17.11 μg/mL, whereas the IC_{50} value of the positive drug epigallocatechin gallate (EGCG) was 69.16 ± 1.83 μg/mL (**Figures 1A,B**). On the other hand, it is clear from **Figures 1C,D** that *M. oleifera* leaf extracts showed considerable elastase inhibitory activity with an IC_{50} value of 253.95 ± 10.30 μg/mL, while the positive control ascorbic acid showed an IC_{50} value of 73.03 ± 5.17 μg/mL.

Screening for the Potential Elastase, Collagenase, and Hyaluronidase Ligands in *M. oleifera*

Recently, affinity ultrafiltration coupled with high-performance liquid chromatography-mass spectrometry (AUF-HPLC-MS) technology has been successfully used to find out the bioactive ingredients in complex samples (21, 22). In this study, the AUF-LC-MS method was employed to screen the potential anti-aging components against elastase, collagenase, and hyaluronidase. After incubation with elastase, collagenase, and hyaluronidase for affinity ultrafiltration, the bound ligands in *M. oleifera* leaves were released and analyzed by LC-MS. As shown in **Figure 2**, it was observed that 10, 8, and 14 phytochemicals from *M. oleifera* leaf extracts exhibited differential bindings to the elastase, collagenase, and hyaluronidase enzymes, respectively. The specific BD of each compound is displayed in **Table 1**. Among them, 4-caffeoylquinic acid (Peak 8) possessed the highest specific BD (49.15%) for collagenase enzyme, followed by quinic acid (37.18%), vicenin-2 (26.92%), etc. Similarly, 4-caffeoylquinic acid (Peak 8) also displayed the highest specific BD (62.34%) for elastase enzyme, followed by vicenin-2 (59.49%), glucomoringin (59.13%), etc. In addition, 3-caffeoylquinic acid (Peak 6) exhibited the strongest specific BD (36.75%), followed

TABLE 1 | The binding degree (BD) and the affinity ultrafiltration coupled with high-performance liquid chromatography-mass spectrometry (AUF-LC/MS) data of the bioactive compounds bound to elastase, collagenase, and hyaluronidase enzymes from *Moringa oleifera* leaf extracts.

Peak No.	RT[a] (min)	BD[b] (%)			$[M-H]^-$	Characteristic fragment (*m/z*)	Identification
		Ela[c]	Col[d]	Hya[e]			
1	2.88	3.43	20.44	-	341	341, 179, 119, 113, 89	Sucrose
2	3.21	36.76	37.18	-	191	191, 173, 127, 93, 85	Quinic acid
3	4.29	10.62	7.12	-	290	290, 200, 170, 154, 128	*N*-Fructosyl pyroglutamate
4	6.00	58.00	8.90	-	326	164, 147, 101	Methyl 4-(α-L-rhamnopyranosyloxy) benzylcarbamate
5	7.54	59.13	13.31	-	570	570, 328, 259, 241,97	Glucomoringin
6	8.49	-	25.83	36.75	353	191, 179, 135	3-Caffeoylquinic acid
7	9.66	-	-	21.87	337	191, 163, 119	3-Coumaroylquinic acid
8	12.65	62.34	49.15	-	353	191, 179, 173, 135	4-Caffeoylquinic acid
9	13.17	58.91	-	-	401	401, 269, 161, 113	Benzyl alcohol-hexose-pentose
10	13.88	59.49	26.91	9.53	593	593, 473, 383, 353	Vicenin-2
11	15.58	39.64	-	10.02	337	173, 163, 119	4-Coumaroylquinic acid
12	17.46	5.98	-	-	612	612, 370, 259, 97	4-(*O*-Acetyl-α-L-rhamnopyranosyloxy) benzyl glucosinolate
13	21.62	-	-	11.53	431	341, 311, 283	Apigenin 8-*C*-glucoside
14	23.04	-	-	10.60	463	463, 301, 300	Quercetin 3-*O*-glucoside
15	24.46	-	-	27.11	593	593, 285	Kaempferol 3-*O*-rutinoside
16	24.89	-	-	11.65	607	545, 505, 463, 301, 300	Quercetin-hydroxy-methylglutaroyl glycoside
17	25.62	-	-	16.63	549	505, 301, 300	Quercetin 3-*O*-(6"-malonylglucoside)
18	26.04	-	-	15.03	447	447, 285, 284, 255	Kaempferol 3-*O*-glucoside
19	27.36	-	-	14.34	477	477, 315, 314, 243	Isorhamnetin 3-*O*-glucoside
20	29.19	-	-	11.38	533	489, 285, 284	Kaempferol 3-*O*-(6"-malonylglucoside)
21	30.11	-	-	14.23	531	531, 463, 301, 300, 271	Quercetin derivative
22	31.78	-	-	13.81	515	515, 285, 284, 269, 255	Kaempferol-di-acetyl-rhamnoside

[a]RT, retention time; [b]BD, binding degree; [c]Ela, elastase; [d]Col, collagenase; [e]Hya, hyaluronidase.

by kaempferol 3-*O*-rutinoside (27.11%), 3-coumaroylquinic acid (21.87%), and so on.

Structural Identification of the Elastase, Collagenase, and Hyaluronidase Ligands by LC-MS

After the affinity ultrafiltration screening procedures, 10, 8, and 14 phytochemicals in *M. oleifera* leaf extracts displayed specific bindings to elastase, collagenase, and hyaluronidase enzymes, respectively, as exhibited in **Figure 2**. These potential bioactive compounds were further identified and characterized by LC-MS. The details of these components of mass spectra data including retention time (RT), quasi-molecular ions ($[M-H]^-$), and the characteristic MS/MS fragments are shown in **Table 1**. As a consequence, a total of 22 potential bioactive ligands in *M. oleifera* leaf extracts were continuously characterized and identified by comparing their mass spectra data and the fragmentation pathways with previous studies (4, 23–28). The representative bioactive ligands in *M. oleifera* leaf extracts with elastase, collagenase, and hyaluronidase enzymes are shown in **Figure 3**.

Molecular Docking Analysis

Molecular docking has been commonly used to evaluate the interaction between ligands and macromolecular receptors at atomic and molecular levels and predict the optimal binding situation by studying their docking energy, site of action, and key residues (29, 30). In this study, a molecular docking strategy was employed to simulate the interactions between elastase, collagenase, and hyaluronidase, and some representative bioactive compounds fished out from *M. oleifera* leaf extracts for the sake of their potential mechanism of action. The molecular docking results are displayed in **Table 2**. Thereinto, 4-caffeoylquinic acid (Peak 8) showed a stronger affinity to elastase with the lower binding energy (BE) of −3.93 kcal/mol and the theoretical IC_{50} value of 1.31 mM, and it was comparable with the positive drug ascorbic acid (−4.01 kcal/mol and 1.14 mM). On the contrary, sucrose displayed a lower affinity to elastase with the BE of −1.00 kcal/mol and the theoretical IC_{50} value of 183.99 mM. As regards to collagenase, 4-caffeoylquinic acid (Peak 8) also displayed a higher affinity to collagenase with the lower BE of −4.74 kcal/mol, and the theoretical IC_{50} value of 0.33 mM, which was weaker than the positive drug epigallocatechin gallate (−5.96 kcal/mol and 0.04 mM) but stronger than *N*-fructosyl pyroglutamate (Peak 3, −2.87 kcal/mol and 7.92 mM). In addition, the results of the 2D and 3D ligand-to-protein interactions between collagenase and *N*-fructosyl pyroglutamate (Peak 3), 4-caffeoylquinic acid (Peak 8), vicenin-2 (Peak 10), and epigallocatechin gallate are shown in **Figure 4**. With respect to hyaluronidase, 3-caffeoylquinic

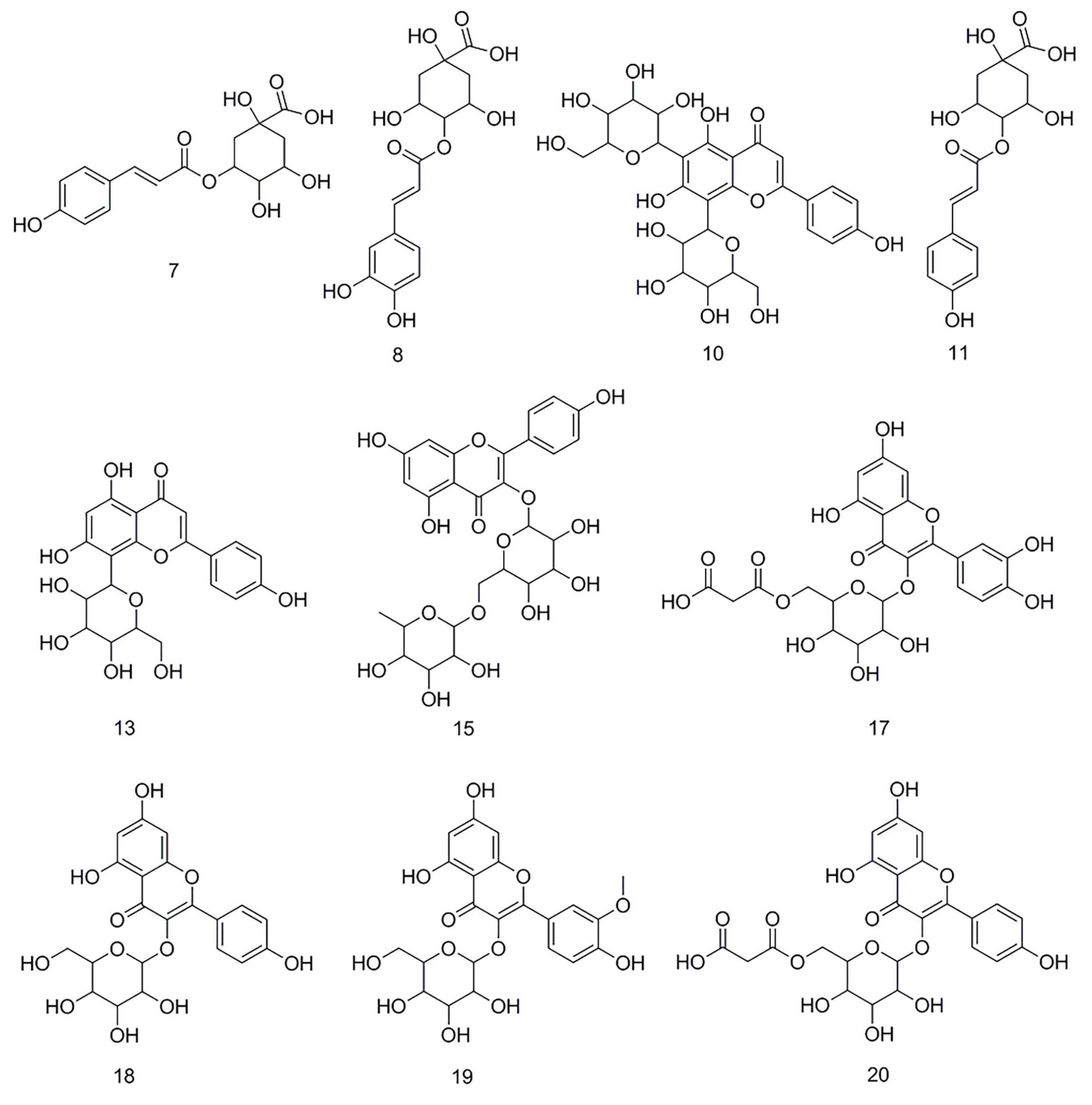

FIGURE 3 | The representative bioactive compounds figured out and identified in *M. oleifera* leaf extracts.

acid (Peak 6) exhibited a strong affinity to hyaluronidase, and its BE and theoretical IC_{50} value were computed as −4.25 kcal/mol and 0.77 mM, respectively, lower than the positive drug epigallocatechin gallate (−5.03 kcal/mol and 0.20 mM). In the meantime, vicenin-2 (Peak 10) exhibited a lower affinity to hyaluronidase with the BE of −2.02 kcal/mol and the theoretical IC_{50} value of 33.17 mM. As displayed in **Tables 1**, **2**, it was found that descending orders of BEs of some representative potential ligands screened out from *M. oleifera* leaf extracts in the molecular docking results were consistent with their BDs in the affinity ultrafiltration results. For example, 4-caffeoylquinic acid (Peak 8) with the highest BD exhibited the strongest affinity to elastase and collagenase, possessing the most potential anti-elastase and anti-collagenase activities by molecular docking analysis. Similarly, 3-caffeoylquinic acid (Peak 6) with high BD exerted good affinity to hyaluronidase, owning potential anti-hyaluronidase effect by molecular docking analysis.

TABLE 2 | The molecular docking results of the presentative active ingredients in *M. oleifera* leaf extracts and positive drugs against elastase, collagenase, and hyaluronidase, respectively.

No.	Compounds	Protein	BE[a] (kcal/mol)	IC_{50} (mM)	H-bond atoms[b]
1	Sucrose	Elastase	−1.00	183.99	Ala113, Trp115, Glu141
2	*N*-Fructosyl pyroglutamate	Collagenase	−2.87	7.92	Leu181, Ala182, Pro238, Tyr240
3	3-Caffeoylquinic acid	Hyaluronidase	−4.25	0.77	Arg47, Asp111, Glu113
4	4-Caffeoylquinic acid	Elastase	−3.93	1.31	Asn112, Trp115
		Collagenase	−4.74	0.33	Arg214, Val215, Glu219
5	Vicenin-2	Elastase	−2.80	8.91	Trp115, Glu141, Glu164, Asp221
		Collagenase	−4.52	0.49	Glu219, Pro 238
		Hyaluronidase	−2.02	33.17	Arg47, Asp56, Gly58, Ser304
6	Kaempferol 3-*O*-glucoside	Hyaluronidase	−3.80	1.65	Arg47, Tyr55, Asp56, Gln98, Ser304
7	Ascorbic acid[c]	Elastase	−4.01	1.14	Asn112, Ala113, Trp115, His144, Glu164, His223
8	Epigallocatechin gallate[d]	Collagenase	−5.96	0.04	Asp175, Gly179, Asn180, Leu181, Ala182, Glu219, Tyr237
		Hyaluronidase	−5.03	0.20	Asp111, Glu113, Tyr184, Gly302

[a]BE, binding energy; [b]H-bond, hydrogen bond; [c,d]positive drug; Ala, alanine; Arg, arginase; Asn, asparagine; Asp, aspartic acid; Gln, glutamine; Glu, glutamic acid; Gly, glycine; His, histidine; Leu, leucine; Pro, proline; Ser, serine; Trp, tryptophan; Tyr, tyrosine; Val, valine.

DISCUSSION

In vitro Collagenase and Elastase Inhibitory Activities

Recently, plenty of studies has indicated that *M. oleifera* possesses anti-aging activity and can delay skin aging (11, 13, 31). For example, a previous study found that *M. oleifera* leaf extracts possess the most powerful life span extending property of *C. elegans* (11). However, most of them used animal test models or cell models, and there is scarcely any research at the protein molecular level. Therefore, this study determines the inhibitory activities of *M. oleifera* leaf extracts on elastase and collagenase enzymes *in vitro*. The results indicated that M. *oleifera* leaf extracts exerted considerable anti-aging effects with IC_{50} values of 253.95 ± 10.30 μg/mL against elastase and 355.58 ± 17.11 μg/mL against collagenase. In a similar study, it was found that *Eucalyptus camaldulensis* bark extract showed IC_{50} values of 343.3 ± 5.4 μg/mL against elastase and 416.3 ± 5.6 μg/mL against collagenase (32). In another study, Freitas et al. measured the elastase and collagenase inhibitory activities of *Fucus spiralis* in 11 fractions, and the inhibitory effects of different fractions on elastase were from 3.0 μg/mL to 1,000 μg/mL (IC_{50} values), whereas the inhibitory effects on collagenase were 0.037–1,000 μg/mL (IC_{50} values) (33). In addition, a previous study found that *Phyllanthus emblica* displayed IC_{50} values of 387.85 ± 8.78 μg/mL against elastase, whereas *Manilkara zapota* was 35.73 ± 0.61 μg/mL against elastase enzyme (34). Compared with those plant materials, *M. oleifera* possessed moderate anti-elastase and anti-collagenase effects. To the best of our knowledge, this is the first study to determine the anti-elastase and anti-collagenase activities of *M. oleifera* leaf extracts.

Screening for the Potential Ligands in *M. oleifera* Against Elastase, Collagenase, and Hyaluronidase

Generally, the conventional strategy to screen bioactive components from the medicinal plants by enzyme inhibitory assays is both time-consuming and labor-intensive. For this purpose, affinity ultrafiltration based on the interactions between small bioactive molecules and the corresponding target enzymes coupled with high-performance liquid chromatography-mass spectrometry technology was developed in recent decades (35, 36). In this study, the AUF-HPLC/MS method was employed to fish out and identify 10, 8, and 14 potential bioactive phytochemicals in *M. oleifera* leaf extracts against elastase, collagenase, and hyaluronidase, respectively. To further investigate the underlying mechanisms of *M. oleifera* leaf extracts in the multi-constituent and multi-target manner, the potential active phytochemicals fished out from *M. oleifera* with multiple-target enzymes including elastase, collagenase, and hyaluronidase were then reconstructed as interaction network diagrams to better illuminate the relationships between the multicomponents and their corresponding target enzymes, as exhibited in **Figure 5**. According to the BD of each compound figured out from *M. oleifera* leaf extracts, Peaks 4, 5, 8, 9, and 10 exerted higher affinities with elastase, and they were preliminarily speculated to be the main active anti-elastase constituents. Furthermore, Peaks 2 and 8 exhibited relatively higher binding affinities with collagenase compared with other ligands, and they were inferred to be the primary anti-collagenase active ingredients. Moreover, Peak 6 displayed a stronger binding affinity to hyaluronidase, which may be the potential active anti-hyaluronidase compounds in *M. oleifera* leaf extracts. Interestingly, the major peaks in *M. oleifera* leaf extracts such as Peaks 14 and 18 were nearly undetected when subjected to bio-affinity ultrafiltration with elastase and collagenase. On the contrary, the dominant peaks including Peaks 14 and 18 were detected when subjected to bio-affinity ultrafiltration with hyaluronidase. More importantly, the results indicated that the potential active ligands of elastase and collagenase have a higher degree of overlap, while hyaluronidase is less overlapped with the other two enzymes, indicating that the active sites of elastase and collagenase may be similar, whereas the active sites of hyaluronidase may be different with elastase

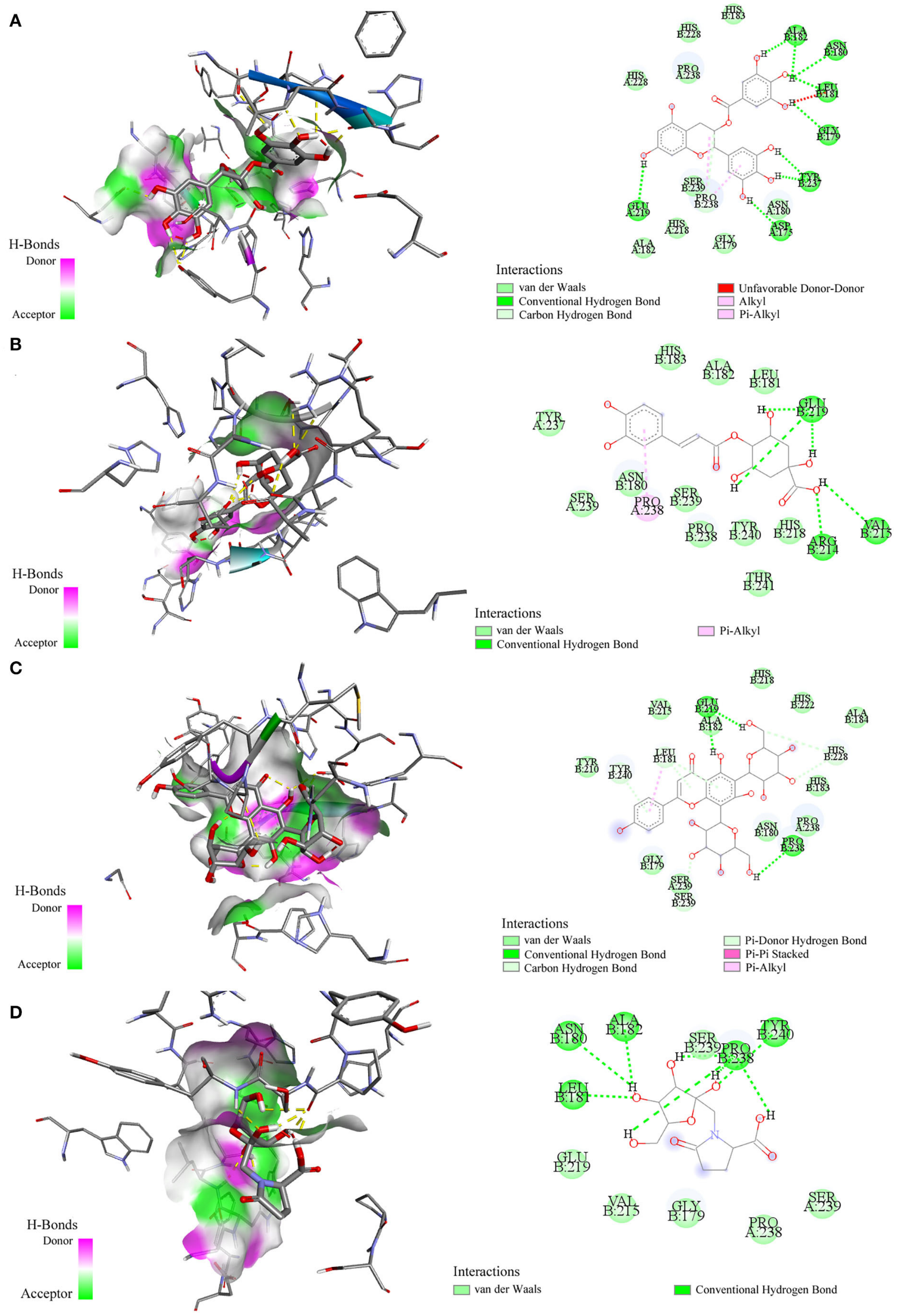

FIGURE 4 | Interactions between collagenase and epigallocatechin gallate **(A)** 4-caffeoylquinic acid **(B)** vicenin-2 **(C)** and N-fructosyl pyroglutamate **(D)** by molecular docking analysis, respectively.

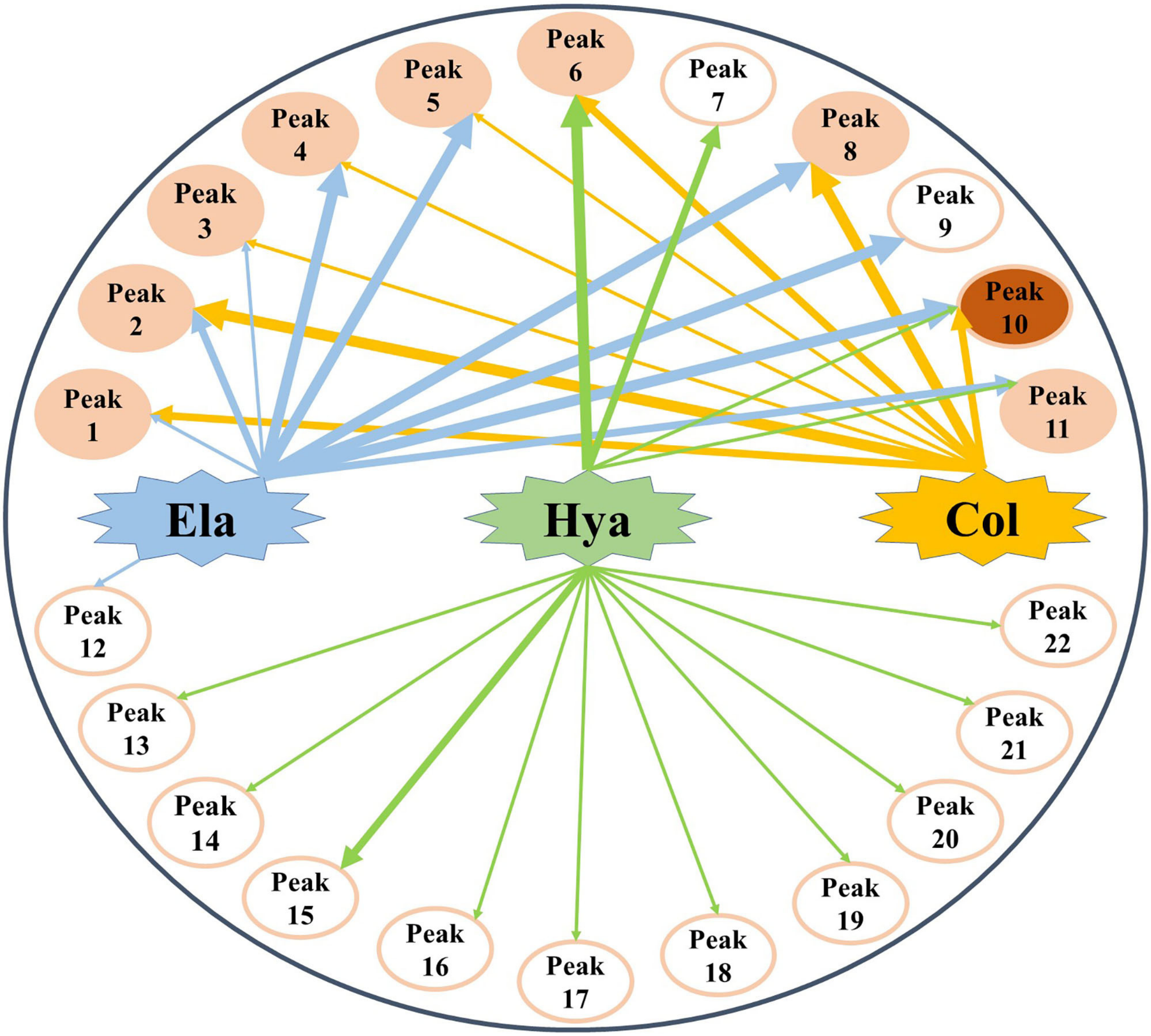

FIGURE 5 | The multicomponent and multi-target network between target enzymes and their corresponding potential bioactive ligands screened out from *M. oleifera* leaf extracts. The thicknesses of lines roughly represent the binding intensity for their corresponding interactions. Ela, elastase; Hya, hyaluronidase; Col, collagenase.

and collagenase. In the meantime, these shared common active phytochemicals (Peaks 1, 2, 3, 4, 5, 6, 8, 10, and 11) screened out from *M. oleifera* leaf extracts may exert synergistic effects in anti-aging activities, especially Peak 10 showed a good binding affinity with these all three enzymes. Meanwhile, those compounds with higher BDs mostly were phenolic acids and flavonoids and suggested that flavonoids and phenolic acids were the main potential antiaging components in *M. oleifera* leaf extracts. The results were similar to previous research (17, 37).

In addition, the bioactive activity of one compound is closely related to its structure. The structure-activity relationship was illuminating in this study by taking 4-caffeoylquinic acid (Peak 8) and 3-caffeoylquinic acid (Peak 6) as an example. It was reported that caffeoyl groups bound to quinic acid are important for activity (38). This may be due to the two neighboring phenolic structures as well as the α, β-conjugated unsaturated ester structure of the caffeoyl group increased the benzene ring planar conjugation. Moreover, the previous research found that quinic acid esterified with caffeoyl groups at the C-4 position showed higher anti-free radical activity compared with acylation at the C-3 or C-5 positions (39). Interestingly, in this study, 4-caffeoylquinic acid (Peak 8) showed a higher BD value than 3-caffeoylquinic acid (Peak 6) in *M. oleifera* leaf extracts with collagenase. It suggested that quinic acid esterified with caffeoyl groups at the C-4 position showed a stronger binding affinity with collagenase compared with acylation at the C-3 position.

Molecular Docking Analysis

As exhibited in **Table 1**, some potential active constituents had been quickly figured out from *M. oleifera* leaf extract against elastase, collagenase, and hyaluronidase. Thereinto, 4-caffeoylquinic acid (Peak 8), quinic acid (Peak 2), and vicenin-2 (Peak 10) possessed the relatively higher BD (49.15%, 37.18%, and 26.92%) to collagenase enzyme, and *N*-fructosyl pyroglutamate (Peak 3) showed relatively lower BD (7.12%). Furthermore, 4-caffeoylquinic acid (Peak 8) also exhibited the highest specific BD (62.34%) for elastase enzyme; on the contrary, sucrose (Peak 1) possessed the lowest BD (3.43%). In addition, 3-caffeoylquinic acid (Peak 6) displayed the greatest higher BD (36.75%), whereas vicenin-2 (Peak 10) possessed the relatively lower BD (9.53%). The molecular docking results of these components and positive drugs including ascorbic acid and epigallocatechin gallate against elastase, collagenase, and hyaluronidase are displayed in **Table 2**, which indicated that the potential active ligands with higher BD possessed lower binding energy (BE) to enzymes and lower theoretical IC_{50} values. For example, 4-caffeoylquinic acid (Peak 8), vicenin-2 (Peak 10) and *N*-fructosyl pyroglutamate (Peak 3) possessed the BE of −4.74, −4.52, and −2.87 kcal/mol, as well as the theoretical IC_{50} values of 0.33, 0.49, and 7.92 mM, respectively. The results were consistent with their results of BD with collagenase. In addition, the main peaks such as 18 and 14 in *M. oleifera* leaf extracts were fished out by binding with hyaluronidase, while terms of elastase and collagenase were undetected. Meanwhile, the active components screened out by binding with elastase and collagenase were similar. Furthermore, the molecular docking results also supported this finding. For example, 4-caffeoylquinic acid (Peak 8) possessed the BE values of −3.93 and −4.74 kcal/mol, as well as the theoretical IC_{50} values of 1.31 and 0.33 mM with elastase and collagenase, respectively.

Moreover, these potential active components formed diverse numbers of hydrogen bonds (H-bond) with different types of amino acid residues of elastase, e.g. Asn112, Ala113, Trp115, Glu141, Glu164, and Asp221. As for collagenase, the amino acid residues formed H-bonds with these potential active constituents, including Leu181, Ala182, Arg214, Val215, Glu219, Pro238, Tyr240, and so on. Similarly, Arg47, Tyr55, Asp56, Gly58, Gln98, Asp111, Glu113, Ser304, and the like formed H-bonds with potential active ligands binding with hyaluronidase. Meanwhile, the positive drug ascorbic acid formed H-bonds with amino acid residues of Asn112, Ala113, Trp115, His144, Glu164, and His223 at elastase. 4-Caffeoylquinic acid (Peak 8) with higher BD showed the H-bonds with the acid residues of Asn112 and Trp115 at elastase. It can be inferred that the residues Asn112 and Trp115 were the key residues of elastase. Additionally, this interaction may influence the elastase structure and activity. In addition, the positive drug EGCG formed H-bonds with the residues Asp111, Glu113, Tyr184, and Gly302 of hyaluronidase, and 3-caffeoylquinic acid (Peak 6) with high special binding affinity formed H-bonds with the residues Arg47, Asp111, and Glu113 of hyaluronidase. The result suggested that the residues Asp111 and Glu113 were the potential crucial residues of hyaluronidase. Moreover, there are some other forces including the van der Waals force, Pi-Alkyl, Alkyl, and Pi-Pi stacked forces contributed to the interactions between the three enzymes and those potential active ligands in the molecular docking analysis. Taking collagenase as an example, more details about the interaction between collagenase and its potential active ligands as well as the positive drug EGCG are displayed in **Figure 4**. Overall, the results of molecular docking analysis were consistent with affinity ultrafiltration. Therefore, these phytochemicals screened out from *M. oleifera* leaf extracts were promising to be developed as anti-aging agents.

CONCLUSION

At present, the potential bioactive phytochemicals and the underlying mechanism of *M. oleifera* leaf extracts for anti-aging activity remained elusive. In this study, the *in vitro* inhibitory assays against elastase and collagenase first confirmed that *M. oleifera* leaf extracts possessed promising anti-elastase and anti-collagenase activities. Then, 10, 8, and 14 potential bioactive phytochemicals were screened out from *M. oleifera* leaf extracts against elastase, collagenase, and hyaluronidase using the AUF-HPLC-MS approach, respectively. In addition, further verification of representative active components was employed by molecular docking analysis. To the best of our knowledge, this is the first study to systematically study the anti-elastase and anti-collagenase activities of *M. oleifera in vitro*, the potential bioactive constituents, as well as underlying mechanisms by AUF-HPLC-MS method and molecular docking analysis. In brief, the results indicated that *M. oleifera* leaf extracts exhibited an outstanding anti-aging effect, and *M. oleifera* leaves were a very promising natural source of anti-skin aging ingredients, which can be further explored in cosmetics and cosmeceutical industries combating aging and skin wrinkling.

DATA AVAILABILITY STATEMENT

The original contributions presented in the study are included in the article/supplementary material, further inquiries can be directed to the corresponding author.

AUTHOR CONTRIBUTIONS

YX: investigation, data curation, formal analysis, software, validation, and writing – original draft. GC: data curation, formal analysis, writing – review and editing, and funding acquisition. MG: conceptualization, methodology, resources, visualization, and project administration, supervision, writing – review and editing, and funding acquisition. All authors contributed to the article and approved the submitted version.

FUNDING

This study was partly supported by the Natural Science Foundation of Hubei Province (Grant No. 2019CFB254 to GC).

ACKNOWLEDGMENTS

The authors would like to thank Prof. Guangwan Hu for his assistance in the authentication of the plant material.

REFERENCES

1. Bahadir Acikara O, Ilhan M, Kurtul E, Smejkal K, Kupeli Akkol E. Inhibitory activity of *Podospermum canum* and its active components on collagenase, elastase and hyaluronidase enzymes. *Bioorg Chem.* (2019) 93:103330. doi: 10.1016/j.bioorg.2019.103330
2. Bose B, Choudhury H, Tandon P, Kumaria S. Studies on secondary metabolite profiling, anti-inflammatory potential, *in vitro* photoprotective and skin-aging related enzyme inhibitory activities of *Malaxis acuminata*, a threatened orchid of nutraceutical importance. *J Photochem Photobiol B.* (2017) 173:686–95. doi: 10.1016/j.jphotobiol.2017.07.010
3. Dhakad AK, Ikram M, Sharma S, Khan S, Pandey VV, Singh A. Biological, nutritional, and therapeutic significance of *Moringa oleifera* Lam. *Phytother Res.* (2019) 33:2870–903. doi: 10.1002/ptr.6475
4. Xu YB, Chen GL, Guo MQ. Correlations between phytochemical fingerprints of *Moringa oleifera* leaf extracts and their antioxidant activities revealed by chemometric analysis. *Phytochem Anal.* (2021) 32:698–709. doi: 10.1002/pca.3016
5. Chen GL, Xu YB, Wu JL Li N, Guo MQ. Anti-inflammatory properties and potential bioactive components from *Moringa oleifera* leaves revealed by affinity ultrafiltration LC–MS and molecular docking. *ACS Food Sci Technol.* (2021) 1:1953–62. doi: 10.1021/acsfoodscitech.1c00275
6. Garcia-Beltran JM, Mansour AT, Alsaqufi AS, Ali HM. Esteban MA. Effects of aqueous and ethanolic leaf extracts from drumstick tree *(Moringa oleifera)* on gilthead seabream (*Sparus aurata* L) leucocytes, and their cytotoxic, antitumor, bactericidal and antioxidant activities. *Fish Shellfish Immunol.* (2020) 106:44–55. doi: 10.1016/j.fsi.2020.06.054
7. Xie J, Luo FX, Shi CY, Jiang WW, Qian YY, Yang MR, et al. *Moringa oleifera* alkaloids inhibited PC3 cells growth and migration through the COX-2 mediated Wnt/β-Catenin signaling pathway. *Front Pharmacol.* (2020) 11:523962. doi: 10.3389/fphar.2020.523962
8. Bao YF, Xiao JB, Weng ZB, Lu XY, Shen XC, Wang F, et al. A phenolic glycoside from *Moringa oleifera* Lam. improves the carbohydrate and lipid metabolisms through AMPK in db/db mice. *Food Chem.* (2020) 311:125948. doi: 10.1016/j.foodchem.2019.125948
9. Xie J, Wang Y, Jiang WW, Luo XF Dai TY, Peng L, et al. *Moringa oleifera* leaf petroleum ether extract inhibits lipogenesis by activating the AMPK signaling pathway. *Front Pharmacol.* (2018) 9:1447. doi: 10.3389/fphar.2018.01447
10. Ajagun-Ogunleye MO, Ebuehi OAT. Evaluation of the anti-aging and antioxidant action of *Ananas sativa* and *Moringa oleifera* in a fruit fly model organism. *J Food Biochem.* (2020) 44:e13426. doi: 10.1111/jfbc.13426
11. Chauhan AP, Chaubey MG, Patel SN, Madamwar D, Singh NK. Extension of life span and stress tolerance modulated by DAF-16 in *Caenorhabditis elegans* under the treatment of *Moringa oleifera* extract. *3 Biotech.* (2020) 10:504. doi: 10.1007/s13205-020-02485-x
12. Nair DA, James TJ, Sreelatha SL, Kariyil BJ, Nair SN. *Moringa oleifera* (Lam.): a natural remedy for ageing? *Nat Prod Res.* (2020) 7:1–7. doi: 10.14719/pst.2020.7.4.936
13. Ali A, Akhtar N, Chowdhary F. Enhancement of human skin facial revitalization by moringa leaf extract cream. *Postepy Dermatol Alergol.* (2014) 31:71–6. doi: 10.5114/pdia.2014.40945
14. Feng HX, Chen GL, Zhang YL, Guo MQ. Exploring multifunctional bioactive components from *Podophyllum sinense* using multi-target ultrafiltration. *Front Pharmacol.* (2021) 12:749189. doi: 10.3389/fphar.2021.749189
15. Chen GL, Xu YB, Wu JL Li N, Guo MQ. Hypoglycemic and hypolipidemic effects of *Moringa oleifera* leaves and their functional chemical constituents. *Food Chem.* (2020) 333:127478. doi: 10.1016/j.foodchem.2020.127478
16. Wang SQ, Huai JX, Shang Y, Xie LL, Cao XT, Liao J, et al. Screening for natural inhibitors of 5-lipoxygenase from Zi-shen pill extract by affinity ultrafiltration coupled with ultra performance liquid chromatography-mass spectrometry. *J Ethnopharmacol.* (2020) 254:112733. doi: 10.1016/j.jep.2020.112733
17. Stavropoulou MI, Stathopoulou K, Cheilari A, Benaki D, Gardikis K, Chinou I, et al. NMR metabolic profiling of greek propolis samples: Comparative evaluation of their phytochemical compositions and investigation of their anti-ageing and antioxidant properties. *J Pharm Biomed Anal.* (2021) 194:113814. doi: 10.1016/j.jpba.2020.113814
18. Angelis A, Mavros P, Nikolaou PE, Mitakou S, Halabalaki M, Skaltsounis L. Phytochemical analysis of olive flowers' hydroalcoholic extract and *in vitro* evaluation of tyrosinase, elastase and collagenase inhibition activity. *Fitoterapia.* (2020) 143:104602. doi: 10.1016/j.fitote.2020.104602
19. Liu Y, Muema FW, Zhang YL, Guo MQ. Acyl quinic acid derivatives screened out from *Carissa spinarum* by SOD-affinity ultrafiltration LC-MS and their antioxidative and hepatoprotective activities. *Antioxidants (Basel).* (2021) 10:1302. doi: 10.3390/antiox10081302
20. Jiao JJ, Yang YZ, Wu ZF Li BT, Zheng Q, Wei SF, et al. Screening cyclooxygenase-2 inhibitors from *Andrographis paniculata* to treat inflammation based on bio-affinity ultrafiltration coupled with UPLC-Q-TOF-MS. *Fitoterapia.* (2019) 137:104259. doi: 10.1016/j.fitote.2019.104259
21. Chen GL, Wu JL Li N, Guo MQ. Screening for anti-proliferative and anti-inflammatory components from *Rhamnus davurica* pall. using bio-affinity ultrafiltration with multiple drug targets. *Anal Bioanal Chem.* (2018) 410:3587–95. doi: 10.1007/s00216-018-0953-6
22. Chen GL, Guo MQ. Screening for natural inhibitors of Topoisomerases I from *Rhamnus davurica* by affinity ultrafiltration and high-performance liquid chromatography-mass spectrometry. *Front Plant Sci.* (2017) 8:1521. doi: 10.3389/fpls.2017.01521
23. Maldini M, Maksoud SA, Natella F, Montoro P, Petretto GL, Foddai M, et al. '*Moringa oleifera*: study of phenolics and glucosinolates by mass spectrometry'. *J Mass Spectrom.* (2014) 49:900–10. doi: 10.1002/jms.3437
24. Clifford MN, Knight S, Kuhnert N. Discriminating between the six isomers of dicaffeoylquinic acid by LC-MS$^{(n)}$. *J Agric Food Chem.* (2005) 53:3821–32. doi: 10.1021/jf050046h
25. Rodriguez-Perez C, Quirantes-Pine R, Fernandez-Gutierrez A, Segura-Carretero A. Optimization of extraction method to obtain a phenolic compounds-rich extract from *Moringa oleifera* Lam leaves. *Ind Crops Prod.* (2015) 66:246–54. doi: 10.1016/j.indcrop.2015.01.002
26. Sahakitpichan P, Mahidol C, Disadee W, Ruchirawat S, Kanchanapoom T. Unusual glycosides of pyrrole alkaloid and 4'-hydroxyphenylethanamide from leaves of *Moringa oleifera*. *Phytochemistry.* (2011) 72:791–5. doi: 10.1016/j.phytochem.2011.02.021
27. Amaglo NK, Bennett RN, Curto RBL, Rosa EAS, Turco VL, Giuffrida A, et al. Profiling selected phytochemicals and nutrients in different tissues of the multipurpose tree *Moringa oleifera* L. grown in Ghana. *Food Chem.* (2010) 122:1047–54. doi: 10.1016/j.foodchem.2010.03.073
28. Xu YB, Chen GL, Guo MQ. Antioxidant and anti-inflammatory activities of the crude extracts of *Moringa oleifera* from Kenya and their correlations with flavonoids. *Antioxidants (Basel).* (2019) 8:296. doi: 10.3390/antiox8080296
29. Chen GL, Seukep AJ, Guo MQ. Recent advances in molecular docking for the research and discovery of potential marine drugs. *Mar Drugs.* (2020) 18:545. doi: 10.3390/md18110545
30. Sivakumar KC, Haixiao J, Naman CB, Sajeevan TP. Prospects of multitarget drug designing strategies by linking molecular docking and molecular dynamics to explore the protein-ligand recognition process. *Drug Dev Res.* (2020) 81:685–99. doi: 10.1002/ddr.21673
31. Jadoon S, Karim S, Bin Asad MH, Akram MR, Khan AK, Malik A, et al. Anti-aging potential of phytoextract loaded-pharmaceutical creams for human skin cell longevity. *Oxid Med Cell Longev.* (2015) 2015:709628. doi: 10.1155/2015/709628

32. Radwan RA, El-Sherif YA, Salama MM. A novel biochemical study of anti-ageing potential of *Eucalyptus camaldulensis* bark waste standardized extract and silver nanoparticles. *Colloids Surf B Biointerfaces.* (2020) 191:111004. doi: 10.1016/j.colsurfb.2020.111004
33. Freitas R, Martins A, Silva J, Alves C, Pinteus S, Alves J, et al. Highlighting the biological potential of the brown seaweed *Fucus spiralis* for skin applications. *Antioxidants (Basel).* (2020) 9:611. doi: 10.3390/antiox9070611
34. Pientaweeratch S, Panapisal V, Tansirikongkol A. Antioxidant, anti-collagenase and anti-elastase activities of *Phyllanthus emblica*, *Manilkara zapota* and silymarin: an *in vitro* comparative study for anti-aging applications. *Pharm Biol.* (2016) 54:1865–72. doi: 10.3109/13880209.2015.1133658
35. Chen GL, Tian YQ, Wu JL Li N, Guo MQ. Antiproliferative activities of Amaryllidaceae alkaloids from *Lycoris radiata* targeting DNA topoisomerase I. *Sci Rep.* (2016) 6:38284. doi: 10.1038/srep38284
36. Cai YZ, Wu LF, Lin X, Hu XP, Wang L. Phenolic profiles and screening of potential α-glucosidase inhibitors from *Polygonum aviculare* L. leaves using ultra-filtration combined with HPLC-ESI-qTOF-MS/MS and molecular docking analysis. *Ind Crops Prod.* (2020) 154:112673. doi: 10.1016/j.indcrop.2020.112673
37. Shoko T, Maharaj VJ, Naidoo D, Tselanyane M, Nthambeleni R, Khorombi E, et al. Anti-aging potential of extracts from *Sclerocarya birrea* (A. *Rich)* hochst and its chemical profiling by UPLC-Q-TOF-MS. *BMC Complement Altern Med.* (2018) 18:54. doi: 10.1186/s12906-018-2112-1
38. Miyamae Y, Kurisu M, Han J, Isoda H, Shigemori H. Structure-activity relationship of caffeoylquinic acids on the accelerating activity on ATP production. *Chem Pharm Bull.* (2011) 59:502–7. doi: 10.1248/cpb.59.502
39. Tamayose CI, dos Santos EA, Roque N, Costa-Lotufo LV, Ferreira MJP. Caffeoylquinic acids: separation method, antiradical properties and cytotoxicity. *Chem Biodivers.* (2019) 16:e1900093. doi: 10.1002/cbdv.201900093

Conflict of Interest: The authors declare that the research was conducted in the absence of any commercial or financial relationships that could be construed as a potential conflict of interest.

Frontiers in Nutrition

ORIGINAL RESEARCH
published: 27 May 2022
doi: 10.3389/fnut.2022.886988

Lycopene in Combination With Sorafenib Additively Inhibits Tumor Metastasis in Mice Xenografted With Lewis Lung Carcinoma Cells

*Ya-Ping Chan[1], Cheng-Hung Chuang[2], Inn Lee[3] and Nae-Cherng Yang[3,4]**

[1] Department of Food Science and Biotechnology, National Chung Hsing University, Taichung, Taiwan, [2] Department of Nutrition, Hungkuang University, Taichung, Taiwan, [3] Department of Nutrition, Chung Shan Medical University, Taichung, Taiwan, [4] Department of Nutrition, Chung Shan Medical University Hospital, Taichung, Taiwan

Cancer metastasis is the leading cause of death in cancer patients. However, it is unclear whether lycopene can act as an adjuvant to increase the anti-metastatic activity of anticancer drugs. Here, we examined the anti-lung-metastatic effects and the mechanism of lycopene in combination with sorafenib in C57BL/6 mice xenografted with Lewis lung carcinoma (LLC) cells. The mice were divided into five groups: (1) tumor control; (2) lycopene (5 mg/kg); (3) sorafenib (30 mg/kg); (4) lycopene (2 mg/kg) + sorafenib (30 mg/kg); (5) lycopene (5 mg/kg) + sorafenib (30 mg/kg). The results showed that lycopene reduced the number of metastatic tumors in the lungs, which was further suppressed by the combined treatment with sorafenib. The activities of matrix metalloproteinase (MMP)-2 and−9 were further inhibited and TIMP-1 and−2, and NM23-H1, the MMPs negative modulators, were further activated in the combined treatment. Mechanistically, we found that lycopene and sorafenib could additively inhibit the mitogen-activated protein kinase (MAPK) pathways, as shown by the protein phosphorylation of ERK1/2, JNK1/2 and p38 were reduced additively. Overall, the present study demonstrates that lycopene in combination with sorafenib additively inhibits the lung metastasis of tumor, indicating lycopene has potential as an adjuvant for sorafenib in cancer treatment.

Keywords: lycopene, anti-metastasis, adjuvant, sorafenib, MAPK pathway, NOX4

Edited by:
Soon Sung Lim,
Hallym University, South Korea

Reviewed by:
Kulathida Chaithirayanon,
Mahidol University, Thailand
Frank Thies,
University of Aberdeen,
United Kingdom

Correspondence:
Nae-Cherng Yang
naeman@csmu.edu.tw

Specialty section:
This article was submitted to
Food Chemistry,
a section of the journal
Frontiers in Nutrition

Received: *01 March 2022*
Accepted: *14 April 2022*
Published: *27 May 2022*

Citation:
Chan Y-P, Chuang C-H, Lee I and Yang N-C (2022) Lycopene in Combination With Sorafenib Additively Inhibits Tumor Metastasis in Mice Xenografted With Lewis Lung Carcinoma Cells.
Front. Nutr. 9:886988.
doi: 10.3389/fnut.2022.886988

INTRODUCTION

According to the World Health Organization, lung cancer has the highest mortality rate of all cancers. In the United States, statistics from 2013 to 2018 show that men account for approximately 46.9% of lung cancer and women account for 32.0% (1). Cancer metastasis is a complicated process, which is one of the main causes of the recurrence and death of cancer patients. During the metastasis, cancer cells *in situ* move to other tissues and organs from the blood circulation or the lymphatic system through proliferation, adhesion, invasion, and migration. The metastasizing cells will proliferate in large numbers *in situ* and secrete proteolytic enzymes, such as the matrix metalloproteinases (MMPs), which degrade the extracellular matrix and blood vessel wall. The metastasizing cells penetrate the blood vessel wall by invasiveness, and migrate in the circulation, extravasate out of the blood vessels, colonize in the distant tissue, initiate angiogenesis, and finally grow at the new site (2, 3). Therefore, inhibiting cancer metastasis can be one of the strategies to effectively treat lung cancer.

Lycopene is a lipophilic natural compound with an acyclic and tetraterpene hydrocarbon compound containing 11 conjugated and two non-conjugated double bonds (4). It exists in nature as an all-transform structure. It is the most abundant carotenoid in tomatoes and can also be found in apricots, melons, papayas, grapes, peaches, watermelons, and cranberries (4, 5). Studies have shown that lycopene possesses a variety of functions such as anti-oxidation (6, 7) anti-inflammation (8), immunomodulation (9), enhancement of gap junctional communication (10), induction of phase II enzymes (11), inhibition of cell proliferation (12), anti-cancer (13, 14), anti-angiogenesis (9, 15), and anti-metastasis (16–18). In anti-metastatic studies, lycopene has been found to inhibit the metastasis of human hepatoma SK-Hep-1 cells in athymic nude mice (17). Moreover, we recently reported that lycopene inhibits the metastasis of human liver adenocarcinoma SK-Hep-1 cells by downregulation of the NADPH oxidase 4 (NOX4) proteins (18). It is known that adjuvant is defined as a substance that helps and enhances the effect of a drug or treatment (19). To this topic, lycopene had been demonstrated to have synergism from the combination of oxaliplatin in a human ovarian cancer cell line (20), suggesting that the adjuvant property on the anticancer of lycopene. However, the adjuvant potential of lycopene against the metastasis of lung cancer cells remains unknown.

Sorafenib is a first-line drug used in the clinical treatment of advanced liver cancer and kidney cancer so as to improve the overall survival for the patients (21, 22). Side effects of sorafenib include loss of appetite, diarrhea, hair thinning, nausea or vomiting, hand-foot syndrome, or weight loss. Adjuvant for the sorafenib treatment may not only increase the anticancer efficacy, but also ease the side effects of sorafenib. Sorafenib is a multiple kinase inhibitor whose mechanism is to inhibit the Raf / MEK / ERK [i.e., the extracellular signal-regulated kinase (ERK) pathway] signaling to decrease the tumor growth and angiogenesis, and to induce the tumor cell apoptosis (23–25). In the colorectal cancer model of nude mice by subcutaneous injection of HuH7 cells, sorafenib (10 mg/kg) was combined with triptolide, and triptolide (0.21 mg/kg) can inhibit the ERK pathway and the AKT / mTOR pathway to reduce tumor growth (26). The anti-metastasis effect of sorafenib had been demonstrated by using the model of nude mice induced by *in situ* transplantation of the LM3-R cells to induce liver cancer (27); they found that sorafenib (30 mg/kg) given daily in combination with daily subcutaneous injection of 10 mg/kg zoledronic acid (ZA) or intraperitoneal injection of clodrolip 100 mg/kg twice a week for 35 days, and sorafenib combined with ZA or clodrolip is more effective in anti-metastasis than sorafenib alone (27). However, the lung anti-metastasis efficacy of sorafenib in combination with lycopene in mice remains unknown.

In this study, the effects of lycopene in combination with sorafenib to inhibit cancer metastasis in mice xenografted with the Lewis lung carcinoma (LLC) cells were investigated. We hypothesized that lycopene could have an additive effect with sorafenib to inhibit the lung metastasis of tumors in the C57BL/6 mice xenografted LLC cells, because lycopene and sorafenib may act at the same target of the mitogen-activated protein kinase (MAPK) signaling pathway. The MAPK pathway mainly can be divided into ERK, c-Jun N-terminal kinase (JNK), and p38 pathways (28). As described above, the ERK pathway should be one of the main targets that sorafenib can have as an anti-cancer property (23–26). In addition, a study showed that the expression of matrix metalloproteinase (MMP)-2 was enhanced by the reactive oxygen species (ROS) through ROS-MAPK axis i.e., via the activation of ERK, JNK, and p38 pathways by the increased ROS (29). In addition, it had been demonstrated that lycopene could increase the MMP-2, MMP-9, and NM23-H1 expression via the inhibition of the NADPH oxidase (NOX) 4 to inhibit the metastasis of SK-Hep-1 cells (18). NOXs make up the only known enzyme family with the sole function of producing ROS (30, 31). Because of the existence of the ROS-MAPK axis (29, 32, 33), the inhibition of NOX4 by lycopene, theoretically, will decrease the ROS in cells and then inactivate the three MAPK pathways. In addition, the anti-oxidative property of lycopene itself could also decrease the ROS level to inactivate the three MAPK pathways. Thus, we mechanistically hypothesized that the expression of the MMPs will be additively inhibited by the treatment of lycopene combined with sorafenib via the additive inhibition on the three MAPK pathways, and eventually have an additive effect on the anti-lung-metastasis of the tumor. Besides, the additive effects of lycopene and sorafenib on the other negative modulators of metastasis, including the tissue inhibitors of the matrix metalloproteinase (TIMP)-1 and TIMP-2, and NM23-H1, an anti-metastatic protein, were also evaluated.

MATERIALS AND METHODS

Materials

All chemicals used were of analytical grade. Dulbecco's Modified Eagle Medium (DMEM), non-essential amino acid (NEAA), penicillin, sodium pyruvate, trypsin, fetal bovine serum (FBS) were purchased from GIBCO/BRL (Rockville, MD, USA). Lycopene (purity = 98%; Lot. CTN3163) was obtained from Wako (Osaka, Japan). Sorafenib was obtained from Bayer Corporation (West Haven, CT). Cremophor® EL (polyoxyethylated castor oil), coin oil, -mercaptoethanol, bromophenol blue, glycerol, glycine, N, N, N', N'-tetramethylethylenediamine (TEMED), polyoxyethylenesorbitan monolaurate (TWEEN® 20), sodium chloride, sodium dodecyl sulfate for electrophoresis (≥98.5%), Tris-HCl, Tris-base were purchased from Sigma Chemical company (St. Louis, MO, USA). Methanol (99.8%),

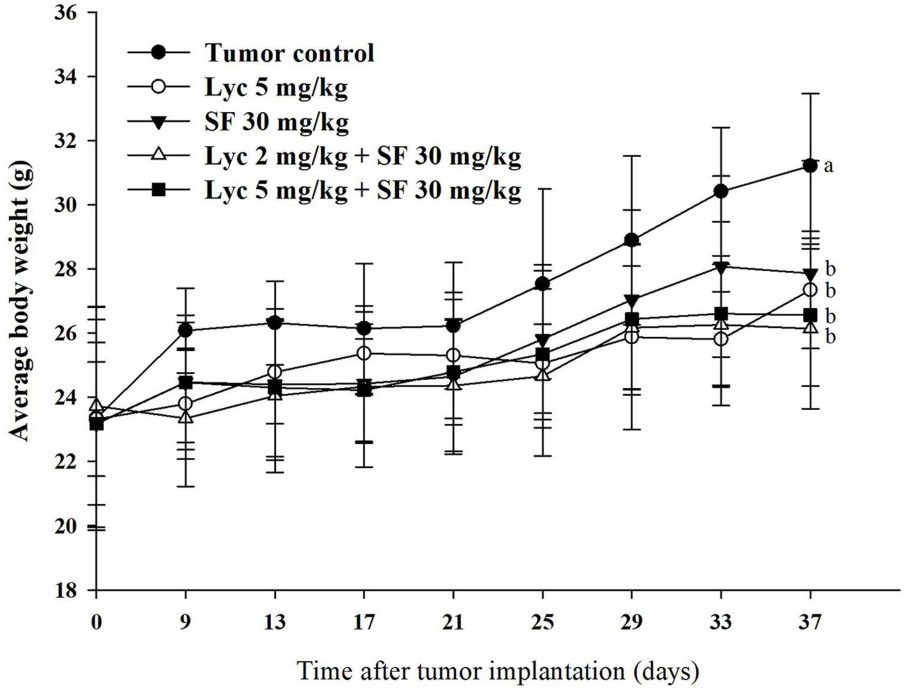

FIGURE 1 | Effects of lycopene (Lyc) alone, sorafenib (SF) alone, or their combination on the body weight change in the C57BL/6 mice xenografted LLC cells during entire experimental period. LLC cells were injected subcutaneously into the right flank of the C57BL/6 mice. Nine days after the tumor cell injection, mice were orally supplemented with SF (30 mg/kg) daily, Lyc (5 mg/kg) twice per week or the combined treatment (mice were supplemented with SF (30 mg/kg) daily, and Lyc (2 and 5 mg/kg) twice per week) for 28 days. Data are means ± SD, $n = 7–8$; values not sharing an alphabetic letter are significantly different ($P < 0.05$).

TABLE 1 | Inhibitory effects of lycopene (Lyc) alone, sorafenib (SF) alone, or their combination on the lung metastasis in the C57BL/6 mice xenografted LLC cells[1].

Groups	*n*	No. of metastasis (lung)	Inhibition (%)	Fold of inhibition (synergistic or additive effects)[2]
Tumor control	8	11.4 ± 3.7^a	-	-
Lyc 5 mg/kg	7	7.0 ± 3.2^b	38.6	-
SF 30 mg/kg	8	6.9 ± 3.7^b	39.5	-
Lyc 2 mg/kg + SF 30 mg/kg	8	5.1 ± 1.9^b	55.3	-
Lyc 5 mg/kg + SF 30 mg/kg	8	1.8 ± 1.7^c	84.2	1.07

[1] *LLC cells (1×10^5 cells/100L) were injected (s.c.) into C57BL/6 mice for 9 days, and the mice were orally administered with SF (30 mg/kg) daily, Lyc (5 mg/kg) twice per week, or the combined treatment (mice were supplemented with SF (30 mg/kg) daily, and Lyc (2 and 5 mg/kg) twice per week) for 28 days. After the mice were sacrificed, the tumor metastasis to the lungs of the mice was visually counted. Values are means ± SD from seven to eight mice. Values not sharing an alphabetic letter are significantly different (P < 0.05).*

[2] *The additive effect is calculated as (the percent inhibition of lycopene + sorafenib)/[(the percent inhibition of lycopene) + (the percent inhibition of sorafenib)].*

40% Bis-Acrylamide (29:1) solution obtained from Merck Chemical Company (Darmstadt, German). Immobilon™ PVDF (polyvinylidene fluoride transfer membranes), ECL chemiluminescent detection kit were obtained from Millipore Corporation (Beaford, MA, USA). Ammonium persulfate (APS) was obtained from GE Healthcare Bio-Sciences AB (Uppsala, Sweden). Mitogen-activated protein kinases (MAPKs) antibodies including p38, ERK1/2 and JNK1/2, and their phosphorylated protein were purchased from Cell Signaling Technology (Bevly, MA). The anti-NOX4 and tissue inhibitor of matrix metalloproteinase (TIMP)-1 antibody were purchased from Abcam (California, USA). Tissue inhibitor of matrix metalloproteinase (TIMP)-2 antibody, NM23-H1, secondary antibody anti-rabbit IgG, anti-mouse IgG were purchased from Genetex (California, USA).

Cell Culture

Mouse lung cancer cell line [Lewis Lung carcinoma (LLC) cells] (BCRC NO. 60050) was purchased from the Biological Resources Conservation and Research Center of the Institute of Food Industry Development (Hsinchu, Taiwan). The culture medium used Dulbecco's Modified Eagle Medium (DMEM) medium supplemented with 10% (v/v) FBS, 0.37% (w/v) NaHCO3, penicillin (100 unit/mL), and cultured in CO2 incubator at 37°C and 5% CO2.

Animals and Groups

Male mice of C57BL/6 strain (5 weeks old) were purchased from Lesco Biotechnology Co., Ltd. (Yilan, Taiwan). This animal study was approved by the Animal Management Committee of the National Chung Hsing University (Approval Number: 104-048).

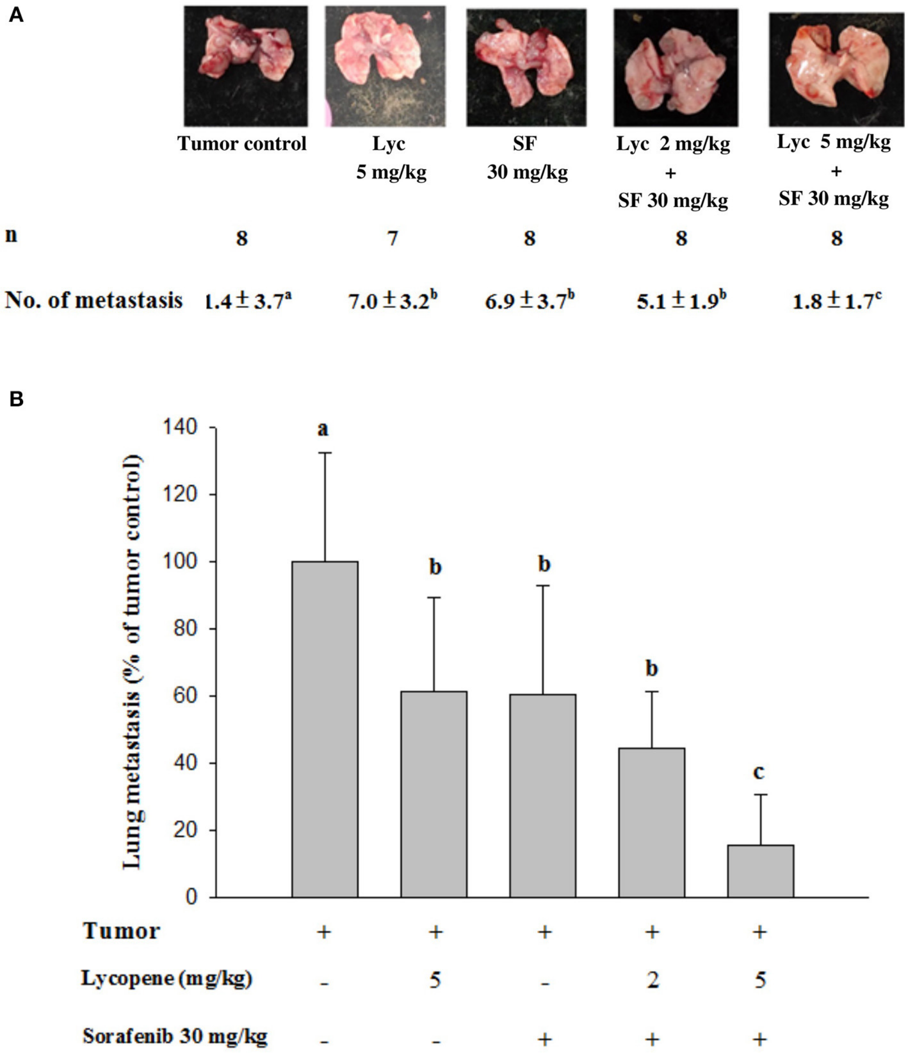

FIGURE 2 | Effects of lycopene (Lyc) alone, sorafenib (SF) alone, or their combination on lung metastasis in the xenografted mice. LLC cells were injected subcutaneously into the right flank of the C57BL/6 mice. Nine days after the tumor cell injection, the mice were orally supplemented with SF (30 mg/kg) daily, Lyc (5 mg/kg) twice per week or the combined treatment (mice were supplemented with SF (30 mg/kg) daily, and Lyc (2 and 5 mg/kg) twice per week) for 28 days. **(A)** Macroscopic observation of lung metastasis. **(B)** The quantitative results of the lung metastasis. Data are means ± SD, *n* = 7–8; values not sharing an alphabetic letter are significantly different ($P < 0.05$).

The mice were raised in the animal room with controlled room temperature 25 ± 2°C, humidity 65 ± 5%, and alternating 12-h-light/-dark cycles. After the mice were adapted for 1 week, the LLC cells ($1 \times 10^5/100\mu l$) were inoculated into the back of mice by subcutaneous injection. Primary tumor formation was visually observed approximately 9 days after the cancer cell injection. Following on, the mice were divided into five groups: (1) tumor control group; (2) Lycopene (5 mg/kg) alone; (3) Sorafenib (30 mg/kg) alone; (4) Sorafenib (30 mg/kg) + Lycopene (2 mg/kg); (5) Sorafenib (30 mg /kg) + lycopene (5 mg/kg). Mouse body weight and primary tumor area were measured twice weekly for a further 28 days and then sacrificed. During the rearing period, we used standard rodent chow and free access to water. The contents of the three major nutrients in the feed were 64% carbohydrate, 12% fat, and 24% protein, and each gram contained 3.18 kcal. The longest and shortest diameters of primary tumors were measured using calipers. The tumor area was calculated as $\pi \div 4 \times$ length × width.

Administration of Lycopene and Sorafenib in Mice

Lycopene was dissolved in corn oil and dosed at 2 mg/kg and 5 mg/kg according to the mouse body weight. Lycopene was tube-fed twice a week. Sorafenib was dissolved in Cremophor® EL/95 % ethanol (50:50) to prepare a four-fold stock solution every 3 days, which was stored at room temperature, diluted with sterile deionized water according to the mouse body weight to prepare a dose of 30 mg/kg. Sorafenib was administered by a feeding tube once daily. It is known that the corn oil and the Cremophor EL/95% ethanol have no anti-cancer activity and are frequently

TABLE 2 | Inhibitory effects of lycopene (Lyc) alone, sorafenib (SF) alone, or their combination on the primary tumor area and tumor weight in the C57BL/6 mice xenografted LLC cells[1].

Groups	*n*	Tumor weight (g)	Tumor area (cm^2)	Tumor area inhibition (%)	Fold of tumor area inhibition (synergistic or additive effects)[2]
Tumor control	8	9.2 ± 2.3^{a}	5.3 ± 1.1^{a}	-	-
Lyc 5 mg/kg	7	6.6 ± 1.6^{b}	3.9 ± 0.7^{bc}	26.4	-
SF 30 mg/kg	8	6.0 ± 2.3^{b}	4.2 ± 1.3^{b}	20.8	-
Lyc 2 mg/kg + SF 30 mg/kg	8	5.9 ± 1.0^{b}	3.3 ± 0.8^{bc}	37.7	-
Lyc 5 mg/kg + SF 30 mg/kg	8	4.8 ± 1.0^{b}	2.9 ± 0.7^{c}	45.3	0.96

[1] *LLC cells (1 × 10^5 cells/100L) were injected (s.c.) into the C57BL/6 mice for 9 days, and the mice were orally administered with SF (30 mg/kg) daily, Lyc (5 mg/kg) twice per week, or the combined treatment (mice were supplemented with SF (30 mg/kg) daily, and Lyc (5 mg/kg) twice per week) for 28 days. The results of the surface area and weight of the primary tumor on day 37 are shown. Values are means ± SD from seven to eight mice. Values not sharing an alphabetic letter are significantly different ($P < 0.05$).*

[2] *The additive effect is calculated as (the percent inhibition of tumor area of lycopene + sorafenib)/[(the percent inhibition of tumor area of lycopene) + (the percent inhibition of tumor area of sorafenib)].*

used as the vehicle of the agents for anti-cancer researches. Thus, we did not include both the vehicle controls into the study for the reduction of the used number of the tested animals.

Organs Weighting and Lung Tumor Metastases Counting

After the mice were sacrificed, the dorsal primary tumor, lung, liver, spleen, and kidney were removed, weighed separately, and the number of tumor metastases to the lung was counted visually. Organs were stored at −80°C, or soaked in the 10% formalin, for subsequent experiments.

Analysis of MMPs Activity by Zymography

The activities of MMP-2 and MMP-9 in the blood were measured using gelatin zymography according to a protocol with some minor modifications (18). The blood was collected by the orbital blood sampling procedures before the mice were sacrificed. The samples were stored in a centrifuge tube containing K3EDTA anticoagulant, centrifuged at 4°C, 3,000 rpm for 10 min, and the supernatant was collected and stored at −80°C for subsequent experiments. A proper volume of plasma was electrophoresed via 8% sodium dodecyl sulfate–polyacrylamide gel electrophoresis (SDS–PAGE) containing 0.1% gelatin. After electrophoresis, the gel was washed with 2.5% (v/v) Triton X-100 twice for 30 min and then incubated with reaction buffer (2 M Tris-HCl (pH 8.0), 1 M $CaCl_2$, and 1% NaN_3) for 12–15 h at 37°C. The gel was stained with Coomassie brilliant blue R-250 for 30 min and then destained in solutions containing 10% (v/v) acetic acid and 50% (v/v) methanol. The relative MMP-2 and MMP-9 activities were quantified using MatroxInspector version 2.1.

Western Blotting

Protein expression of MMP-2, MMP-9, NOX4, MAPKs, TIMP-1, TIMP-2, and NM23-H1 were measured by Western blotting. 10 mg of the lung were added to 200L of tissue extract buffer, ground and centrifuged at 10,000 × g for 10 min at 4°C. The supernatant was collected and stored at −80°C. The proteins (40 μg) from the supernatant were resolved by SDS–PAGE and transferred onto a polyvinylidene fluoride (PVDF) membrane. After being blocked with Tris-buffered saline (TBS) buffer containing 5% non-fat milk, the membrane was washed three times with TBS buffer containing 0.1% (v/v) Tween 20 for 1 h and then incubated with the various primary antibodies at 4°C overnight. The membrane was incubated with a fluoresce-in-conjugated secondary antibody for 1 h and then detected with an ECL chemiluminescent detection kit (Amersham Co., Bucks, U.K.). The relative density of protein expression was quantified with AlphaEaseFC Analysis software.

Histopathological Staining

The lung tissues were removed from the mice, immersed in 10 times the volume of 10% formalin buffer solution for fixation, and pulsated on a shaker overnight. The fixed tissue was rinsed with running water for 30 min, and then the tissue was dehydrated in 70%, 80%, 85%, 90%, and 95% alcohol for 1 hour. The tissue was then immersed 3 times in 100% alcohol for 1.5 h, then twice in xylene, and twice in liquid paraffin at 57°C for 2 hours. The tissue was embedded in liquid paraffin and cut into 2 μm sections with a tissue microtome. After staining with the hematoxylin and eosin, the tissue sections were observed with an optical microscope.

Statistical Analysis

Data from more than three independent tests were analyzed using the analysis of variance (ANOVA), followed by the Least significant difference (LSD) mean comparisons using the SPSS v.14.0 software (SPSS, Inc., Chicago, USA). *P*-values <0.05 were considered statistically significant. Potential synergistic or additive effects of lycopene plus sorafenib were evaluated by comparing the total inhibition (or activation) obtained by the sum of the individual treatment's effects with the extent of inhibition (or activation) obtained by a combination of treatments, i.e., using observed percentage inhibition (or activation) and the formula:

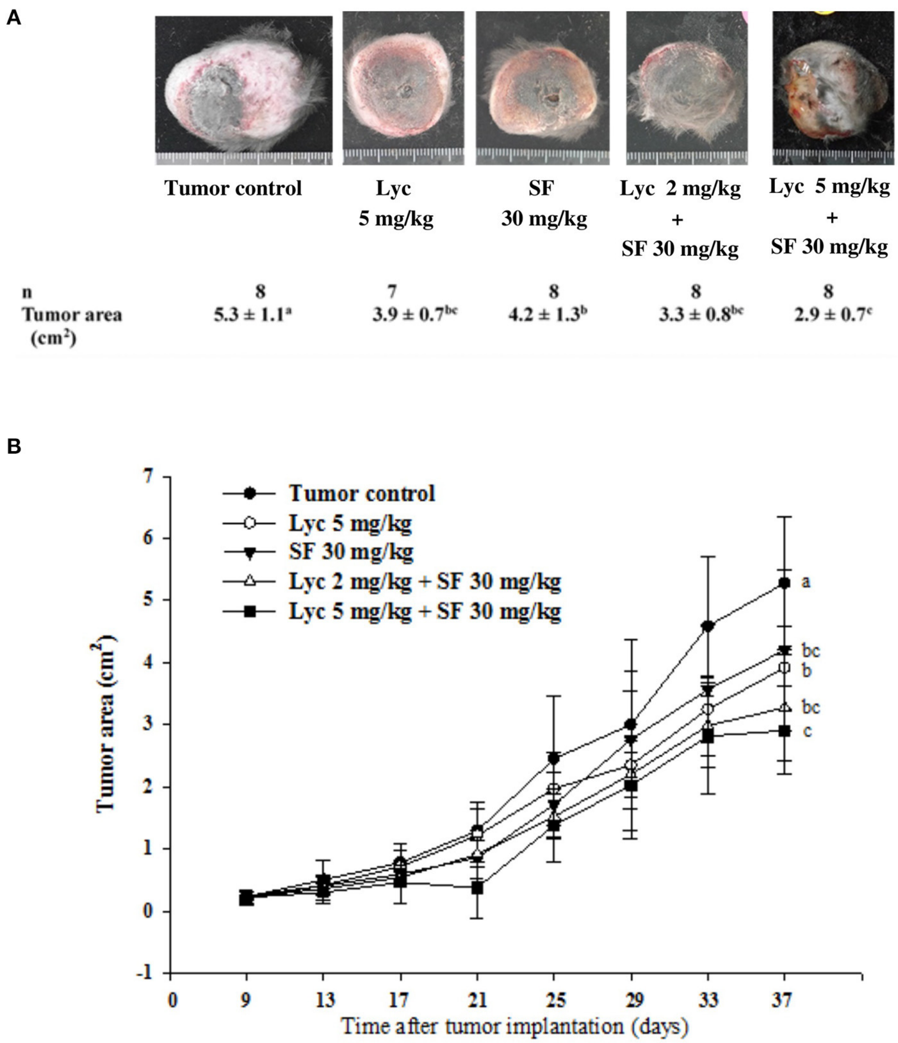

	Tumor control	Lyc 5 mg/kg	SF 30 mg/kg	Lyc 2 mg/kg + SF 30 mg/kg	Lyc 5 mg/kg + SF 30 mg/kg
n	8	7	8	8	8
Tumor area (cm^2)	5.3 ± 1.1^a	3.9 ± 0.7^{bc}	4.2 ± 1.3^b	3.3 ± 0.8^{bc}	2.9 ± 0.7^c

FIGURE 3 | Effects of lycopene (Lyc) alone, sorafenib (SF) alone, or their combination on the primary tumor area in the xenografted mice during the entire experimental period. LLC cells were injected subcutaneously into the right flank of the C57BL/6 mice. Nine days after the tumor cell injection, the mice were orally supplemented with SF (30 mg/kg) daily, Lyc (5 mg/kg) twice per week or the combined treatment [mice were supplemented with SF (30 mg/kg) daily, and Lyc (2 and 5 mg/kg) twice per week] for 28 days. The formula for calculating the tumor area is: $\pi \div 4 \times$ length $\times$ width. **(A)** Images of primary tumor. **(B)** The quantitative results of the primary tumor area. Data are means ± SD, $n = 7$–8; values not sharing an alphabetic letter are significantly different ($P < 0.05$).

(the percent inhibition of lycopene + sorafenib) / [(the percent inhibition of lycopene) + (the percent inhibition of sorafenib)] (34). According to this formula, a value >1.0 is synergistic, a value of 0.5–1.0 is additive, while a value <0.5 is antagonistic (34). The same goes for the activation formula.

RESULTS

Effects of Lycopene (Lyc) Alone, Sorafenib (SF) Alone, or Their Combination on the Body Weight and Organ Weight

As shown in **Figure 1**, the weight of each treatment group was significantly different from that of the control group at the end of the administrative day, ($P < 0.05$), but there was no significant difference between the treatment groups ($P > 0.05$). The organ weight, including the relative organ weight of liver, lung, spleen and kidney had no significant difference between the groups (**Supplementary Table S1**). The relative organ weight means that the organ weight was divided by the body weight of the mouse.

Effects of Lycopene (Lyc) Alone, Sorafenib (SF) Alone, or Their Combination on the Lung Metastasis

Mice were sacrificed on day 37, and the tumor metastasis to the lungs of the mice was visually counted. The results showed that the administration of Lyc (5 mg/kg) and SF (30 mg/kg) alone significantly inhibited the number of tumors in

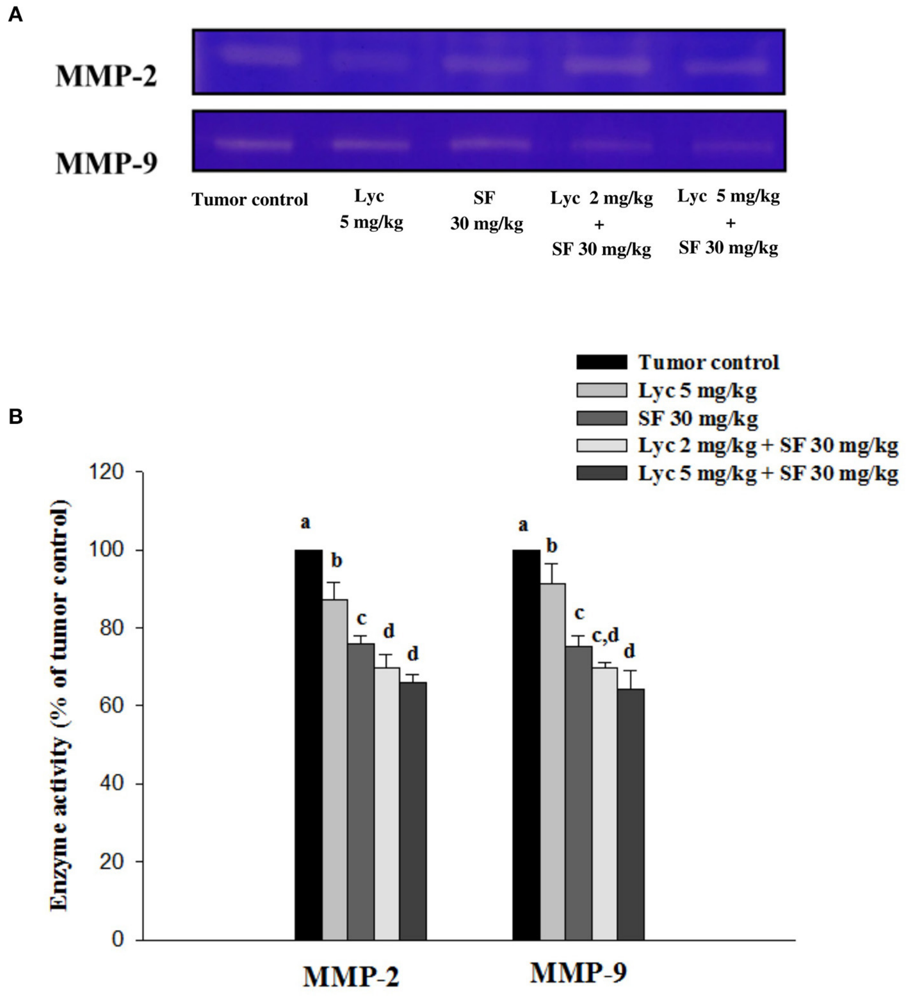

FIGURE 4 | Effects of lycopene (Lyc) alone, sorafenib (SF) alone, or their combination on MMP-2 and MMP-9 activities in plasma of the C57BL/6 mice xenografted LLC cells. Nine days after the tumor cell injection, mice were orally supplemented with SF (30 mg/kg) daily, Lyc (5 mg/kg) twice per week or the combined treatment (mice were supplemented with SF (30 mg/kg) daily, and Lyc (2 and 5 mg/kg) twice per week) for 28 days. **(A)** Zymography analysis of MMP-2 and MMP-9 activities. **(B)** Quantitative results of zymography of MMP-2 and MMP-9 activities. Data are means ± SD, $n = 7$–8; values not sharing an alphabetic letter are significantly different ($P < 0.05$).

the lungs as compared with the tumor control group, with the inhibition rates of 38.6 and 39.5%, respectively ($P < 0.05$, **Table 1**; **Figure 2**). Lyc (2 mg/kg) combined with SF (30 mg/kg) in the combined group could significantly reduce the number of lung tumor metastases as compared with the tumor control group, with an inhibition rate of 55.3% ($P < 0.05$, **Table 1**; **Supplementary Figure S1**). Compared with the tumor control group, the Lyc (5 mg/kg) combined with SF (30 mg/kg) group also significantly reduced tumor growth, with an inhibition rate of 84.2% ($P < 0.05$, **Table 1**; **Figure 2**). The fold of inhibition was 1.07, suggesting that a slight synergistic effect of lycopene in combination with sorafenib to inhibit the tumor number in lung as shown in **Table 1**.

Effects of Lycopene (Lyc) Alone, Sorafenib (SF) Alone, or Their Combination on the Surface Area and Weight of Primary Tumor

For the primary tumor area on day 37, the results showed that the administration of Lyc (5 mg/kg) or SF (30 mg/kg) alone significantly inhibited tumor growth as compared with the tumor control group, with the inhibition rates of 26.4 and 20.8%, respectively ($P < 0.05$, **Table 2**; **Figure 3**). Compared with the tumor control group, the inhibition rate of Lyc (2 and 5 mg/kg) combined with SF (30 mg/kg) was 37.7 and 45.3% ($P < 0.05$, **Table 2**; **Figure 3**). In the tumor weight, the results showed that the treatments could significantly reduce tumor weight as compared with the tumor control group no matter

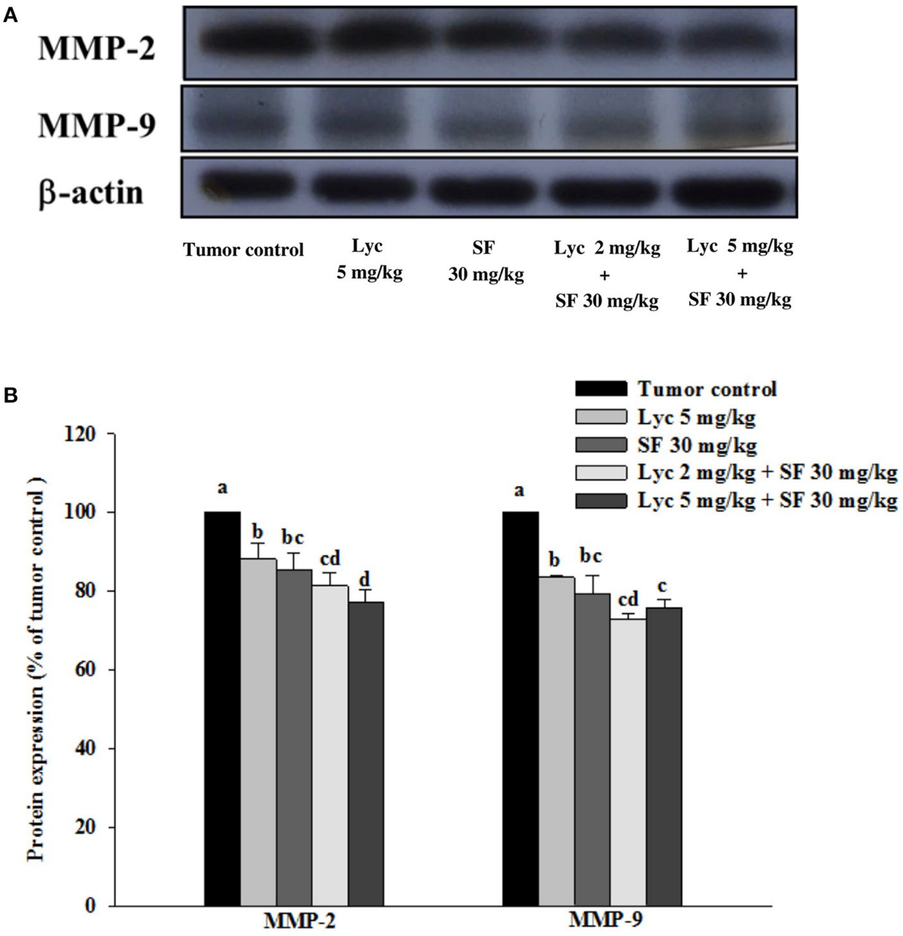

FIGURE 5 | Effects of lycopene (Lyc) alone, sorafenib (SF) alone, or their combination on MMP-9 and MMP-2 protein expressions in lung tissues of the C57BL/6 mice xenografted LLC cells. Nine days after tumor cell injection, the mice were orally supplemented with SF (30 mg/kg) daily, Lyc (2 and 5 mg/kg) twice per week or the combined treatment (mice were supplemented with SF (30 mg/kg) daily, and Lyc (2 and 5 mg/kg) twice per week) for 28 days. **(A)** Western blot analysis of MMP-9, MMP-2 and-actin. **(B)** Quantitative results of the protein expressions of MMP-9 and MMP-2. Data are means ± SD, *n* = 7–8; values not sharing an alphabetic letter are significantly different ($P < 0.05$).

whether Lyc (5 mg/kg) and SF (30 mg/kg) were administered alone or in combination ($P < 0.05$, **Table 2**; **Figure 3**). The fold of inhibition was 0.96, suggesting that an additive effect of lycopene in combination with sorafenib to inhibit the area of primary tumor as shown in **Table 2**.

Effects of Lycopene (Lyc) Alone, Sorafenib (SF) Alone, or Their Combination on MMP-2 and MMP-9 Activity in Plasma

After the mice were sacrificed, the orbital blood of the mice was collected, and the enzymatic activities of MMP-2 and MMP-9 in the plasma were determined by zymography. The enzyme activities of MMP-2 and MMP-9 in the plasma of the tumor control group were set at 100%. The results showed that Lyc (5 mg/kg) alone could significantly inhibit MMP-2 and MMP-9 enzyme activities as compared to the tumor control group as the inhibition rates were 12.9% and 8.6%, respectively ($P < 0.05$, **Figure 4**; **Supplementary Table S2**); SF (30 mg/kg) given alone also significantly inhibited MMP-2 and MMP-9 enzyme activities as compared to the tumor control group as the inhibition rates were 24.1% and 24.9% ($P < 0.05$, **Figure 4**; **Supplementary Table S2**). The Lyc (2 mg/kg) combined with SF (30 mg/kg) group could significantly reduce the MMP-2 and MMP-9 enzyme activities as compared with the tumor control group, and the inhibition rates of both were about 30% ($P < 0.05$, **Figure 4**; **Supplementary Table S2**). Lyc (5 mg/kg) combined with SF (30 mg/kg) could significantly reduce the activity of MMP-2 and MMP-9 enzymes as compared with the tumor control group, with the inhibition rates of 34.2 and 35.6%, respectively ($P < 0.05$, **Figure 4**; **Supplementary Table S2**). The fold of inhibition in MMP-2 and MMP-9 were 0.92 and 1.07, respectively, suggesting an additive to a slightly synergistic effect of lycopene in combination with sorafenib on the inhibition of MMP-2 and MMP-9 activities are as shown in **Supplementary Table S2**.

Effects of Lycopene (Lyc) Alone, Sorafenib (SF) Alone, or Their Combination on MMP-9 and MMP-2 Protein Expressions in Lung Tissues

After the mice were sacrificed, the lung tissue was collected and homogenized, and the expression of MMP-2 and MMP-9 proteins in the lung tissue was analyzed by Western blot. The results showed that the group administered with Lyc (5 mg/kg) and SF (30 mg/kg) alone, compared with the tumor control group, significantly inhibited the protein expression of MMP-2 for 12.0 and 14.6% ($P < 0.05$, **Figure 5**; **Supplementary Table S3**). In the combined group, Lyc (2 mg/kg) combined with SF (30 mg/kg) significantly inhibited the protein expression of MMP-2 in the lungs, which was 18.7% ($P < 0.05$, **Figure 5**; **Supplementary Table S3**). The Lyc (5 mg/kg) combined with the SF (30 mg/kg) group also significantly inhibited the expression of MMP-2 protein in the lungs, with an inhibition rate of 22.9% ($P < 0.05$, **Figure 5**; **Supplementary Table S3**). Lycopene had similar results on the expression of MMP-9 (**Figure 5**; **Supplementary Table S3**). The fold of inhibition in MMP-2 and MMP-9 expressions were 0.86 and 0.65, respectively, suggesting that an additive effect of lycopene in combination with sorafenib on the inhibition of MMP-2 and MMP-9 expressions is as shown in **Supplementary Table S3**.

Effects of Lycopene (Lyc) Alone, Sorafenib (SF) Alone, or Their Combination on the Phosphorylation of p38, ERK1/2 and JNK1/2 Proteins in Lung Tissues

After the mice were sacrificed, the lung tissue was collected and homogenized, and the phosphorylation of p38, ERK1/2 and JNK1/2 proteins in the lung tissue was analyzed by Western blot. The results showed that the group administered with Lyc (5 mg/kg) and SF (30 mg/kg) alone, compared with the tumor control group, significantly inhibited the phosphorylation of p38 for 16.7 and 20.9% ($P < 0.05$, **Figure 6**; **Supplementary Table S4**). In the combined group, Lyc (2 mg/kg) combined with the SF (30 mg/kg) significantly inhibited the phosphorylation of p38 in the lungs, which was 27.1% ($P < 0.05$, **Figure 6**; **Supplementary Table S4**). The Lyc (5 mg/kg) combined with the SF (30 mg/kg) group also significantly inhibited the phosphorylation of p38 in the lungs by 24.4% ($P < 0.05$, **Figure 6**; **Supplementary Table S4**). The fold of inhibition in the phosphorylation of p38 was 0.65, suggesting that an additive effect of lycopene in combination with sorafenib on the inhibition of p38 phosphorylation is as shown in **Supplementary Table S4**. Lycopene had similar results on the phosphorylation of ERK1/2 (**Figure 6**; **Supplementary Table S4**) and JNK1/2 (**Figure 6**; **Supplementary Table S5**), except the fold of inhibitions showed the additive with slightly synergistic effects.

Effects of Lycopene (Lyc) Alone, Sorafenib (SF) Alone, or Their Combination on TIMP-1, TIMP-2 and NM23-H1 Protein Expressions in Lung Tissues

After the mice were sacrificed, the lung tissue was collected and homogenized, and the expression of TIMP-1, TIMP-2, and NM23-H1 proteins in the lung tissue was analyzed by Western blot. The results showed that the group administered with Lyc (5 mg/kg) and SF (30 mg/kg) alone, compared with the tumor control group, significantly activated the protein expression of TIMP-1 for 9.6% and 16.7% ($P < 0.05$, **Figure 7**; **Supplementary Table S6**). In the combined group, Lyc (2 mg/kg) combined with SF (30 mg/kg) significantly activated the protein expression of TIMP-1 in the lungs, which was 28.2% ($P < 0.05$, **Figure 7**; **Supplementary Table S6**). The Lyc (5 mg/kg) combined with SF (30 mg/kg) group also significantly activated the expression of TIMP-1 protein in the lungs, with an activation rate of 40.8% ($P < 0.05$, **Figure 7**; **Supplementary Table S6**). The fold of activation in TIMP-1 expression was 1.55, suggesting that a synergistic effect of lycopene in combination with sorafenib on the activation of TIMP-1 expression is as shown in **Supplementary Table S6**. Lycopene had similar results on the expressions of TIMP-2 and NM23-H1 proteins (**Figure 7**; **Supplementary Table S6**).

Effects of Lycopene (Lyc) Alone, Sorafenib (SF) Alone, or Their Combination on NOX4 Protein Expression in Lung Tissues

After the mice were sacrificed, the lung tissue was collected and homogenized, and the expression of NOX4 protein in the lung tissue was analyzed by Western blot. The results showed that the group administered with Lyc (5 mg/kg) alone, compared with the tumor control group, significantly inhibited the protein expression of NOX4 for 30.6% ($P < 0.05$, **Figure 8**; **Supplementary Table S7**). The SF (30 mg/kg) alone had no significant inhibition on the expression of NOX4 ($P > 0.05$, **Figure 8**; **Supplementary Table S7**). The Lyc (5 mg/kg) combined with the SF (30 mg/kg) group showed a significant inhibition on the expression of NOX4 protein with an efficacy similar to the Lyc (5 mg/kg) alone group ($P > 0.05$) as compared to the Lyc (5 mg/kg) alone group (**Figure 8**; **Supplementary Table S7**).

Effects of Lycopene (Lyc) Alone, Sorafenib (SF) Alone, or Their Combination on the Histopathological Analysis of Lung Tissues

As presented in **Supplementary Figure S1** in the **Supplementary Material**, the results showed that the multiple, slight to moderate tumor cells were observed to metastasize to the lung via the blood or lymphatic vessels, forming tumor emboli (arrows in **Supplementary Figure S1**), and growing into the lung parenchyma in the groups of tumor control (A and B), Lyc alone (5 mg/kg) (C and D) and SF alone (30 mg/kg) (E and F) after the hematoxylin and eosin (H&E) staining of the lung sections. Alternatively, the multiple, minimal to slight, tumor

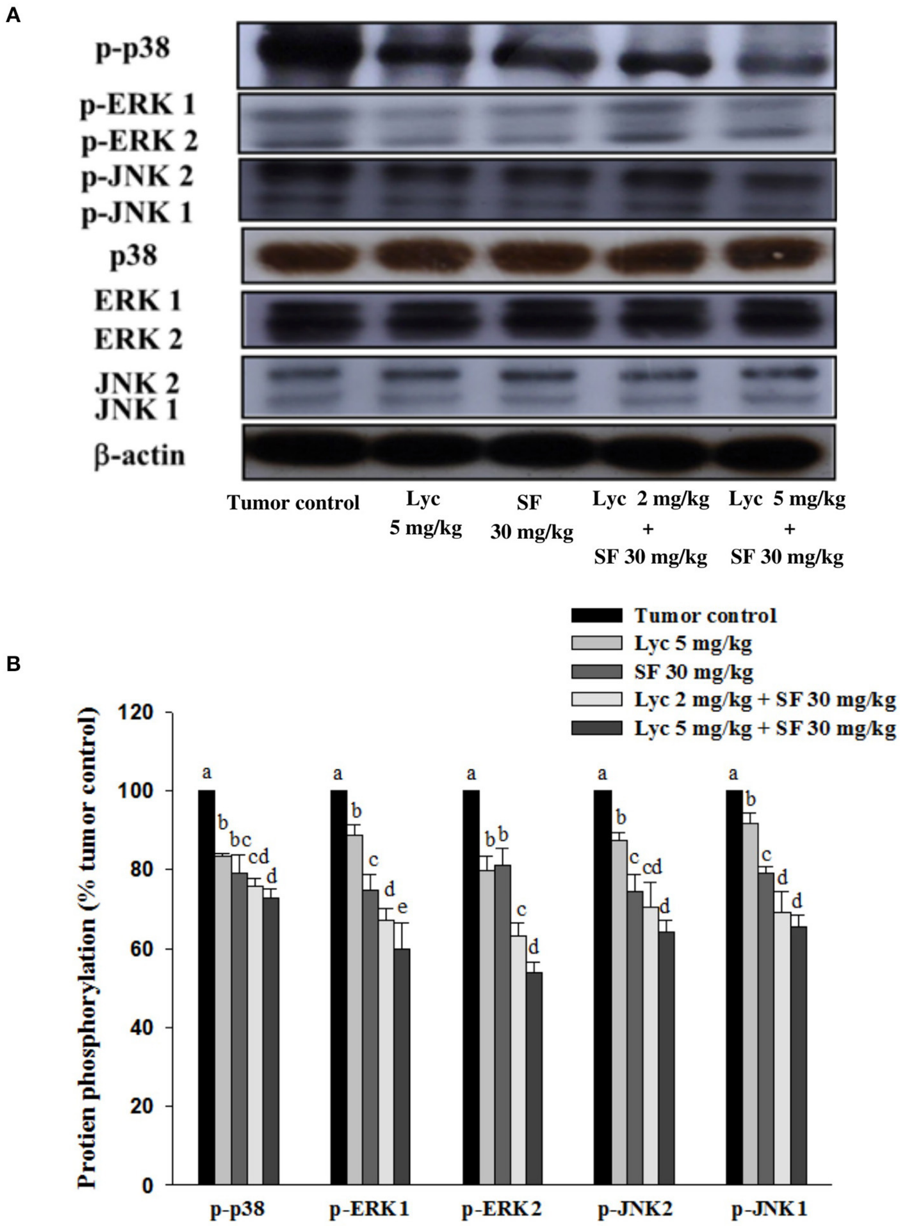

FIGURE 6 | Effects of lycopene (Lyc) alone, sorafenib (SF) alone, or their combination on the phosphorylation of p38, ERK1/2 and JNK1/2 proteins in lung tissues of the C57BL/6 mice xenografted LLC cells. Nine days after tumor cell injection, the mice were orally supplemented with SF (30 mg/kg) daily, Lyc (5 mg/kg) twice per week or the combined treatment (mice were supplemented with SF (30 mg/kg) daily, and Lyc (2 and 5 mg/kg) twice per week) for 28 days. **(A)** Western blot analysis of p-p38, p38, p-ERK1/2, ERK1/2, p-JNK1/2, JNK1/2 and -actin. **(B)** Quantitative results of the protein phosphorylation of p38, ERK1/2, and JNK1/2. Data are means ± SD, $n = 7–8$; values not sharing an alphabetic letter are significantly different ($P < 0.05$).

cells were observed to metastasize to the lungs as the tumor emboli (arrows in **Supplementary Figure S1**), and growing into the lung parenchyma in the groups of Lyc (2 mg/kg) combined with SF (30 mg/kg) group (G and H), and the Lyc (5 mg/kg) combined with SF (30 mg/kg) group (I and J). While the tumor control group had multiple tumor foci, the Lyc showed a dose-dependent reduction with SF in the number of lung tumor foci.

DISCUSSION

A synergistic effect of phytochemicals such as lycopene and festin, in combination with anti-cancer drugs, has been found in the literature (19, 20). In this paper, we found that the combination of lycopene and sorafenib has a synergistic effect on the activation of TIMP-1, TIMP-2, and NM23-H1 protein

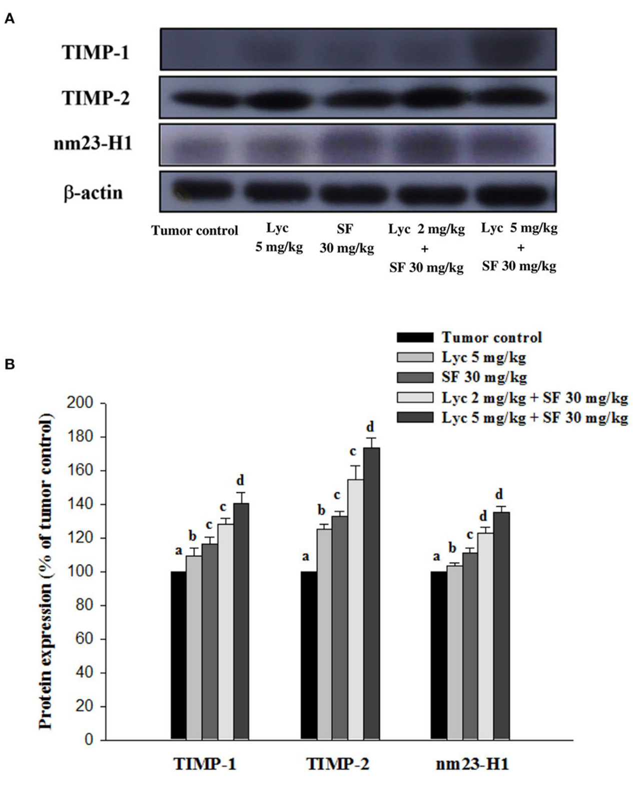

FIGURE 7 | Effects of lycopene (Lyc) alone, sorafenib (SF) alone, or their combination on TIMP-1, TIMP-2 and nm23-H1 protein expression in liver tissues of the C57BL/6 mice xenografted LLC cells. Nine days after tumor cell injection, mice were orally supplemented with SF (30 mg/kg) daily, Lyc (5 mg/kg) twice per week or the combined treatment (mice were supplemented with SF (30 mg/kg) daily, and Lyc (2 and 5 mg/kg) twice per week) for 28 days. **(A)** Western blot analysis of TIMP-1, TIMP-2, nm23-H1 and -actin. **(B)** Quantitative results of the protein expressions of TIMP-1, TIMP-2 and nm23-H1. Data are means ± SD, $n = 7$–8; values not sharing an alphabetic letter are significantly different ($P < 0.05$).

expressions, and has an additive to the slightly synergistic effects on the inhibition of ERK-1, ERK-2, JNK-1, JNK-2, and p38 protein phosphorylation, and the expression of MMP-2 and MMP-9 proteins. In addition, lycopene can inhibit the lung metastasis of the xenografted tumor *in vivo*, and that the combination of lycopene and sorafenib has an additive effect on the lung metastasis. As shown, the numbers of metastasis tumor in the lung were addictively inhibited by the combination treatment. Moreover, the tumor area and weight *in situ* were also additively inhibited by the combination treatment. Taken together, lycopene combined with sorafenib can additively inhibit the primary tumor growth and the lung metastasis of the tumor in the xenografted mice. In addition, the results also support our hypothesis that the combined treatment of lycopene and sorafenib can simultaneously act at the three MAPK pathways, to a modulation of the MMP-2 and MMP-9 expressions, and then has an additive effect on the lung metastasis of the tumor in the xenografted mice. To the best of our knowledge, this paper is the first to report that lycopene and sorafenib can have an additive effect on the inhibition of primary tumor growth and the lung metastasis of tumors, suggesting that lycopene can be an adjuvant candidate for the treatment of cancer by sorafenib.

Cancer cells secrete proteolytic enzymes MMPs, which can degrade extracellular matrix and blood vessel walls, and have a high correlation with cancer metastasis (35, 36). The MMPs, MMP-2, and MMP-9 are the most related to tumor metastasis and invasion, because they have gelatinases activity and can degrade the extracellular matrix (37). The excessive expression of MMP-2 and MMP-9 is also highly correlated with lung cancer metastasis (38). In this study, the MMP-2 and MMP-9 activities and protein expressions showed an additive to the slightly synergistic effects for the combined treatment of lycopene and sorafenib. When the enzyme activity of MMPs are decreased, it can further reduce the degradation of extracellular matrix, thereby inhibiting the invasion of cancer cells and the metastasis of tumor to the lung.

The results in this study support our hypothesis that lycopene and sorafenib could act at the same target of the MAPK signaling pathways. The MAPK pathways have been demonstrated to be involved in many biological processes in cells including the metastasis of cancer cells (39–41). Among the MAPK pathways, the ERK pathway is activated by the epidermal growth factor receptors and Ras / Raf to promote cancer cell proliferation, survival, and metastasis (41). The JNK pathway can mainly regulate cell growth, differentiation and apoptosis and other physiological responses (42). The p38 pathway can directly phosphorylate downstream p53 and p73 to promote cell cycle arrest, apoptosis, cytokine secretion, etc., which in turn affects the cancer cell growth (43). Studies also showed that the MAPK signaling pathways are the upstream signals of MMP-2 (15, 29). In addition, several anti-metastasis agents had been demonstrated via the inhibition of the MAPK signaling pathways (44–46), suggesting that the MAPK pathways are an important target of anti-metastasis (41). Although it has been demonstrated that the ERK pathway is the main biological target of sorafenib, the results in this study demonstrate that all of the ERK, JNK, and p38 pathways can be the targets of sorafenib in the lung tissue of the xenografted mice. Importantly, the three MAPK pathways can be additively inhibited by the combination treatment with lycopene and sorafenib. Thus, the inhibition of MAPKs signaling should play a crucial role in the mechanism of the additive anti-metastasis of the combination treatment of lycopene and sorafenib through modulating the MMP-2 and MMP-9 activities.

In addition, other modulators of MMPs activity including NM23-H1 and TIMPs all showed with a synergistic effect by the combination treatment. NM23 is a family of metastasis suppressor genes, mainly isolated from the melanoma cells. At least eight human nm23 genes have been found, among which nm23-H1 and -H2 are the most widely studied, among which the nm23-H1 gene is highly related to the cancer metastasis (47). When NM23-H1 protein is overexpression, it can inhibit the invasion, migration and adhesion of cancer cells (47–49). TIMPs are endogenous inhibitors of MMPs. There are four genotypes

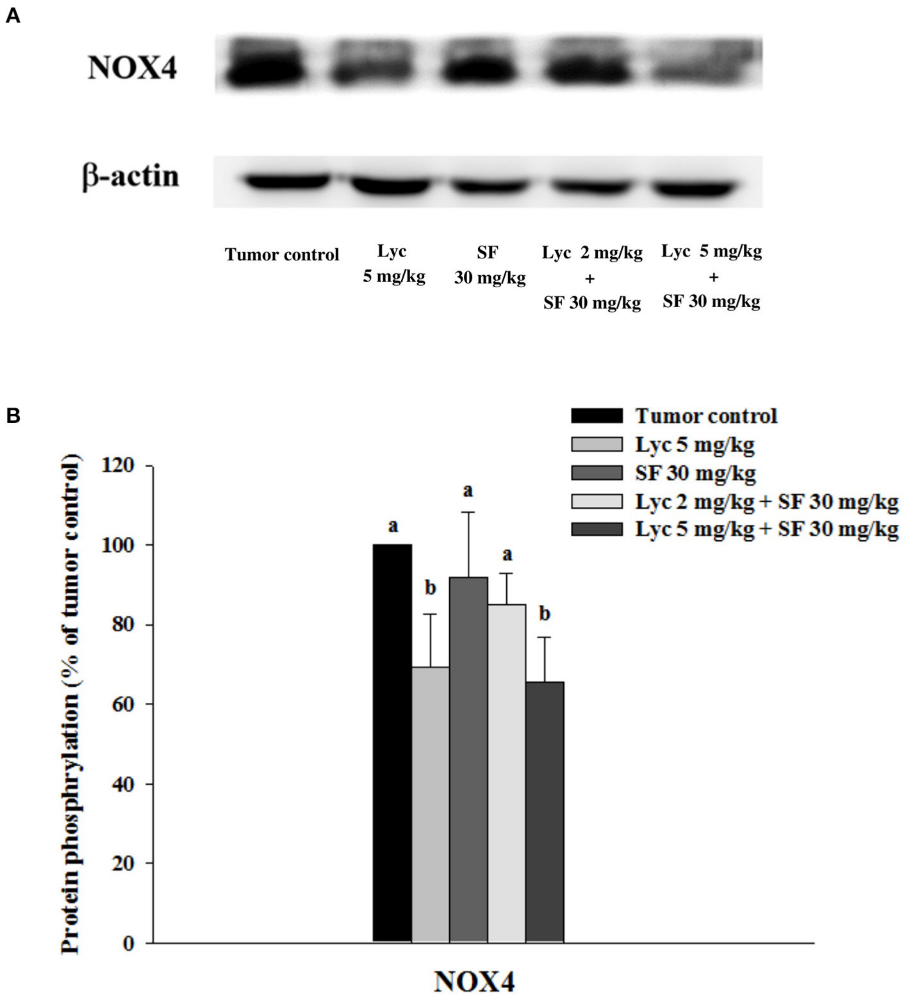

FIGURE 8 | Effects of lycopene (Lyc) alone, sorafenib (SF) alone, or their combination on NOX4 protein expression in lung tissues of the C57BL/6 mice xenografted LLC cells. Nine days after the tumor cell injection, mice were orally supplemented with SF (30 mg/kg) daily, Lyc (5 mg/kg) twice per week or the combined treatment (mice were supplemented with SF (30 mg/kg) daily, and Lyc (2 and 5 mg/kg) twice per week) for 28 days. **(A)** Western blot analysis of NOX4 and -actin. **(B)** Quantitative results of the protein expression of NOX4. Data are means ± SD, $n = 7–8$; values not sharing an alphabetic letter are significantly different ($P < 0.05$).

of TIMPs found in humans: TIMP-1,−2,−3, and−4 (50). TIMP-1 and−2 are inhibitors of MMP-9 and−2, respectively, both of which are bonded in a 1:1 ratio by non-covalent bonds to inhibit the activity of MMPs (51). A study has also pointed out that TIMPs can down-regulate the expression of MMPs and inhibit the metastasis of cancer cells (52). Therefore, the balance between MMPs and TIMPs play an important role in cancer cell metastasis (52). However, the combination treatment showed a synergistic effect on the activation of NM23-H1, TIMP-1, and TIMP-2, which was not consistent with an additive effect of the combination treatment on lung metastases. The synergistic activation of these MMPs modulators only induces an additive reduction of the MMP-2 and MMP-9 activities, suggesting MMPs should be a critical control point for the ability of lung metastasis of the xenografted tumor. Nonetheless, the results in the present study support that NM23-H1, TIMP-1, and TIMP-2 are the upstream molecules before the MMP-2 and MMP-9 proteins by the lycopene and sorafenib alone or combinations.

We have previously found that lycopene can inhibit the metastasis of human liver adenocarcinoma SK-Hep-1 cells by downregulation of the NOX4 protein expression *in vitro* (18). Herein, we confirm that lycopene could downregulate the NOX4 expression in the lung tissue of the mice xenografted with LLC cells *in vivo*. The results in this study support the existence of the NOX4 / ROS / MAPKs / MMPs pathway for lycopene. Besides, it should be noted that the anti-oxidative properties of lycopene itself may also play a role in its anti-metastatic action (6, 18). Based on these results and the literature review, we have proposed mechanisms related to the additively inhibit the lung metastasis

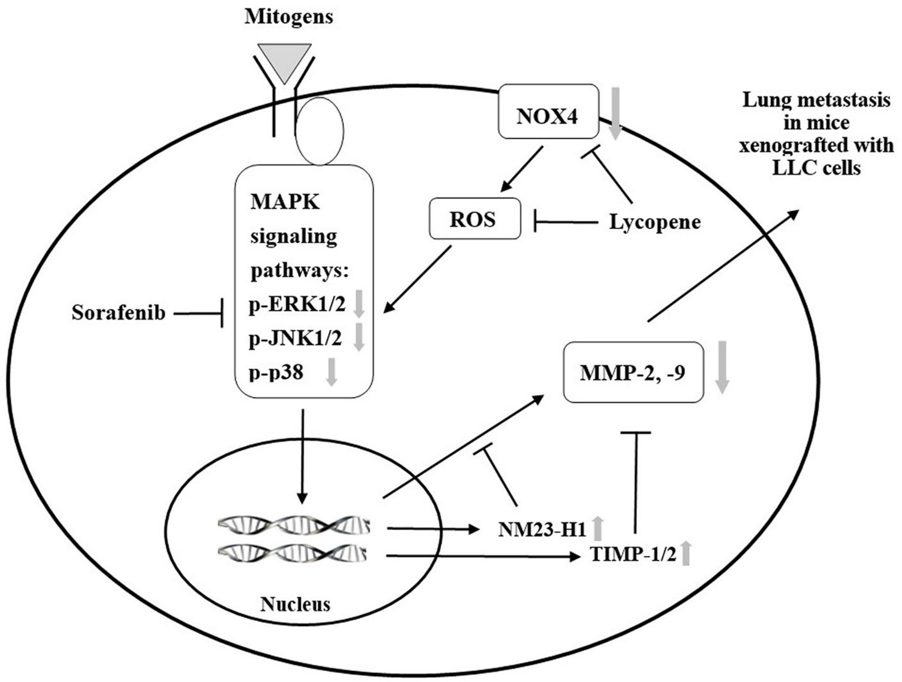

FIGURE 9 | A proposed schematic diagram for the role of mitogen-activated protein kinase (MAPK) signaling pathways in the additive effect of lycopene and sorafenib in the C57BL/6 mice xenogrfied with the Lewis lung carcinoma (LLC) cells. ⊣: inhibition; →: activation or expression. ⬇: inhibition at the protein expression, phosphorylation or activity by the treatment of lycopene and sorafenib. ⬆: activation at the protein expression by the treatment of lycopene and sorafenib.

of the xenografted tumor, as shown in **Figure 9**. Because the kinase-inhibiting property, the sorafenib can directly inhibit the MAPK pathways. In addition, lycopene inhibits the NOX4 activity and also inhibits the MAPK pathways. The additive inhibition of the MAPK pathways should decrease the MMP-2 and MMP-9 expressions through the activation of NM23-H1, TIMP-1, and TIMP-2. On the other hand, the additive inhibition of the MAPK pathways by lycopene and sorafenib may also contribute to the additive effects of these two compounds on primary tumor growth in the mice xenografted with LLC cells.

Previously, Huang et al., (17) had demonstrated that the lycopene supplementation resulted in the dose-dependent increases in lycopene concentrations in the lungs of the nude mice. In this study, since all of the effects of lycopene with sorafenib in the mice xenografted with LLC cells showed having a dose-dependent manner as well, suggesting that the anti-lung-metastatic activity, the observed MMPs activity and the effect on the MAPK signaling pathways etc. should be associated to the content of lycopene in the lungs. Furthermore, the dose of lycopene administered to mice in this article i.e., 5 mg/kg was further estimated to be converted into the amount required for intake for a human adult. We refer to the conversion formula proposed by Reagan-Shaw et al., (53): the human equivalent dosage (mg/kg) = animal dosage (mg/kg) × (animal Km value / hu-man Km value), where Km is the body weight (kg) ÷ body surface area (m2); human Km is approximately 37 and mouse Km is 3. The dosage of 5 mg/kg of lycopene was given to the mice twice a week, which was equivalent to 1.43 mg/kg of lycopene given to mice every day. Thus, the effective dosage of lycopene for a 60-kg healthy adults could be estimated as follows: 1.43 mg/kg/day × 60 kg × (3/37) = 6.96 mg/day of lycopene. Adults human need 6.69 mg/day to achieve an effective dosage of lycopene. Rao and Shen (54) pointed out that when the daily intake of lycopene in healthy adults reaches 57 mg, the concentration of lycopene in the blood may be sufficient to resist oxidative stress and various chronic diseases. A Canadian epidemiological study showed that the average daily intake of lycopene per woman is 6.14 ± 5.35 mg ($n = 101$) (55); another epidemiological study showed that the average daily dietary intake of lycopene in healthy women was 9.25 ± 6.43 mg ($n = 632$), and in breast cancer patients was 7.12 ± 6.73 mg ($n = 122$) (56). Thus, the effective dosage of lycopene to have an anti-metastasis efficacy i.e., 6.96 mg/day obtained by the results of this study is not difficult to achieve from a dietary intake.

CONCLUSION

In summary, we demonstrate that lycopene can significantly inhibit the lung metastasis of tumors in the C57BL/6 mice xenografted with LLC cells *in vivo*, and we found that lycopene combined with the anticancer drug sorafenib can have an additive effect against the lung metastasis. The mechanisms of the additive anti-metastasis effect of lycopene and sorafenib are due to additively inhibit the MAPK signaling pathways, and decrease the MMP-2 and MMP-9 activities through the activation of the NM23-H1, TIMP-1, and TIMP-2 expressions. In addition, lycopene in combination with sorafenib also has an additive effect on the inhibition of tumor growth *in situ*. Based on these results, lycopene has a potential as an adjuvant for the cancer treatment of sorafenib.

DATA AVAILABILITY STATEMENT

The raw data supporting the conclusions of this article will be made available, without undue reservation, upon request to the corresponding author.

ETHICS STATEMENT

The animal study was reviewed and approved by Animal Management Committee of the National Chung Hsing University.

AUTHOR CONTRIBUTIONS

N-CY and C-HC designed the study. Y-PC and IL participated in the experiments. Y-PC and N-CY wrote the draft. N-CY revised the manuscript. All authors approved the final manuscript.

FUNDING

This work was supported by grants from the Ministry of Science and Technology of Taiwan (MOST 105-2320-B-040-017-MY3).

SUPPLEMENTARY MATERIAL

The Supplementary Material for this article can be found online at: https://www.frontiersin.org/articles/10.3389/fnut.2022.886988/full#supplementary-material

REFERENCES

1. Siegel RL, Miller KD, Fuchs HE, Jemal A. Cancer statistics, 2021. *CA Cancer J Clin*. (2021) 71:7–33. doi: 10.3322/caac.21654
2. Steeg PS. Tumor metastasis: mechanistic insights and clinical challenges. *Nat Med*. (2006) 12:895–904. doi: 10.1038/nm1469
3. Talmadge JE, Fidler IJ. AACR centennial series: the biology of cancer metastasis: historical perspective. *Cancer Res*. (2010) 70:5649–69. doi: 10.1158/0008-5472.CAN-10-1040
4. Khan UM, Sevindik M, Zarrabi A, Nami M, Ozdemir B, Kaplan DN, et al. Lycopene: food sources, biological activities, and human health benefits. *Oxid Med Cell Longev*. (2021) 2021:2713511. doi: 10.1155/2021/2713511
5. Mangels AR, Holden JM, Beecher GR, Forman MR, Lanza E. Carotenoid content of fruits and vegetables: an evaluation of analytic data. *J Am Diet Assoc*. (1993) 93:284–96. doi: 10.1016/0002-8223(93)91553-3
6. Miller NJ, Sampson J, Candeias LP, Bramley PM, Rice-Evans CA. Antioxidant activities of carotenes and xanthophylls. *FEBS Lett*. (1996) 384:240–2. doi: 10.1016/0014-5793(96)00323-7
7. Conn PF, Schalch W, Truscott TG. The singlet oxygen and carotenoid interaction. *J Photochem Photobiol B*. (1991) 11:41–7. doi: 10.1016/1011-1344(91)80266-K
8. Palozza P, Parrone N, Catalano A, Simone R. Tomato lycopene and inflammatory cascade: basic interactions and clinical implications. *Curr Med Chem*. (2010) 17:2547–63. doi: 10.2174/092986710791556041
9. Huang CS, Chuang CH, Lo TF, Hu ML. Antiangiogenic effects of lycopene through immunomodualtion of cytokine secretion in human peripheral blood mononuclear cells. *J Nutr Biochem*. (2013) 24:428–34. doi: 10.1016/j.jnutbio.2012.01.003
10. Stahl W, von Laar J, Martin HD, Emmerich T, Sies H. Stimulation of gap junctional communication: comparison of acycloretinoic acid and lycopene. *Arch Biochem Biophys*. (2000) 373:271–4. doi: 10.1006/abbi.1999.1510
11. Talalay P. Chemoprotection against cancer by induction of phase 2 enzymes. *BioFactors*. (2000) 12:5–11. doi: 10.1002/biof.5520120102
12. Levy J, Bosin E, Feldman B, Giat Y, Miinster A, Danilenko M, et al. Lycopene is a more potent inhibitor of human cancer cell proliferation than either alpha-carotene or betacarotene. *Nutr Cancer*. (1995) 24:257–66. doi: 10.1080/01635589509514415
13. Yang CM, Yen YT, Huang CS, Hu M L. Growth inhibitory efficacy of lycopene and β-carotene against androgen-independent prostate tumor cells xenografted in nude mice. *Mol Nutr Food Res*. (2011) 55:606–12. doi: 10.1002/mnfr.201000308
14. Tang FY, Pai MH, Wang XD. Consumption of lycopene inhibits the growth and progression of colon cancer in a mouse xenograft model. *J Agric Food Chem*. (2011) 59:9011–21. doi: 10.1021/jf2017644
15. Chen ML, Lin YH, Yang CM, Hu ML. Lycopene inhibits angiogenesis both in vitro and in vivo by inhibiting MMP-2/uPA system through VEGFR2-mediated PI3K-Akt and ERK/p38 signaling pathways. *Mol Nutr Food Res*. (2012) 56:889–99. doi: 10.1002/mnfr.201100683
16. Huang CS, Shih MK, Chuang CH, Hu ML. Lycopene inhibits cell migration and invasion and upregulates Nm23-H1 in a highly invasive hepatocarcinoma, SK-Hep-1 cells. *J Nutr*. (2005) 135:2119–23. doi: 10.1093/jn/135.9.2119
17. Huang CS, Liao JW, Hu ML. Lycopene inhibits experimental metastasis of human hepatoma SK-Hep-1 cells in athymic nude mice. *J Nutr*. (2008) 138:538–43. doi: 10.1093/jn/138.3.538
18. Jhou BY, Song TY, Lee I, Hu ML, Yang NC. Lycopene inhibits metastasis of human liver adenocarcinoma SK-Hep-1 cells by downregulation of NADPH oxidase 4 protein expression. *J Agric Food Chem*. (2017) 65:6893–903. doi: 10.1021/acs.jafc.7b03036
19. Lin MT, Lin CL, Lin TY, Cheng CW, Yang SF, Lin CL, et al. Synergistic effect of fisetin combined with sorafenib in human cervical cancer HeLa cells through activation of death receptor-5 mediated caspase-8/caspase-3 and the mitochondria-dependent apoptotic pathway. *Tumour Biol*. (2016) 37:6987–96. doi: 10.1007/s13277-015-4526-4
20. Yunos NM, Beale P, Yu JQ, Huq F. Synergism from the combination of oxaliplatin with selected phytochemicals in human ovarian cancer cell lines. *Anticancer Res*. (2011) 31:4283–9.
21. Iyer R, Fetterly G, Lugade A, Thanavala Y. Sorafenib: a clinical and pharmacologic review. *Expert Opin Pharmacother*. (2010) 11:1943–55. doi: 10.1517/14656566.2010.496453
22. Keating GM, Santoro A. Sorafenib: a review of its use in advanced hepatocellular carcinoma. *Drugs*. (2009) 69:223–40. doi: 10.2165/00003495-200969020-00006
23. Wilhelm SM, Carter C, TangL, Wilkie D, McNabola A, Rong H, et al. BAY 43-9006 exhibits broad spectrum oral antitumor activity and targets the RAF/MEK/ERK pathway and receptor tyrosine kinases involved in tumor progression and angiogenesis. *Cancer Res*. (2004) 64:7099–109. doi: 10.1158/0008-5472.CAN-04-1443
24. Nakagawa H, Maeda S. Molecular mechanisms of liver injury and hepatocarcinogenesis: focusing on the role of stress-activated MAPK. *Patholog Res Int*. (2012) 2012:172894. doi: 10.1155/2012/172894

25. Liu L, Cao Y, Chen C, Zhang X, McNabola A, Wilkie D, et al. Sorafenib blocks the RAF/MEK/ERK pathway, inhibits tumor angiogenesis, and induces tumor cell apoptosis in hepatocellular carcinoma model PLC/PRF/5. *Cancer Res.* (2006) 66:11851–8. doi: 10.1158/0008-5472.CAN-06-1377
26. Alsaied OA, Sangwan V, Banerjee S, Krosch TC, Chugh R, Saluja A, et al. Sorafenib and triptolide as combination therapy for hepatocellular carcinoma. *Surgery.* (2014) 156:270–9. doi: 10.1016/j.surg.2014.04.055
27. Zhang W, Zhu XD, Sun HC, Xiong YQ, Zhuang PY, Xu HX, et al. Depletion of tumor-associated macrophages enhances the effect of sorafenib in metastatic liver cancer models by antimetastatic and antiangiogenic effects. *Clin Cancer Res.* (2010) 16:3420–30. doi: 10.1158/1078-0432.CCR-09-2904
28. Reddy KB, Nabha SM, Atanaskova N. Role of MAP kinase in tumor progression and invasion. *Cancer Metastasis Rev.* (2003) 22:395–403. doi: 10.1023/A:1023781114568
29. Zhang Q, Han Q, Yang Z, Ni Y, Agbana YL, Bai H, et al. G6PD facilitates clear cell renal cell carcinoma invasion by enhancing MMP2 expression through ROS-MAPK axis pathway. *Int J Oncol.* (2020) 57:197–212. doi: 10.3892/ijo.2020.5041
30. Maraldi T. Natural compounds as modulators of NADPH oxidases. *Oxid Med Cell Longev.* (2013) 2013:271602. doi: 10.1155/2013/271602
31. Lambeth JD, Krause KH, Clark RA. NOX enzymes as novel targets for drug development. *Semin Immunopathol.* (2008) 30:339–63. doi: 10.1007/s00281-008-0123-6
32. Guo C, Yang M, Jing L, Wang J, Yu Y, Li Y, et al. Amorphous silica nanoparticles trigger vascular endothelial cell injury through apoptosis and autophagy via reactive oxygen species-mediated MAPK/Bcl-2 and PI3K/Akt/mTOR signaling. *Int J Nanomedicine.* (2016) 11:5257–76. doi: 10.2147/IJN.S112030
33. Wang J, Huang J, Wang L, Chen C, Yang D, Jin M, et al. Urban particulate matter triggers lung inflammation via the ROS-MAPK-NF-κB signaling pathway. *J Thorac Dis.* (2017) 9:4398–412. doi: 10.21037/jtd.2017.09.135
34. Song TY, Lin HC, Yang NC, Hu ML. Antiproliferative and antimetastatic effects of the ethanolic extract of Phellinus igniarius (Linnearus: Fries) Quelet. *J Ethnopharmacol.* (2008) 115:50–6. doi: 10.1016/j.jep.2007.09.001
35. Egeblad M, Werb Z. New functions for the matrix metalloproteinases in cancer progression. *Nat Rev Cancer.* (2002) 2:161–74. doi: 10.1038/nrc745
36. Yoon SO, Park SJ, Yun CH, Chung AS. Roles of matrix metalloproteinases in tumor metastasis and angiogenesis. *J Biochem Mol Biol.* (2003) 36:128–37. doi: 10.5483/BMBRep.2003.36.1.128
37. Deryugina EI, Quigley JP. Matrix metalloproteinases and tumor metastasis. *Cancer Metastasis Rev.* (2006) 25:9–34. doi: 10.1007/s10555-006-7886-9
38. Roomi MW, Monterrey JC, Kalinovsky T, Rath M, Niedzwiecki A. Patterns of MMP-2 and MMP-9 expression in human cancer cell lines. *Oncol Rep*. (2009) 21:1323. doi: 10.3892/or_00000358
39. Dhillon AS, Hagan S, Rath O, Kolch W. MAP kinase signalling pathways in cancer. *Oncogene.* (2007) 26:3279–90. doi: 10.1038/sj.onc.1210421
40. Qi M, Elion EA. MAP kinase pathways. *J Cell Sci.* (2005) 118:3569–72. doi: 10.1242/jcs.02470
41. Roberts PJ, Der CJ. Targeting the Raf-MEK-ERK mitogen-activated protein kinase cascade for the treatment of cancer. *Oncogene.* (2007) 26:3291–310. doi: 10.1038/sj.onc.1210422
42. Staples CJ, Owens DM, Maier JV, Cato AC, Keyse SM. Cross-talk between the p38α and JNK MAPK pathways mediated by MAP kinase phosphatase-1 determines cellular sensitivity to UV radiation. *J Biol Chem.* (2010) 285:25928–40. doi: 10.1074/jbc.M110.117911
43. Olson JM, Hallahan AR. p38 MAP kinase: a convergence point in cancer therapy. *Trends Mol Med.* (2004) 10:125–9. doi: 10.1016/j.molmed.2004.01.007
44. Wu YJ, Neoh CA, Tsao CY, Su JH, Li HH. Sinulariolide suppresses human hepatocellular carcinoma cell migration and invasion by inhibiting matrix metalloproteinase-2/-9 through MAPKs and PI3K/Akt signaling pathways. *Int J Mol Sci.* (2015) 16:16469–82. doi: 10.3390/ijms160716469
45. Lu CC, Yang JS, Chiang JH, Hour MJ, Amagaya S, Lu KW, et al. Inhibition of invasion and migration by newly synthesized quinazolinone MJ-29 in human oral cancer CAL 27 cells through suppression of MMP-2/9 expression and combined down-regulation of MAPK and AKT signaling. *Anticancer Res.* (2012) 32:2895–903.
46. Yang JL, Lin JH, Weng SW, Chen JC, Yang JS, Amagaya S, et al. Crude extract of Euphorbia formosana inhibits the migration and invasion of DU145 human prostate cancer cells: The role of matrix metalloproteinase-2/9 inhibition via the MAPK signaling pathway. *Mol Med Rep*. (2013) 7:1403–8. doi: 10.3892/mmr.2013.1380
47. Palmieri D, Horak CE, Lee JH, Halverson DO, Steeg PS. Translational approaches using metastasis suppressor genes. *J Bioenerg Biomembr*. (2006) 38:151–61. doi: 10.1007/s10863-006-9039-9
48. Boissan M, De Wever O, Lizarraga F, Wendum D, Poincloux R, Chignard N, et al. Implication of metastasis suppressor NM23-H1 in maintaining adherens junctions and limiting the invasive potential of human cancer cells. *Cancer Res.* (2010) 70:7710–22. doi: 10.1158/0008-5472.CAN-10-1887
49. Ohba K, Miyata Y, Koga S, Kanda S, Kanetake H. Expression of nm23-H1 gene product in sarcomatous cancer cells of renal cell carcinoma: correlation with tumor stage and expression of matrix metalloproteinase-2, matrix metalloproteinase-9, sialyl Lewis X, and c-erbB-2. *Urology.* (2005) 65:1029–34. doi: 10.1016/j.urology.2004.12.032
50. Baker AH, Edwards DR, Murphy G. Metalloproteinase inhibitors: biological actions and therapeutic opportunities. *J Cell Sci.* (2002) 115:3719–27. doi: 10.1242/jcs.00063
51. McIntush EW, Smith MF. Matrix metalloproteinases and tissue inhibitors of metalloproteinases in ovarian function. *Rev Reprod.* (1998) 3:23–30. doi: 10.1530/ror.0.0030023
52. Bourboulia D, Stetler-Stevenson WG. Matrix metalloproteinases (MMPs) and tissue inhibitors of metalloproteinases (TIMPs): Positive and negative regulators in tumor cell adhesion. *Semin Cancer Biol.* (2010) 20:161–8. doi: 10.1016/j.semcancer.2010.05.002
53. Reagan-Shaw S, Nihal M, Ahmad N. Dose translation from animal to human studies revisited. FASEB J. (2008) 22:659–61. doi: 10.1096/fj.07-9574LSF
54. Rao AV, Shen H. Effect of low dose lycopene intake on lycopene bioavailability and oxidative stress. *Nutr Res.* (2002) 22:1125–31. doi: 10.1016/S0271-5317(02)00430-X
55. Mackinnon ES, Rao AV, Rao LG. Lycopene intake by Canadian women is variable, similar among different ages, but greater than that reported for women in other countries. *J Med Food.* (2009) 12:829–35. doi: 10.1089/jmf.2008.0118
56. Huang JP, Zhang M, Holman CD, Xie X. Dietary carotenoids and risk of breast cancer in Chinese women. *Asia Pac J Clin Nutr*. (2007) 16:437–42.

Conflict of Interest: The authors declare that the research was conducted in the absence of any commercial or financial relationships that could be construed as a potential conflict of interest.

frontiers | Frontiers in Nutrition

ORIGINAL RESEARCH
published: 12 July 2022
doi: 10.3389/fnut.2022.869749

Characterization, Hypoglycemic Activity, and Antioxidant Activity of Methanol Extracts From *Amomum tsao-ko*: *in vitro* and *in vivo* Studies

*Libin Xie [1]†, Dan Yu [2]†, Yanan Li [1], Huidong Ju [1], Jia Chen [1], Lianxia Hu [1] and Longquan Yu [1]**

[1] Shijiazhuang Food Engineering Technology Research Center, School of Chemical Engineering, Shijiazhuang University, Shijiazhuang, China, [2] Department of Nutrition, Third Hospital of Hebei Medical University, Shijiazhuang, China

The dried fruit of *Amomum tsao-ko* is well-known as a spice as well as a Chinese traditional herb. This study aimed to identify the bioactive constituents in the powder of methanol extract from *Amomum tsao-ko* (PMEAT) and to evaluate the hypoglycemic and antioxidant effects of PMEAT, *in vitro* and *in vivo*. We identified 36 phytochemicals in PMEAT by employing HPLC-MS/MS. PMEAT solution was found to have potent α-glucosidase-inhibiting activity (IC_{50}, 0.145 mg/mL) *in vitro*, twice as strong as that of acarbose (IC_{50}, 0.273 mg/mL). To investigate the hypoglycemic activity of PMEAT *in vivo*, we studied the impact of low-dose PMEAT (the addition of 100 mg/kg PMEAT to the mice diet) and high-dose PMEAT (200 mg/kg PMEAT addition) treatments in STZ-induced diabetic mice. After 6 weeks of intervention, significantly decreased fasting blood glucose (FBG) ($p < 0.05$), significantly decreased area under the curve (AUC) of the oral glucose tolerance test ($p < 0.05$), significantly decreased HOMA-IR ($p < 0.05$), and significantly increased HOMA-β ($p < 0.05$) were observed in the high-dose PMEAT group. Moreover, we performed an antioxidant activity experiment *in vitro*. The results showed that PMEAT had a strong ability to scavenge DPPH (IC_{50}, 0.044 mg/mL) as well as ABTS free radicals (IC_{50}, 0.040 mg/mL). In an animal experiment conducted on oxidative damage mice model which was induced by D-glucose and a high-fat diet, we observed significantly increased dismutase (SOD) ($p < 0.01$), glutathione (GSH) ($p < 0.01$), and glutathione peroxidase (GSH-Px) ($p < 0.01$) and significantly reduced malondialdehyde (MDA) and 8-ISO-prostaglandin-PGF2α (8-ISO-PGF2α), after treatment with PMEAT for 90 days. In conclusion, this study reveals the therapeutic potential of *Amomum tsao-ko* for the treatment of diabetes and helps us discover new antioxidant candidates from natural sources.

Keywords: ***Amomum tsao-ko*, methanol extracts, hypoglycemic effect, antioxidant effect, mice**

Edited by:
Zhiqiang Wang,
Hebei University, China

Reviewed by:
Hady Keita,
University of the South Sierra, Mexico
Hock Eng Khoo,
Guilin University of Technology, China

****Correspondence:***
Longquan Yu
ylq29jp@163.com

† These authors share first authorship

Specialty section:
This article was submitted to
Food Chemistry,
a section of the journal
Frontiers in Nutrition

Received: *04 February 2022*
Accepted: *13 June 2022*
Published: *12 July 2022*

Citation:
Xie L, Yu D, Li Y, Ju H, Chen J, Hu L and Yu L (2022) Characterization, Hypoglycemic Activity, and Antioxidant Activity of Methanol Extracts From Amomum tsao-ko: in vitro and in vivo Studies. Front. Nutr. 9:869749.
doi: 10.3389/fnut.2022.869749

INTRODUCTION

In the last three decades, especially high-calorie diets have been shown to affect lipid metabolism and lead to fat accumulation, resulting in obesity, which is a cause of various chronic diseases such as diabetes, hypertension, and cardiovascular disease (1). Many bioactive phytochemicals in natural plants have attracted the attention of researchers due to their hypoglycemic, lipid-lowering, and antioxidant properties (2, 3). Screening the safe, effective, and conveniently extracted compounds from natural plants have become a new direction to managing diabetes and alleviating oxidative damage.

Amomum tsao-ko Crevost et Lemaire (*A. tsao-ko*), a perennial plant classified into the Zingiberaceae family, is a medicinal herb discovered in Southeast Asia. In China, it is mainly distributed in the Guangxi, Guizhou, and Yunnan provinces. *A. tsao-ko* can not only be used as an edible spice but also has therapeutic effects on stomach disorders, dyspepsia, nausea, abdominal pain, and throat infections, as recorded in the *Chinese Pharmacopoeia*. Flavonoids, coumarins, phenols, and diterpenoids were found as bioactive constituents in *A. tsao-ko* extracts, which have been reported to have the activity of anti-obesity (4), bone health promotion (5), anti-inflammation (6), and anti-proliferation (7). He et al. found that amomutsaokols A-K, diarylheptanoids, tsaokopyranols A–M, and 2,6-epoxy diarylheptanoids from a 50% ethanol-water extract of *A. tsao-ko* demonstrated significant α-glucosidase inhibitory activity (8, 9). However, very limited studies have reported the hypoglycemic and antioxidant effects of methanol extracts from *A. tsao-ko*.

Over the past few years, we have carried out systematic research on *A. tsao-ko.* At the earliest, we did animal experiments with 12 kinds of spices (*A. tsao-ko*, star anise, cinnamon, etc.) to study their physiological regulating activities (10). The results indicated that four of them had the effects of reducing body weight and blood lipids, among which the activity of *A. tsao-ko* was the strongest. Next, we added 0.5 and 0.1% of the above four spices to the mouse feed to study if low-dose added spices have a biological effect on mice (11). The results showed that *A. tsao-ko*, aniseed, and cumin had hypoglycemic and hypolipidemic effects when 0.5% was added. When the addition amount was 0.1% (equivalent to 0.5 g/d), only *A. tsao-ko* exhibited hypoglycemic prosperity. Based on the above studies, the activity of the residue, acetone extract, chloroform extract, and methanol extract of *A. tsao-ko* were, respectively, assessed by performing animal experiments (12, 13). The results showed that the effective components of weight loss, lipid reduction, and glucose reduction mainly existed in the methanol extract. Because methanol is toxic, we explored the feasibility of using ethanol solution as a nontoxic solvent instead of a methanol-chloroform mixed solution (14). The results did not show that the ethanol extract had the effects of reducing blood lipids and regulating glucose homeostasis. The reason is probably that the phytochemicals in the *A. tsao-ko* were polar lipid solubles; nevertheless, the introduction of water not only changed the polarity of the solution but also altered the extraction components.

The present study was conducted as a further analysis to identify the bioactive constituents contained in the methanol extracts of *A. tsao-ko.* Because oxidative stress can lead to disorders of glucose metabolism, we currently performed a comprehensive and systematic study on the hypoglycemic and antioxidant activities of the power of methanol extracts of *A. tsao-ko* (PMEAT), *in vivo* and *in vitro*. This study may provide important evidence for the utilization and pharmaceutical development of methanol extracts of *A. tsao-ko.*

MATERIALS AND METHODS

Chemicals

α-Glucosidase Detection Kit was purchased from Shanghai Guyan Industrial Co., Ltd. (Shanghai, China). Acarbose standard sample was purchased from Shijiazhuang Huarong Pharmaceutical Co., Ltd. (Shijiazhuang, China). The Insulin ELISA kit was purchased from Shijiazhuang Huiduan Biotechnology Co., Ltd. (Shijiazhuang, China). Superoxide dismutase (SOD) assay kit, reduced glutathione (GSH) assay kit, glutathione peroxidase (GSH-Px) assay kit, malondialdehyde (MDA) assay kit, and mouse 8-iso prostaglandin F2α (8-ISO-PGF2α) ELISA kit were purchased from Nanjing Jiancheng Bioengineering Institute (Nanjing, China). Other reagents were all analytical grade.

Plant Materials and Preparation of PMEAT

Dried *A. tsao-ko* fruits were purchased from Kunming herbal market in Yunnan province, China. We prepared PMEAT according to the methods of Yan et al. with slight modifications (15). First, *A. tsao-ko* fruits were shelled, freeze-dried, pulverized using a high-speed shredder (HC100, Zhejiang Jinhui Machinery Factory, Yongkang, China) and sieved (100 mesh). A total of 50 g fruit powder was added to the mixed alcohol extracting solution (200 mL chloroform, 400 mL methanol, and 40 mL distilled water) and stayed still for 12 h. After being mixed for 5 min (18,000 r/min), the mixed liquor was crushed for 10 min (70% power, 20–25 Hz) with an ultrasonic cell pulverizer (XD-1200D, Nanjing Xianou Instrument Manufacturing Co., Ltd., Nanjing, China). After being shrunk and filtered by vacuum, the crushed mixture was concentrated and turned into a filter cake, which was added with a half amount of the mixed ethanol extract (100 mL chloroform, 200 mL methanol, and 20 mL distilled water) to complete the first-time extraction. Next, extraction was repeated twice in the same way and the filtrate was collected from three extractions. A 60 g activated silica gel powder was then added to the filtrate and the powdery mixture was obtained after being concentrated using a rotary evaporator (RE-52AA, Shanghai Yarong Biochemical Instrument Factory, Shanghai, China). The powder sample was then put in a self-made silica gel hydrogen column (200–300 mesh, 500 × 250 mm, activated by methanol, acetone, and chloroform for 4 h) and eluted successively with 600 mL chloroform, 600 mL acetone, and 600 mL methanol. Thus, we obtained the methanol eluent, which was then filtered by a microporous membrane (0.22 μm). The powder of methanol extract of *A. tsao-ko* was finally obtained after the evaporative concentration and freeze-drying.

Identification of Bioactive Compounds in PMEAT

Chromatographic separation was performed in a Thermo Ultimate 3000LC system equipped with a Zorbax Eclipse C18 column (1.8 μm × 2.1 × 100 mm) maintained at 30°C (16). The mobile phases were 0.1% formic acid in water (A) and grade acetonitrile (B). The injection volume of the sample was 2 μL and the elution flow rate was 0.30 mL/min. The program of gradient elution was as follows: 0–2 min, 5% B; 2–7 min, 30% B; 7–14 min, 78% B; 14–20 min, 90% B; 20–25 min, 5% B. The ESI-MSn experiments were conducted on a Thermo Q Exactive HF mass spectrometer with a spray voltage of 3.5 kV in positive and negative modes. The sheath gas, auxiliary gas, and sweep gas flow rates were set to 45, 15, and 1 arbitrary unit, respectively. The heater and capillary temperatures were 325 and 330°C, respectively. The S-Lens RF Level was 55%. The analyzer scanned over a mass range of m/z 100–1,500 for a full scan at a mass resolution of 12,000. Data-dependent secondary mass spectrometry scanning (dd-MS2, TopN = 10) was at a mass resolution of 6,000 with an HCD mode.

Determination of α-Glucosidase Inhibiting Activity *in vitro*

The determination procedure of α-glucosidase (α-GIA) inhibiting activity was referred to as the method of Chen et al. (17). In brief, α-glucosidase and PNPG (4-N-trophenyl-α-D-glu-copyranoside) were dissolved in a phosphate buffer solution (PBS) (10 mg/mL, pH 6.8) at 1 U/mL and 12.5 mmol/L, respectively. In addition, PMEAT samples were dissolved in a PBS (10 mg/mL, pH 6.8) to prepare different reaction gradient solutions. Forty microliters each of PMEAT sample solution and α-glucosidase solution were mixed in a 96-well microplate and incubated at 37°C for 15 min. Then, 20 μL of the PNPG solution was added and incubated at 37°C for 15 min. Finally, the reaction was stopped by the addition of 100 μL of Na_2CO_3 solution (pH 6.8). PBS was taken as blank control and was used as a background solution instead of α-glucosidase solution to eliminate the influence of the ground effect. The optical density (OD) of each well was detected using a microplate reader at a wavelength of 405 nm. The inhibition rate against α-glucosidase of two test solutions was calculated as follows:

$$\mathrm{I}(\%) = \frac{\mathrm{OD}blank - (\mathrm{OD}sample - \mathrm{OD}ground)}{\mathrm{ODblank}} \times 100\% \quad (1)$$

Determination of Hypoglycemic Activity *in vivo*

Animals

Eight-week-old male ICR mice (SPF, weight 28–32 g) [Animal license number: SCXK(Jing)2016-0006] were obtained from Beijing Vital River Laboratory Animal Technology Co., Ltd (Beijing, China). Animals were housed in a controlled environment (temperature 20–25°C, humidity 40–60%, 12/12h light/dark cycle) with free access to pellet diet and water. The mice were used for experiments after 1 week of acclimatization.

Animal Model and Experimental Design

First, mice were randomly divided into two groups: a control group (Con, n = 10), fed the basic mouse fodder (starch 47.8%, casein 20%, sucrose 15%, lard 6%, cellulose 5%, minerals 4%, vitamins 2%, and L-methionine 0.2%), and a high-fat diet group (n = 40), fed high-fat diet (HFD basic mouse fodder adding 10% lard, e.g., 25 g lard were added to 250 g basic mouse fodder). From the 7th week, the mice in the HFD group were injected intraperitoneally with 150 mg/kg·BW STZ (Sterptozotocin) solution (STZ was dissolved with 0.1 mol/L pH 4.5 citrate buffer) after fasting for 12 h. Seventy-two hours after injection and fasting for 12 h again, tail vein blood was taken to determine the fasting blood glucose (FBG) concentration of the mice. The mice in the HFD group with HBG levels ≥ 11.1 mmol/L were selected as diabetic mice (18, 19). Finally, a total of 30 mice in the HFD group were confirmed to be successfully established as diabetic mice, together with 10 mice remaining in the control group for the subsequent 6 weeks of experiments.

Thirty diabetic mice were then randomized into three groups (n = 10 per group) as follows: the model group (Mod), the low-dose PMEAT group (PMEAT-L), and the high-dose PMEAT group (PMEAT-H). From week 8 to week 13, the control group was fed with basic mouse fodder, the model group was fed with high-fat diet, the PMEAT-L group was fed with high-fat diet adding 100 mg/kg PMEAT, and the PMEAT-H group was fed with high-fat diet adding 200 mg/kg PMEAT (the study flow chart and design see **Supplementary Figure 1**). Animal identification used 5% picric acid. The food intake and drinking water of each group were recorded on the first day of every week. On the last day of the 7th and 13th week, mice were housed in metabolic cages for 24 h, and the volumes of food intake and water intake were measured. On the same day, weight was also measured for each mouse individually.

Assessment of Impaired Blood Fasting Glucose

The blood glucose levels of tail blood in four mice groups after a 6-h fasting period were measured once every 2 weeks, starting with the 8th week of the experiment (before the PMEAT intervention).

Oral Glucose Tolerance Test

The oral glucose tolerance tests were performed in week 8 (before the PMEAT intervention) and week 13 (after the PMEAT intervention) on every group. After 10 h of fasting, all mice were intraperitoneally injected with a glucose solution (1.5 g/kg·BW). The blood glucose levels of the tail tip were measured at 0 (baseline), 15, 30, 60, and 120 min after the injection, using a one-touch glucometer (UltraTM, American Johnson & Johnson Co., Ltd, New Brunswick, USA). The integrated glucose response (area under the curve, AUC) over 2 h after the glucose overload was calculated as follows (20):

$$\begin{aligned} AUC = {} & [(BG_0 + BG_{15}) + (BG_{15} + BG_{30}) + (BG_{30} + BG_{60})\times 2 \\ & + (BG_{60} + BG_{120})\times 4]\times 0.25\times 0.5 \end{aligned} \quad (2)$$

BGi: blood glucose value at i min.

Assessment of Insulin Resistance

In the 13th week (after 6 weeks of PMEAT intervention), the blood of mice in four groups was collected from the retro-ocular venous after fasting for 10 h. The fasting blood glucose was measured with the OneTouch UltraTM rapid blood glucose meter. The remaining blood was centrifuged (3,000 r/min, 15 min) to collect plasma, and plasma insulin was quantified by an enzyme-linked immunosorbent assay (ELISA) kit. Homeostatic model assessment for insulin resistance (HOMA-IR) and homeostatic model assessment for β cell function

(HOMA-β) were calculated based on fasting blood glucose (FBG) and fasting insulin level (21). Calculation formula: HOMA-IR = FBG (mmol/L) × fasting insulin level (μU/ml)/22.5; HOMA-β = [20 × fasting insulin level (mIU/L)]/[FBG (mmol/L)−3.5] (%).

Determination of Antioxidant Activity *in vitro*

DPPH Radical Scavenging Assay

The DPPH assay was performed according to the method of Cui et al. with slight modifications (22). In brief, 0.3 mL of the diluted test sample and 3 mL 25 μg/mL of a DPPH working solution were added to the test tube, reacted at 30°C in the dark for 40 min, and measured at 516 nm. Methanol was the blank control and rutin and curcumin were the positive controls. The scavenging activity was expressed as an IC_{50} value (mg/mL).

ABTS Radical Scavenging Assay

The ABTS assay was undertaken by the method of Cui et al. with slight modifications (22). First, an ABTS stock solution was prepared by mixing 5 mL of 7 mmol/L ABTS methanol solution and 88 μL of 140 mmol/L potassium per sulfate solution at 25°C in the dark for 16 h. Methanol was used to dilute the stock solution for the absorbance to reach 0.7 ± 0.02 at 734 nm, then to get the ABTS working solution. Next, 0.3 mL of the diluted test sample and 3 mL ABTS working solution were added to the test tube to react at 30°C in the dark for 6 min, and the absorbance was subsequently measured at 734 nm. Methanol was the blank control and rutin and curcumin were the positive controls. The scavenging activity was expressed as an IC_{50} value (mg/mL).

Ferric Reducing Antioxidant Power Assay

The FRAP assay was performed using the method of Guo et al. (23). The FRAP reagent was prepared by mixing 300 mmol/L acetate buffer (pH 3.6), 10 mmol/L TPTZ, and 20 mmol/L $FeCl_3$ at a ratio of 10:1:1 (v/v/v). Subsequently, 0.1 mL of the diluted test sample and 3 mL FRAP reagent were added to the test tube and reacted at 37°C in the dark for 5 min. The absorbance was measured at 596 nm. With the standard solution of $FeSO_4$ as the reference substance, the FRAP result of the samples was presented as the millimoles of $FeSO_4$ required to achieve the same absorbance.

Determination of Antioxidant Activity *in vivo*

Animal Model and Experimental Design

To evaluate the antioxidant activity of PMEAT *in vivo*, we performed another 90-day animal experiment based on the oxidative damage mouse model (24). After 1 week of acclimation, mice (the strain and raising environment were the same as the mice in the hypoglycemic animal experiment) were randomly divided into four different groups: a control group (Con, n = 12), a model group (Mod, n = 12), a low-dose PMEAT group (PMEAT-L, n = 12), and a high-dose PMEAT group (PMEAT-H, n = 12). The mice in the control group were fed a basic diet for 8 weeks. The mice in the model group were fed a high-fat diet (HFD) for 8 weeks. The mice in the PMEAT-L and PMEAT-H groups were treated with HFD adding 100 mg/kg PMEAT and HFD adding 200 mg/kg PMEAT for 8 weeks, respectively. During this same 8-week period, the mice in each group except the control group were intraperitoneally injected with D-galucose (125 mg/kg·d) once per day (15). After the D-galactose injection was terminated, each group continued to be treated with its diet for another 5 weeks to complete the 90-day experiment plan (the study flow chart and design see **Supplementary Figure 2**).

At the end of the feeding experiment, all mice fasted for 24 h (not having food and water), then blood and liver tissues were collected after sacrificing (25, 26). Blood samples from all mice were spun for 15 min at 3,000 rpm. The plasma was then isolated and used to assess the levels of SOD, GSH, GSH-Px, MDA, and 8-ISO-PGF2α using appropriate test kits (16). The liver tissues were ground and spun for 20 min at 3,000 rpm to get a 10% homogenate. The supernatants were then collected, and the levels of SOD, GSH, GSH-Px, and MDA were assessed using the corresponding test kits (16).

Statistical Analysis

Statistical analysis was performed using SPSS version 26.0. Data were tested for normal distribution with the Shapiro–Wilk test. One-way ANOVA followed by Tukey's-SHD and Student's t-test were performed to examine the differences among treatment groups for the analysis of the hypoglycemic indicators (fasting blood glucose, glucose tolerance AUC, HOMA-IR, and HOMA-β) and antioxidant indices (plasma SOD, plasma GSM, plasma GSH-Px, plasma MDA, plasma 8-ISO-PGF2α, liver tissue SOD, liver tissue GSM, liver tissue GSH-Px, and liver tissue MDA). P-value < 0.05 indicated that the difference between groups was statistically significant.

RESULTS

Bioactive Constituents Identified in PMEAT

To elucidate the substance basis of the pharmacologic effect, a HPLC-MS/MS full-spectrum analysis in positive and negative ionization modes was performed (**Figure 1**). The fragment information was compared with the Thermo mzCloud and Thermo mzValu databases. The phytochemicals in the PMEAT were summarized and displayed in **Table 1**. Twenty-one flavonoids including 8-prenylnaringenin (No 3), dihydrokaempferol (No 6), isorhamnetin 3-alactoside (No 8), avicularin (No 11), epicatechin (No 12), hesperetin (No 13), hyperoside (No 14), isorhamnetin (No 15), padmatin (No 18), procyanidin A2 (No 19), quercetin (No 20), rutin (No 21), ambocin (No 23), isorhamnetin-3-O-glucoside (No 26), isorhamnetin-3-O-rutinoside (No 27), naringin (No 28), procyanidin B1 (No 29), astragalin (No 31), catechin (No 32), luteolin (No 34), and quercetin-3β-D-glucoside (No 35) were identified. Four coumarins including 5,6,7-trimethoxycoumarin (No 1), 6-methylcoumarin (No 2), 4-hydroxycoumarin (No 10), and isofraxidin (No 25) were identified. Three phenols were identified in PMEAT, namely gentisyl alcohol (No 7), metoprolol analogs (No 16), and vanillin (No 22). Eight other phytochemicals were identified, namely atenolol analogs (No 4), coniferaldehyde (No 5), 2'-O-methyladenosine (No 9),

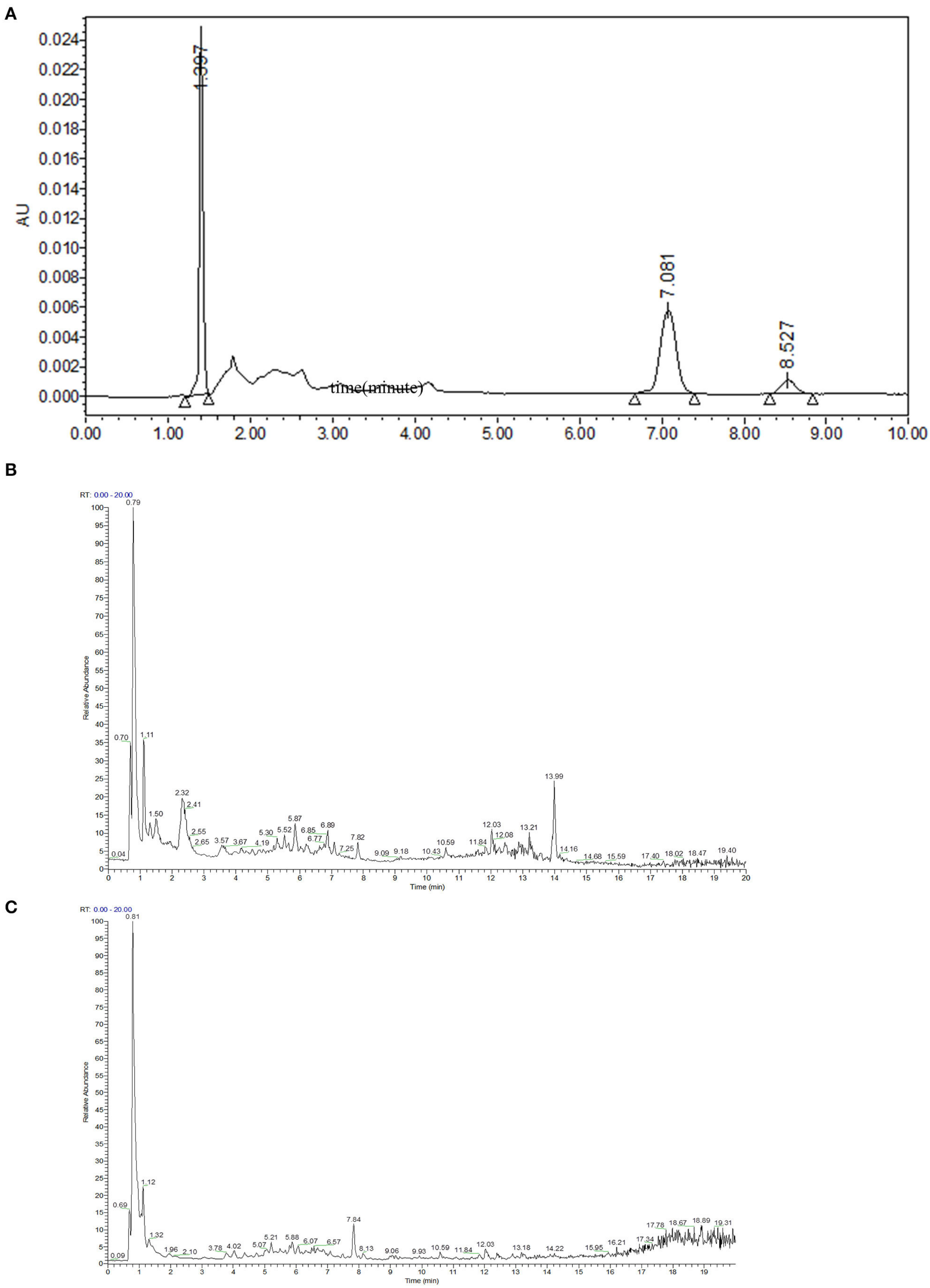

FIGURE 1 | Separation and identification of phytochemicals in PMEAT by HPLC-MS/MS. **(A)** The HPLC analysis chart. **(B,C)** The base peak chromatogram (BPC) for phytochemicals in *A. tsao-ko* methanol extract in the ESI+ **(B)** and ESI– **(C)** modes.

TABLE 1 | Identification of phytochemicals in PMEAT by HPLC-MS/MS.

No	RT (min)	Calc. MW	Annotation MW	Adducts	Annot. DeltaMass (ppm)	Formula	Identification	Activity
1	9.038	236.06815	236.06847	(M + H)+	−1.38	$C_{12} H_{12} O_5$	5,6,7-Trimethoxycoumarin	Antioxidant (41)
2	7.484	160.05234	160.05243	(M + H)+	−0.59	$C_{10} H_8 O_2$	6-Methylcoumarin	Antioxidant (42)
3	10.344	340.13069	340.13107	(M + H)+	−1.12	$C_{20} H_{20} O_5$	8-Prenylnaringenin	Monoacylglycerol lipase inhibitor (43)
4	6.306	266.16283	266.16304	(M + H)+	−0.8	$C_{14} H_{22} N_2 O_3$	Atenolol	β-Blocker (44)
5	10.072	178.06302	178.06299	(M + H)+	0.15	$C_{10} H_{10} O_3$	Coniferaldehyde	Reduce intracellular triglyceride (45)
6	5.937	288.06319	288.06339	(M + H)+	−0.69	$C_{15} H_{12} O_6$	Dihydrokaempferol	Antioxidant (46)
7	6.029	140.04734	140.04734	(M + H)+	−0.05	$C_7 H_8 O_3$	Gentisyl alcohol	Antioxidant (47)
8	7.075	478.11098	478.11113	(M + H)+	−0.31	$C_{22} H_{22} O_{12}$	Isorhamnetin 3-galactoside	Plasminogen activator inhibitor (48);DPP-IV inhibitor (54)
9	1.69	281.11223	281.1124	(M + H)+	−0.62	$C_{11} H_{15} N_5 O_4$	2'-O-Methyladenosine	–
10	12.219	162.03156	162.03169	(M + H)+	−0.85	$C_9 H_6 O_3$	4-Hydroxycoumarin	α-Glucosidase inhibitor (49)
11	6.967	434.08455	434.08491	(M + H)+	−0.83	$C_{20} H_{18} O_{11}$	Avicularin	α-Glucosidase inhibitor (50)
12	5.877	290.07881	290.07904	(M + H)+	−0.77	$C_{15} H_{14} O_6$	Epicatechin	α-Glucosidase inhibitor (51); Antioxidant (52)
13	5.085	302.07875	302.07904	(M + H)+	−0.95	$C_{16} H_{14} O_6$	Hesperetin	α-Glucosidase inhibitor (51); Antioxidant (53)
14	6.676	464.09545	464.09548	(M + H)+	−0.07	$C_{21} H_{20} O_{12}$	Hyperoside	Antioxidant (55)
15	7.073	316.05791	316.0583	(M + H)+	−1.25	$C_{16} H_{12} O_7$	Isorhamnetin	α-Glucosidase inhibitor (54)
16	4.897	267.18324	267.18344	(M + H)+	−0.74	$C_{15} H_{25} N O_3$	Metoprolol	β-Blocker (44)
17	2.338	265.16756	265.16779	(M + H)+	−0.89	$C_{15} H_{23} N O_3$	Oxprenolol	β-Blocker (44)
18	7.493	318.07356	318.07395	(M + H)+	−1.22	$C_{16} H_{14} O_7$	Padmatin	-
19	7.921	576.12645	576.12678	(M + H)+	−0.56	$C_{30} H_{24} O_{12}$	Procyanidin A2	Antioxidant (56)
20	6.675	302.04247	302.04265	(M + H)+	−0.61	$C_{15} H_{10} O_7$	Quercetin	α-Glucosidase inhibitor (50)
21	6.456	610.15318	610.15338	(M + H)+	−0.33	$C_{27} H_{30} O_{16}$	Rutin	Antioxidant (53)
22	6.556	152.04735	152.04734	(M + H)+	0.04	$C_8 H_8 O_3$	Vanillin	α-Glucosidase inhibitor (57); antioxidant (58)
23	6.969	564.14833	564.14791	(M – H) –	0.75	$C_{26} H_{28} O_{14}$	Ambocin	-
24	6.384	267.14717	267.14706	(M – H) –	0.42	$C_{14} H_{21} N O_4$	Atenolol acid	β-Blocker (44)
25	5.752	222.05253	222.05282	(M – H) –	−1.3	$C_{11} H_{10} O_5$	Isofraxidin	NF-$_\kappa$B inhibitor (59); antioxidant (59)
26	7.075	478.11137	478.11113	(M – H) –	0.52	$C_{22} H_{22} O_{12}$	isorhamnetin-3-O-glucoside	α-Glucosidase inhibitor (54)
27	6.857	624.16969	624.16903	(M – H) –	1.05	$C_{28} H_{32} O_{16}$	isorhamnetin-3-O-rutinoside	α-Glucosidase inhibitor (54)
28	6.729	580.17976	580.17921	(M – H) –	0.96	$C_{27} H_{32} O_{14}$	Naringin	α-Glucosidase inhibitor (60); antioxidant (60)
29	5.623	578.14284	578.14243	(M – H) –	0.71	$C_{30} H_{26} O_{12}$	Procyanidin B1	α-Glucosidase inhibitor (51); aldose reductase inhibitor (61); antioxidant (52)
30	5.497	168.04149	168.04226	(M – H) –	−4.59	$C_8 H_8 O_4$	Vanillic acid	Antioxidant (58)
31	7.418	448.101	448.10056	(M – H) –	0.97	$C_{21} H_{20} O_{11}$	Astragalin	Antioxidant (62)
32	5.354	290.07915	290.07904	(M – H) –	0.37	$C_{15} H_{14} O_6$	Catechin	Antioxidant (12)
33	6.965	194.05736	194.05791	(M – H) –	−2.85	$C_{10} H_{10} O_4$	Ferulic acid	Antioxidant (18)
34	9.849	286.04777	286.04774	(M – H) –	0.12	$C_{15} H_{10} O_6$	Luteolin	α-Glucosidase inhibitor (14)
35	6.677	464.096	464.09548	(M – H) –	1.12	$C_{21} H_{20} O_{12}$	Quercetin-3β-D-glucoside	α-Glucosidase inhibitor (51); antioxidant (21)
36	0.8	342.11661	342.11621	(M – H) –	1.16	$C_{12} H_{22} O_{11}$	α,α-Trehalose	Antioxidant (29)

oxprenolol (No 17), atenolol acid analogs (No 24), vanillic acid (No 30), ferulic acid (No 33), and α,α-trehalose (No 36).

Based on the content data of the constituents and the findings, we inferred that phenols, flavonoids, and oligosaccharides were probably the main compounds that exhibited the hypoglycemic and antioxidant activities (27, 28). Among the above 36 phytochemicals, in particular, the α,α-trehalose in PMEAT, a natural non-reducing disaccharide, has been reported to possess

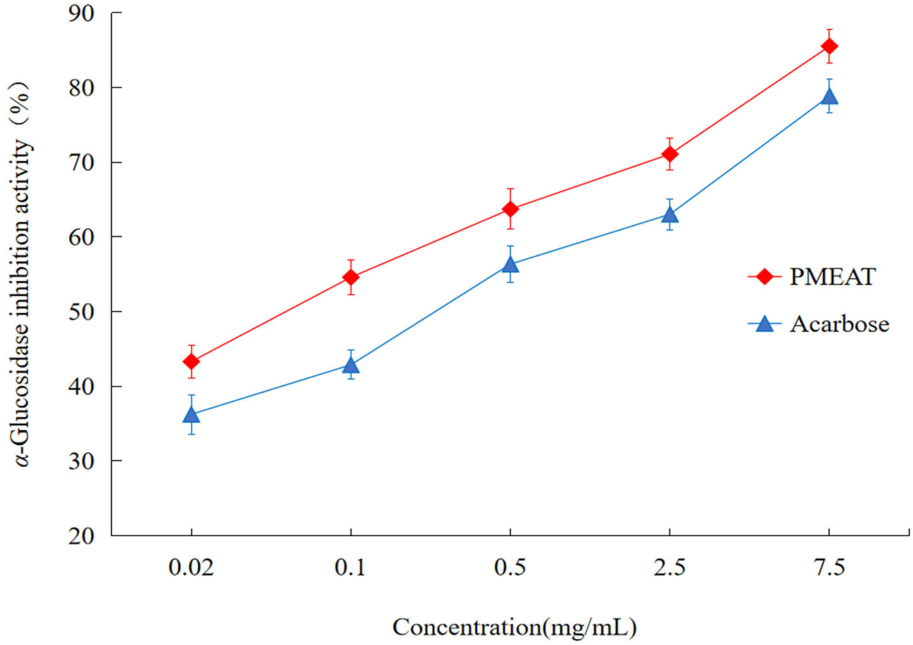

FIGURE 2 | The *in vitro* α-glucosidase inhibitory activity of PMEAT. The line chart depicting the inhibition rate against α-glucosidase of PMEAT (red color) and acarbose (blue color) at different solution concentrations. Three parallel samples for the two test solutions were used to perform this *in vitro* experiment.

a pleiotropic role in various physiological conditions such as oxidative stress protection, inflammation prevention, and inhibition of protein denaturation and neurodegeneration (29). According to the quantitative analysis, its content proportion in PMEAT was not <13%. These findings suggest that the antioxidant and hypoglycemic effects of *A. tsao-ko* may be mainly attributed to this category of phytochemicals.

Inhibitory Activity Against α-Glucosidase *in vitro*

To assess the *in vitro* hypoglycemic effect of PMEAT, α-GIA was investigated (**Figure 2**). We observed inhibition against α-glucosidase by PMEAT and acarbose in a dose-dependent relationship. Compared with the positive control (acarbose, IC_{50} 0.273 mg/mL), PMEAT had a higher α-GIA (IC_{50} 0.154 mg/mL). When the concentration of the PMEAT solution was 0.5 mg/mL, the inhibition rate reached 63.72%. The above strong inhibitory activity against α-glucosidase was probably attributed to a variety of phenolic and coumarins compounds in PMEAT. Many researchers have also confirmed that 4-Hydroxycoumarin, Avicularin, Epicatechin, Hesperetin, Quercetin, Procyanidin B1, and Quercetin-3β-D-glucoside have varying degrees of α-glucosidase inhabitation activities (49–51).

Hypoglycemic Activity of PMEAT *in vivo*

The results of FBG are shown in **Figure 3A**. After the PMEAT treatment for 6 weeks, the FBG level in the PMEAT-H group was lower than that in the Mod group ($p < 0.05$). No significant difference was observed in PMEAT-L group when compared with the Mod group. As shown in **Figure 3B**, after 6 weeks of intervention with PMEAT, the AUC of the PMEAT-L group and the PMEAT-H group was lower than that in the Mod group ($p < 0.05$). The HOMA-IR of the PMEAT-H group was significantly ($p < 0.05$) lower than that in the Mod group as shown in **Figure 3C**. Moreover, the HOMA-β of the PMEAT-H group was significantly ($p < 0.05$) higher than that in the Mod group presented in **Figure 3D**. There are many ways of the mechanisms of hypoglycemic effect in the human body. Without mechanism research performed in this study, we could only infer that it was the contents of avicularin, epicatechin, hesperetin, and other components listed in **Table 1** with α-glucosidase inhibitory activity in the PMEAT which contributed to the *in vivo* anti-diabetic properties. The compounds probably prevented oligosaccharides in food from decomposing into monosaccharides, and thus reducing the glucose absorption in the intestine and protected islet cells, and consequently enhanced glucose tolerance (30, 31).

Antioxidant Activity of PMEAT *in vitro*

In this article, various assays (DPPH, ABTS, and FRAP) were used to comprehensively evaluate the antioxidant activities of *A. tsao-ko* methanol extracts. As shown in **Figure 4A**, when the concentration of PMEAT was higher than 0.08 mg/mL, the scavenging effect of PMEAT on DPPH free radicals was stronger than that of curcumin. The IC_{50} of DPPH scavenging of PMEAT was 0.044 mg/mL. Moreover, the scavenging rate curve of PMEAT coincided with the curve of rutin when the solution concentration increased to 0.12 mg/mL. The result of the ABTS radical scavenging of PMEAT is presented in **Figure 4B**. It shows that PMEAT had stronger activity against ABTS free radicals

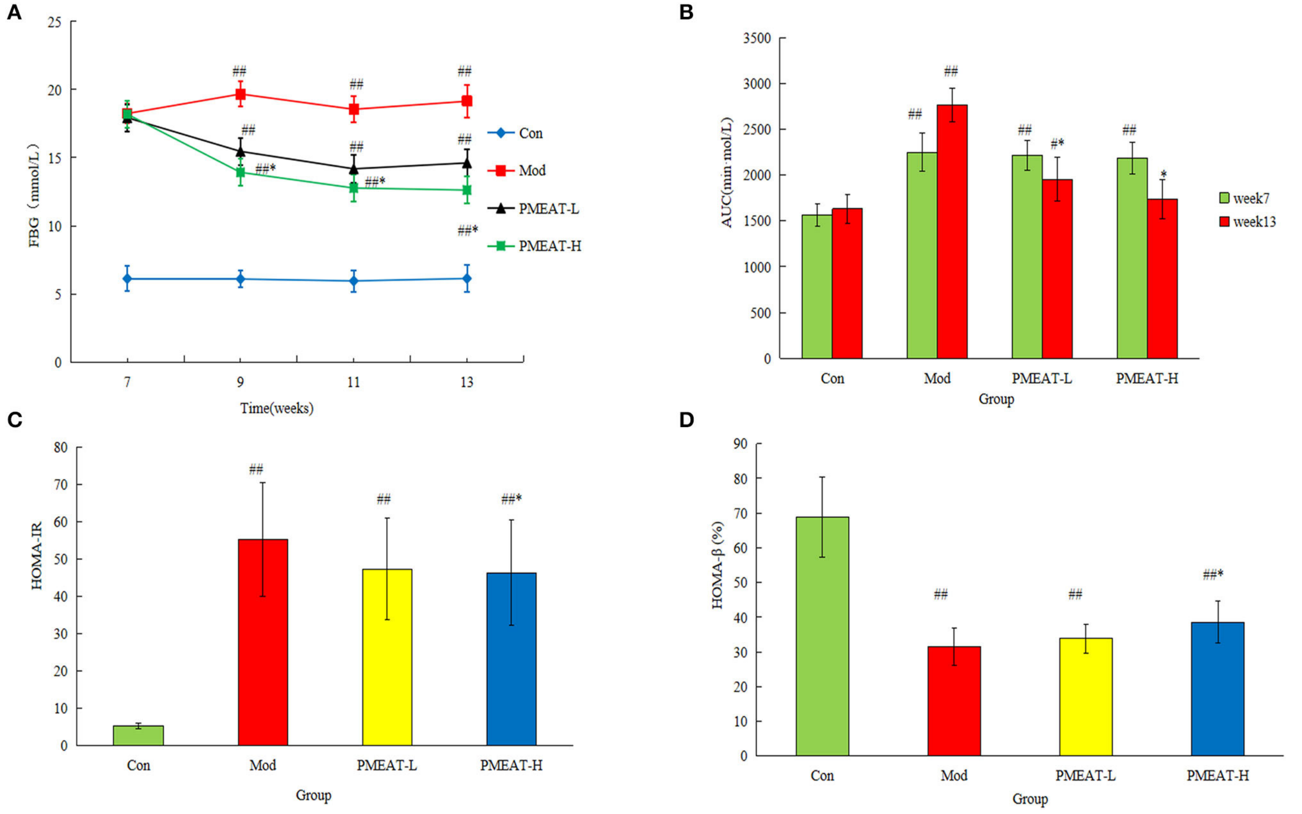

FIGURE 3 | The hypoglycemic effect of PMEAT on STZ-induced diabetic mice. **(A)** Fasting blood glucose of four observed groups at different time points. **(B)** AUC of four observed groups. **(C)** HOMA-IR of four observed groups. **(D)** HOMA-β of four observed groups. One-way ANOVA was applied to examine the differences among four groups. Superscript $^{\#}$ and $^{\#\#}$ indicate statistically significant differences compared with the Con group ($p < 0.05$) and ($p < 0.01$), respectively. Superscript * indicate statistically significant differences compared with the Mod group ($p < 0.05$). Con, control group; Mod, model group; PMEAT-L, low-dose PMEAT group; PMEAT-H, high-dose PMEAT group.

than rutin and curcumin when the concentration increased to 0.12 mg/mL. The IC_{50} was 0.04 mg/mL. FRAP assay is an indirect method based on a redox reaction to represent the antioxidant capacity of a test sample. The linear relationship between absorbance and $FeSO_4$ concentrations produced a significant straight line ($Y = 0.674X + 0.0511$, $R^2 = 0.9996$). As shown in **Figures 4C,D**, the FRAP values of the three tested substances increased as the concentrations increased, and showed a time-dependent feature. However, the FRAP values of PMEAT were lower than that of rutin and curcumin at the same concentration and same time point. This indicates that the methanol extract of *A. tsao-ko* is inferior to rutin and curcumin in total antioxidant capacity.

It was probably due to α, α-trehalose, and procyanidin A2 identified in the PMEAT led to the *in vitro* antioxidant activity. As explicated in a review article by Chaitanya et al. (29), trehalose possessed an antioxidant activity by targeting cell progression, angiogenesis, and metastasis pathways at the molecular level. In addition, Wang et al. (56) reported that procyanidin A2 protected cells against the damage from inflammation and oxidative injury by targeting NF-kB, MAPK, and Nrf2 pathways in RAW264.7 cells. As a mixture of natural ingredients, PMEAT contained plenty of components that belonged to different categories and had complex structures, and thus its total antioxidant capacity was lower than that of the standard samples (rutin and curcumin).

Antioxidant Activity of PMEAT *in vivo*

As shown in **Figure 5**, compared with the control group, the mice in the model group induced by D-galactose plus HFD showed a statistically significant decrease in the levels of SOD, GSH, and GSH-Px in plasma. On the other hand, levels of MDA and 8-ISO-PGF2α in the model group were significantly higher than that in the control group. However, the addition of PMEAT to the diet more obviously reversed these biochemical abnormalities in plasma after the oxidative damage. These antioxidant effects were dose-dependent, which means the PMEAT-H group was more effective than the PMEAT-L group in terms of the indices of SOD, GSH, and GSH-Px in plasma. As presented in **Figure 6**, similar antioxidant effects were seen for the indices of SOD, GSH, GSH-Px, and MDA in liver tissue. Many studies (52, 53) have proved that the natural plants which contained flavonoids,

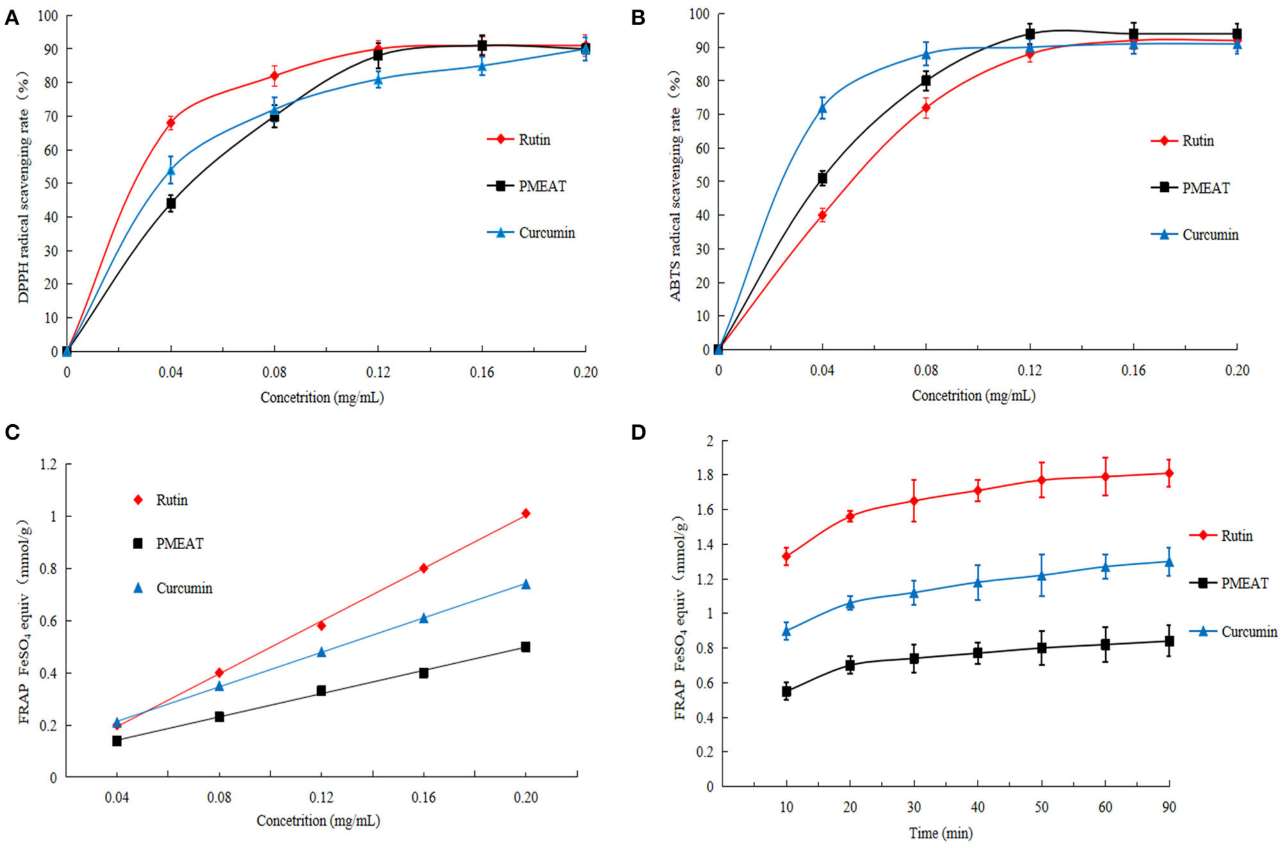

FIGURE 4 | The *in vitro* antioxidant activity of PMEAT. **(A)** DPPH scavenging effect of rutin, PMEAT, and curcumin. **(B)** ABTS scavenging effect of rutin, PMEAT, and curcumin. **(C)** Result of FRAP assay of rutin, PMEAT, and curcumin. **(D)** FRAP time-dependent curve of rutin, PMEAT, and curcumin.

phenols, and other ingredients with definite antioxidant effects would generally exhibit a good repairing effect on oxidative damage *in vivo*.

DISCUSSION

As a traditional Chinese medicine, *A. tsao-ko* has been studied by a few researchers at home and abroad (4–9). Using water extraction, ethanol extraction, and petroleum ether extraction, Liu et al. performed a comprehensive chemical investigation and found that the peel and the seeds of *A. tsao-ko* contained a variety of chemical components, including saccharide, protein, amino acids, phenolic compounds, tannins, organic acids, saponins, flavonoids, anthraquinone, coumarin, lactones, steroids, terpenoids, volatile oil, anthocyanins, and so on (32). Based on the previous results of animal experiments conducted with extracts by different extracting solvents, this study focused on the methanol extracts of *A. tsao-ko*, which were, nevertheless, seldom studied by other researchers. High-performance liquid chromatography with a mass spectrometry analysis revealed a total of 36 chemical components in PMEAT. To our knowledge, this is the first time the chemicals in the methanol extracts from the *A. tsao-ko* were isolated and qualitatively analyzed.

An accumulating body of evidence has shown that diabetic patients suffer from manifested oxidative stress due to hyperglycemia, hyperinsulinemia, and insulin resistance (33). Oxidative stress may bring about a variety of adverse effects to diabetes mellitus patients, such as endodermis cell injury and diabetic nephropathy. As a strategy to counteract the negative effect of oxidative stress, antioxidant-based therapy is becoming a promising way to minimize the complications associated with oxidative stress (34). This is why we examined both the anti-diabetic and the antioxidant effects of PMEAT in this study.

We evaluated the hypoglycemic activity of *A. tsao-ko in vitro* by an α-glucosidase assay. The IC_{50} of PMEAT on α-glucosidase was 0.145 mg/mL, which was lower than that of acarbose. Zhang et al. also investigated the hypoglycemic potential of methanol extract from *A. tsao-ko* by α-glucosidase assay and reported that the IC_{50} of α-glucosidase was 1.76 mg/mL (35). Under the action of α-glucosidase, glucose is released from the carbohydrates in food and enters the blood through the intestine, thereby leading to the increase of postprandial blood glucose. By slowing down the decomposition of starch into glucose, an α-glucosidase inhibitor delays or inhibits the absorption of glucose, and thus effectively reduces the postprandial hyperglycemia (36).

When blood glucose rises, appropriate amounts of insulin would be secreted from β cells to regulate the balance among

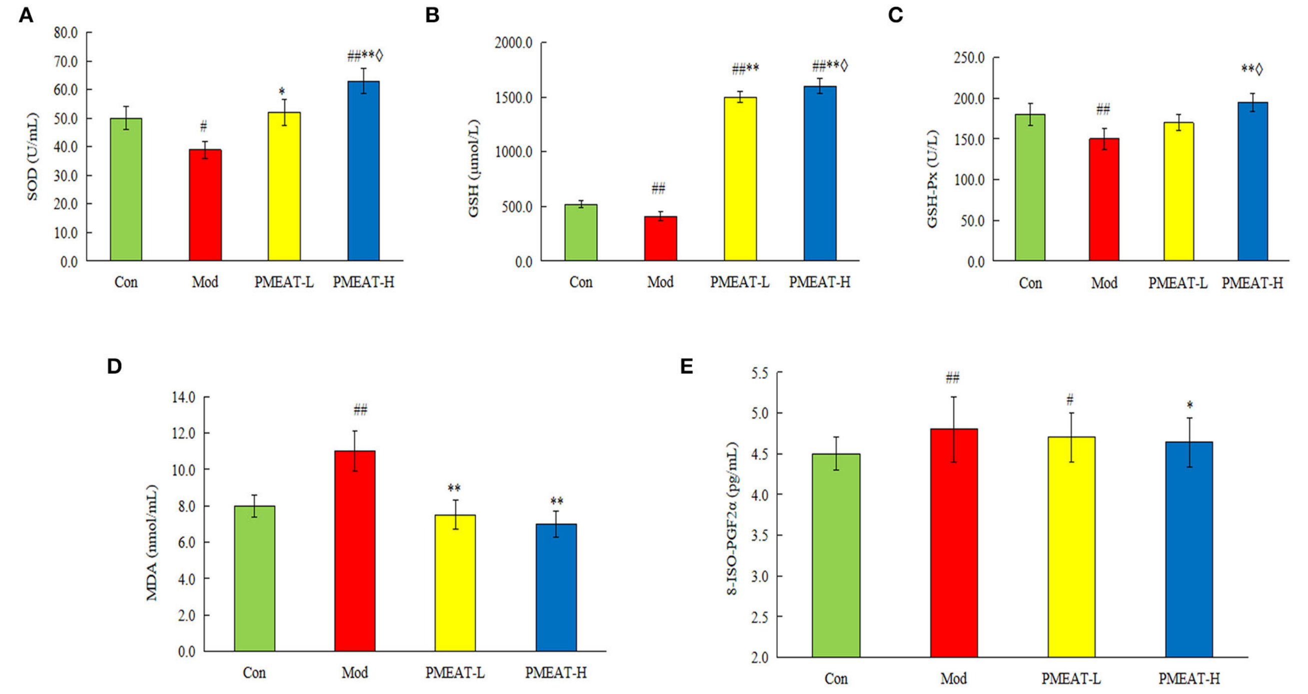

FIGURE 5 | Effect of PMEAT treatment on plasma SOD, GSH, GSH-Px, MDA, and 8-ISO-PGF2α. **(A)** Plasma SOD of four observed groups. **(B)** Plasma GSH of four observed groups. **(C)** Plasma GSH-Px of four observed groups. **(D)** Plasma MDA of four observed groups. **(E)** Plasma 8-ISO-PGF2α of four observed groups. One-way ANOVA was applied to examine the differences among the three groups. Superscript $^{\#}$ and $^{\#\#}$ indicate statistically significant differences compared with the Con group ($p < 0.05$) and ($p < 0.01$), respectively. Superscript * and ** indicate statistically significant differences compared with the Mod group ($p < 0.05$) and ($p < 0.01$), respectively. Superscript ◇ indicates a statistically significant difference compared with the PMEAT-L group ($p < 0.05$). Con, control group; Mod, model group; PMEAT-L, low-dose PMEAT group; PMEAT-H, high-dose PMEAT group.

muscle glycogen, liver glycogen, and blood glucose levels. In the current study, because of the cytotoxic effects of STZ on β cells, diabetic mice showed the symptoms of polyphagia, polyuria, polydipsia, and a severe loss in body weight. After the intervention with PMEAT for 6 weeks, the hyperglycemia, FBG, impaired glucose tolerance, and insulin resistance in mice were effectively improved, respectively. A similar finding was seen in the study performed by He et al. (37).

As many studies reported, polyphenols exhibited α-GIA through binding to α-glucosidase molecules. Polyphenols contain at least one aromatic ring with one or more hydroxyl groups in addition to other substituents. The interaction forces between polyphenols and α-glucosidase are expected to include hydrogen bonding and hydrophobic force. Electron delocalization between C=C (or C=O) and aromatic rings in polyphenols has been reported to enhance hydrophobic (π-π) interactions with α-glucosidase (38). Flavonoids, present in a wide variety of plant extracts, are the main substances in the polyphenols family. Its structure is represented by a benzene ring, condensed with a heterocyclic six-membered pyran or pyrone ring, which carries a phenyl ring in the second or third position as a substituent. In our study, 21 kinds of chemicals that belonged to flavonoids were identified in PMEAT (**Table 1**). Therefore, we speculate that the above *in vitro* and *in vivo* anti-diabetic effects of *A. tsao-ko* may be attributed to the biological activities of the flavonoid components.

Rutin and curcumin are often used as positive controls for the assessment of free radical scavenging capacity. In this study, the antioxidant capacity was evaluated from the perspectives of DPPH and ABTS free radical scavenging capacity. We found that the scavenging effect of DPPH and ABTS free radicals of PMEAT was inferior to that of curcumin at low concentrations but stronger than that of curcumin at high concentrations. The scavenging capacity of PMEAT on DPPH was weaker than that of rutin, but the scavenging effect on ABTS free radicals was stronger than that of rutin. These experimental results may be because the methanol extract from *A. tsao-ko* was a complex mixture and could not exhibit obvious antioxidant capacity at low concentrations. The antioxidant capacity increased considerably when the PMEAT solution reached a higher active concentration. This is consistent with the results of our previous studies (12, 13).

In *in vivo* study, an oxidative damage model of mice was established by D-galactose combined with a high-fat diet. Herein, we found that PMEAT treatment restored SOD, GSH-Px, and 8-ISO-PGF2α levels in the mice administered D-galactose to levels closer to or higher than those in the healthy mice. These results suggest that PMEAT can mitigate oxidative damage *in vivo*.

About the components associated with the antioxidant activity in PMEAT, we think that polyphenols and their derivatives,

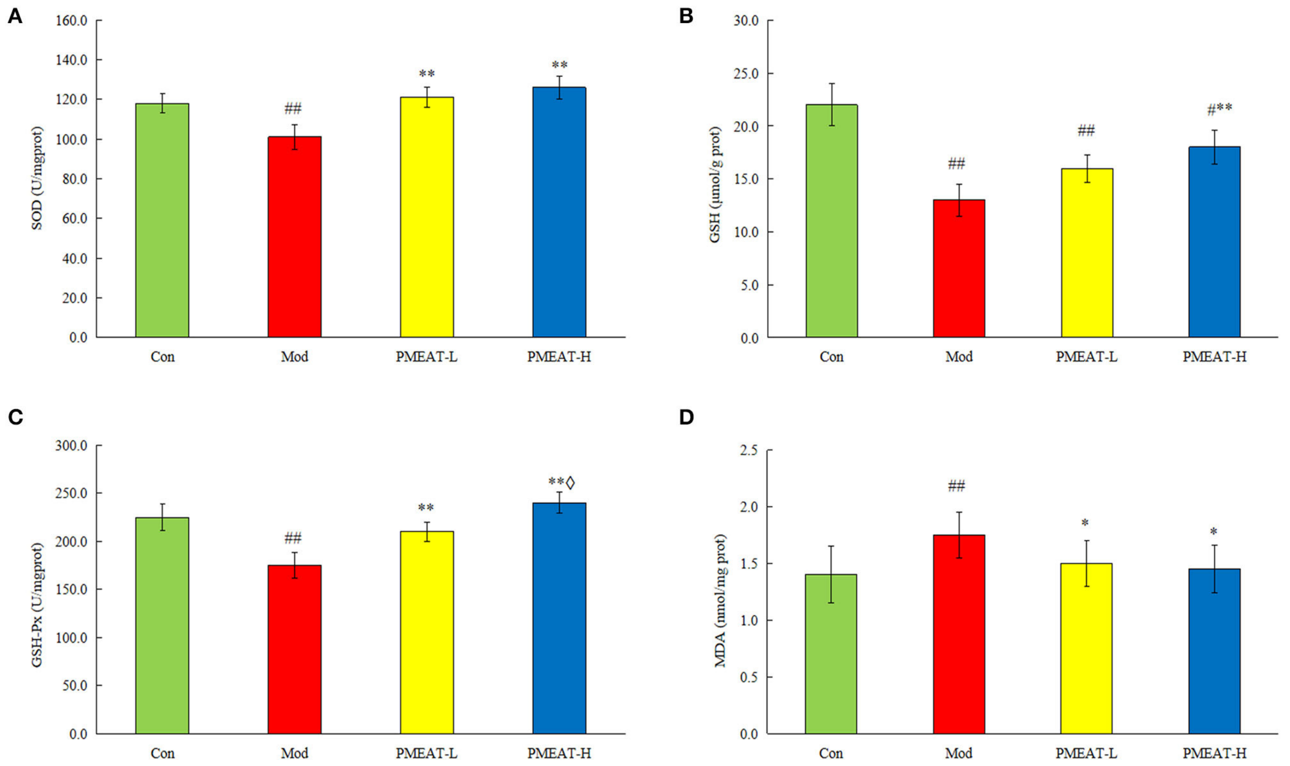

FIGURE 6 | Effect of PMEAT treatment on liver tissue SOD, GSH, GSH-Px, MDA, and 8-ISO-PGF2α. **(A)** Concentration of SOD in liver tissue of four observed groups. **(B)** Concentration of GSH in liver tissue of four observed groups. **(C)** Concentration of GSH-Px in liver tissue of four observed groups. **(D)** Concentration of MDA in liver tissue of four observed groups. One-way ANOVA was applied to examine the differences among four groups. Superscript $^{\#}$ and $^{\#\#}$ indicate statistically significant differences compared with the Con group ($p < 0.05$) and ($p < 0.01$), respectively. Superscript * and ** indicate statistically significant differences compared with the Mod group ($p < 0.05$) and ($p < 0.01$), respectively. Superscript ◇ indicates a statistically significant difference compared with the PMEAT-L group ($p<0.05$). Con, control group; Mod, model group; PMEAT-L, low-dose PMEAT group; PMEAT-H, high-dose PMEAT group.

polysaccharides, and coumarins probably played the regulating role. Consistently, Yuan et al. studied the flavonoids extract of *A. tsao-ko* and established that they had strong DPPH free radical scavenging ability (39). Li et al. found in the *in vitro* experiment that polyphenols extracted from *A. tsao-ko* exhibited DPPH and ABTS free radical scavenging ability (40). Anti-oxidation is an important property of polyphenols. The ortho-phenolic hydroxyl in the phenolic hydroxyl structure (catechol or pyrogallol) can be easily oxidized, thereby making polyphenols have a strong ability to capture free radicals as well as reactive oxygen species. In addition, multiple ortho-phenolic hydroxyls in polyphenols can be utilized as a poly-ligand to act with metal ions, thereby forming stable five-ring chelates. By making the metal ions inactive in this way, polyphenol molecules effectively regulate the oxidation process. Nevertheless, the specific bioactive compounds correlated to the biological effects still need further research.

CONCLUSION

Flavonoids, phenols, coumarins, oligosaccharides, and other bioactive constituents were identified in methanol extracts from *A. tsao-ko*. We confirmed the hypoglycemic potential of *A. tsao-ko* methanol extracts by α-glucosidase inhibition assay *in vitro* and STZ-induced mice intervention experiments *in vivo*. In addition, we verified the antioxidant activity of methanol extracts from *A. tsao-ko* by using free radical scavenging assays *in vitro* and D-glucose-induced mice intervention experiments *in vivo*. There were dose-effect relationships observed in the hypoglycemic and antioxidant properties of methanol extracts from *A. tsao-ko*. The functional mechanism of PMEAT and its impact on the human body have not yet been fully researched. Additional preclinical and clinical studies are required for the potential use of this natural herbal resource.

DATA AVAILABILITY STATEMENT

The original contributions presented in the study are included in the article/**Supplementary Material**, further inquiries can be directed to the corresponding author/s.

ETHICS STATEMENT

The animal study was reviewed and approved by Ethics Committee of Shijiazhuang University (approve number is SJZXY 20200501).

AUTHOR CONTRIBUTIONS

LY designed and supervised the study. LX, DY, YL, HJ, JC, and LH were involved in animal experimentation. YL and HJ performed the statistical analyses and interpreted the data. LX and DY drafted the manuscript. JC revised the article critically for important intellectual content. All authors approved the final version of the manuscript to be submitted. All authors contributed to the article and approved the submitted version.

FUNDING

This study was funded by the Foundation of the Department of Education of Hebei Province (QN2020525) and the Medical Science Research Project, Health Commission of Hebei Province (Key Science and Technology Research Program, No. 20210299).

ACKNOWLEDGMENTS

We thank all the participants and staff at the School of Chemical Engineering of Shijiazhuang University for their contribution to the study.

SUPPLEMENTARY MATERIAL

The Supplementary Material for this article can be found online at: https://www.frontiersin.org/articles/10.3389/fnut.2022.869749/full#supplementary-material

REFERENCES

1. Arroyo-Johnson C, Mincey KD. Obesity epidemiology worldwide. *Gastroenterol Clin North Am.* (2016) 45:571–79. doi: 10.1016/j.gtc.2016.07.012
2. Wang ZQ, Zhang YX, Yan HY. In situ net fishing of α-glucosidase inhibitors from evening primrose (*Oenothera biennis*) defatted seeds by combination of LC-MS/MS, molecular networking, affinity-based ultrafiltration, and molecular docking. *Food Funct.* (2022) 13:2545–58. doi: 10.1039/D1FO03975J
3. Darabi P, Khazali H, Natanzi MM. Therapeutic potentials of the natural plant flavonoid apigenin in polycystic ovary syndrome in rat model: via modulation of pro-inflammatory cytokines and antioxidant activity. *Gynecol Endocrinol.* (2020) 36:582–87. doi: 10.1080/09513590.2019.1706084
4. Park JH, Ahn EK, Hwang MH, Park YJ, Cho YR, Ko HJ, et al. Improvement of obesity and dyslipidemic activity of *amomum tsao-ko* in C57BL/6 mice fed a high-carbohydrate diet. *Molecules.* (2021) 26:1638. doi: 10.3390/molecules26061638
5. Shim KS, Hwang YH, Jang SA, Kim T, Ha H. Ethanol extract of *amomum tsao-ko* ameliorates ovariectomy-induced trabecular loss and fat accumulation. *Molecules.* (2021) 26:784. doi: 10.3390/molecules26040784
6. Kim JG, Jang H, Le TP, Hong HR, Lee MK, Hong JP, et al. Pyranoflavanones and pyranochalcones from the fruits of *Amomum tsao-ko*. *J Nat Prod.* (2019) 82:1886–92. doi: 10.1021/acs.jnatprod.9b00155
7. Hong SS, Lee JE, Jung YW, Park JH, Lee JA, Jeong W, et al. Monoterpenoids from the fruits of *amomum tsao-ko* have inhibitory effects on nitric oxide production. *Plants.* (2021) 10:257. doi: 10.3390/plants10020257
8. He XF, Zhang XK, Geng CA, Hu J, Zhang XM, Guo YQ, et al. Tsaokopyranols A–M, 2,6-epoxydiarylheptanoids from Amomum tsao-ko and their α-glucosidase inhibitory activity. *Bioorg Chem.* (2020) 96:103638. doi: 10.1016/j.bioorg.2020.103638
9. He XF, Wang HM, Geng CA, Hu J, Zhang XM, Guo YQ, et al. Amomutsaokols A–K, diarylheptanoids from *amomum tsao-ko* and their α-glucosidase inhibitory activity. *Phytochemistry.* (2020) 177:112418. doi: 10.1016/j.phytochem.2020.112418
10. Yu LQ, Shirai N, Suzuki H. Effects of some Chinese spices on body weights, plasma lipids, lipid peroxides, and glucose, and liver lipids in mice. *Food Sci Technol Res.* (2007) 13:155–61. doi: 10.3136/fstr.13.155
11. Yu LQ, Suzuki H. Effects of *tsao-ko* turmeric and garlic on body fat content and plasma lipid glucose and liver lipid levels in mice (A comparative study of spices). *Food Sci Technol Res.* (2007) 13:241–46. doi: 10.3136/fstr.13.241
12. Yu LQ, Shirai N, Suzuki H, Hosono T, Nakajima Y, Kajiwara M, et al. Effect of lipid extracted from *tsao-ko*(*Amomum tsao-ko* Crevost et Lemaire)on digestive enzyme activity, antioxidant activity,plasma and liver lipids, and blood glucose levels of mice. *J Nutr Sci Vitaminol.* (2008) 54:378–83. doi: 10.3177/jnsv.54.378
13. Yu LQ, Shirai N, Suzuki H, Sugane N, Hosono T, Nakajima Y, et al. The effect of methanol extracts of *tsao-ko* (*Amomum tsao-ko* Crevost et Lemaire) on digestive enzyme and antioxidant activity *in vitro,* and plasma lipids and glucose and liver lipids in mice. *J Nutr Sci Vitaminol.* (2010) 56:171–76. doi: 10.3177/jnsv.56.171
14. Yu LQ, Wang HY, Duan SD, Zhang WN. Effect of the ethanol extracts of *Amomum tsao-ko* on mouse physiology. *Food Scie Technol.* (2012) 37:182–86. doi: 10.13684/j.cnki.spkj.2012.10.009
15. Yan Q, Yu LQ, Chen Y, Wang HT, Zhang QY, Wei G. Study on mechanism of antioxidant effect of methanol extracts from *tsao-ko* (*amomum tsao-ko* crevost et lemaire) in aged mice induced by D-galactose. *Sci Technol Food Industry.* (2014) 35:351–56. doi: 10.13386/j.issn1002-0306.2014.06.085
16. Wang XM, Chang XY, Luo XM, Su MF, Xu R, Chen J, et al. An integrated approach to characterize intestinal metabolites of four phenylethanoid glycosides and intestinal microbe-mediated antioxidant activity evaluation *in vitro* using UHPLC-Q-Exactive high-resolution mass spectrometry and a 1,1-diphenyl-2-picrylhydrazyl-based assay. *Front Pharmacol.* (2019) 10:826. doi: 10.3389/fphar.2019.00826
17. Cheng XX, Chen LY, Zheng SJ, Tang XM, Yang Q. Fingerprint establishment content determination and α-glucosidase inhibitory activity study of polysaccharide from Desmodium Styracifolium. *China Pharmacy.* (2020) 31:182–89. doi: 10.6039/j.issn.1001-0408.2020.02.11
18. Guo CR, Zhang CF, Li L, Wang ZZ, Xiao W, Yang ZL. Hypoglycemic and hypolipidemic effects of oxymatrine in high-fat diet and streptozotocin-induced diabetic rats. *Phytomedicine.* (2014) 21:807–14. doi: 10.1016/j.phymed.2014.02.007
19. Tahara A, Matsuyama-Yokono A, Shibasaki M. Effects of antidiabetic drugs in high-fat diet and streptozotocin–nicotinamide-induced type 2 diabetic mice. *Eur J Pharmacol.* (2011) 655:108–16. doi: 10.1016/j.ejphar.2011.01.015
20. Guo CC, Zhang XY, Yu YX, Xie L, Chang CQ. Effects of chlorogenic acid on glucose toleranceand its curve characteristics in high-fat diet-induced obesity rats. *J Peking Univ.* (2020) 52:269–74. doi: 10.19723/j.issn.1671-167x.2020.02.012
21. Zhang Z, Xu JY, Chen JP, Liu WX, Pu SH, Li HQ, et al. Effect of mulberry on glucose regulation in mice fed with high-fat diet. *Chinese J Public Health.* (2020) 36:1157–59. doi: 10.11847/zgggws1119596
22. Cui T, Li XY, Wang RF, An XN, Cui C, Gao Z. Determination of methanol content in hawthorn wine and its DPPH & ABTS free radicals scavenging activities. *Liquor Making Sci Technol.* (2015) 7:17–20. doi: 10.13746/j.njkj.2015022
23. Guo CJ, Yang JJ, Li YF, Xu J, Wei JY, Jiang YG. Antioxidant capacity of different parts of fruits determined by FRAP assay. *Chinese J Public Health.* (2003) 19:841–43. doi: 10.3321/j.issn:1001-0580.2003.07.038
24. NHFPC. *National Food Safety Standard-Procedures for Toxicological Assessment of Food*. Beijing.
25. Qian Y, Zhang J, Zhou X, Yi RK, Mu JF, Long XY, et al. *Lactobacillus plantarum* CQPC11 isolated from *Sichuan* pickled cabbages antagonizes D-galactose-induced oxidation and aging in mice. *Molecules.* (2018) 23:3026. doi: 10.3390/molecules23113026

26. Zhao X, Song JL, Yi RK, Li GJ, Sun P, Park KY, et al. Comparison of antioxidative effects of insect tea and its raw tea (kuding tea) polyphenols in kunming mice. *Molecules.* (2018) 23:204. doi: 10.3390/molecules23010204
27. He XF, Chen JJ, Li TZ, Zhang XK, Guo YQ, Zhang XM, et al. Nineteen new flavanol-fatty alcohol hybrids with α-glucosidase and PTP1B dual inhibition: one unusual type of antidiabetic constituent from *amomum tsao-ko*. *J Agric Food Chem.* (2020) 68:11434–48. doi: 10.1021/acs.jafc.0c04615
28. Liu LJ, Zhao YM, Ming J, Chen J, Zhao GH, Chen ZY, et al. Polyphenol extract and essential oil of *Amomum tsao-ko* equally alleviate hypercholesterolemia and modulate gut microbiota. *Food Funct.* (2021) 12:12008–21. doi: 10.1039/D1FO03082E
29. Chaitanya NS, Devi A, Sahu S, Alugoju P. Molecular mechanisms of action of trehalose in cancer: a comprehensive review. *Life Sci.* (2021) 269:118968. doi: 10.1016/j.lfs.2020.118968
30. Cani PD, Bibiloni R, Knauf C, Waget A, Neyrinck AM, Delzenne NM, et al. Changes in gut microbiota control metabolic endotoxemia-induced inflammation in high-fat diet-induced obesity and diabetes in mice. *Diabetes.* (2008) 57:1470–81. doi: 10.2337/db07-1403
31. Rouzbehan S, Moein S, Homaei A, Moein MR. Kinetics of α-glucosidase inhibition by different fractions of three species of Labiatae extracts: a new diabetes treatment model. *Pharm Biol.* (2017) 55:1483–8. doi: 10.1080/13880209.2017.1306569
32. Liu XL, Qiu HY, Wang Q, Wu LY, Zhang CH. Qualitative study on chemical constituents of *Amomum tsao-ko*. *China Condiment.* (2011) 36:104–6. doi: 10.3969/j.issn.1000-9973.2011.01.030
33. Tepić S, Petković A, Srejović I, Jeremić N, Zivković V, Loncarević S, et al. Impact of hyperbaric oxygenation on oxidative stress in diabetic patients. *Undersea Hyperbaric Med.* (2018) 45:9–17. doi: 10.22462/01.02.2018.2
34. Rad NR, Movahedian A, Feizi A, Aminorroaya A, Aarabi MH. Antioxidant effects of astaxanthin and metformin combined therapy in type 2 diabetes mellitus patients: a randomized double-blind controlled clinical trial. *Res Pharm Sci.* (2022) 17:219–30. doi: 10.4103/1735-5362.335179
35. Zhang XF, Tang YJ, Guan XX, Lu X, Li J, Chen XL, et al. Flavonoid constituents of *Amomum tsao-ko* Crevost et Lemarie and their antioxidant and antidiabetic effects in diabetic rats–*in vitro* and *in vivo* studies. *Food Funct.* (2022) 13:437–50. doi: 10.1039/D1FO02974F
36. Flores-Bocanegra L, Gonzalez-Andrade M, Bye R, Linares E, Mata R. α-Glucosidase inhibitors from *Salvia circinata*. *J Nat Prod.* (2017) 80:1584–93. doi: 10.1021/acs.jnatprod.7b00155
37. He XF, Chen JJ, Huang XY, Hu J, Zhang XK, Guo YQ, et al. The antidiabetic potency of *Amomum tsao-ko* and its active flavanols, as PTP1B selective and α-glucosidase dual inhibitors. *Ind Crops Prod.* (2020) 160:112908. doi: 10.1016/j.indcrop.2020.112908
38. Xiao JB, Ni XL, Kai GY, Chen XQ. A review on structure–activity relationship of dietary polyphenols inhibiting α-amylase. *Crit Rev Food Sci Nutr.* (2013) 53:497–506. doi: 10.1080/10408398.2010.548108
39. Yuan Y, Zhang X, Chen BQ, Yang G. Extraction method and DPPH radical scavenging activity of flavonoids from *Amomum tsao-ko*. *Food Res Dev.* (2017) 38:63–8. doi: 10.3969/j.issn.1005-6521.2017.15.014
40. Li ZJ, Wang HY, Gu LL, Hang Y, Zheng YL, Zhang MX, et al. Extraction and LC-MS/MS analysis of the polyphenols from *Amomum tsao-ko*. *Sci Technol Food Industry.* (2017) 38:294–9. doi: 10.13386/j.issn1002-0306.2017.08.049
41. Zhu LJ, Luo D, Lv N, Li YK, Mi QL, Wang J, et al. Two new coumarins from the roots and stems of nicotiana tabacum and their bioactivity. *Chem Nat Comp.* (2020) 56:806–10. doi: 10.1007/s10600-020-03157-1
42. Celikezen FC, Orek C, Parlak AE, Sarac K, Turkez H, Tozlu ÖÖ. Synthesis, structure, cytotoxic and antioxidant properties of 6-ethoxy-4-methylcoumarin. *J Mol Struct.* (2020) 1205:127577. doi: 10.1016/j.molstruc.2019.127577
43. Tung MC, Fung KM, Hsu HM, Tseng TS. Discovery of 8-prenylnaringenin from hop (*Humulus lupulus* L.) as a potent monoacylglycerol lipase inhibitor for treatments of neuroinflammation and Alzheimer's disease. *RSC Adv.* (2021) 11:31062–72. doi: 10.1039/D1RA05311F
44. Abu-Zeitone A, Peterson DR, Polonsky B, McNitt S, Moss AJ. Efficacy of different beta-blockers in the treatment of long QT syndrome. *J Am Coll Cardiol.* (2014) 64:1352–8. doi: 10.1016/j.jacc.2014.05.068
45. Gai HY, Zhou F, Zhang YX, Ai JY, Zhan JC, You YL, et al. Coniferaldehyde ameliorates the lipid and glucose metabolism in palmitic acid-induced HepG2 cells via the LKB1/AMPK signaling pathway. *J Food Sci.* (2020) 85:4050–60. doi: 10.1111/1750-3841.15482
46. Amic A, Milenkovic D, Markovic Z, Cagardova D, Rodriguez GP, Dimitric MJ. Impact of the phenolic O-H vs. C-ring C-H bond cleavage on the antioxidant potency of dihydrokaempferol. *New J Chem.* (2021) 45:7977–86. doi: 10.1039/D1NJ00690H
47. Chen L, Fang YC, Zhu TJ, Gu QQ, Zhu WM. Gentisyl alcohol derivatives from the marine-derived fungus *Penicillium terrestre*. *J Nat Prod.* (2008) 71:66–70. doi: 10.1021/np070421v
48. Ku SK, Kim TH, Lee S, Kim SM, Bae JS. Antithrombotic and profibrinolytic activities of isorhamnetin-3- O -galactoside and hyperoside. *Food Chem Toxicol.* (2013) 53:197–204. doi: 10.1016/j.fct.2012.11.040
49. Shen Q, Shao JL, Peng Q, Zhang WJ, Ma L, Chan AS, et al. Hydroxycoumarin derivatives: novel and potent α-glucosidase inhibitors. *J Med Chem.* (2010) 53:8252–9. doi: 10.1021/jm100757r
50. Li SJ, Wang RM, Hu XP, Li CF, Wang L. Bio-affinity ultra-filtration combined with HPLC-ESI-qTOF-MS/MS for screening potential α-glucosidase inhibitors from *Cerasus humilis* (Bge.) Sok. leaf-tea and *in silico* analysis. *Food Chem.* (2022) 373:131528. doi: 10.1016/j.foodchem.2021.131528
51. Rasouli H, Hosseini-Ghazvini SM, Adibi H, Khodarahmi R. Differential α-amylase/α-glucosidase inhibitory activities of plant-derived phenolic compounds: a virtual screening perspective for the treatment of obesity and diabetes. *Food Funct.* (2017) 8:1942–54. doi: 10.1039/C7FO00220C
52. Yu JW, Li W, You BY, Yang SY, Xian WY, Deng Y, et al. Phenolic profiles, bioaccessibility and antioxidant activity of plum (*Prunus Salicina* Lindl). *Food Res Int.* (2021) 143:110300. doi: 10.1016/j.foodres.2021.110300
53. Magiera S, Baranowska I, Lautenszleger A. UHPLC–UV method for the determination of flavonoids in dietary supplements and for evaluation of their antioxidant activities. *J Pharm Biomed Anal.* (2015) 102:468–75. doi: 10.1016/j.jpba.2014.10.004
54. Li MQ, Bao X, Zhang XT Ren HB, Cai SB, Hu XS, et al. Exploring the phytochemicals and inhibitory effects against α-glucosidase and dipeptidyl peptidase-IV in Chinese pickled chili pepper: insights into mechanisms by molecular docking analysis. *LWT Food Sci Technol.* (2022) 162:113467. doi: 10.1016/j.lwt.2022.113467
55. Gao JM, Niu S, Li K, Li DF, Chen NN, Li HB. Antioxidant effects of hyperoside in aging mice induced by D-galactose. *Pharmacol Clin Chinese Mater Med.* (2017) 33:57–9. doi: 10.13412/j.cnki.zyyl.2017.01.016
56. Wang QQ, Gao HW, Yuan RY, Han S, Li XX, Tang MW, et al. Procyanidin A2, a polyphenolic compound, exerts anti-inflammatory and anti-oxidative activity in lipopolysaccharide-stimulated RAW264.7 cells. *PLoS ONE.* (2020) 15:e0237017. doi: 10.1371/journal.pone.0237017
57. Huneif MA, Alshehri DB, Alshaibari KS, Dammaj MZ, Mahnashi MH, Majid SU, et al. Design, synthesis and bioevaluation of new vanillin hybrid as multitarget inhibitor of α-glucosidase, α-amylase, PTP-1B and DPP4 for the treatment of type-II diabetes. *Biomed Pharmacother.* (2022) 150:113038. doi: 10.1016/j.biopha.2022.113038
58. Bai YC, Jian JH, Liu DH, Zhao XB. Synthesis, characterization and application of a new biomass-based antioxidant derived from vanillin and methyl ethyl ketone. *J Clean Prod.* (2021) 316:128315. doi: 10.1016/j.jclepro.2021.128315
59. Lu W, Cui Y, Zhang LL. Isofraxidin exerts anti-diabetic, antilipidemic, and antioxidant effects and protects renal tissues via inhibition of NF-$_k$B in Streptozotocin-induced diabetic rats. *Mol Cell Toxicol.* (2022) 1:1–11. doi: 10.1007/s13273-021-00204-y
60. Zhou XQ, Chen YQ, Yin ZP, Liang Q, Zang JW, Tang DB, et al. Inhibitory effect of naringin on α-glucosidase and its mechanism. *Sci Technol Food Industry.* (2022) 43:157–64. doi: 10.13386/j.issn1002-0306.2021080184
61. Wang ZQ, Wu ZY, Zuo GL, Lim SS, Yan HY. Defatted seeds of *Oenothera biennis* as a potential functional food ingredient for diabetes. *Foods.* (2021) 10:538. doi: 10.3390/foods10030538

62. Yu YF, Li HY, Zhang B, Wang JW, Shi XP, Huang JZ, et al. Nutritional and functional components of mulberry leaves from different varieties: evaluation of their potential as food materials. *Int J Food Properties*. (2018) 21:1495–507. doi: 10.1080/10942912.2018.1489833

Conflict of Interest: The authors declare that the research was conducted in the absence of any commercial or financial relationships that could be construed as a potential conflict of interest.

Advantages of publishing in Frontiers

OPEN ACCESS
Articles are free to read
for greatest visibility
and readership

FAST PUBLICATION
Around 90 days
from submission
to decision

HIGH QUALITY PEER-REVIEW
Rigorous, collaborative,
and constructive
peer-review

TRANSPARENT PEER-REVIEW
Editors and reviewers
acknowledged by name
on published articles

Frontiers
Avenue du Tribunal-Fédéral 34
1005 Lausanne | Switzerland

Visit us: www.frontiersin.org
Contact us: frontiersin.org/about/contact

REPRODUCIBILITY OF RESEARCH
Support open data
and methods to enhance
research reproducibility

DIGITAL PUBLISHING
Articles designed
for optimal readership
across devices

FOLLOW US
@frontiersin

IMPACT METRICS
Advanced article metrics
track visibility across
digital media

EXTENSIVE PROMOTION
Marketing
and promotion
of impactful research

LOOP RESEARCH NETWORK
Our network
increases your
article's readership